

# **Laser-Induced Functional Carbon Nanofibers for Electrochemical Sensing**

Dissertation zur Erlangung des  
**Doktorgrades der Naturwissenschaften**

(Dr. rer. nat.)

an der Fakultät Chemie und Pharmazie  
der Universität Regensburg  
Deutschland



Vorgelegt von

**Marcel Simsek**

aus Hilpoltstein

im Jahr 2020





# **Laser-Induced Functional Carbon Nanofibers for Electrochemical Sensing**

Dissertation zur Erlangung des  
**Doktorgrades der Naturwissenschaften**

(Dr. rer. nat.)

an der Fakultät Chemie und Pharmazie  
der Universität Regensburg  
Deutschland



Vorgelegt von

**Marcel Simsek**

aus Hilpoltstein

im Jahr 2020

Die vorliegende Dissertation entstand in der Zeit von Oktober 2017 bis Dezember 2020 am Institut für Analytische Chemie, Chemo- und Biosensorik der Universität Regensburg.

Die Arbeit wurde angeleitet von Prof. Dr. Antje J. Bäumner.

Promotionsgesuch eingereicht am: 02.12.2020

Kolloquiumstermin: 04.02.2021

## **Prüfungsausschuss**

Vorsitzender: Prof. Dr. Oliver Tepner

Erstgutachterin: Prof. Dr. Antje J. Bäumner

Zweitgutachter: PD Dr. Axel Dürkop

Drittprüfer: Prof. Dr. Reinhard Rachel



## Acknowledgements

First, I want to especially thank **Prof. Dr. Antje J. Baeumner** for providing me the chance to carry out my research studies. I would also like to thank for her motivational guidance whenever scientific challenges or questions came up so that I never felt lost. I highly appreciated the working atmosphere at the institute which was pleasant while still always being goal-oriented thanks to her leadership.

I would like to share special thanks with my supervisor **Dr. Nongnoot Wongkaew** for the immense help from the beginning on, covering experimental studies or developing writing expertise. Without her my total research outcome and personal development would surely have been less pronounced.

Further, I wish to thank **PD Dr. Axel Duerkop** for involving me in the research project about biogenic amine detection. I am also thankful for his input on research related and general questions and his immediate willingness of taking the role of my second reviewer.

I want to express my gratitude to **Prof. Dr. Reinhard Rachel** for training me on scanning electron microscopy, for taking time to help me to improve whenever possible and for being my third reviewer. I really appreciate as all of this is not self-evident from a professor belonging to a different institute.

I want to thank **Dr. Marc Schlosser** for the support with EDX and XRD experiments. Also, I am grateful for the help by **Apl. Prof. Dr. Rainer Mueller** with thermogravimetric analysis and Brunauer-Emmet-Teller surface area analysis. I would like to thank **Prof. Dr. Oliver Tepner** for being chairman in my doctoral examination.

In addition, I want to say thanks to all **lab members** that helped me directly on experiments but also indirectly by being friendly and enabling enjoyable scientific environment.

Last but not least, I want to thank my **parents** and **family members** for all of their ongoing support carrying me through difficult times.



## **Declaration of Collaborations**

This work was conducted in large degrees of experimental and theoretical work solely by the author. However, at some points collaborations with other researchers were conducted to generate results, which is stated in this chapter in accordance with §8 Abs. 1 Satz 2 Punkt 7 of the “Ordnung zum Erwerb des akademischen Grades eines Doktors der Naturwissenschaften (Dr. rer. nat.) an der Universität Regensburg vom 18. Juni 2009“.

### **Laser-Induced Carbon Nanomaterials and Their Hybrids for Non-Enzymatic Electrochemical Sensing (Chapter 1)**

Parts of this chapter will be further used as a manuscript that is intended to be submitted to Analytical and Bioanalytical Chemistry as a critical review article in a topical collection focusing on biomimetic recognition elements. The author and Dr. Nongnoot Wongkaew contributed equally in literature search and manuscript preparation.

### **A Robust Strategy Enabling Addressable Porous 3D Carbon-Based Functional Nanomaterials in Miniaturized Systems (Chapter 3)**

This chapter has been published. The author and Dr. Nongnoot Wongkaew contributed equally in designing and conducting the experiments and evaluating the data. Dr. Nongnoot Wongkaew and Prof. Dr. Antje J. Baeumner wrote the manuscript draft. Dr. Arumugam Palaniappan and Arne Behrent carried out preliminary studies. Prof. Dr. Antje J. Baeumner and Dr. Sheela Berchmans led the project administration and promoted manuscript preparation. Prof. Dr. Reinhard Rachel supported SEM imaging and Apl. Prof. Dr. Rainer Mueller helped with surface area analysis. Part of the SEM images was recorded at the Council of Scientific and Industrial Research - Central Electrochemical Research Institute, Karaikudi, India. Additionally, Dr. Thomas Hirsch and Prof. Dr. Husam N. Alshareef contributed with comments on the preparation of the manuscript for publication.

### **Printable 3D Carbon Nanofiber Networks with Embedded Metal Nanocatalysts (Chapter 4)**

This chapter has been published. The author and Dr. Nongnoot Wongkaew conceived the studies and wrote the manuscript. Prof. Dr. Antje J. Baeumner led the project administration and promoted manuscript preparation. The author performed the experiments. Dr. Marc Schlosser carried out EDX and XRD measurements. Kilian Hoecherl supported experiment implementation and validation. TEM imaging was performed by Prof. Dr. Reinhard Rachel.

### **Non-Enzymatic Detection of Hydrogen Peroxide via Laser-Induced Carbon Nanofiber Hybrids (Chapter 5)**

This chapter has not been published. All experiments were performed by the author. The author wrote this chapter and Dr. Nongnoot Wongkaew contributed with strategic discussions on the finalization. Prof. Dr. Antje J. Baeumner was the leader of this project.

## Table of Contents

<b>Used Symbols and Abbreviations .....</b>	<b>1</b>
<b>List of Figures.....</b>	<b>4</b>
<b>List of Figures (Supporting Information) .....</b>	<b>7</b>
<b>List of Tables.....</b>	<b>9</b>
<b>List of Tables (Supporting Information).....</b>	<b>10</b>
<b>1 Laser-Induced Carbon Nanomaterials and Their Hybrids for Non-Enzymatic Electrochemical Sensing.....</b>	<b>11</b>
1.1 Abstract .....	11
1.2 Introduction .....	12
1.3 Non-Enzymatic Electrochemical Sensors .....	15
1.3.1 State of the Art, Definition and Advantages.....	15
1.3.2 Material Dimension, Preparation and Impact on Sensing .....	16
1.3.3 Metal-Based Catalysts .....	20
1.3.4 Carbon and Derivatives .....	22
1.3.5 Analytes .....	24
1.4 Laser-Induced Carbon Nanomaterials and Their Hybrids .....	31
1.4.1 Laser-Induced Carbonization.....	31
1.4.2 Lasing Parameters vs. Carbon Quality .....	32
1.4.3 Laser-Induced Functional Nanocatalysts.....	33
1.4.4 Laser-Induced Carbon Nanofibers.....	34
1.4.5 Sensing Applications .....	36
1.5 Conclusion and Outlook.....	40
<b>2 Motivation and Structure of the Thesis .....</b>	<b>43</b>
<b>3 A Robust Strategy Enabling Addressable Porous 3D Carbon-Based Functional Nanomaterials in Miniaturized Systems.....</b>	<b>47</b>
3.1 Abstract .....	47
3.2 Introduction .....	48
3.3 Material and Methods .....	52
3.3.1 Electrospinning of Matrimid® Nanofibers.....	52
3.3.2 Laser-Induced Carbonization of Electrospun Matrimid® Nanofibers .....	52
3.3.3 Morphology Characterization .....	52



3.3.4	Electrochemical and Electrical Characterization.....	52
3.3.5	Chemical Characterization.....	53
3.4	Results and Discussion.....	54
3.4.1	Effect of Electrospinning Conditions in Combination with Laser Power .....	54
3.4.2	Role of Iron.....	54
3.4.3	Effect of Laser Input on Characteristics of LCNF Electrodes.....	57
3.4.4	Applications of LCNFs as High Performance Electrodes for Electrochemical Sensors.....	59
3.5	Conclusion.....	61
3.6	Supporting Information.....	62
<b>4</b>	<b>Printable 3D Carbon Nanofiber Networks with Embedded Metal Nanocatalysts.....</b>	<b>69</b>
4.1	Abstract .....	69
4.2	Introduction .....	70
4.3	Materials and Methods.....	73
4.3.1	Preparation of LCNF .....	73
4.3.2	Morphology Characterization.....	73
4.3.3	Electrochemical Characterization.....	74
4.3.4	Mechanical Stability Test .....	74
4.4	Results and Discussion.....	75
4.4.1	Effect of Nickel Content on LCNF Morphology.....	75
4.4.2	Influence of Lasing Power on LCNF Morphology.....	78
4.4.3	Mechanical Stability of Embedded Metal Nanocatalysts.....	79
4.4.4	Electrochemical Glucose Sensing.....	80
4.5	Conclusion.....	85
4.6	Supporting Information.....	86
<b>5</b>	<b>Non-Enzymatic Detection of Hydrogen Peroxide via Laser-Induced Carbon Nanofiber Hybrids .....</b>	<b>93</b>
5.1	Abstract .....	93
5.2	Introduction .....	94
5.3	Materials and Methods.....	96
5.3.1	Fabrication of LCNF Electrodes.....	96
5.3.2	Electrochemical Characterization.....	96
5.3.3	Chemical Reduction.....	96
5.4	Results and Discussion.....	98
5.4.1	Effect of Varying Palladium Salts and Content.....	98
5.4.2	Non-Enzymatic H <sub>2</sub> O <sub>2</sub> Sensing.....	100

5.4.3	Chemical Reduction of Metal Compounds in LCNF .....	103
5.4.4	Bimetallic LCNF hybrids .....	103
5.5	Conclusion.....	106
<b>6</b>	<b>Conclusion and Future Perspectives .....</b>	<b>107</b>
<b>7</b>	<b>Summary.....</b>	<b>113</b>
<b>8</b>	<b>Zusammenfassung .....</b>	<b>115</b>
<b>9</b>	<b>References.....</b>	<b>119</b>
	<b>Curriculum Vitae .....</b>	<b>146</b>
	<b>Publications.....</b>	<b>148</b>
	<b>Presentations.....</b>	<b>149</b>
	<b>Eidesstattliche Erklärung.....</b>	<b>151</b>



## Used Symbols and Abbreviations

In the following, all used symbols and abbreviations, besides commonly known abbreviations, are explained. The page number refers to the first appearance in this thesis.

Symbol	Meaning	Page
$a$	Activity ( $\text{mol}\cdot\text{l}^{-1}$ )	13
$A$	Surface area ( $\text{m}^2$ )	13
$c$	Concentration ( $\text{mol}\cdot\text{l}^{-1}$ )	13
$\delta$	Diffusion layer thickness (m)	13
$D$	Diffusion coefficient ( $\text{m}^2\cdot\text{s}^{-1}$ )	13
$E$	Potential (V)	13
$F$	Faraday constant ( $96,485 \text{ C}\cdot\text{mol}^{-1}$ )	13
$I$	Current (A)	13
$I_{2D}$	Intensity of the 2D band (a.u.)	55
$I_D$	Intensity of the D band (a.u.)	55
$I_G$	Intensity of the G band (a.u.)	55
$k^0$	Standard rate constant ( $\text{m}\cdot\text{s}^{-1}$ )	56
$n$	Number of electrons	13
$R$	Universal gas constant ( $8.314 \text{ J}\cdot\text{mol}^{-1}\cdot\text{K}^{-1}$ )	13
$t$	Time (s)	58
$T$	Temperature (K)	13
Abbreviation	Meaning	Page
AA	Ascorbic acid	72
AC	Activated carbon	83
ATP	Attapulgite (palygorskite)	83
ATR	Attenuated total reflection	53
CNF	Carbon nanofiber	19
CNH	Carbon nanohorn	29
CNT	Carbon nanotube	24
CQD	Carbon quantum dot	23
CS	Chitosan	26
CV	Cyclic voltammetry	13
CVD	Chemical vapor deposition	16
DPI	Dots per inch	32

DPV	Differential pulse voltammetry	14
EC	Electrochemical	100
EDX	Energy-dispersive X-ray	45
EIS	Electrochemical impedance spectroscopy	30
eNi	Electrodeposited nickel	80
ERGO	Electrochemically reduced graphene oxide	28
ESA	Electroactive surface area	13
Fe(acac) <sub>3</sub>	Iron(III) acetylacetonate	96
FTIR	Fourier transform infrared spectroscopy	53
GCE	Glassy carbon electrode	83
Glu	Glucose	84
GO	Graphene oxide	28
GQD	Graphene quantum dot	23
HAC	Heteroatom-enriched activated carbon	83
HPDFO	High power density focusing optics	32
HPLC-MS	High-performance liquid chromatography-mass spectrometry	15
ITO	Indium tin oxide	35
LCNF	Laser-induced carbon nanofiber	35
LIG	Laser-induced graphene	32
LOD	Limit of detection	23
LSG	Laser-scribed graphene	28
MB	Methylene blue	26
MNP	Magnetic/Metallic nanoparticle	18
MWCNT	Multi-walled carbon nanotube	24
N	Number of electrodes scribed in one row	57
NADH	Nicotinamide adenine dinucleotide	35
NADPH	Nicotinamide adenine dinucleotide phosphate	94
NC	Nitrogen-doped carbon	83
ND	Not determined	56
Ni(acac) <sub>2</sub>	Nickel(II) acetylacetonate	72
NiHCF	Nickel hexacyanoferrate	81
NP	Nanoparticle	16
NW	Nanowire	83
OMC	Ordered mesoporous carbon	83
ORR	Oxygen reduction reaction	17
PAN	Polyacrylonitrile	34

PANI	Polyaniline	37
PB	Phosphate buffer	74
Pd(acac) <sub>2</sub>	Palladium(II) acetylacetonate	35
PDMS	Polydimethylsiloxane	25
PEDOT:PSS	Poly(3,4 ethylenedioxythiophene) polystyrene sulfonate	12
PET	Polyethylene terephthalate	35
PF	Pyrogallol-formaldehyde mixture	83
PI	Polyimide	32
ppb	Parts per billion	37
QD	Quantum dot	18
rGO	Reduced graphene oxide	26
ROS	Reactive oxygen species	94
rpm	Revolutions per minute	74
SD	Standard deviation	55
SEM	Scanning electron microscopy	31
SECM	Scanning electrochemical microscopy	17
SMWNT	Straight multi-walled carbon nanotubes	83
SPCE	Screen-printed carbon electrode	59
SPGE	Screen-printed gold electrode	59
SWCNT	Single-walled carbon nanotube	24
TCD	Tip-to-collector distance	54
TEM	Transmission electron microscopy	45
UA	Uric acid	72
UCNP	Upconverting nanoparticle	18
UPS	UV photoelectron spectroscopy	22
w/	With	80
w/o	Without	90
w/v	Weight per volume	52
XPS	X ray photoelectron spectroscopy	22
XRD	X-ray diffraction	77

## List of Figures

Figure 1.1: Overview of nanomaterials with different dimensions for electrochemical biosensors. Adapted with permission from Wongkaew <i>et al.</i> <sup>2</sup> .....	19
Figure 1.2: Laser-induced carbonization of commercial available polyimide foil (a) and respective scanning electron microscopy (SEM) images of the generated owl shape (b). Zoom-in of the circled part in (b) shows the sweeping line pattern typically obtained by the laser (c). The porous structure of LIG can be seen in the insets of (c) and the side view image of LIG surface on PI foil (d). Adapted with permission from Lin <i>et al.</i> <sup>110</sup> .....	31
Figure 1.3: Schemes of common carbon nanofiber preparation techniques CVD and thermal carbonization of electrospun nanofibers and the novel strategy of laser-induced carbonization of electrospun nanofibers.....	36
Figure 1.4: Wearable sensing systems based on laser-induced graphene. Panel i: Laser engraved lab-on-a-chip mounted on different body parts and wireless monitoring of uric acid, tyrosine, respiration rate and temperature via smartphone. Adapted with permission from Yang <i>et al.</i> <sup>161</sup> Panel ii: Scheme of transferring LIG generated on polyimide foil (a) by casting with PDMS (b) and subsequent peeling off (c). The LIG is now bound to PDMS (d) which offers elastic properties (e). Adapted with permission from Lamberti <i>et al.</i> <sup>162</sup> Panel iii: Transfer of LIG to Scotch brand tape that can be taped to the body and monitor analytes directly in produced sweat. Adapted with permission from Prabhakaran and Nayak. <sup>164</sup> Panel iv: Transfer of LIG to gas-permeable silicon elastomer sponges (a). Multi-sensing abilities and demonstration of the flexible behavior of the sensor (b). Adapted with permission from Sun <i>et al.</i> <sup>165</sup> .....	38
Figure 3.1: Facile construction of high performance carbon nanofiber electrodes via electrospinning and one-step laser-induced carbonization for electrochemical sensors in miniaturized systems. ....	48
Figure 3.2: Schematic illustration of electrospinning (a). Laser carbonization of electrospun nanofibers (b). A photograph of LCNF electrodes (c). SEM images of LCNFs (i and ii) after lasing a 15 min-fiber mat at 1.2 W (d) and 1.5 W (e) laser power, respectively. SEM images of LCNF (i and ii) after lasing a 30 min-fiber mat at 1.2 W (f) and 1.5 W (g), respectively. Corresponding current signals are shown in panel (iii). Matrimid <sup>®</sup> nanofibers here contained 3 % iron. Scale bars of (i) and (ii) are 20 $\mu\text{m}$ and 10 $\mu\text{m}$ , respectively.....	50
Figure 3.3: SEM images of fibers in the absence and presence of iron before lasing (i and iv) and after lasing (ii, iii, v and vi) with a laser power of 1.5 W (a). The red arrows indicate the integrity of fibers. Comparison of Raman spectra of nanofibers and LCNFs in the presence (i) and absence (ii) of iron (b).....	55
Figure 3.4: Effect of iron content and lasing technique on electrode fabrication. Dimension, design and lasing technique are shown underneath (a). The corresponding electroanalytical performance of LCNF electrodes evaluated by cyclic voltammetry using $[\text{Fe}(\text{CN})_6]^{4-/3-}$ (b). ND = not determined.....	56
Figure 3.5: Side views of a LIG electrode (a), electrospun Matrimid <sup>®</sup> nanofibers on ITO/PET (b) and LCNF on ITO/PET (c). The nanofiber samples contain 5 % iron.....	57

Figure 3.6: Effect of laser input on LCNF properties. Electrode designs for testing the hypothesis (a). The relationship between electrode number (N) in a row on laser input ( $t_{\text{total}}/t_{\text{N(i)}}$ ) per electrode (b). The inset SEM images display LCNF morphologies when lased the fibers with the electrode design shown in (a). The correlation of the electroanalytical and electrical properties of the LCNF with N (c). Electrochemical characterization of LCNFs lased at various N with different electrode width while maintaining ( $t_{\text{total}}/t_{\text{N(i)}}$ ) at 15 per electrode. Shown are the normalized actual cyclic voltammograms, the inset provides the calculated peak-to-peak separation (d)..... 58

Figure 3.7: Electroanalytical performance of LCNF electrodes towards some model biomarkers compared with SPCE and SPGE electrodes for NADH (a), hydrazine (b) and dopamine (c). The analytes were prepared with 1 mM concentration in 0.1 M phosphate buffer (pH 7.0). ..... 59

Figure 4.1: A simple approach of generating patternable 3D hybrids of laser-induced carbon nanofibers with embedded metal nanocatalyst..... 71

Figure 4.2: SEM images of the electrospun PI nanofibers (a) and LCNF after carbonization for different Ni salt contents (b). EDX elemental mapping showing the distribution of nickel molecules for LCNF (c). EDX was recorded with different samples compared to (b)..... 75

Figure 4.3: (i) SEM image of LCNF showing the selected field for EDX analysis (a). The lines enclose the carbonized part. Elemental mapping of nickel (b), carbon (c) and oxygen (d) demonstrating changes in non-scribed and scribed regions. Scale bars are 100  $\mu\text{m}$ . (ii) TEM images of Ni-LCNF at different magnifications. The lattice fringe spacing value of 0.34 nm was determined by TEM software. (iii) SEM images of electrospun solid Matrimid<sup>®</sup> nanofibers (a, b) and hollow LCNFs (c, d). All nanofibers displayed in this figure contained 25 % Ni. .... 76

Figure 4.4: Microscopic images of LCNF electrodes containing 25 % Ni after scribing with 0.9, 1.2, 1.5 and 1.8 W laser power (a). Corresponding SEM images of the top view (b) and side view (c). The scale bars are 10  $\mu\text{m}$ . The red circle (at 0.9 W) indicates an area where fibers were incompletely carbonized. .... 79

Figure 4.5: Amperometric response of LCNF containing different concentrations of Ni (5, 15 and 25 %) and 5 % Fe as control towards glucose injection (a). One injection step equals 1 mM glucose. Dose response upon glucose injection in 10  $\mu\text{M}$  steps (0-100  $\mu\text{M}$ , orange box), 100  $\mu\text{M}$  steps (100-1,000  $\mu\text{M}$ , blue box) and 1,000  $\mu\text{M}$  steps (1,000-10,000  $\mu\text{M}$ ) ( $n \geq 3$ ) (b). The potential was fixed at 0.55 V and the detection matrix consisted of 0.5 M NaOH..... 82

Figure 4.6: Amperometric response of LCNF containing different percentages of Ni towards successive 100  $\mu\text{M}$  glucose (Glu) addition and final addition of potential interferents ascorbic acid (AA) and uric acid (UA) (both 5  $\mu\text{M}$ ) ( $n = 3$ ) (a). Zoom-in of the amperograms for 5/15 % Ni content with noticeable steps after the addition of interferents (b). Amperometric response of LCNF containing 25 % Ni (c) and 5 % Ni (d) after the addition of 1 mM Glu and 50  $\mu\text{M}$  of AA and UA each. For 5 % Ni, the signals of both interferents are significantly higher than that of glucose, whereas for the 25 % Ni only glucose leads to an obvious signal response. The potential was fixed at 0.55 V and the detection matrix consisted of 0.5 M NaOH. In the case of fluctuating signals, the mean value was taken for evaluation. .... 84

Figure 5.1: Spinning solutions containing 15 % (w/v) Matrimid<sup>®</sup> and 15/25/35 % Pd(acac)<sub>2</sub> (a) or 15 % PdCl<sub>2</sub> (b). The red arrow at 35 % Pd(acac)<sub>2</sub> solution indicates precipitating metal salt. The PdCl<sub>2</sub> solution was mixed with NaCl (molar ratio of 2:1 to PdCl<sub>2</sub>) and the pictures show the change after heating on a hot plate at 70 °C compared to before. .... 98



- Figure 5.2: Photographs of Pd-LCNF containing 25 % Pd(acac)<sub>2</sub> obtained from 1.2 W and 1.5 W laser power (a) and Fe-LCNF containing 15/25 % Fe(acac)<sub>3</sub> obtained from 1.2 W and 0.9 W laser power respectively (b). ..... 99
- Figure 5.3: Cyclic voltammograms of 25 % Pd-LCNF in 0.1 M PB 10 mM H<sub>2</sub>O<sub>2</sub> w/o EC pretreatment (a) and w/ pretreatment at -1 V for 3 min for control and 10 mM H<sub>2</sub>O<sub>2</sub> (b). Cyclic voltammograms (three cycles) w/o H<sub>2</sub>O<sub>2</sub> (c) and w/ 100 μM H<sub>2</sub>O<sub>2</sub> (d) after pretreatment by 20 CV cycles from -0.8 V to 1 V in 0.5 M NaOH. The arrows in (d) describe the changes in heights of anodic and cathodic peak with ongoing cycling. .... 101
- Figure 5.4: Amperometric response of LCNF containing 25 % Pd, 25 % Fe (a), 5 % and 15 % Fe (b) towards successive 100 μM H<sub>2</sub>O<sub>2</sub> addition. The potential was fixed at -0.5 V and the detection matrix consisted of 0.1 M PB. .... 102
- Figure 5.5: Amperometric response of LCNF electrodes containing 25 % Pd or Fe towards 100 μM H<sub>2</sub>O<sub>2</sub> (n ≥ 3) after incubation 3 h and 24 h and without incubation. .... 103
- Figure 5.6: Cyclic voltammograms of Pd/Fe-LCNF electrodes containing 12.5 % of each metal salt in 0.1 M PB w/o and w/ 100 μM H<sub>2</sub>O<sub>2</sub> (a). The arrow indicates a current signal difference that can be linked to H<sub>2</sub>O<sub>2</sub>. Amperogram for 100 μM H<sub>2</sub>O<sub>2</sub> injections (b). The potential was fixed at -0.25 V and the detection matrix consisted of 0.1 M PB. .... 104

## List of Figures (Supporting Information)

- Figure S3.1: Preliminary investigation on finding out the proper substrate for collecting nanofibers. The photographs show the LCNF electrodes derived from Matrimid<sup>®</sup> nanofiber mat electrospun on ITO/PET sheet (a), aluminum foil (b), glass slide (c) and wax paper (d). ..... 62
- Figure S3.2: Effect of fiber mat density spun at various settings (area-time-TCD) on macroscopic morphologies of LCNF electrode at various laser powers (a). Quantification of the roughness of LCNFs (b). Effect of the electrospinning time on the microscopic fiber morphology (TCD = 10 cm). The red arrow indicates the obtained fiber structures after laser-induced carbonization (c). ..... 63
- Figure S3.3: Panel (i): cyclic voltammograms at various scan rates for LCNF electrodes lased at 1.5 W (a), 1.2 W (b) and screen-printed carbon electrode (SPCE) (c) ran in 1 mM ferri/ferrocyanide (in 0.1 M phosphate buffer, pH 7.0, 0.1 M KCl). Panel (ii): Randles-Sevcik plots for the corresponding voltammograms in panel (i). The diameter of the electrodes was 3 mm<sup>2</sup>. The nanofibers contained 3 % iron..... 64
- Figure S3.4: FTIR-ATR spectra of LCNF electrodes. LCNF + Matrimid<sup>®</sup> NFs-ITO/PET was prepared from applying the laser out of focus (-2 mm) 30 times..... 65
- Figure S3.5: Effect of laser power on LCNF fabrication (15 min-fiber mat) (a). Setup for lasing a nanofiber mat with high number of electrodes in a row (30 min-fiber mat). The photographs (inset) show the LCNF electrodes after scribing on the front and back side (b). Matrimid<sup>®</sup> nanofibers in (a) and (b) contain 3 % and 5 % iron, respectively. .... 66
- Figure S3.6: The  $t_{total}/t_{N(i)}$  of 15 per electrode was applied to the designs that consist of various electrode numbers and widths while maintaining  $t_{total}$ .  $t_{N(i)}$  for N2, N4 and N8 is ca. 1.08 s, 2.17 s and 4.34 s, respectively. .... 66
- Figure S3.7: Three cycles of cyclic voltammograms of 1 mM ferri/ferrocyanide from LCNF electrode treated with 1 min UV/ozone. The LCNF electrode was prepared from 5 % iron nanofibers and lased at 1.5 W laser power with a speed of 762 mm·s<sup>-1</sup> (a). Contact angles of (i) LCNF electrode and (ii) UV/ozone-treated LCNF electrode (b). Cyclic voltammogram of 1 mM dopamine using UV/ozone-treated LCNF electrode (c). .... 67
- Figure S4.1: SEM images of LCNFs for different Ni salt contents at high magnification showing significantly more pronounced fibrous structures of 25 % Ni compared to 5 % and 15 % (a) and low magnification demonstrating homogenous overall morphology (b). .... 86
- Figure S4.2: SEM images of LCNF containing 15 % Ni and 5 % Fe demonstrating morphological similarities. .... 87
- Figure S4.3: Photographs of LCNF (1.5 mm x 14 mm) observed for Ni content variation (5 %, 15 %, 25 %, 35 %) in combination with laser power variation (0.9 W, 1.2 W, 1.5 W, 1.8 W).... 87
- Figure S4.4: TEM images of different 25 % Ni-LCNFs at different magnifications. The lighter grey color of the inner part of LCNF compared to the rims indicates that fewer atoms are present inside. This could point to hollow-like structure of carbon nanofibers. .... 88

Figure S4.5: EDX spectra before (a) and after (b) incubation in PB for LIG (laser-induced graphene on Kapton foil) and Fe-LCNF with electrodeposited Ni (eNi) and Ni-LCNF. The incubation was conducted by a shaking incubator (VWR Incubating Orbital Shaker, Professional 3500) for 5 h (50 rpm) at 37 °C with the samples burdened on the ground of a Petri dish that was filled with PB. LIG and Fe-LCNF loose almost the complete Ni during incubation while LCNF with Ni that was embedded during electrospinning shows no loss..... 88

Figure S4.6: SEM images of 25 % Ni-LCNFs at high (a) and low magnification (b). The LCNF electrode has been used for electrochemical glucose detection at 0.55 V with several consecutive glucose injections under stirred condition as commonly done in this study. Afterwards, the electrode was blow-dried with nitrogen stream prior to SEM imaging. Fibrous structure is still maintained indicating favorable mechanical stability for electroanalytical applications. The red arrows point out the area that is covered with the solution residues from the measurement..... 89

Figure S4.7: Cyclic voltammograms of LCNF in 0.5 M NaOH w/o glucose (40 cycles) and subsequent run (10 cycles) w/ 0.5 mM glucose (a). First cycle (b) and last cycle (10th) (c) w/ 0.5, 1 and 2 mM glucose. Oxidation and reduction peak currents, observed after scan rate variation, plotted against the square root of the scan rate (d). The associated measurements were performed in 0.5 M NaOH w/ and w/o 1 mM glucose. .... 90

Figure S4.8: Cyclic voltammograms at various scan rates for Ni-LCNF with different Ni content (i). Randles-Sevcik plots for the corresponding cyclic voltammograms ( $n = 4$ ). For evaluation the ferri/ferrocyanide peak couple at lower potential (ca. 280/210 mV) was taken (ii). The peak couple at 660/620 mV relates to the formation of nickel hexacyanoferrate (NiHCF) species. The measurements were performed with 1 mM ferri/ferrocyanide in 0.1 M phosphate buffer (0.1 M KCl, pH 7.0). .... 91

Figure S4.9: Amperometric response of LCNF generated at 0.9 W, 1.2 W, 1.5 W and 1.8 W towards 100  $\mu$ M glucose (Glu) ( $n = 3$ ). The average working area of the not-fully carbonized electrodes for 0.9 W laser power was determined by ImageJ using microscopic pictures and the current was normalized to the same area as for the other lasing settings..... 92

Figure S4.10: Dose-response curve ( $n \geq 3$ ) for 25 % Ni-LCNF towards successive glucose addition into 0.25 M NaOH matrix w/ and w/o 0.25 M NaCl (a). Respective amperograms in 0.25 M NaOH matrix w/o (b) and w/ 0.25 M NaCl (c). The detection potential was fixed at 0.55 V. To keep the total molarity at the same level as for the presented glucose detection experiments (0.5 M NaOH) and to have a ratio of 1:1 (NaOH:NaCl) the NaOH concentration was decreased to 0.25 M. .... 92

## List of Tables

Table 1.1: Comparison of enzymatic vs. non-enzymatic sensor approaches.....	16
Table 1.2: Summary of analytes detected with miscellaneous non-enzymatic sensors. ....	28
Table 4.1: Nickel content before and after shaking incubation for different electrodes determined by EDX.....	80
Table 4.2: Comparison of the analytical performance of most recent nickel-carbon hybrid materials towards non-enzymatic glucose sensing.....	83

## List of Tables (Supporting Information)

Table S3.1: Chemical compositions of Matrimid<sup>®</sup> nanofibers and LCNFs containing 5 % iron determined by elemental analysis (unless stated otherwise). ..... 65

Table S3.2: Evaluation of cyclic voltammograms for 1 mM dopamine using various carbon-based electrodes (LCNF contained 5 % iron). ..... 67

# 1 Laser-Induced Carbon Nanomaterials and Their Hybrids for Non-Enzymatic Electrochemical Sensing

## 1.1 Abstract

Non-enzymatic electrochemical sensors possess superior stability in comparison to traditional enzyme-based sensors. Herein, an introduction to the subject of catalysis by nanomaterials will be given. The different catalytic abilities of metal materials namely noble metal, non-noble metal and metal hybrids will be discussed. Various kinds of carbon nanomaterials and their composites have been employed as a transducer. An overview of the current methods to create such materials will be debated together with their tested analytes. Then, we will put forward the potentiality of using laser irradiation to generate carbon nanomaterial electrodes and the advantages over conventional preparation methods. We will highlight the way it works, precursors/substrates to be used and how lasing parameters and ambient conditions impact the properties of generated carbon. Importantly, the variety of functionalities, metal- or heteroatom-doped carbon, e.g. nitrogen and sulfur that have been demonstrated by laser irradiation but used for other applications will be given. The achievements so far with respect to non-enzymatic electrochemical sensing by composites generated with this technique will be summarized. Finally, we will propose further potential applications of laser-induced carbon nanomaterials such as wearables and point-of-care sensors and discuss suggestions for potential improvements.

---

*Parts of this chapter will be further used as a manuscript that is intended to be submitted to Analytical and Bioanalytical Chemistry as a critical review article in a topical collection focusing on biomimetic recognition elements.*

### *Author contributions*

The author and Dr. Nongnoot Wongkaew contributed equally in literature search and manuscript preparation.

## 1.2 Introduction

There is a great demand for (bio)sensing systems for almost all fields of life as the awareness of humans in terms of environment, health and sustainability rapidly increases. At the same time a sensor has to fulfill many requirements such as easy operation, reliability and of course low costs. The main parts of a biosensor are the biorecognition element and the transducer. The first binds to a specific analyte e.g. in aqueous solution and thus enables selectivity. Those can be enzymes, DNA, cells etc. Upon binding to the biorecognition element the transducer recognizes this event and transforms it into a measurable output signal e.g. electrical, optical, pH value, mass change and many more.<sup>1,2</sup>

Electrochemical detection techniques are very popular due to their high sensitivity, fast and simple measurements while working with affordable equipment. This also includes portable devices and miniature sensors with wireless readout, making electrochemical sensors highly suitable for point-of-care analysis. In general, an electrochemical setup consists of at least two electrodes including a working and reference electrode. A working electrode is where the electrochemical reaction of interest takes place. This reaction can be influenced by a reference electrode which is applied to either set a potential difference to the working electrode or measure it, depending on the electrochemical process made use of. In a three-electrode system the current can be measured by an additional counter (auxiliary) electrode e.g. in voltammetric experiments. With a three-electrode configuration, the potential at the working electrode can be controlled more efficiently as it is not disturbed by a counter reaction taking place at the reference electrode as occurs in the two-electrode system. All electrodes can be made of a wide variety of different materials e.g. based on metal, carbon or semiconductors which all serve different purposes.<sup>3</sup> Hereby, the potential window, the range in which a substrate is inert, in an electrolyte of interest is an important selection criterion. Besides preventing the electrode from damage, this also includes avoiding side-reactions such as oxygen or hydrogen evolution that could possibly disturb electrochemical analysis. For example, gold can be applied between -0.1 to 1.3 V without getting damaged,<sup>4</sup> whereas PEDOT:PSS (poly(3,4-ethylenedioxythiophene) polystyrene sulfonate), a conductive polymer mixture, can be also used at more negative potentials (-1.0 to 1.0 V).<sup>5</sup> However, conductivity of gold is four orders of magnitude higher than the one of PEDOT:PSS and the cost difference also needs to be considered.<sup>2</sup> Carbon materials, e.g. glassy carbon, are often utilized due to their low costs while offering chemical stability and simple processing. They possess wide potential windows in several electrolytes, e.g. from -0.6 to 1.7 V for glassy carbon in 0.1 M NaOH, which facilitates multiple application possibilities.<sup>4</sup>

Electroanalytical methods can be grouped in coulometric, potentiometric, voltammetric, capacitive and conductimetric methods with each comprising many subclasses. For example in the group of voltammetry several techniques such as cyclic voltammetry, amperometry and differential pulse voltammetry are very popular. Voltammetry includes all principles where the current depending on the applied potential is determined. In case of amperometry the detection potential is held constant, which is normally the potential at which a chemical reduction or oxidation reaction is expected or already known to occur.<sup>6,7</sup> The measured signal then changes with time due to interaction of analyte molecules with the electrode surface to which the certain potential is set. This results in a current response proportional to the analyte concentration. The concentration range which can be detected mainly depends on the electrode material, more precisely the electroactive surface area (ESA) that is available for interaction with the analyte, but also on the diffusion of the analyte (thickness of diffusion layer,  $\delta$ , and analyte diffusion coefficient,  $D$ ). The current,  $I$ , can hence be expressed by following equation:

$$I = n \cdot F \cdot A \cdot D \cdot c_0 \cdot \delta^{-1} \quad (1.1)$$

with the number of electrons transferred,  $n$ , the Faraday constant,  $F$  (96,485 C·mol<sup>-1</sup>), the surface area,  $A$ , and the initial analyte concentration,  $c_0$ .<sup>8</sup>

Cyclic voltammetry (CV) is a powerful technique to explore reaction mechanisms. While scanning the potential,  $E$ , back and forth, oxidation (sweeping from negative to positive direction) and reduction (sweeping from positive to negative direction) reactions occur when reaching its proper potential. This is indicated by a peak, whose height can be correlated to the concentration of the respective species reacting and the width can give a hint on the amount of electrons being transferred. The Nernst equation describes this behavior:

$$E = E^0 + \frac{RT}{nF} \ln \frac{a(\text{Ox})}{a(\text{Red})} \quad (1.2)$$

$$\Delta E_p = |E_{p,\text{Ox}} + E_{p,\text{Red}}| = 2.303 \frac{RT}{nF} \quad (1.3)$$

with the universal gas constant,  $R$  (8.314 J·mol<sup>-1</sup>·K<sup>-1</sup>), and the activities,  $a$ , for the oxidized (Ox) and reduced (Red) species respectively. At low concentrations the equation can be simplified by replacing the activity by the concentrations. A completely electrochemical reversible reaction results in a peak-to-peak separation,  $\Delta E_p$ , of 57 mV (at a temperature,  $T$ , of 25 °C) between oxidation and reduction peak (compare equation 1.3). Thus redox markers with reversible reaction behavior such as ferri/ferrocyanide, [Fe(CN)<sub>6</sub>]<sup>4-/3-</sup>, or hexaamineruthenium, [Ru(NH<sub>3</sub>)<sub>6</sub>]<sup>2+/3+</sup>, are often used to characterize the electrochemical behavior of an electrode material. In ideal case electrodes with low electron transfer barriers and diffusion limitations come close to a  $\Delta E_p$  of



57 mV (for one electron systems).<sup>9</sup>

Differential pulse voltammetry (DPV) is a method that, as the name already implies, makes use of pulses while scanning through a potential range. The potential of the pulse amplitude is set constant and the current difference between before and at the end of each pulse is measured and plotted against the potential. With this non-faradaic (capacitive) current, which would otherwise produce background signals is getting reduced. Therefore, DPV allows the measurement of low analyte concentrations.<sup>10</sup>

The following chapters briefly introduce catalytic principles and mechanisms with regard to non-enzymatic electrochemical sensors. Different carbon and metal-based catalysts and their respective synthesis as well as applications will be discussed on examples focusing mainly on the recent advances from 2015 till 2020. Special attention is given to the process of laser-induced carbonization and the nanomaterials created by this novel strategy. The findings are concluded and future perspectives of carbon material analytical sensors prepared by laser irradiation will be presented.

## 1.3 Non-Enzymatic Electrochemical Sensors

### 1.3.1 State of the Art, Definition and Advantages

Non-enzymatic electrochemical sensing features benefits over the traditional detection techniques employing enzymes such as higher robustness and stability, affordable costs and mass-production feasibility. Enzyme-free strategies also do not need complicated immobilization steps and can potentially be reused after solving surface fouling issues. Especially sterilization steps, which are often necessary for medical application of sensors to prevent contamination, are a demanding task in fabricating enzymatic sensors. However, non-enzymatic sensors encounter some drawbacks especially lower analyte specificity compared to enzymes, which commonly comes with more interference by other prevalent molecules in analyzed samples. A comparison of general enzymatic vs. non-enzymatic properties is shown in Table 1.1. So far most non-enzymatic approaches are also limited when measurements are performed directly in real conditions.<sup>11–14</sup> Hereby, one of the challenges is that several of the composites, e.g. transition metals (Cu, Ni, Fe, etc.) for the detection of neurotransmitters, only work reliably at alkaline pHs due to the sensing mechanisms' inherent demand of hydroxide ions and others need at least buffered solutions mostly phosphate-buffered saline at neutral pH.<sup>15</sup> The latter one comes closer to real physiological media as the pH value is set neutral. However, the salts contained in the buffer can lead to electrode poisoning by chlorides or phosphates adulterating the electrochemical performance. The analyte detection with sensors demanding alkaline or buffered solutions is most often performed by standard addition method, which comes with a dilution of the real sample. This is practical to do in a laboratory but not suitable for on-site or *in vivo* applications. However, there have been some research groups proposed strategies to address the challenges, especially with undiluted real samples. For example, Park *et al.* developed a system for continuous glucose monitoring in whole blood and serum consisting of multiple polymer membranes to exclude proteins and repel charged interfering molecules from the electroactive nanoporous platinum.<sup>16</sup> Another potential solution is presented by Zhu *et al.* who fabricated a wearable sensor for the detection of perspiration glucose based on a gold electrode modified with fluorocarbons. By application of a highly negative potential as a pretreatment step, a localized alkaline condition within the diffusion layer near the electrode surface was generated. The glucose in the sweat was then oxidized at 0.2 V resulting in measured concentrations that are in agreement with HPLC-MS results.<sup>17</sup> Still there is a lot room for improvement to reach a breakthrough in non-enzymatical sensing.

Table 1.1: Comparison of enzymatic vs. non-enzymatic sensor approaches.

Parameter	Enzymatic	Non-Enzymatic
Selectivity	High ☺	Moderate ☺
Sensitivity	High ☺	Moderate ☺
Costs	High ☹	Low to moderate ☺
Mass-production ability	Complicated ☹	Easy ☺
Sterilization ability	Low ☹	Easy ☺
Storage conditions (e.g. long-term)	Complicated ☹	Easy ☺
Biostability (e.g. biodegradation)	Moderate ☺	High ☺
Biocompatibility (e.g. toxicity)	Good ☺	Sometimes Difficult ☹
Mechanical stability	Low ☹	High ☺
Environmental stability (e.g. temperature)	Low ☹	Moderate ☺

### 1.3.2 Material Dimension, Preparation and Impact on Sensing

A catalyst generally is defined as something that accelerates chemical reactions while being non-consumed itself. The binding of molecules to the catalyst can lead to several alternative reaction pathways that occur at lower activation energy and, therefore, circumvent kinetic hindrance. With focus on the topic of this review, in electrocatalysis the catalyst acts as a mediator that transfers electrons between molecules and the electrode surface during electrochemical reactions. The fabrication of nanocatalysts is achieved by different strategies which can be divided in bottom-up and top-down approaches. The former includes methods that start with initial material which can be anything from nano-sized or even smaller down to single atoms that build up into nanocatalysts. A popular example is the synthesis of colloidal nanoparticles (NPs) from metal seeds. Those are mixed with surfactants and reducing agents in a solvent and the growth of nanoparticles is carried out at certain temperatures and reaction times dependent on the desired morphology of the product.<sup>18</sup> Self-assembly is a phenomenon that occurs spontaneously on account of a large number of interaction forces such as van der Waals, electrostatic, hydrogen bonding, wettability or steric effects driven by entropy. However, synthesis of nanomaterials by self-assembly is rarely done uncontrolled but performed under influence of templates, electrical or magnetic fields or by regulating a certain feeding rate of so-called building blocks which allow to tailor size and shape and, therefore, catalytic properties.<sup>19</sup> Another popular bottom-up technique is chemical vapor deposition (CVD). As the name already implies, CVD makes use of molecules in gaseous phase that are deposited on a substrate to grow nanostructures. Top-down methods rely on reducing the

size of initial materials with rather large dimensions into nano-sizes. A typical example is graphene which can be prepared not only by bottom-up but also by top-down approaches from graphite such as mechanical, electrical or chemical exfoliation.<sup>20</sup>

Size and shape of a certain material play key roles in its catalytic functionalities.<sup>21,22</sup> While naturally occurring enzymes contain active binding sites that are mainly determining the specificity towards a substrate, for non-enzymatic sensing elements studied in research groups the catalytic activity must be tailored by choice of the composites and morphological dimensions. This often is a challenging task on the one hand, but on the other hand it also allows creating new distinctive features, which can be multi-analyte sensing possibility by combining different catalysts or fine tuning the detection range window to specify the application. A typical example for its size-dependent catalytic properties is gold. In bulk it is chemically inert and only able to interact with other molecules after ionization at very high potentials. This is due to its occupied *d*-band. With decreasing size down towards nanoparticles, gold is getting more and more catalytically active at lower temperatures and potentials needed respectively. The primary reason that can also be stated for other metals is the increase of edges and corners compared to the total surface. Those are mainly responsible for molecule adsorption and, therefore, catalytic activity. For gold this includes oxidation and reduction of CO<sub>x</sub>, selective hydrogenation and oxidative decomposition to name just a few examples.<sup>23</sup> Also the decrease in size down towards molecular range results in changes of the electronic state as the *d*-bands are getting narrower till close to the Fermi level.<sup>22</sup>

When focusing on the shape of certain nanomaterials there is a broad variety from zero-dimensional (0D) nanoparticles to highly complex 3D structures. In electrocatalysis the catalysts' shape has a pivotal impact on selectivity as well as sensitivity. This is not only due to potential binding interactions but also from guided flow of electrons. With respect to the binding sites the atomic arrangement needs to be considered. Those, e.g. (111) and (100) surfaces as specified with Miller indices (*hkl*), differ from the amount and position of potential interaction sites, leading to different catalytic activities.<sup>24</sup> Sánchez-Sánchez *et al.* have studied the shape-dependent catalytic behaviors of different platinum nanoparticles. By scanning electrochemical microscopy (SECM) they were able to image the variations in rate for oxygen reduction reaction (ORR) from four shape types of platinum (tetrahedral-octahedral, cubic, spherical, hexagonal) and also catalytic activity differences whether H<sub>2</sub>SO<sub>4</sub> or HClO<sub>4</sub> were used for solutions.<sup>25</sup> To tailor the shape additional agents, ions and seeds with structure-directing shapes are commonly applied during colloidal synthesis.<sup>18</sup> For more details on shape-controlled synthesis and applied examples the review of Solla-Gullón *et al.* can be recommended.<sup>26</sup>

In the following a detailed view on the different nanomaterial dimensions, their respective preparation strategies and field of use is presented. A corresponding overview of several nanomaterials in all dimensions can be found at Figure 1.1. 0D nanomaterials are defined by possessing nanometer dimensions ( $< 100$  nm) in all directions (x, y and z). Their ultra-small size enables nano-effects that alternate the properties compared to larger-sized structures of the same component. Most prevalent of this class are metallic and magnetic nanoparticles (both commonly abbreviated as MNPs), quantum dots (QDs) and upconverting nanoparticles (UCNPs). They can be prepared by physical methods e.g. laser ablation, ultrasonication, lithography or different evaporation approaches and chemical methods such as CVD, wet-chemistry or by the means of micells.<sup>20,27–29</sup> 0D nanomaterials are rarely used alone for electrochemical sensing<sup>30,31</sup> but mostly to fabricate hybrids with nanomaterials of higher order and/or for labeling and electrode modifications. 1D to 3D nanomaterials can also serve as support for 0D particles that are immobilized or embedded to introduce novel functionalities to the whole composite. Examples include doping of nanofibers with nanoparticles by electrospinning technique.<sup>32,33</sup> Post-modification of as-prepared nanomaterials by electrodeposition,<sup>34–37</sup> chemical anchoring<sup>38,39</sup> and thermal reduction<sup>40,41</sup> are also commonly employed. Nowadays, also more environmentally friendly and sustainable ways of preparation named green/biological methods are in the focus on superseding traditional protocols that might apply solvents or other toxic chemicals. Hereby, it is made use of microorganisms (bacteria, viruses, plants etc.), but also enzymes, proteins or smaller biological structures (amino acids and saccharides).<sup>42,43</sup>

Single nanofibers, nanotubes and nanowires have in common, that their length is often several orders in magnitude higher than their nano-sized diameter. This so-called high aspect ratio classifies them as 1D nanomaterials. There are also shorter one-dimensional structures namely nanorods and nanobelts. Nanotubes are a special case as they also offer hollow spaces that are beneficial for incorporating high amounts or even larger molecules. The fabrication of all of those is possible by similar strategies as for 0D nanomaterials, e.g. CVD, but there is a variety of other possibilities namely drawing, polymerization or electrospinning.<sup>44,45</sup> Electrospinning is a popular method considering mass-production feasibility. It operates by applying a high voltage between a grounded metal collector and a metal needle that is connected via tubing to a syringe filled with polymer solution. The polymer solution is pumped at constant flow rate through the tubing till it arrives the needle tip where it gets ejected and accelerated towards the collector due to the electrical charges. During this the polymer solvent evaporates and solid nanofibers deposit on the collector.<sup>46</sup> This method enables 3D mats of 1D nanofibers in a short time. There are different approaches of generating conductive nanofibers by electrospinning. Most prevalent are carbon

nanofibers (CNFs) and polymers that own semiconductor abilities such as polyaniline, polypyrrole, polythiophene or PEDOT:PSS. They represent a class of polymers that maintain their conductivity due to changes in the  $\pi$ -system of the conjugated aromatic groups either by chemical or electrochemical doping. Electrospun carbon nanofibers are commonly prepared by thermal carbonization of electrospun precursor nanofibers, mostly polyacrylonitrile, which thus turn conductive.<sup>47</sup> More detail on the fabrication and outstanding properties of CNFs in electrochemical sensors will be elaborated in later chapters.

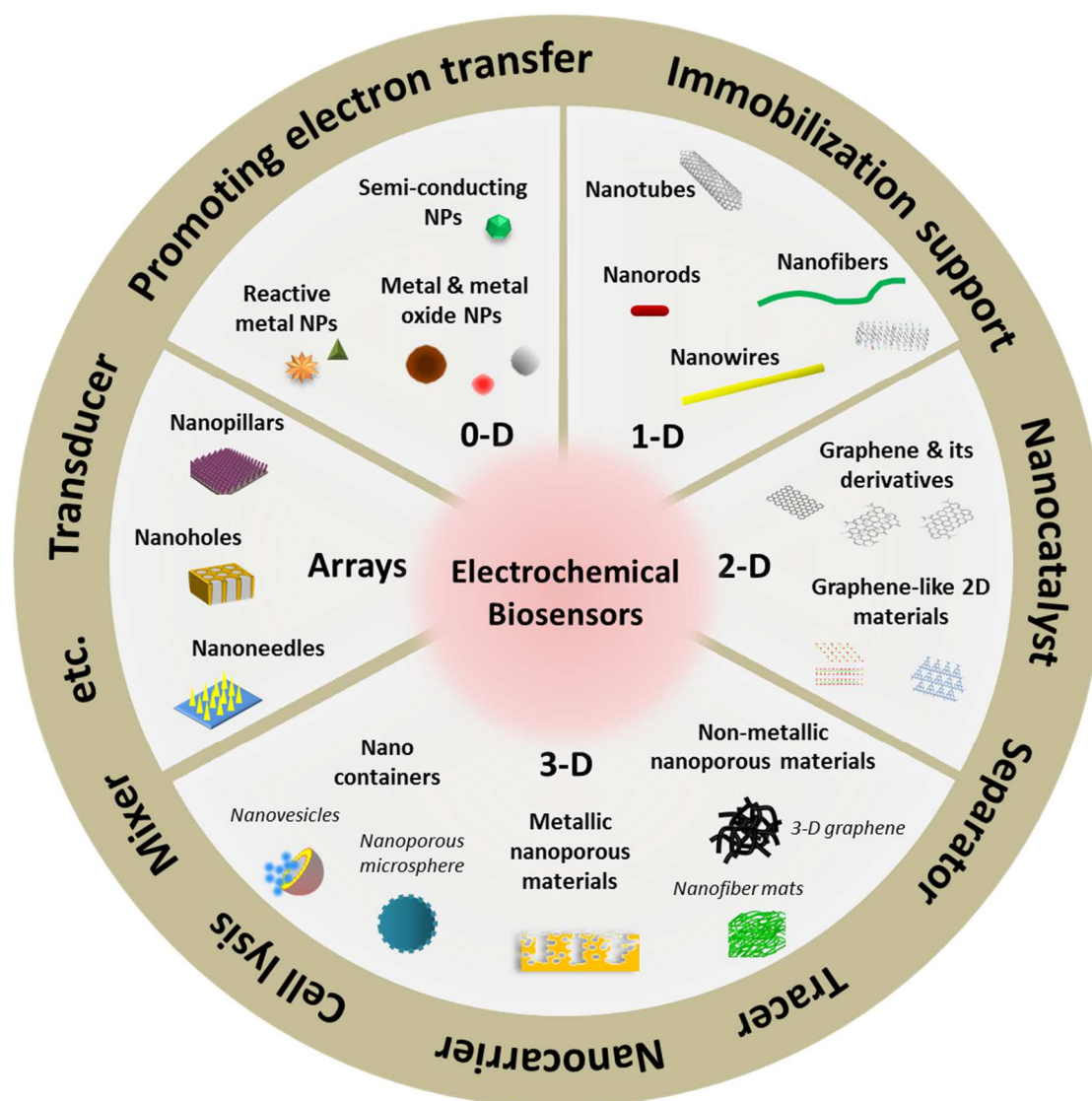


Figure 1.1: Overview of nanomaterials with different dimensions for electrochemical biosensors. Adapted with permission from Wongkaew *et al.*<sup>2</sup>

Metal free structures such as graphene, hexagonal boron nitride or black phosphorus and layered structures of metal chalcogenides, transition metals (oxides, hydroxides, carbides, nitrides) or metal-organic frameworks are to be found in the group of 2D materials. As extensively studied material, graphene is still one of the most often applied sensing materials due to its high electron

transfer capabilities. It consists of carbon molecules connected to each other forming a honeycomb lattice while keeping the single molecule thickness in this structure while the size in the other two dimensions is unlimited. Graphene is generally prepared by two different strategies which are bottom-up and top-down approaches. The first is achieved by chemical synthesis from scratch, which includes CVD, pyrolysis and epitaxial growth, where single atoms are connected at high temperatures leading to highest quality of graphene. The latter is much more often utilized. Here, exfoliation either chemically or mechanically and the reduction of graphene oxide are frequent ways of generating graphene on larger scale while keeping the costs moderate. As the electrocatalytic abilities of bare graphene are quite poor, several enhancement strategies such as introducing dopants or defects, hybridization or alloying with other materials are commonly carried out.<sup>20,48,49</sup>

3D nanomaterials, which own dimensions larger than 100 nm in all directions, are highly popular for their large surface-to-volume ratio and high porosity e.g. foams, graphite and nanofiber mats. They offer many interaction sites increasing the sensitivity when they are applied for sensing. Additionally, the high amount of branches enables many pathways for electron transport. 3D structures can be built up by almost any nanomaterial which is part of the groups with lower dimensions from 0D to 2D, as already pointed out at the respective previous paragraph. Vesicles also belong to 3D nanomaterials when they are over 100 nm in size, to mention another example. Their main feature is that they are able to be loaded with molecules that can be also released again, which is of high interest in drug delivery research. The similar is also possible with nanocontainers. Self-assembly is the most common way of fabricating nanovesicles e.g. liposomes. Here, it is made use of different phases (organic/nonorganic, polar/nonpolar) that are limited in miscibility. Such principles comprise reverse phase evaporation or thin film hydration. However, the drawbacks are the laborious number of fabrication steps as well as the post-synthesis stabilization steps and the use of large amounts of solvent.<sup>50</sup>

### 1.3.3 Metal-Based Catalysts

A broad variety of metals is easily available on affordable costs and thus the application and sensor material possibilities seem infinitely. Therefore, we want to group the different classes of metals that are utilized in catalysis which are noble metals, non-noble metals and metal composites. For non-noble metals we will focus on oxides, as they are much more extensively studied compared to sulfide and phosphide analogues.

Noble metals such as gold (Au), palladium (Pd), silver (Ag) and platinum (Pt) serve as popular electrode materials due to their excellent conducting properties, inertness and ease of modification

but can also be integrated as sensing elements into systems in the form of nanostructures. With respect to electrocatalytic glucose detection, electrodes with modified noble metal as sensing systems also work at neutral pH, which is beneficial for measuring directly in real samples. Explanations for this benefit over non-noble metal can be found in many factors. In general the electrocatalytic abilities of noble metals are superior over non-noble equivalents. As reactive OH<sup>-</sup> ions, which are known for their impact in catalytic processes, are in lower presence at neutral pH values, the adsorption of those few molecules in combination with the excellent conductivity of precious metals still allows catalytic mechanism to be observed. Another important point is the rising instability of metal oxides with decreasing pH, which is not the case for highly stable noble metals. Major drawbacks of the noble metals lie in their high costs due to low abundance and the potential surface poisoning by halide ions, which is a challenge when detecting in neutral pH matrices. This is in contrast to conducting the measurement in alkaline conditions where metals are negatively charged and hence are able to repel negatively charged interferents such as Cl<sup>-</sup>. If not dimensioned in nanostructures they also only provide sluggish reaction kinetics, e.g. bulk gold is a poor electrocatalyst due to the low amount of interaction sites relatively to the total surface.<sup>12,23</sup>

Non-noble metals are able to circumvent those disadvantages. Typically, oxides of transition metals are capable of undergoing (electro)chemical redox reactions which are taking place due to interaction with different molecules. Popular and intensively researched examples are iron oxides, e.g. Fe<sub>2</sub>O<sub>3</sub> and Fe<sub>3</sub>O<sub>4</sub>, manganese oxides, e.g. MnO, MnO<sub>2</sub> and Mn<sub>3</sub>O<sub>4</sub>, copper oxides, e.g. CuO and Cu<sub>2</sub>O and others, e.g. TiO<sub>2</sub>, NiO, Co<sub>3</sub>O<sub>4</sub> or ZnO.<sup>51</sup> Non-precious metals mostly need certain measurement matrix conditions such as adsorbed hydroxide ions as discussed before to retain electrocatalytic activity. Due to their affordable prices they have been widely applied for the detection of many different analytes such as glucose which will be discussed in detail in a later chapter. Their sensitivity and stability may not be of primary concern for further development. However, the need of strong alkaline medium to enable the reaction is a major obstacle for applying them *in vivo*, especially as wearable or implantable sensors. In contrast to the inert noble counterparts (unless ultra-small nanoparticles), most of non-noble metal oxides are toxic to humans and the environment.<sup>52–54</sup> Therefore, for *in vivo* sensor development special care must be taken to ensure no toxic components entering into the body. This challenge still impedes the translation from non-enzymatic sensor concepts to final devices or systems useable by potential patients.

As many researchers found, combining different metals in one composite can facilitate the overall sensing performance. This not only includes multi-functionalities but also the synergistic effects which result in better sensitivity compared to the single metals. Metals can also be alloyed to obtain



completely new features that cannot be achieved when simply mixing single components. This is due to the atomic proximity with resulting change in the electronic *d*-band structure that enables catalytic activity of transition metals.<sup>55,56</sup> Gorzkowski and Lewera investigated the catalytic formic acid oxidation with palladium monolayer deposited on platinum nanoparticles. By X-ray and UV photoelectron spectroscopies (XPS and UPS) they validated that the electron density is increased close to the Fermi level due to the monolayer deposition, which results in enhanced catalytic activity compared to palladium nanoparticles alone.<sup>57</sup> Some reactions require the involvement of more than one type of metal catalysts to happen at all. The reasons can lie in unresponsive reactants, cascade reactions or potential need of activating different reactants. Multi-metallic materials include hybrids of noble metals, non-noble metals and also combinations of both with any desired percentage content for all of those. They do not necessarily need to be within the same structure but can also coexist in different phases within one sensing material.

### 1.3.4 Carbon and Derivatives

There is a tremendous interest in carbon materials owing to their superior mechanical and chemical stability. Ease of modification and outstanding electron transfer capabilities put them into focus for electrochemical sensors, especially when they are combined with non-precious metal nanocatalysts that are not very conductive alone but improve analytical sensitivity. Carbon materials comprise a variety of derivatives such as (reduced) graphene (oxide), graphite, fullerene, diamond, hydrogen and heteroatom doped carbon (nitrogen, boron, chlorine, phosphorus, fluorine, sulfur), nano- or macrostructures such as carbon nanofibers/-tubes, flower-alike, cubes, onions etc. and infinite combination opportunities of those.<sup>58–60</sup> In the following they are considered in more detail.

During traditional synthesis e.g. by CVD, the generated carbon is not fully free of defects and impurities which are mostly carbonaceous and metallic derived ones. Those introduce electrocatalytic abilities such as for the ORR or the reduction of CO<sub>2</sub>, hydrazine and others. However, to reach satisfying sensing result, most of the sophisticated carbon materials have in common that they offer a huge surface area and porosity with multiple interaction sites. This is primarily the intended goal in order to facilitate interaction of potential analytes with functional groups, mainly oxygen, and defects that are present on the edges of carbon structures. Both can influence molecule adsorption and desorption as well as heterogeneous electron transfer rates.<sup>61</sup> Zhu *et al.* presented a carbon nanohorn/graphene oxide hybrid sensor for the electrochemical detection of 4-nitrochlorobenzene. The partially unzipped nanohorns (graphene oxide) provide abundant active sites that, together with the electron transfer capabilities of retained nanohorns,

led to great sensing performance (limit of detection, LOD 10 nM).<sup>62</sup> By simple air annealing process Zhu *et al.* were able to enhance defects, oxygen groups and other factors of carbon fiber paper. With the resulting product, high-performance electrochemical nitrite-detection with 70 nM LOD, a wide linear-range of 0.1-3,839  $\mu\text{M}$  and high sensitivity ( $930.4 \mu\text{A}\cdot\text{mM}^{-1}\cdot\text{cm}^{-2}$ ) could be enabled.<sup>63</sup> Recently, pencil graphite has gained high interest as carbon source for electrodes due to its wide availability, low costs and simple processability. Vishnu *et al* demonstrated the detection of purines from fresh fish samples with pre-anodized pencil graphite. The pre-anodization step results in several functional oxygen rich groups that are the key for purine oxidation abilities.<sup>64</sup>

Modified carbon is significantly more studied compared to carbon materials alone due to the larger application possibilities. Common ways of doping carbon are by (hydro)thermal annealing in a certain gas atmosphere or by mixing graphene with heteroatom-donating chemicals (e.g. ammonia or urea for N-doping),<sup>65-71</sup> microwave-assisted synthesis<sup>72-75</sup> and plasma methods.<sup>76-78</sup> Metal-carbon hybrids are frequently studied for obvious benefits introduced by the metal which are as already discussed sensitivity, selectivity and multiple fabrication possibilities. Nevertheless, there is an increasing interest in metal-free sensing materials. Especially noble metals are often limited in abundance and thus expensive, which hampers commercialization of sensors utilizing those. For most applications in (bio)medical sensing field, biocompatibility is undoubtedly of paramount importance e.g. with respect to wearable or implantable sensors. This includes the mechanical and chemical stability of the whole sensing material as well as potential toxicity of some metal components. Doping graphitic carbon with heteroatoms, as one of the alternative modification strategies, was found to lead to catalytic activity as well, such as for the ORR, without the need of additional metal. This is because the dopants influence the charge distribution, binding ability and spin density of carbon atoms in a way that promotes  $\text{O}_2$  adsorption and bond breaking. Therefore, the type of heteroatom dopant as well as the total amount and distribution plays a key role in catalytic activity of doped carbon.<sup>79</sup> Current trends guide towards carbon materials doped with multiple heteroatoms to improve catalytic efficiency. The synergistic effect that derives from the interaction of different co-dopants among themselves can activate  $\pi$ -electrons and change catalytic binding behavior. Still the metal-free carbon materials need extensive improvement in catalytic properties to be able to fully substitute the metal-containing ones.<sup>80</sup>

Carbon quantum dots (CQDs) and graphene quantum dots (GQDs) as examples for carbon nanomaterials have evolved as alternatives to semiconductor quantum dots, which are commonly made of toxic heavy metals. Further advantages of them include their chemical inertness as well as high stability and biocompatibility. GQDs are basically defined as single layered graphene with

lateral sizes lower than 100 nm, whereas CQDs can consist of multiple layers of graphene, which together make a total diameter typically below 10 nm. Therefore, the amount of edges (with functional groups) relative to the total surface is very high which results in superior electrochemical activity. Due to their very small size, 0D nanomaterial QDs also offer quantum confinement effects that are considered to be responsible for their numerous unique properties. Besides their popular fluorescence characteristic, they also offer electrocatalytic abilities, such as towards the ORR.<sup>81,82</sup> To achieve this, the catalytic properties of CQDs can be tuned by heteroatom doping, as described earlier, and reach superior performance comparable to metal-based catalysts.<sup>83</sup> This makes CQDs a suitable candidate for replacement of standard catalysts applying platinum and other expensive metals.

1D carbon nanostructures, primarily nanofibers and nanotubes (CNTs), are among the most popular carbon materials for biosensor development because of the already discussed benefits of high surface-to-volume ratio with multiple interaction and modification sites, excellent electron-transfer properties, biocompatibility and simple fabrication methods. Compared to carbon nanotubes the carbon nanofibers offer more edge sites on the outer wall as they consist of graphene sheets with varying shapes that are stacked together. Those edge plane defects can enhance the interaction with analytes and the electron transfer.<sup>84</sup> Carbon nanotubes comprise the groups of single-walled carbon nanotubes (SWCNTs) with one graphene layer rolled up and multi-walled carbon nanotubes (MWCNTs) where multiple tubes enclose each other. Depending on their chirality they can possess metal or semiconductor characteristics. In case of MWCNTs the existence of just one metallic layer leads to a metallic behavior of the overall structure. The electrochemical properties of MWCNTs are lower than those of SWCNTs because of the inconsistent chirality deriving from the different tubes. Their main attribute is the enormous mechanical strength. To obtain CNTs different methods such as laser-assisted as well as CVD and arc discharge can be picked for synthesis.<sup>85,86</sup>

### 1.3.5 Analytes

Target species of electrochemical sensors must be electroactive, which means that they can be oxidized or reduced at certain potentials that are applied in order to detect them. This comes with a change in the signal, which depends on the electrochemical detection strategy such as current in amperometry. The sensing system must fulfill the requirement of selectively recognizing this action in ideal case without interference by other electroactive molecules or at least allow separation by differences in detection potential. The following chapter deals with some of the prominent analytes in research, associated challenges and potential solutions. The analytes and

associated sensor validation parameters of all reviewed publications are summarized in Table 1.2.

Most intensively studied analyte by far is glucose due to rising numbers of diabetes mellitus patients that still have to use invasive techniques to measure blood glucose levels by themselves. Therefore, healthcare is the main driving source in developing glucose sensors.<sup>12,15,21,87,88</sup> Glucose is also present in sweat (0.06-0.11 mM), saliva (0.23-0.38 mM), urine (2.78-5.55 mM) and ocular fluid (0.05-0.5 mM) which can be easier obtained non-invasively. However, glucose levels are often lower compared to blood (4.9-6.9 mM) and other potential interferents such as uric acid and salts in urine can be issues that need to be addressed.<sup>89</sup> Ideally, a sensor should be ready to be used when exposed to real biological samples without additional preliminary steps and some researchers already tried to tackle this issue as discussed in chapter 1.3.1. Especially for people with stronger diabetes disease that require regular insulin infusions, continuous glucose measurement systems are highly beneficial to be able to react quickly to abnormal levels. With respect to non-invasive monitoring there are several challenges that need to be overcome before potential commercialization. Bae *et al.* developed a microfluidics-integrated sweat sensor patch made of micropatterned polydimethylsiloxane (PDMS) to ensure stretchability, which is highly desired for wearables. In their platform, stretchable cotton fibers served as sweat collector by capillary forces and nanoporous gold enabled non-enzymatic electrochemical sensing.<sup>90</sup> However, there is still the question left how accuracy is affected by the amount of sweat different persons produce. Ocular fluid brings the advantage of being continuously produced by the healthy eye, which enables detection of biomolecules in tear fluid by contact lenses. As the glucose concentration range and the sample value are very low, a satisfying sensitivity of contact lens sensors so far can only be reached by including enzymes such as presented by Yao *et al.*<sup>91</sup> For monitoring glucose in saliva, wireless detection strategies including mouthguard-based approaches<sup>92</sup> and sensing on tooth enamel<sup>93</sup> can be proposed. As the long-term stability of enzymes and, therefore, the use for continuous monitoring is insufficient, a breakthrough in non-enzymatic wearable sensors with respect to selectivity is yet to be achieved. Also, it should be kept in mind that the glucose transition from blood to other body liquids comes with a lag in time which could have serious consequence for risk patients when not recognizing critical changes of glucose in one of those fluids fast enough.

Hydrogen peroxide,  $\text{H}_2\text{O}_2$ , is an important molecule in biomedicine and as a member of the reactive oxygen species, it is an indicator of several diseases that are linked to oxidative stress. Its strong oxidative properties are utilized for disinfection and sterilization but make it also crucial to supervise  $\text{H}_2\text{O}_2$  levels in food and chemical industry, environmental monitoring or pharmaceutical field. Thus depending on the field of application, the range of hydrogen peroxide concentration significantly varies from low micromolar to high millimolar and, therefore, the requirements for a

sensing system do as well.<sup>13</sup>  $\text{H}_2\text{O}_2$  can be enzymatically detected at low values by the help of heme proteins such as horseradish peroxidase which has been successfully achieved decades ago.<sup>94</sup> Nowadays, the active Fe-containing heme center of the enzyme is tried to be mimicked by various non-enzymatic sensing materials. Recent developments imply a vast variety of metal nanostructures e.g. noble metals (Au, Pt, Ag, Pd), transition metals and their respective oxides (Co, Fe, Ni, Cu), alloys and carbon materials.<sup>13,95</sup> Mollarasouli *et al.* constructed GQDs modified with chitosan (CS) as immobilization matrix for methylene blue (MB) that offers a reversible redox mediator mechanism for the detection of  $\text{H}_2\text{O}_2$ . Because of the wide linear range from 1-2,900  $\mu\text{M}$  and 2,900  $\mu\text{M}$  to 11.78 mM their GQDs-CS/MB can be used for several different samples. They validated this and reached adequate recovery of  $\text{H}_2\text{O}_2$  in several food and water samples without being affected by numerous biomolecules and inorganic salts.<sup>96</sup> Kogularasu *et al.* achieved a very low LOD of 15 nM which enabled them to detect low contents of hydrogen peroxide in contact lens cleaning solutions and disinfectant solutions even after spiking into measurement matrix. They constructed polyhedral shaped  $\text{Co}_3\text{O}_4$  metal-catalyst and encapsulated them into porous graphene oxide with peroxidase-like catalytic activity.<sup>97</sup> An approach for *in vivo* detection of  $\text{H}_2\text{O}_2$  released from living cells was presented by Bai *et al.* They prepared a platinum nanoparticles/reduced graphene oxide (rGO)-chitosan-ferrocene carboxylic acid nano-hybrid and triggered different cell types with ascorbic acid. Among them, tumor cells generated higher current response related to higher hydrogen peroxide levels that derive from morbid cell growth. With respect to future sensor development, those strategies could be very meaningful in monitoring and recognizing tumor growth in human body but also checking therapeutic success.<sup>98</sup>

When searching the internet for non-enzymatic electrochemical biosensors it can instantly be observed that most of them concentrate on glucose or hydrogen peroxide. Still there is an almost endless number of important analytes to be considered and some work groups are trying to solve the challenges that come with the development of novel enzyme-free detection strategies. A continuously emerging field is healthcare as it takes more or less a fundamental part in the lives of everybody. Hereby an associated area is drug detection. Khairy *et al.* studied the simultaneous determination of codeine, acetaminophen and caffeine with cerium oxide nanoparticle modified screen-printed electrodes to give just one example.<sup>99</sup> In addition, sensors verifying hormones such as progesterone,<sup>100</sup> estradiol,<sup>101</sup> testosterone<sup>102</sup> or epinephrine<sup>103</sup> or neurotransmitter levels such as dopamine,<sup>104</sup> glutamate<sup>105</sup> or acetylcholine<sup>106</sup> gain increasing evolution. Validating body cholesterol values,<sup>107</sup> which can become abnormal mainly from unhealthy lifestyle, is also in focus as of significant increased risks of heart attack. Further, people more and more propel the understanding of disease development on the genetic base as changes of the DNA building blocks

come from or result in those. For this reasons Boopathy *et al.* fabricated a guanine sensor based on graphene oxide/ $\alpha$ -MnO<sub>2</sub> binary nanosheets. They reached picomolar LOD and have proven the ability of their sensor material to determine guanine content in real calf thymus DNA sample.<sup>108</sup> A good overview about other progress on non-enzymatic electrochemical sensors for medical purposes is given by Martinkova *et al.*<sup>109</sup> Concluding, the development of non-enzymatic sensing approaches for various analytes in all fields of life is still in its infancy. It must be the first aim to exactly understand the interaction mechanisms of nanomaterials and target analyte to ensure not only sensitivity but also specificity in particular in complex real matrices.

Table 1.2: Summary of analytes detected with miscellaneous non-enzymatic sensors.

Analyte	Material	Method	Linear range	LOD	Reference
Uric acid	Preanodized 4B-pencil graphite electrode	DPV	3-21 $\mu\text{M}$	0.17 $\mu\text{M}$	64
	N-doped carbon nanofibers		50-200 $\mu\text{M}$	1 $\mu\text{M}$	69
	Au NP/N-doped graphene	Amperometry	0-600 $\mu\text{M}$	0.13 $\mu\text{M}$	73
	Pt/LSG	DPV	1-63 $\mu\text{M}$	0.22 $\mu\text{M}$	118
$\text{H}_2\text{O}_2$	3D-P-doped graphene	Amperometry	0.2 $\mu\text{M}$ -41.2 mM	0.17 $\mu\text{M}$	65
	ERGO/GCE		1-16 $\mu\text{M}$	0.7 $\mu\text{M}$	71
	S-doped graphene		0.1-18 mM	0.7 $\mu\text{M}$	75
	GQDS-chitosan/methylene blue		1 $\mu\text{M}$ -2.9 mM, 2.9 mM-11.78 mM	0.7 $\mu\text{M}$	96
	3D GO- $\text{Co}_3\text{O}_4$ polyhedrons		0.05-400 $\mu\text{M}$	15 nM	97
	Pt/RGO-chitosan-ferrocene		0.02-3 $\mu\text{M}$ , 3 $\mu\text{M}$ -10 mM	0.2 $\mu\text{M}$	98
	Pd/CNF		0.2 $\mu\text{M}$ -20 mM	0.2 $\mu\text{M}$	135
	P-doped plasma-etched graphene	DPV	0.1-120 $\mu\text{M}$	6 nM	66
Dopamine	N-doped carbon nanofibers		1-10 $\mu\text{M}$ , 10-200 $\mu\text{M}$	0.5 $\mu\text{M}$	69
	Au-P-doped graphene		0.1-180 $\mu\text{M}$	2 nM	70
	N-doped carbon dots	Amperometry	0.1-100 $\mu\text{M}$	4.5 nM	73

Analyte	Material	Method	Linear range	LOD	Reference
Dopamine	Au NP/N-doped graphene	DPV	0.05-8 $\mu$ M	1.2 nM	74
	Core-shell Mo NPs@f-MWCNT	Amperometry	0.01 $\mu$ M-1.609 mM	1.26 nM	104
	Pt/LSG	DPV	0.5-56 $\mu$ M	0.07 $\mu$ M	118
Ascorbic acid	N-doped carbon nanofibers		50-3,000 $\mu$ M	50 $\mu$ M	69
	Pt/LSG		10-890 $\mu$ M	6.1 $\mu$ M	118
Glucose	Microwave N-doped graphene	CV	14.52 $\mu$ M-10 mM	14.52 $\mu$ M	72
	LSG/Cu-NPs	Amperometry	1 $\mu$ M-4.54 mM	0.35 $\mu$ M	117
	Ni NP carbon nanofiber paste		2 $\mu$ M-2.5 mM	1 $\mu$ M	136
	Ni-LCNF		10-100 $\mu$ M, 100 $\mu$ M-5 mM	0.3 $\mu$ M	141
4-nitrochlorobenzene	CNHs/GO/GCE	DPV	0.1-90 $\mu$ M	10 nM	62
Nitrite	Air annealed carbon fiber paper	Amperometry	0.1-3,838.5 $\mu$ M	0.07 $\mu$ M	63
Hypoxanthine	Prenodized 4B-pencil graphite electrode	DPV	6-30 $\mu$ M	1.09 $\mu$ M	64
Xanthine			8-36 $\mu$ M	0.40 $\mu$ M	
Carbendazim	P-doped helical carbon nanofibers		0.1-35 $\mu$ M	0.038 $\mu$ M	68
Acetaminophen	CeO <sub>2</sub> NP		0.09-7 $\mu$ M	0.051 $\mu$ M	99



Analyte	Material	Method	Linear range	LOD	Reference
Codeine	CeO <sub>2</sub> NP	DPV	0.09-50 $\mu$ M	0.043 $\mu$ M	99
Caffeine			5-286 $\mu$ M	2.4 $\mu$ M	
Progesterone	Carbon nanospheres/carbon fiber paper	CV EIS DPV	37.39 pM-0.25 nM	0.012 nM	100
Estradiol	Pd/N-doped RGO	DPV	0.1-2 $\mu$ M, 2-400 $\mu$ M	1.8 nM	101
Testosterone	Molecular imprinted polymer GO	EIS	1 fM-1 $\mu$ M	0.4 fM	102
Epinephrine	Nanoporous Au film	DPV	20-190 $\mu$ M	2.43 $\mu$ M	103
Acetylcholine	NiAl layered double hydroxides/carbon dots	Amperometry	5 $\mu$ M- 6.885 mM	1.7 $\mu$ M	106
Cholesterol	Graphene- $\beta$ -cyclodextrin	DPV	1-100 $\mu$ M	1 $\mu$ M	107
Guanine	GO/ $\alpha$ -MnO <sub>2</sub> binary nanosheets		50 nM-10.5 $\mu$ M	23.9 pM	108
NADH	Pd/CNF	Amperometry	0.2-716.6 $\mu$ M	0.2 $\mu$ M	135

## 1.4 Laser-Induced Carbon Nanomaterials and Their Hybrids

### 1.4.1 Laser-Induced Carbonization

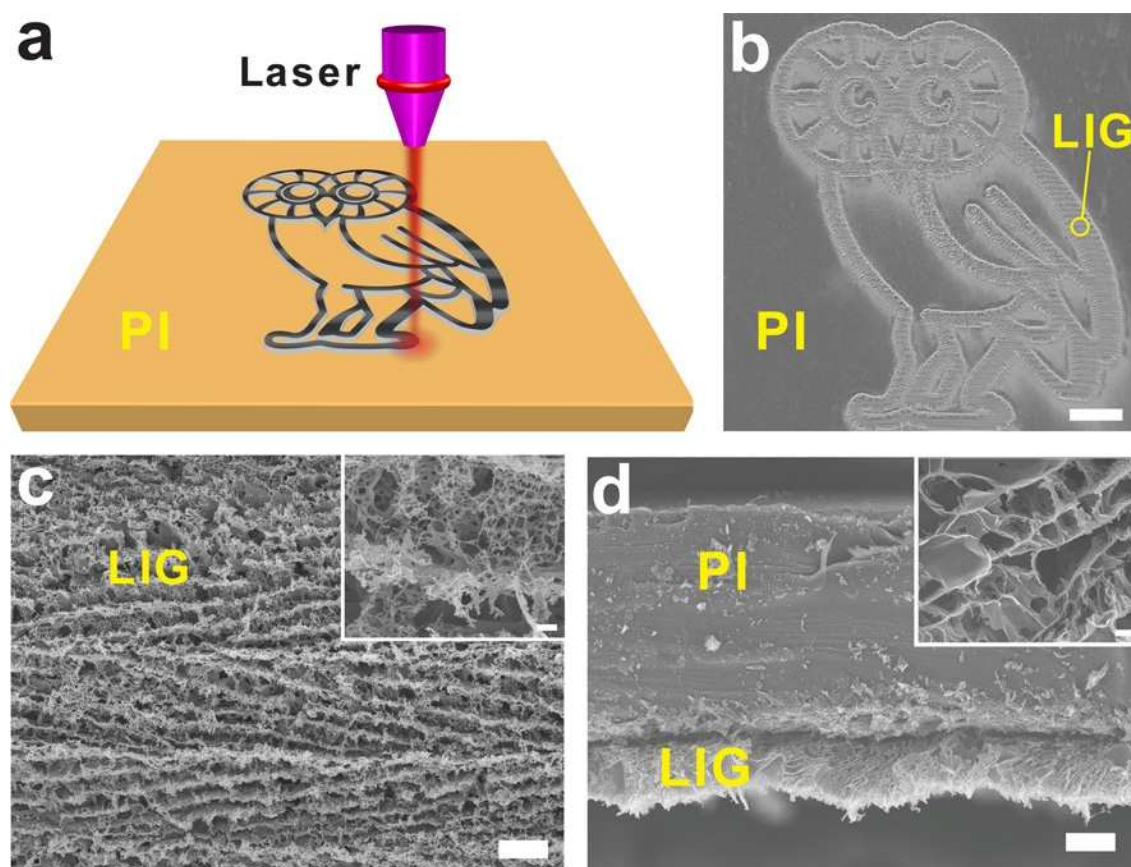


Figure 1.2: Laser-induced carbonization of commercial available polyimide foil (a) and respective scanning electron microscopy (SEM) images of the generated owl shape (b). Zoom-in of the circled part in (b) shows the sweeping line pattern typically obtained by the laser (c). The porous structure of LIG can be seen in the insets of (c) and the side view image of LIG surface on PI foil (d). Adapted with permission from Lin *et al.*<sup>110</sup>

Laser-induced carbonization is a quite new method to prepare novel carbon goods. For laser irradiation different types of lasers, either pulsed or continuous wave such as the most popular CO<sub>2</sub>-laser (typically 10.6  $\mu\text{m}$  wavelength), are suitable.<sup>111</sup> The generation of conductive graphene from non-conductive commercial polymers with this technique was first reported by the group of Tour (Figure 1.2).<sup>110</sup> The laser scribing process itself is simple, quick and equipment as well as initial materials are highly affordable and readily available. Additionally, any carbonization pattern can be designed with standard PC software and the lasing is carried out fully automatically, which makes this approach suitable for large-scale fabrication. Common strategies such as thermal carbonization and CVD are rather inflexible because of several heat treatment steps and associated required processing times taking many hours. Further, complicated set-ups including inert gas atmosphere are essential. Therefore, these methods could be replaced by laser-induced

carbonization, which additionally offers electrode design flexibility. Lots of different substrates as demonstrated for wood,<sup>112</sup> cloth, food or paper<sup>113,114</sup> can be transferred into conductive carbon-based electrodes which broadens the range of potential applications. Most intensively employed is polyimide foil (PI, Kapton) which acts as precursor for laser-induced graphene (LIG) electrodes (also sometimes referred to laser-scribed graphene, LSG).

### 1.4.2 Lasing Parameters vs. Carbon Quality

Commercial laser systems offer the advantage of switchable lenses for respective desired application. Their architecture results in varying conditions of the focus namely focal length, spot size and depth of focus. In the focal point energy and heat density are the highest and decrease equally with increasing or decreasing distance according to the Gaussian beam characteristics.<sup>115</sup> With respect to this it must also be kept in mind that the thicker a sample the more likely to have morphological differences through the whole specimen thickness after carbonization. The 2.0" lens, which is often the standard lens system for CO<sub>2</sub>-devices, can be used for carbonizing or cutting several materials. Due to the rather high tolerance (depth of focus) of 2.54 mm it is easy to find the correct focus even for materials that do not possess evenly flat surface. However, this aspect and the average focal point of 127  $\mu\text{m}$  make the lens less suitable for scribing/cutting fine structures. In this case, a high-power density focusing optics (HPDFO) should be employed. As stated by its name, the energy input is concentrated on a very small focus spot (25  $\mu\text{m}$ ) allowing very high resolution. This comes also with the drawback of high divergence/low focal range tolerance. In addition, the increased energy per illuminated spot can result in distortion of sensitive materials (e.g. polymer foils). The energy input can be fine-tuned by the dots-per-inch (DPI) setting in the laser software which though affects the duration of the lasing process.

Further software settings of the CO<sub>2</sub>-laser have direct impact on the generated carbon structure and quality. Focusing on laser-induced graphene, it is of utmost importance to optimize parameters of the system namely lasing power and speed to obtain carbon with high quality. Generally, increasing the lasing power comes with the need of increasing speed as well and longer lasing exposure times should be ensembled with lower power. Hereby, the morphological features e.g. flake/pore size, layering or gap width usually deviate from different possible parameter combinations and the choice depends on the preferred application and the energy absorption ability of the material to be carbonized. The energy input by the laser and carbonization respectively can also be tailored by changing the distance of the material surface relatively to the laser focal point. In a later chapter we discuss the carbonization of electrospun nanofibers with inherent metal complexes, which assist in distributing the laser input energy evenly resulting in high integrity of

the carbon nanofiber morphology.

The atmosphere in which the lasing process takes place also has a strong effect on the obtained features. Differences in morphology as well as the introduction of functional surface groups and defects by scribing in ambient conditions compared to controlled gas atmospheres such as O<sub>2</sub>, Ar and H<sub>2</sub> lead to significant changes in wettability and electrochemical properties.<sup>116</sup> Lastly, our group found that the scribing direction affects to electrochemical performance of carbonized electrodes. Common CO<sub>2</sub>-laser systems are scribing in one direction e.g. from left to right, before returning to the starting point and continuing with an adjacent line underneath the one carbonized previously. Therefore, for carbonization of patterns with differences in x- and y-length the number of carbonization lines differs when scribing along the x-axis compared to y-axis. This comes with morphological differences such as smaller vs. larger structures (surface area) or pores (-size) that again may further influence electrochemical behavior. Concluding, when developing a new laser-carbonization-based composite the influence of many parameters needs to be studied first and fully understood to customize towards desired material features.

### 1.4.3 Laser-Induced Functional Nanocatalysts

The fabrication of functional materials by laser scribing technology has moved into focus due to the simple generation of diverse nanocatalyst-carbon hybrids. Laser-induced graphene modified with various metal nanoparticles such as copper<sup>117</sup> or platinum<sup>118</sup> has proved its excellent electrochemical sensing abilities. However, the mechanical and chemical stability of metal nanoparticles deposited on LIG surface is rather low. It was demonstrated, also for the first time by Tours' research group, that metal oxides can be embedded into graphene by doping polyimide films with metal precursor and subsequently carbonize.<sup>119</sup> The obtained nanocrystal containing LIG showed electrocatalytic activity for the ORR. This work has triggered several other research groups started to fabricate hybrids of laser-induced graphene with metal composites. Deng *et al.* deposited a mixture of citric acid (carbon source), ammonium molybdate and sodium sulfide on glass slides and generated laser-induced MoS<sub>2</sub>/carbon hybrids for the catalytic evolution of hydrogen.<sup>120</sup> As an alternative way Clerici *et al.* spin-coated MoS<sub>2</sub> flakes on polyimide foil and afterwards laser carbonized it to receive electrodes for supercapacitor application.<sup>121</sup> The same preparation principle was also performed with Ti<sup>4+</sup>-containing poly(amic acid) to modify LIG with TiO<sub>2</sub> instead of MoS<sub>2</sub>.<sup>122</sup> Rodrigues *et al.* covered polyimide foil with Zn/ZnO precursor paste before laser scribing.<sup>123</sup> Recently, You *et al.* prepared a flexible composite from laser-carbonized polyimide foil which was coated with chitosan hydrogel ink containing different noble metal nanocatalyst precursors.<sup>124</sup> Future concepts could involve the preparation of metal alloy-carbon

hybrids with multiple functions directly by laser. Similar to the laser surface alloying technique, where commonly a metal powder is distributed on a surface of another metal (e.g. chromium on copper<sup>125</sup> or aluminum on titanium<sup>126</sup>) and alloyed afterwards by laser power, different metal powders could be alloyed and united with a carbon matrix at the same time.

Heteroatom-doped graphene can also be generated by employing laser scribing technique instead of common methods, (hydro)thermal annealing or plasma synthesis, that require cost-intensive devices. A simple route of doping LIG with boron atoms was shown by Peng *et al.* who mixed poly(amic acid) with boric acid and laser-carbonized the polyimide sheet that was obtained after imidization. The resulting B-LIG possessed multiple-time enhanced areal capacitance as well as energy density which makes it a promising candidate for microsupercapacitor development.<sup>127</sup> In a similar way, Zhang *et al.* achieved doping of LIG with nitrogen levels as high as 13 %. They casted Cu-foils with solutions of polyimide and urea, as nitrogen source, prior to laser irradiation. Additionally, they performed the laser scribing in N<sub>2</sub>-atmosphere to enhance the binding of nitrogen molecules to the carbon.<sup>128</sup> Kim *et al.* presented a different approach of preparing N-doped LIG which is by laser carbonization of a polyimide layer that was deposited on LIG that has been carbonized from an initial polyimide layer before. The authors propose that the significantly increased nitrogen content of densified LIG results from *in situ* doping deriving from the second polyimide layer.<sup>129</sup> An effective manner to synthesize sulfur-doped graphene is to use sulfonated poly(ether ether ketone) as LIG precursor instead of polyimide as demonstrated by the studies of Lamberti *et al.*<sup>130</sup>

#### 1.4.4 Laser-Induced Carbon Nanofibers

Common strategies to fabricate carbon nanofibers are CVD and thermal carbonization. The first involves the growth of carbon materials from bottom by heat-induced decomposition of a carbon source and deposition of those gaseous molecules on a substrate. Structure directing templates and metal catalysts are utilized to obtain nanofibers or -tubes with desired geometrical specifications.<sup>131,132</sup> The latter is done by multiple thermal treatment steps of electrospun nanofibers. Here, mostly polyacrylonitrile (PAN) serves as carbon precursor. PAN has an outstanding electrospinnability, the fiber diameter can easily be controlled, which also comprises very thin diameters down to 100 nm, and the carbon yield is at the upper end of scale. Before actual thermal carbonization, the fibers need to be heat-treated at ca. 300 °C for several hours to preserve the fiber integrity and prevent the aggregation of fibers at carbonization afterwards. Subsequently, thermal carbonization is conducted in inert atmosphere at relative higher temperature (normally ca. 1,000 °C) for another few hours to obtain carbon nanofibers.<sup>133</sup> The

carbonization occurs due to removal of volatile organic species which comes with different phenomena such as crosslinking and reorganization.<sup>134</sup> Huang *et al.* created palladium-containing carbon nanofibers by electrospinning PAN/Pd(acac)<sub>2</sub> solutions with subsequent thermal treatment steps. Those revealed electrocatalytic activity towards H<sub>2</sub>O<sub>2</sub> reduction and nicotinamide adenine dinucleotide (NADH) oxidation.<sup>135</sup> Similar Liu *et al.* created Ni-loaded carbon nanofibers for application in glucose sensing.<sup>136</sup> Even though great performances of non-enzymatic sensors were demonstrated in the previous studies and both techniques offer advantages of high carbon quality (CVD) or high production yield (thermal carbonization), there are also many drawbacks to consider. In order to apply CNFs prepared by those mentioned methods for electrochemical sensing, they have to be further processed. Thermal carbonized nanofiber mats need to be shortened and dispensed in a solvent e.g. by agitation prior to modification of an electrode material such as glassy carbon or carbon paste by drop-casting.<sup>137,138</sup> Sometimes binder materials such as additional polymers e.g. Nafion are necessary to strengthen the adhesion onto the substrate.<sup>139</sup> In this case the electrochemical properties of obtained electrodes can be negatively affected. The aforementioned limitations make those approaches unsuitable for large-scale production. Additionally, the electrode design is rather limited.

Alternatively, our research group recently developed a simple method of generating carbon nanofibers by electrospinning polyimide nanofibers with subsequent laser-induced carbonization at ambient conditions as displayed in Figure 1.3.<sup>140</sup> This laser-induced carbon nanofibers (LCNFs), prepared on indium tin oxide coated polyethylene terephthalate (ITO/PET) substrate offer porous 3D morphology which is beneficial for sensing purposes owing to the high number of potential interaction sites. Similar to the work from Ye *et al.*, who embedded nanocrystals into polyimide films,<sup>119</sup> we integrated nanocatalytic functions but into LCNFs by simply doping the polyimide spinning solution with the respective metal salt. The strategy could successfully be adapted to different metals namely Fe,<sup>140</sup> Ni<sup>141</sup> and Pd so far in which several other metal-doped LCNFs will also be feasible to be created in future. Compared to common LIG the porosity and electroactive surface area of LCNFs can be enhanced multiple times due to the 3D structure, which results in improved electrochemical performance. Additionally, Ni-LCNFs showed excellent mechanical stability of the metal particles in the matrix compared to electrodeposition method, where those can detach during incubation in liquid medium. This is crucial when mechanical forces such as flow or stirring are applied to enhance mass-transport. The high mechanical stability ensures its applicability for *in vivo* measurements, especially for sensors with potential toxic metal composites. Further creation of free-standing LCNFs will pave the way for a number of applications, in particular towards point-of-care testing. Furthermore, LCNF-based sensors as

wearables are highly attractive especially for *in vivo* detection of metabolites with cells since approaches utilizing LIG have demonstrated cell adhesion compatibility<sup>142</sup> and biosafety was confirmed (tested with zebrafish<sup>143</sup>). Additionally, LCNFs are promising for (bio)medical application such as scaffolds, wound healing and breath masks.

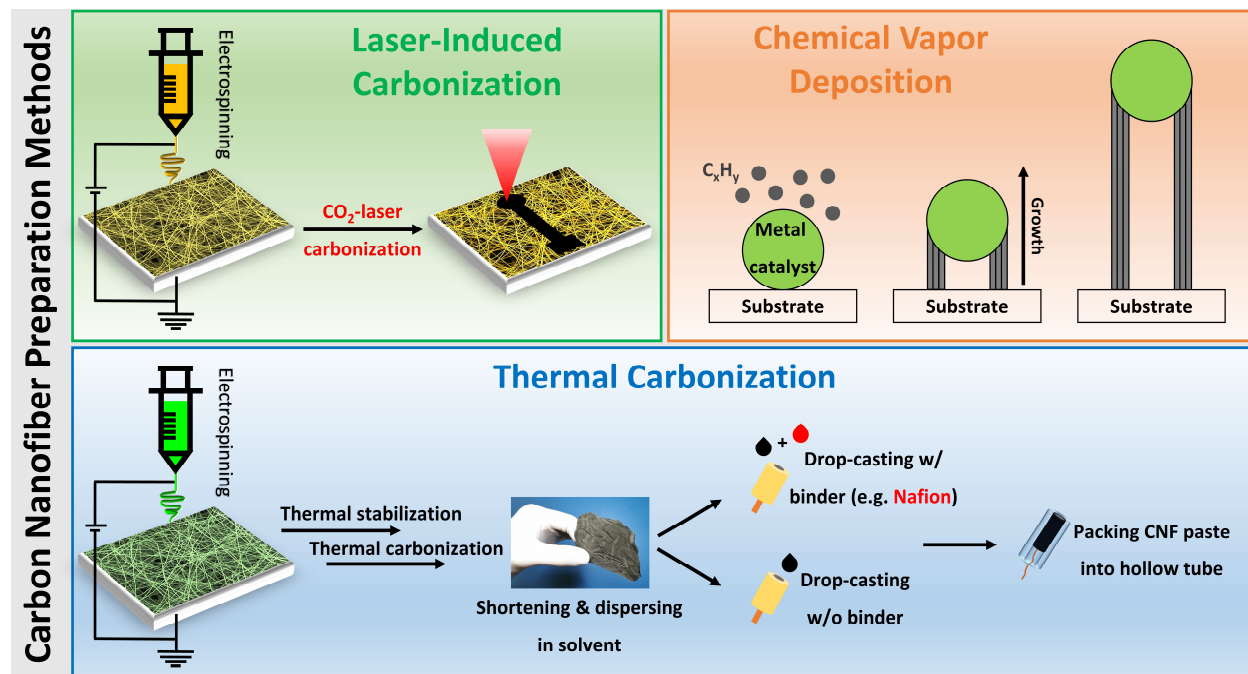


Figure 1.3: Schemes of common carbon nanofiber preparation techniques CVD and thermal carbonization of electrospun nanofibers and the novel strategy of laser-induced carbonization of electrospun nanofibers.

### 1.4.5 Sensing Applications

Laser-induced carbon nanomaterials are highly promising for a wide range of applications such as energy storage,<sup>144–146</sup> anti-biofouling,<sup>147,148</sup> or desalination<sup>149</sup>. As already described, they also own magnificent features which make them ideal contenders for application in non-enzymatic electrochemical sensing. Hereinafter, by now existing sensing platforms based on laser-induced carbon are highlighted.

As the mechanical stability of LIG is sufficient, it has already been developed towards sensing of multiple analytes in aqueous media. Zhang *et al.* decorated LIG, which was generated on PI foils, with copper nanoparticles by substrate-assisted electroless deposition. They connected LIG to zinc foil and immersed it into copper solution. Due to the potential difference between the zinc and the copper ions, copper nanoparticles were deposited on the LIG surface. They were able to amperometrically quantify glucose in the range of 1  $\mu\text{M}$  to 6 mM with a LOD of 0.39  $\mu\text{M}$ . Also, they could detect glucose from human blood serum sample that was injected into NaOH matrix without significant signal interference.<sup>150</sup> Laser-induced carbon electrodes were yet successfully prepared for the enzyme-free electrochemical detection of  $\text{H}_2\text{O}_2$ ,<sup>151,152</sup> dopamine, ascorbic acid,

uric acid<sup>118</sup> and biogenic amines.<sup>153</sup> A more advanced solution for the detection of many analytes in an aqueous mixture was presented by Yu *et al.* who fabricated a LIG sensor array based on the electronic tongue principle. Their systems consist of six units that were each functionalized with different composites such as gold, rGO and polyaniline (PANI). By principle component analysis of impedance data, their sensor was able to distinguish between sweet (sugar), salty (NaCl) and sour (vinegar) at thresholds lower than possible for a human tongue.<sup>154</sup>

Apart from non-enzymatic sensing in solution-based detections, the high porosity and large surface area of laser-induced carbon materials ideally lends itself to sensing of gaseous molecules. Stanford *et al.* prepared LIG with a surface area of  $\sim 350 \text{ m}^2 \cdot \text{g}^{-1}$  which they successfully employed for the detection of a variety of gases ( $\text{CO}_2$ ,  $\text{N}_2$ , Air, Ar,  $\text{O}_2$ , He,  $\text{H}_2$ ). By application of a high voltage (5 V), Joule heating occurred at the microgap between two LIG electrodes, which resulted in a change of the resistivity. After exposure of the sensor to a gas, changes in resistance could be translated to the thermal conductivity, which has typical values for different gases.<sup>155</sup> With a similar strategy Yang *et al.* were able to detect  $\text{NO}_2$  down to 1.5 ppb (parts per billion). They coated Ag ink on a serpentine interconnect region of LIG to enable localized Joule heating and improved sensitivity as well as selectivity by modification with rGO/MoS<sub>2</sub>. To measure components of a gaseous mixture, they proposed an array of LIG modified with several nanocomposites with each having a different selectivity.<sup>156</sup> Zhu *et al.* picked the approach of simulating the turbinate-like structure of a dog nose that is known for its outstanding odor perception abilities. After decoration of their LIG with Pd nanoparticles, the resistance change of the artificial nose sensor towards 2 %  $\text{H}_2$  at ambient conditions could be detected.<sup>157</sup> By introducing GO, interdigitated LIG electrodes have also already been applied as capacitive humidity sensors, for breath analysis and monitoring plant transpiration.<sup>158,159</sup>

Future trends guide towards point-of-care sensors and wearable electronics due to the increasing awareness in health monitoring. Tao *et al.* were among the first to report a wearable device based on LIG. They showed the functionality of LIG as an artificial throat which can generate and detect different sounds due to mechanical vibration and is, therefore, promising for disabled people.<sup>160</sup> Recently, Yang *et al.* presented a lab-on-a-chip wearable patch completely created by laser engraving. The sensor consists of multiple layers including a microfluidic module that allows the dynamic sweat sampling while wearing and medical adhesive layers for mounting the whole patch on the skin. Additionally, the device is connected to a reusable flexible printed circuit board which makes wireless readout possible (Figure 1.4i). They have verified *in situ* uric acid and tyrosine measurements and were able to correlate the obtained signals with healthy patients and patients with hyperuricemia or gout making their lab-on-a-chip very useful for early diagnosis and



prevention of this disease.<sup>161</sup> By simple casting with elastomeric substrate, e.g. PDMS and peeling off, Lamberti *et al.* demonstrated for the first time the transfer of LIG electrodes from polyimide onto flexible, transparent and stretchable polymers (Figure 1.4ii).<sup>162</sup> Similar approaches of transferring LIG to a wearable substrate were carried out by several other research groups. For example, Xuan *et al.* decorated LIG with silver nanowire prior to PDMS casting to enhance the conductivity under mechanical deformations. After peeling off the PDMS composite, they electroplated Pt and Au NPs on the surface to enhance analyte sensing abilities. They showed the direct detection of glucose in human sweat and proposed the application as wearable.<sup>163</sup> Prabhakaran and Nayak were even able to demonstrate the direct sensing in secreted body sweat. They modified their LIG by deposition of copper salt with subsequent focused sunlight treatment to obtain crystalline Cu nanoparticles. By transferring the LIG to a Scotch brand tape the electrode can be taped on the body (Figure 1.4iii). Before, NaOH solution was drop-casted and dried on the electrode surface whereby the alkaline conditions were retained. Therefore, they could directly detect glucose in sweat secreted on body without the need of injection into NaOH matrix.<sup>164</sup>

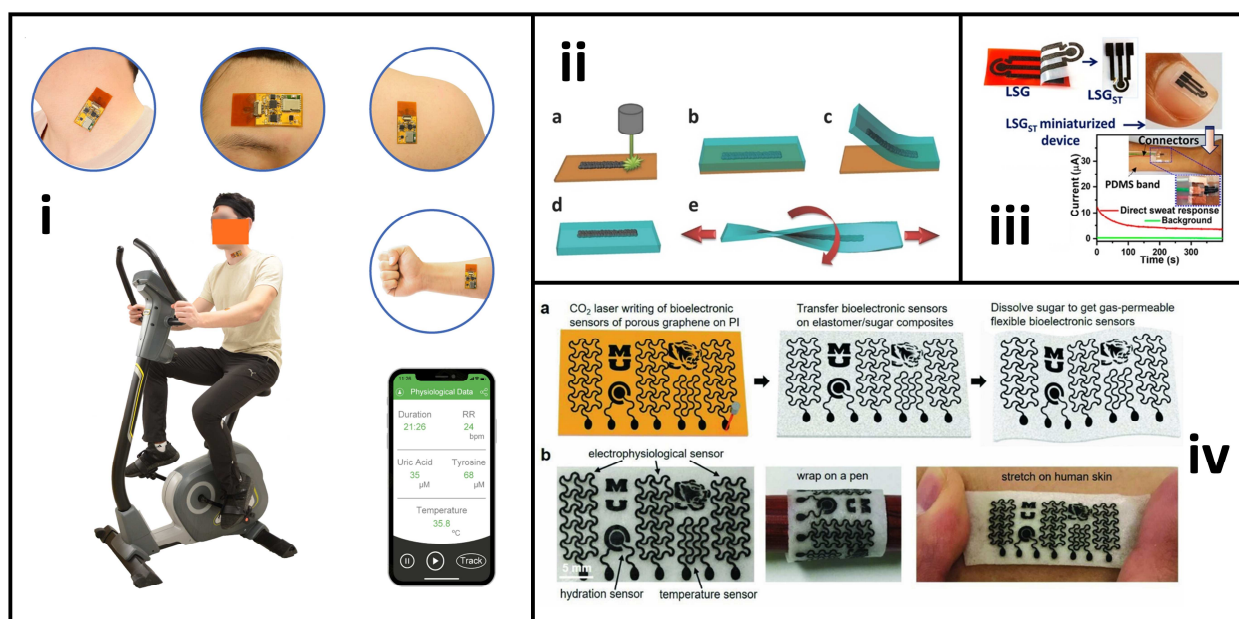


Figure 1.4: Wearable sensing systems based on laser-induced graphene. Panel i: Laser engraved lab-on-a-chip mounted on different body parts and wireless monitoring of uric acid, tyrosine, respiration rate and temperature via smartphone. Adapted with permission from Yang *et al.*<sup>161</sup> Panel ii: Scheme of transferring LIG generated on polyimide foil (a) by casting with PDMS (b) and subsequent peeling off (c). The LIG is now bound to PDMS (d) which offers elastic properties (e). Adapted with permission from Lamberti *et al.*<sup>162</sup> Panel iii: Transfer of LIG to Scotch brand tape that can be taped to the body and monitor analytes directly in produced sweat. Adapted with permission from Prabhakaran and Nayak.<sup>164</sup> Panel iv: Transfer of LIG to gas-permeable silicon elastomer sponges (a). Multi-sensing abilities and demonstration of the flexible behavior of the sensor (b). Adapted with permission from Sun *et al.*<sup>165</sup>

Sun *et al.* realized the transfer of LIG to elastomeric silicone/sugar composites, which are also gas-

permeable and can comfortably be worn on the skin and survive multiple bending without meaningful resistance change (Figure 1.4iv). Their prototype is able to monitor temperature and hydration changes and allows the water permeation which reduces inflammation risks at long-time wearing.<sup>165</sup> The aim of the studies from Chhetry *et al.* was the sensing of strain changes due small movements on the human skin such as wrist pulse. They hybridized LIG with MoS<sub>2</sub> to achieve an electromechanical stability for over 12,000 strain/release cycles, which is an idea that could be also be adapted to improve wearable electrochemical sensors.<sup>166</sup> Another highly fascinating field is soft robotics that can interact with humans. In this regard, Ling *et al.* fabricated LIG-based soft electrothermal actuators with several shapes that are capable of reconfigurable 3D assembly by mechanic guidance such as gesture control. Further, the potential application as artificial muscle was investigated and the ability to lift a mass of about 110 times of the own weight was found out. Their soft robotic finger is able to reversible wrap around a human finger on demand and carry out electrocardiogram measurements.<sup>167</sup> Those approaches can be role models for the development of wearable non-enzymatic sensors that can also interact with humans on demand.

## 1.5 Conclusion and Outlook

Non-enzymatic electrochemical sensors are powerful tools that promise great functional stability compared to enzymes-based approaches while being highly affordable and operable in a fast and sensitive manner. The catalytic activity of nanomaterials can be tailored by their size and shape which both determine the number of active sites available for interaction and guide electron flow. For introduction of an analyte specificity, an almost unlimited pool of metal-based catalysts is available. However, there are still only a hand full of solutions presented that enable sensing in real sample solutions or *in vivo*. One of the main issues is the need of alkaline media as reactive hydroxide ions are adsorbed on the metal surface and are responsible for catalytic interaction with analyte molecules. Noble metals are less dependent on basic conditions as their electronic properties are usually more advanced than those of non-noble metals. Nevertheless, metal surface charges vary with pH and, therefore, interference by other molecules can increase at neutral pH. To solve this, further anti-interferent modifications are necessary, which increases the amount of sensor preparation steps. Additionally, the necessity of noble-metals impedes commercialization due to high costs.

Carbon nanomaterials have become a popular choice because of their outstanding properties such as high electron transfer abilities, mechanical stability, introducible functionality and biocompatibility. It is, therefore, not surprising that they are often chosen as transducer matrix for hybridization with catalytic elements in order to accomplish excellent sensing performance. The classical ways of their synthesis include laborious and time-consuming steps required and are often limited in exploiting the full beneficial features due to inefficient integration of traditional approaches. Laser-induced carbonization stepped into the focus as this alternative technique allows to directly carbonize different substrates in a short time into conductive structures with the additional benefit of electrode design flexibility. The variation of lasing parameters and conditions makes the precise control of the obtained carbonized morphology possible, which permits the tunability of conductivity as well as wettability. Using electrospun nanofibers as precursors showed up as an efficient strategy to generate laser-induced carbon nanofibers. Assembled in a 3D network, they own a high porosity and surface area which results in superior fast electron transfer. By doping the electrospinning solutions with metal salts, nanocatalytic competences of the carbon nanofibers are yielded which can be matched to different analytes.

The future development of laser-induced carbon materials will thus be exciting to carry out. Focus of current research is more and more related to the practicability of sensing systems where it should be easy to be used, require less sample handling and minimal or untrained operators. The patient

or end-user should be able to make use of such sensors without complicated instructions. With respect to laser-induced nanomaterials, the miniaturization ability and possible mass-production capability can be the breakthrough criteria for developing the next generation point-of-care sensors. Another pathway in the right direction is the presented studies on laser-induced carbon nanomaterials for wearables. However, most of them so far are investigated towards measurement of physical changes such as strain, temperature etc. and there is still a lack of sensors for the monitoring of important metabolites such as glucose or hydrogen peroxide whose anomalous levels can be linked to diseases. As the cell adhesion and growth was demonstrated and biosafety was confirmed recently for LIG, investigations towards application in and on human body are becoming closer.

Heteroatom-doping of carbon nanomaterials has been proven to increase catalytic abilities. In combination with the introduction of nanocatalytic metal, hybrids can realize magnificent sensing performance due to synergistic effects. Thus, heteroatom-doping of laser-induced carbon by controlled atmospheres during lasing process together with metal modifications could result in highly sensitive and robust non-enzymatic electrochemical sensors. The choice of little amount of noble metal even could be a compromise to make the application in real biological media possible without significantly increasing costs.



## 2 Motivation and Structure of the Thesis

Electrochemical analyte detection has several advantages over other detection techniques, which are among others the affordable equipment, high sensitivity and fast response. Sensors in combination with enzymatic biorecognition elements have been established for a long time due to their high selectivity and sensitivity. However, drawbacks for application of enzymes lie in their expensiveness and low stability (biological, chemical and environmental). Instead, nowadays non-enzymatic sensing stepped into focus because of much better stability and lower costs compared to enzymatic approaches. **Chapter 1** comprises the recent progress in non-enzymatic electrochemical sensing with focus on laser-induced carbon nanomaterials. State-of-the-art, definition and advantages of non-enzymatic electrochemical sensors are briefly summarized. In the following catalytic mechanisms themselves are discussed and the context of how size and shape of certain materials impact on their catalytic properties is represented. Here the generation of nanomaterials with different dimensions from 0D to 3D and their characteristics is recessed. Metal-based catalysis is a rising field in non-enzymatic sensing. Therefore, the groups of noble metals, non-noble metals and composites are highlighted. Another important class is made up by the carbon nanomaterials which possess several exciting features for electrochemistry. Thus, examples of their derivatives such as carbon quantum dots and graphene quantum dots are given and modified carbon is compared to carbon materials alone. With respect to sensing, the challenges of most popular analytes and a few potential solutions found by researchers are presented. It is lead through the novel topic of laser-induced carbon materials by explaining the working principle and the effects that several lasing parameters have on the obtained carbon quality. Picking up the earlier discussed catalytic features of metal and carbon materials, laser-induced functional materials containing nanocatalytic metal and doping-features are introduced. The new strategy of preparing carbon nanofibers with catalytic functionalities by laser-induced carbonization of electrospun nanofibers, which was developed during studies related to this thesis, with its benefits over conventional carbon nanofiber generation methods is presented. Concluding the chapter, already developed applications of laser-induced carbon and future prospective are shown.

The main goal of this thesis is to demonstrate the fabrication of carbon nanofibers (CNFs) with electrochemical sensing abilities by laser-induced carbonization of electrospun nanofibers. Conventionally, synthesis of carbon nanofibers is achieved by two different methods which are chemical vapor deposition (CVD) and thermal carbonization of electrospun nanofibers. Both approaches face some drawbacks that hinder the translation into commercial products. The thermal treatment steps are laborious and essential vacuum conditions necessitate cost-intensive devices.

Additionally, the complexity of the integration into electrochemical (miniaturized) devices is very high, especially for carbon nanofibers obtained from thermal carbonization. Here, the fibers often afterwards need to be shortened and dispersed in a proper solvent prior to drop-casting on an electrode support. This sometimes also requires detrimental binders that could hamper later sensing abilities. Laser-induced generation of carbon nanomaterials is chosen to be investigated in this work due to its potential to overcome those challenges. Further, the high surface-to-volume ratio of electrospun 3D nanofiber mats is favorable for electroanalytical detection and additives, which introduce different functional properties, can easily be incorporated during electrospinning process. However, there are many questions to be answered initially before establishing the as-fabricated carbon nanofibers for electroanalytical sensing applications. In the following chapters the associated studies are presented.

In **chapter 3** the strategy development of carbonization of electrospun polyimide nanofibers by CO<sub>2</sub>-laser irradiation is presented from scratch. This method allows the one-step generation of laser-induced carbon nanofibers (LCNFs) at ambient conditions, meaning without the need of laborious inflexible steps, vacuum or high temperatures during carbonization compared to CVD and thermal carbonization. It is revealed how LCNF morphology is linked to electrochemical properties by varying lasing power and fiber mat thickness through different electrospinning collecting durations. Furthermore, the role of metal salt content in LCNFs, introduced by doping electrospinning solutions, in combination with different laser scribing strategies (continuous vs. discontinuous) is discussed. After optimization of metal content and lasing parameters, the morphological properties of the material are characterized and kinetic studies are carried out to understand electron transfer abilities. Different electrode designs and amount of electrodes in one lasing step are tested for fixed lasing conditions to be able to ensure the reliability of preparing LCNF electrodes and predict ideal electrochemical features. This chapter ends with a comparison of iron-containing LCNFs with commercially available screen-printed gold and carbon electrodes with respect to electrochemical behavior (detection potential, peak current). Here, the sensing of several analytes is investigated to verify the real application possibilities of the new LCNF electrode nanomaterial.

Based on the findings from chapter 3, LCNFs with nanocatalytic functionalities are explored which is presented in **chapter 4**. Nickel was chosen as metallic ingredient of LCNFs due to the catalytic ability towards glucose oxidation which is one of the most important analytes because of the continuous increase of diabetes numbers. The morphology of Ni-LCNFs is studied in dependence of nickel content and lasing parameters and compared to Fe-LCNFs from previous chapter. In detail morphology (hollow vs. solid) of Ni-LCNFs compared to electrospun nanofibers is indicated

by SEM and TEM (scanning and transmission electron microscopy). Also, the formation of Ni nanoparticles within the carbon matrix is observed from TEM imaging. Energy-dispersive X-ray (EDX) measurements, before and after shaking incubation mimicking application at physiological conditions, are carried out for Ni-LCNFs vs. electrodeposited nickel on LCNFs and laser-induced graphene (LIG) to investigate the mechanical stability of metal nanoparticles. This is done in order to examine potential application possibility *in vivo* where the stability of sensor components, especially (toxic) metal, should be ensured. Further, the glucose sensing mechanism and sensing characteristics of Ni-LCNFs are investigated. With amperometry the linear range, sensitivity and limit of detection are quantified and compared to already existing platforms to demonstrate the usability of LCNFs for catalytic analyte detection. Common interferents for glucose detection which are present in real samples, ascorbic acid and uric acid, are investigated at their pertinent concentrations verifying the catalytic sensitivity introduced by nickel. The studies are performed to demonstrate the preparation of carbon nanofibers containing nanocatalytic metal nanoparticles by laser-induced carbonization, which could thus be also of relevance for a variety of other catalysis-related applications.

Regarding the last aspect, it was the aim of the research results presented in **chapter 5** to enable non-enzymatic detection of hydrogen peroxide.  $\text{H}_2\text{O}_2$  plays key roles in many metabolic processes e.g. it is released locally after wounding. Monitoring the respective levels allows supervising the healing process. Among many metals, palladium and iron salts have shown catalytic reduction of hydrogen peroxide. Hence, the electrospinnability of palladium-containing polyimide nanofibers is investigated and optimized in relation to metal content. The sensitivity of Pd-LCNFs towards  $\text{H}_2\text{O}_2$  is tried to be improved by electrochemical treatment of electrodes and also chemical reduction of metal species by incubation of electrodes with  $\text{NaBH}_4$ . First experiments with bimetallic LCNFs, including both iron and palladium salts, explore the change of catalytic behavior compared to monometallic counterparts. The chapter ends with proposals how the sensitivity of metal-containing LCNFs can be further refined to allow detection of hydrogen peroxide at low levels necessary for final wound healing sensor development.

**Chapter 6** concludes the overall results presented in the previous chapters. The key findings but also challenges are addressed. Suggestions for solving the latter are made by revealing potential next steps and experiments. Additionally, in this chapter an outlook on future perspectives of LCNF with respect to different sensing application fields is given.





### **3 A Robust Strategy Enabling Addressable Porous 3D Carbon-Based Functional Nanomaterials in Miniaturized Systems**

#### **3.1 Abstract**

3D-porous carbon nanomaterials and their hybrids are ideal materials for energy storage and conversion, biomedical research and wearable sensors, yet today's fabrication methods are too complicated and inefficient to implement into miniaturized systems. Instead, it is shown here that 3D-carbon nanofibrous electrodes of various designs, shapes and sizes, on flexible substrates, under ambient conditions and without complicated equipment and procedures can simply be “written” via a one-step laser-induced carbonization on electrospun nanofibers. Analytical functionalities are realized as full control over native polymer chemistry doping of the polymer (e.g. with metals) is provided. Similarly, being able to control mat morphology and its impact on the electroanalytical performance was studied. Ultimately, optimized writing conditions were harnessed for superior (bio)analytical sensing of important biomarkers (NADH, dopamine). The new procedure hence paves the way for future controlled studies on this 3D nanomaterial, for a multitude of functionalization and design possibilities and for mass production capabilities necessary for their application in the real world.

---

*This chapter has been published and formatted to fit this thesis:*

Wongkaew, N.; Simsek, M.; Arumugam, P.; Behrent, A.; Berchmans, S.; Baeumner, A. J. A Robust Strategy Enabling Addressable Porous 3D Carbon-Based Functional Nanomaterials in Miniaturized Systems. *Nanoscale* **2019**, *11*, 3674–3680.

#### *Author contributions*

The author and Dr. Nongnoot Wongkaew contributed equally in designing and conducting the experiments and evaluating the data. Dr. Nongnoot Wongkaew and Prof. Dr. Antje J. Baeumner wrote the manuscript draft. Dr. Arumugam Palaniappan and Arne Behrent carried out preliminary studies. Prof. Dr. Antje J. Baeumner and Dr. Sheela Berchmans led the project administration and promoted manuscript preparation.

### 3.2 Introduction

Carbon nanofibers (CNFs) assembled in a 3D network exhibit a remarkably large surface area and high porosity with a number of edge sites that are attractive to use as transducers for vapor-gas sensing and electrochemical sensors in miniaturized systems. In particular, CNFs can overcome diffusion limitation in microfluidic systems that results in high analytical performance and short response time.

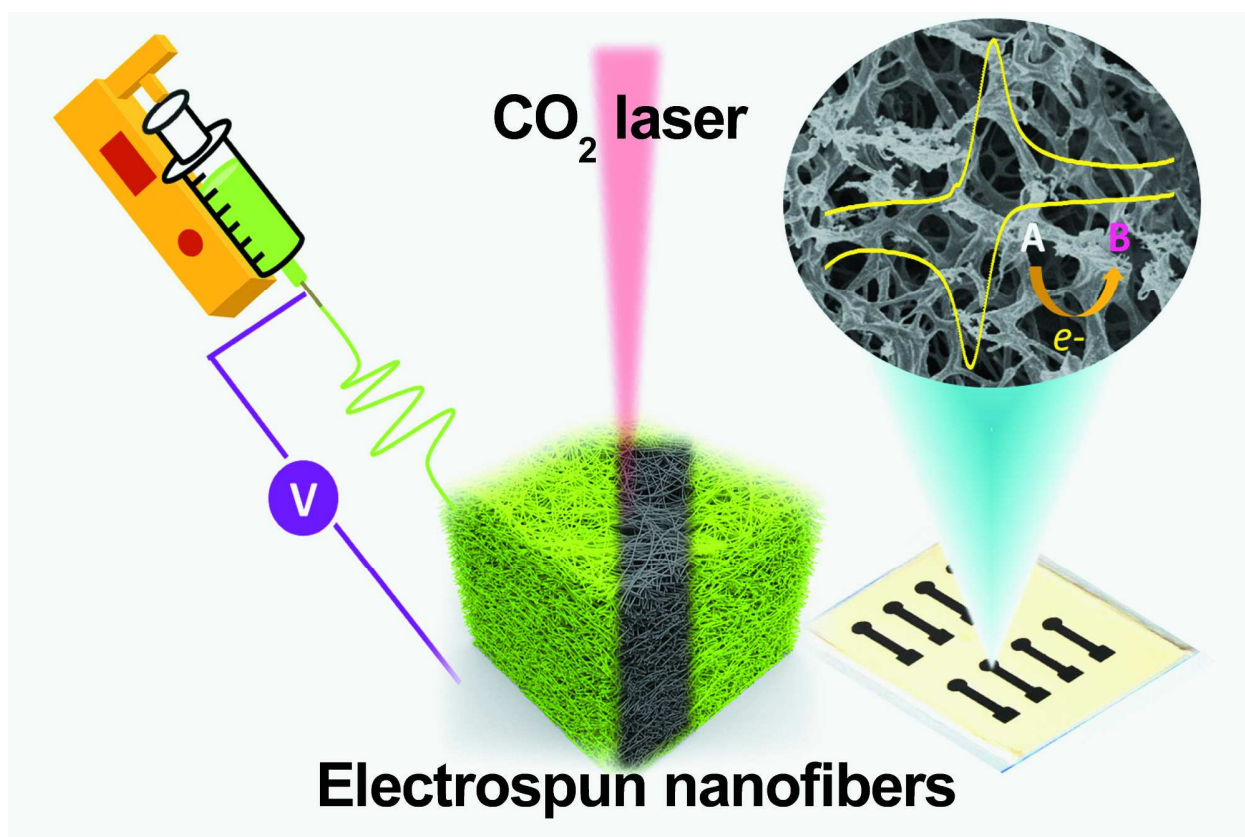


Figure 3.1: Facile construction of high performance carbon nanofiber electrodes via electrospinning and one-step laser-induced carbonization for electrochemical sensors in miniaturized systems.

Electrospinning followed by heat-induced carbonization is popular for CNF generation as it is versatile, has a high yield and low cost. Electrospinning can massively produce continuous nanofibers by applying an electrostatic force to a polymer solution (Figure 3.1 and Figure 3.2a) and when using a precursor polymer, e.g. polyacrylonitrile, CNFs are typically generated upon stabilization and heat-induced carbonization. CNFs have been successfully applied as electrochemical transducers enabling high detection sensitivity and an exceptionally wide detection range.<sup>168</sup> However, the integration of CNFs into devices is currently inefficient and does not exploit the full benefits of its 3D-porous structures. For example, electrospun CNFs have to be shortened and dispersed in a solvent prior to drop-casting onto electrode supports.<sup>135</sup> In some case,

non-conductive binders are needed to strengthen adhesion between the CNFs and the electrode supports.<sup>169</sup> A laborious packing procedure of CNF paste into a tube holder has also been proposed.<sup>138</sup> Those conventional approaches lead to poor sensing performance and reproducibility of CNF-based electrodes and hinder the scale-up and pattern ability of sensor fabrication.

Laser-induced carbonization, developed by Tour's group, has proven to be an outstanding technique to generate laser-induced graphene-based electrodes (LIGs) on any carbonizable substrate with cost-effective, pattern ability and mass-production capability.<sup>170</sup> Polyimide (PI) sheet is a common substrate successfully used for the construction of 2D-graphene electrodes. Recently, 3D-printed laser-induced graphene foams were proposed by using a 3D-printing process based on laminated object manufacturing.<sup>171</sup> The technique relies on scribing stacked multiple LIG layers, where binding agents were applied between the adjacent LIG sheets. This method is unfortunately only practical for generating electrodes with larger thickness, i.e.  $> 100\ \mu\text{m}$ , which are of limited use in miniaturized systems. Moreover, an introduction of additional functionalities is restricted only to occur after LIG generation. Using electrospun nanofibers as a precursor substrate can address these issues. Even though a few previous studies have already demonstrated the capability of laser for carbonization of electrospun nanofibers, none have focused on sensor applications and one-step lasing induced CNF generation (Figure 3.1).<sup>172,173</sup>

As electrospun nanofibers are typically built up as 3D porous structures ( $\mu\text{m}$  range in mat thickness), exposing them to a laser requires investigation into possibly uneven distribution of the laser power in z-direction, i.e. top layer fibers get exposed with the strongest laser power. In addition, in densely packed fiber mats penetration with sufficient laser power to the bottom part has to be ensured. Furthermore, without a thermal stabilization step thermal damaging is likely to occur as the nature of pristine electrospun nanofibers is fluffy and delicate, hindering the generation of CNFs with high integrity. Moreover, metal salts, e.g. iron, have been widely introduced into the polymer solution either to promote the formation of an ordered carbon structure,<sup>174</sup> or to generate metal nanocatalysts embedded CNFs during thermal carbonization.<sup>135</sup> Addition of such metal promoters/precursors (or other materials with excellent heat conductivity) into the nanofibers can lead to different heat-transfer properties, which consequently affect to the lasing process and ultimately the CNF characteristics. However, no previous study has addressed these issues so far, especially in light of application towards electrochemical sensors.

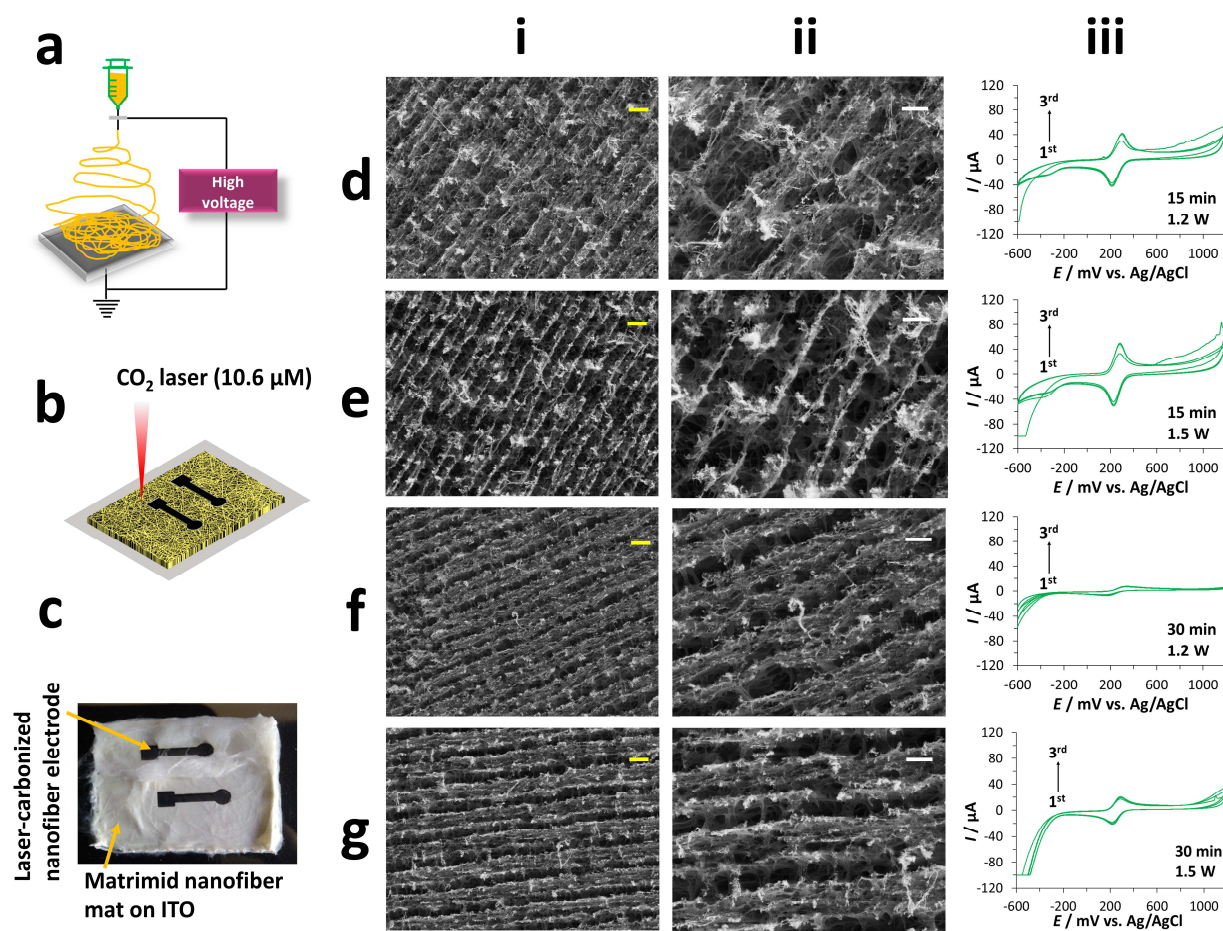


Figure 3.2: Schematic illustration of electrospinning (a). Laser carbonization of electrospun nanofibers (b). A photograph of LCNF electrodes (c). SEM images of LCNFs (i and ii) after lasing a 15 min-fiber mat at 1.2 W (d) and 1.5 W (e) laser power, respectively. SEM images of LCNF (i and ii) after lasing a 30 min-fiber mat at 1.2 W (f) and 1.5 W (g), respectively. Corresponding current signals are shown in panel (iii). Matrimid® nanofibers here contained 3 % iron. Scale bars of (i) and (ii) are 20 μm and 10 μm, respectively.

Our present investigations aim to unravel the relationship between nanofiber mat morphology and laser-exposing conditions on the laser-induced carbon nanofibers (LCNFs) as well as the resulting electroanalytical performance. Here, Matrimid® 5218 is chosen as a polymer precursor because it is a solvent soluble PI so that imidization is not necessary, as required when polyamic acid is used. The composition of the spinning solution and electrospinning conditions were followed as reported by Chung *et al.*<sup>174</sup> The as-spun fiber mat was lased using a CO<sub>2</sub>-laser in ambient conditions (Figure 3.2a+b). It was found out that only flat heat-dissipating substrates such as ITO on PET foils promoted reliable pyrolyzation and nanofiber-mat formation even under unoptimized conditions (Figure 3.2c) in contrast to glass, wax paper and aluminum foil (Figure S3.1). The superior uniformity could be attributed to the higher mat thickness on ITO than the insulating materials (wax paper and glass slide). In the case of aluminum foil as collecting substrate, overheating probably affected the formation of a uniform carbon electrode.

The electrospinning and the laser scribing process offer a number of variables that may influence the overall electroanalytical performance of the LCNFs, e.g. the structure of the nanofiber mat, polymer chemistry and the energy input per electrode. Thus, we studied (i) the effect of nanofiber mat density, (ii) the effect of iron doping as it leads to better heat dissipation along the polymer fibers and (iii) continuous and discontinuous scribing conditions, in which the former process allows for cooling of scribed locations. In each scenario, a couple of key conditions were investigated to determine process effects on electroanalytical characteristics.

### **3.3 Material and Methods**

#### **3.3.1 Electrospinning of Matrimid® Nanofibers**

The nanofibers were fabricated by electrospinning of a solution containing 15 % (w/v) Matrimid® 5218 (Huntsman Advanced Materials (Europe) BVBA, Belgium) and iron(III) acetylacetonate ( $\geq 99.9$  % trace metals basis, Sigma-Aldrich, Germany) dissolved in N,N-dimethylacetamide (Merck, Germany). The mixture was stirred at least 18 h prior use. The percentage of iron(III) acetylacetonate content, abbreviated as iron or Fe, reported here was relative to the mass of polymer. Electrospinning was carried out using 10  $\mu\text{L}\cdot\text{min}^{-1}$  flow rate, 12 kV applied voltage and 15 cm tip-to-collector distance (unless stated otherwise). The nanofiber mat was deposited on an ITO/PET sheet (a sheet resistivity of 60  $\Omega\cdot\text{sq}^{-1}$ , Sigma-Aldrich, Germany) with 3.5 cm  $\times$  4.5 cm collecting area (unless stated otherwise).

#### **3.3.2 Laser-Induced Carbonization of Electrospun Matrimid® Nanofibers**

A CO<sub>2</sub>-laser (10.6  $\mu\text{m}$ ) with a maximum power of 30 W (VLS 2.30, Universal Laser Systems, Polytech Systeme GmbH, Germany) was employed for inducing carbonization process of the as-spun nanofibers. The lasing process was carried out at a speed of 60 % (maximum speed is 1,270  $\text{mm}\cdot\text{s}^{-1}$ ) with an image density of 1,000 DPI for all experiments.

#### **3.3.3 Morphology Characterization**

A 3D-confocal laser scanning microscope (Olympus LEXT 3D Measuring Laser Microscope OLS4000, Germany) was used for imaging the LCNF electrodes and the nanofiber mats in the large field of view. The roughness of fiber mats and electrodes was determined by the OLS4000 software. SEM (Zeiss/LEO 1530, Germany) was used to image LCNFs and pristine fibers.

#### **3.3.4 Electrochemical and Electrical Characterization**

The cyclic voltammetry runs from -0.6 V to 1.2 V were performed by using a potentiostat (CV-50W Voltammetric Analyzer, Bioanalytical Systems, USA) with a three-electrode system consisting of LCNF electrode, Pt wire and Ag/AgCl (3 M KCl) as a working, a counter and a reference electrode, respectively. The scan rate was controlled at 50  $\text{mV}\cdot\text{s}^{-1}$  (unless stated otherwise). 1 mM ferri/ferrocyanide (in 0.1 M phosphate buffer, 0.1 M KCl, pH 7.0) was employed as a redox marker for determining peak-to-peak separation. Sheet resistances of electrodes were determined by four-point probe technique.

### **3.3.5 Chemical Characterization**

Raman spectroscopy (DXR<sup>TM</sup> 3 Raman microscope, Thermo Fisher Scientific GmbH, Germany) and Fourier transform infrared spectroscopy with attenuated total reflectance (FTIR-ATR, Agilent Cary 630 FTIR, USA) were used to monitor the formation of graphitic carbon from Matrimid<sup>®</sup> precursor. X-ray photoelectron spectroscopy (XPS) and elemental analysis were used to determine the chemical compositions of the materials.



## 3.4 Results and Discussion

### 3.4.1 Effect of Electrospinning Conditions in Combination with Laser Power

The morphology of the electrospun nanofiber mat with respect to its density can be controlled by electrospinning conditions, e.g. through the tip-to-collector distance (TCD) and the collecting time. In our preliminary study (Figure S3.2), fiber mat densities derived from varying these parameters greatly affected the proper lasing condition and final LCNF morphology. Keeping conditions constant, we were able to optimize and then routinely generate highly porous and fibrous LCNF electrodes, which are ideal for most electroanalytical applications. Further, SEM and electroanalytical studies show that larger pores and wider spacing in LCNFs are generated from less dense fiber mats (Figure 3.2d+e) than those from denser fiber mats (Figure 3.2f+g) for both lasing powers studied and benefit the electroanalytical behavior. Larger pore sizes lead to greater current intensity, which suggests that those electrodes have a larger electroactive surface area (ESA).

Interestingly, at such morphology, the applied laser power significantly affects not only to LCNF morphology (Figure 3.2d vs. Figure 3.2e) but also the electron transfer kinetic and the ESA. Here, the LCNF electrode from 15 min mat lased at 1.5 W provides a rapid electron transfer kinetic as indicated by the identical peak potentials observed at various scan rates ( $25\text{-}150\text{ mV}\cdot\text{s}^{-1}$ ) for  $[\text{Fe}(\text{CN})_6]^{4-/3-}$  (Figure S3.3a). On the contrary, lasing with 1.2 W results in potential shifts upon increasing the scan rate (Figure S3.3b). The ESA of LCNF-1.5 W estimated by Randles-Sevcik equation<sup>175</sup> was ca. 3 times higher than that of LCNF-1.2 W and 4 times greater than the geometric area (Figure S3.3a-ii and b-ii). Our results indicate that optimal fabrication conditions can be accurately controlled through the electrospinning and lasing process and that the presence of fibrous structures is highly beneficial for electroanalytical applications.

### 3.4.2 Role of Iron

Kim *et al.* have proven that iron plays a crucial role in the heat-carbonization process of electrospun Matrimid<sup>®</sup> nanofibers.<sup>174</sup> We thus investigated the role of iron in LCNF electrode generation. The spinning solution containing 5 % iron produces more uniform and smooth fibers but their fiber thickness ( $374 \pm 58$ ) nm is comparable to the fibers without iron doping ( $418 \pm 131$ ) nm (Fig. 2a-i and a-iv). At the same laser settings, the top layer of fibers without iron tend to remain fused together after lasing (Figure 3.3a-ii) while fibers doped with iron exhibit fibrous-like structures also on the top (Figure 3.3a-v). Moreover, LCNFs without iron generate hollow and distorted fiber structures (Figure 3.3a-iii), whereas LCNF-doped iron provides better

fiber integrity (Figure 3.3a-vi). These results suggest that iron plays a significant role in facilitating heat transfer along the fibers which consequently maintain fiber integrity.

The Raman spectra (Figure 3.3b) confirm that Matrimid<sup>®</sup> nanofibers are converted into graphitic carbon as shown by the presence of G, D and 2D band at ca. 1580  $\text{cm}^{-1}$ , 1340  $\text{cm}^{-1}$  and 2670  $\text{cm}^{-1}$ , respectively.<sup>176</sup> The  $I_D/I_G$  ratios shown in Figure 3.3b indicate that there is a high number of edge/defect sites in all LCNFs irrespective of the presence of iron. Moreover, as shown by the  $I_{2D}/I_G$  ratios, the LCNFs in both cases consist of a multilayer graphene structure. The disappearance of peaks attributed to organic groups of Matrimid<sup>®</sup> nanofibers studied by FTIR-ATR (Figure S3.4) also ensures the completed carbonization of nanofibers at 1.5 W laser power.<sup>177</sup> Furthermore, from elemental analysis (Table S3.1), an increase of carbon from 73.6 % to 89.3 % and a drastic reduction of hydrogen, nitrogen and oxygen demonstrates the highly efficient conversion of Matrimid<sup>®</sup> precursors into LCNFs. Moreover, the XPS data reveals that an atomic iron content of  $(0.65 \pm 15) \%$  was found in LCNFs made of nanofibers containing 5 % iron(III) acetylacetonate. This is consistent with the theoretical value (0.75 %).

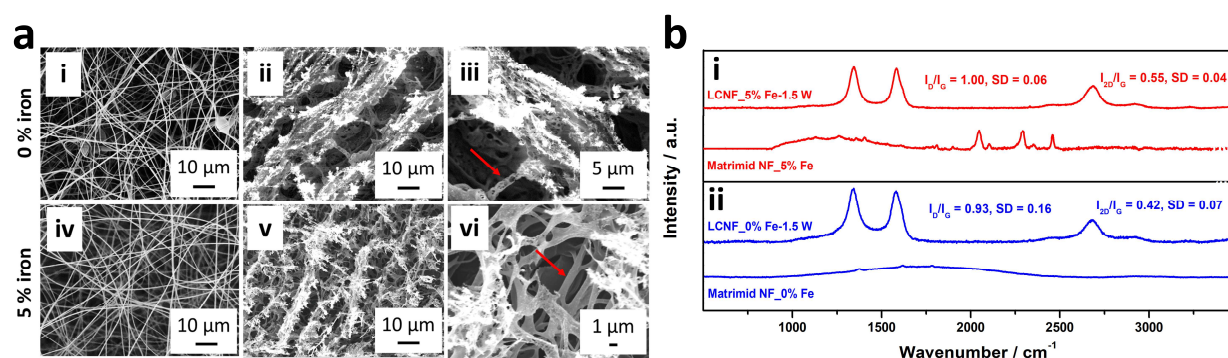


Figure 3.3: SEM images of fibers in the absence and presence of iron before lasing (i and iv) and after lasing (ii, iii, v and vi) with a laser power of 1.5 W (a). The red arrows indicate the integrity of fibers. Comparison of Raman spectra of nanofibers and LCNFs in the presence (i) and absence (ii) of iron (b).

The effect of heat dissipation on LCNF formation was further investigated using natural cooling during the scribing process in combination with varying the iron content. Minimal heat dissipation was achieved by scribing an entire electrode feature at a time prior to scribing the next electrode (discontinuous electrode scribing) and using no iron within the Matrimid<sup>®</sup> polymer dope. Maximum heat dissipation was obtained by allowing cooling time between each scribed line on an electrode feature as the laser moved across all electrodes in a row prior to returning to scribe the next adjacent line (continuous electrode scribing). It was observed that the temperature/cooling effect is an important LCNF fabrication design element and can be controlled by doping with iron. For example, in the case of discontinuous scribing, low laser power and low iron content (0 % and

3 % iron) are required to obtain the desired electrode features (Figure 3.4a). On the contrary, high iron content and high laser power are needed when continuous scribing over large lasing areas is performed, in particular with dense nanofiber mats (see also Figure S3.5a+b). The electrochemical performance, indicated by peak-to-peak separation ( $\Delta E_p$ ), correlates directly with these findings (Figure 3.4b). Here, optimal scribing conditions (such as continuous scribing at 1.2 W and 1.5 W for fibers containing 5 % iron) present the smallest  $\Delta E_p$  and the smallest variation across all electrodes scribed, which indicates a highly uniform generation of LCNFs. We can overall conclude from the results that laser-induced carbonization necessitates a proper cooling time to render greater fiber integrity and that increasing metal-doping of the polymer allows using lower laser power or faster scribing speeds.

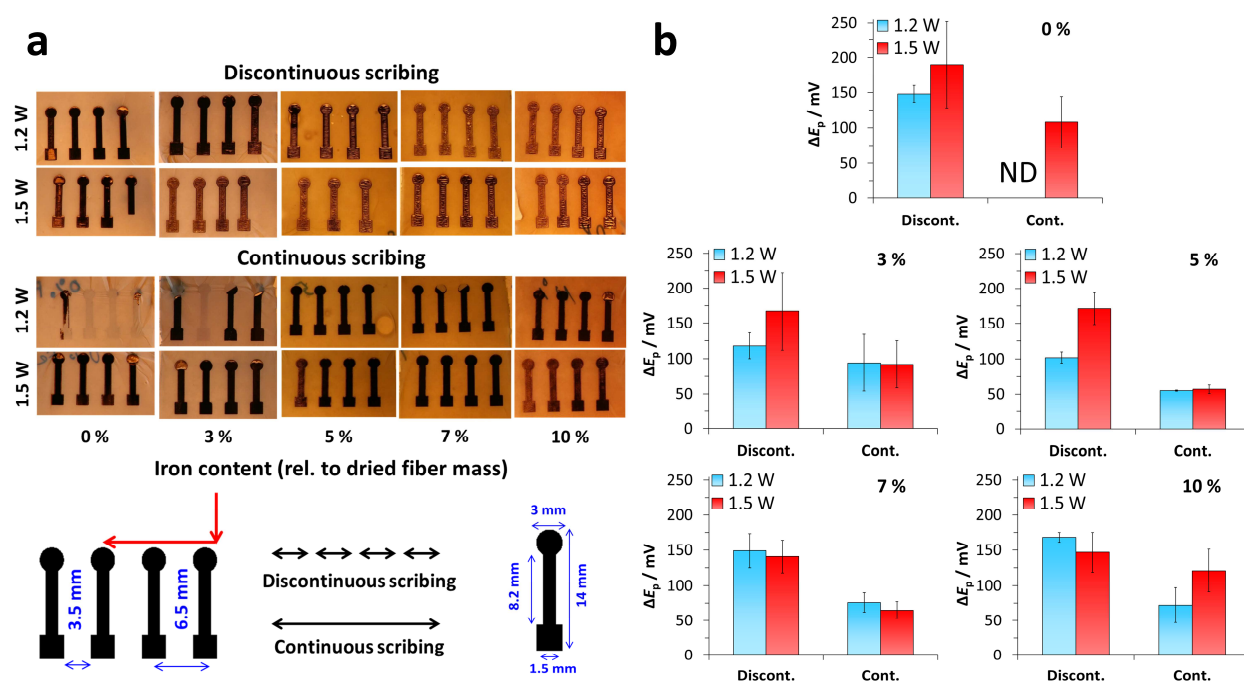


Figure 3.4: Effect of iron content and lasing technique on electrode fabrication. Dimension, design and lasing technique are shown underneath (a). The corresponding electroanalytical performance of LCNF electrodes evaluated by cyclic voltammetry using  $[\text{Fe}(\text{CN})_6]^{4-/3-}$  (b). ND = not determined.

Under optimum conditions, CNFs based on laser-induced carbonization exhibit relatively high edge-plane site density and defects, which are favorable for inner-sphere redox systems. The LCNF electrodes provide rapid electron transfer rates for  $[\text{Fe}(\text{CN})_6]^{4-/3-}$  and dopamine as indicated by  $k^0 = (0.043 \pm 0.016) \text{ cm} \cdot \text{s}^{-1}$  and  $(0.015 \pm 0.004) \text{ cm} \cdot \text{s}^{-1}$ , respectively. The values are greater than that obtained from electrospun CNF electrodes based thermal treatment (at 1,200 °C) where  $k^0$  values of 0.0025 and 0.0029  $\text{cm} \cdot \text{s}^{-1}$  were reported for  $[\text{Fe}(\text{CN})_6]^{4-/3-}$  and dopamine, respectively.<sup>178</sup> Furthermore, LCNF electrodes yield a  $k^0$  of  $(0.043 \pm 0.018) \text{ cm} \cdot \text{s}^{-1}$  for  $[\text{Ru}(\text{NH}_3)_6]^{2+/3+}$ , an outer-sphere redox system with kinetics strongly dependent on the density of electronic states. The  $k^0$  is

an order of magnitude greater than that of thermally created electrospun CNFs treated at 1,000 °C and 1,100 °C. In addition to high edge-plane site density and defects introduced by laser-induced carbonization, embedded iron should also play a significant role in promoting the rapid electron transfer kinetics. Thus, LCNFs demonstrate excellent electroanalytical performance while requiring only simple instrumentation for their fabrication.

As shown in Figure 3.5, the proposed strategy can generate porous 3D-carbon network, which cannot be obtained by lasing on a PI sheet. The high porosity enables efficient percolation when the LCNF mats are applied as electrodes to miniaturized analytical systems. The average pore size of the LCNF mat is ca.  $(4 \pm 1) \mu\text{m}$  (Figure 3.5c), which is an order of magnitude smaller than that of commercially available graphene foam.<sup>1</sup> The thickness of LCNF electrode is slightly higher than that of the pristine fiber mat (Figure 3.5b+c). The mean diameter of nanofibers is significantly larger after treatment, changing from  $(348 \pm 50) \text{ nm}$  to  $(699 \pm 206) \text{ nm}$ .

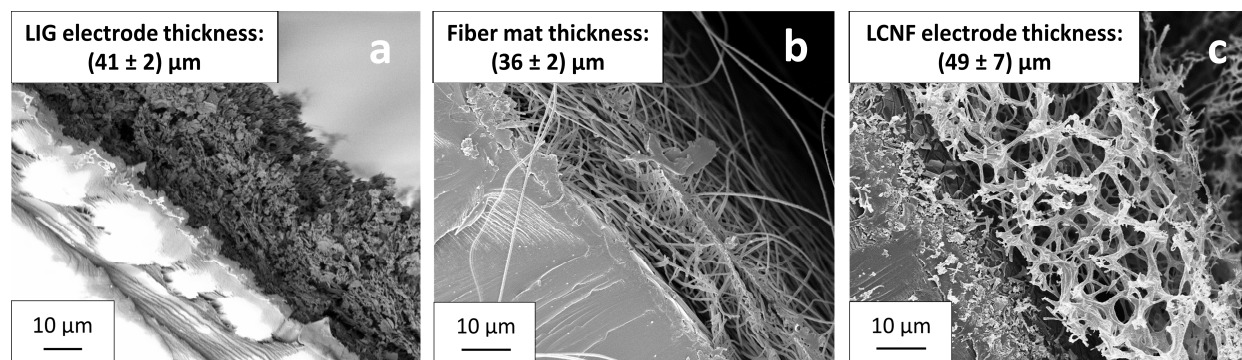


Figure 3.5: Side views of a LIG electrode (a), electrospun Matrimid® nanofibers on ITO/PET (b) and LCNF on ITO/PET (c). The nanofiber samples contain 5 % iron.

The as-spun 15 % (w/v) Matrimid® nanofibers with varied iron content from 0 % to 10 % did not show significant differences in their diameters. The possible influence of the fiber diameter on carbonization conditions to generate LCNFs could therefore not be investigated, but will be part of a subsequent study.

The LCNF electrodes possess a mechanical stability that is similar to LIG electrodes, which is sufficient for general electroanalytical experiments and integration into miniaturized systems. Also, since rinsing and blowing LCNF electrodes with water and N<sub>2</sub> stream, respectively, do not affect their morphology and property, further post-(bio)modification is easily feasible.

### 3.4.3 Effect of Laser Input on Characteristics of LCNF Electrodes

The effect of these findings on design constraints for electrode fabrication was investigated by scribing various electrode numbers (N) in a row. The electrode patterns consisted of 1, 4, 16 and

32, termed as N1, N4, N16 and N32, respectively, (Figure 3.6a) (the setup is illustrated in Figure S3.5b).

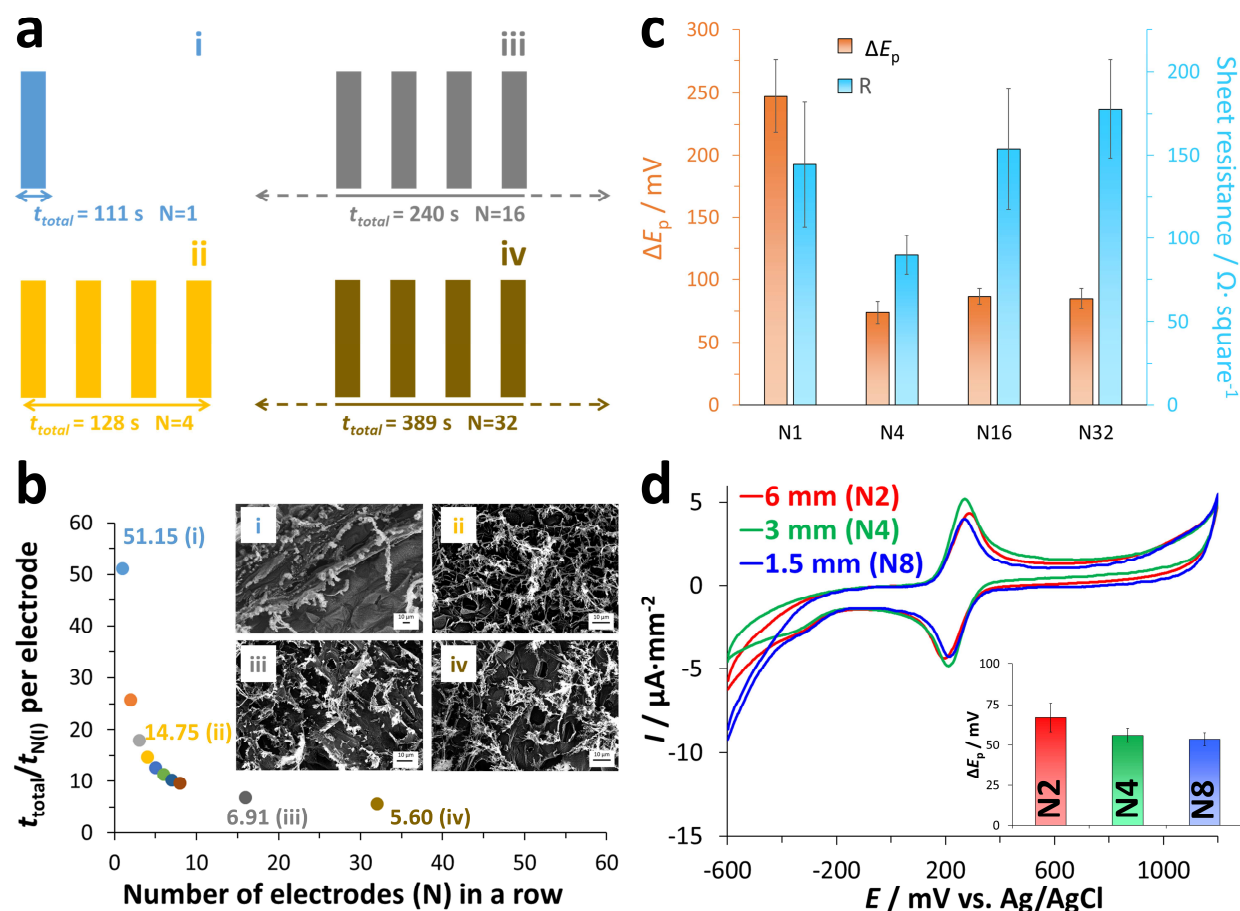


Figure 3.6: Effect of laser input on LCNF properties. Electrode designs for testing the hypothesis (a). The relationship between electrode number (N) in a row on laser input ( $t_{total}/t_{N(i)}$ ) per electrode (b). The inset SEM images display LCNF morphologies when lased the fibers with the electrode design shown in (a). The correlation of the electroanalytical and electrical properties of the LCNF with N (c). Electrochemical characterization of LCNFs lased at various N with different electrode width while maintaining ( $t_{total}/t_{N(i)}$ ) at 15 per electrode. Shown are the normalized actual cyclic voltammograms, the inset provides the calculated peak-to-peak separation (d).

The ratio of time required for completing the process for a specific electrode pattern ( $t_{total}$ ) to the travelling time of the laser spent on each electrode ( $t_{N(i)}$ ) is evaluated for various N (Figure 3.6b).  $t_{total}$  is relative to the distance of the overall design, for example, for the electrode dimension of 3 mm × 14 mm, scribed with 762 mm·s<sup>-1</sup> laser speed and 1,000 DPI,  $t_{N1}$  and  $t_{N32}$  are estimated to be 2.17 s and 69.44 s, respectively. It can be seen that a large difference in LCNF morphology occurs with a small N (below 10) while the variation is reduced with a higher N. It correlates to large differences in the  $t_{total}/t_{N(i)}$  ratio. Interestingly, the laser input governed properties of morphology (Figure 3.6b (inset, i to iv)), electrochemical and electrical characteristics (Figure 3.6c) in which at a  $t_{total}/t_{N(i)}$  ratio of 15 is optimal. We thus created N2, N4 and N8 designs

(Figure S3.6) and scribed them under these optimal conditions, resulting in electrodes with highly comparable electroanalytical characteristics, as predicted, in which the same  $\Delta E_p$  and current magnitude are obtained (Figure 3.6d). We, therefore, propose that highly reliable LCNFs can be fabricated under these given conditions allowing for their large-scale production.

### 3.4.4 Applications of LCNFs as High Performance Electrodes for Electrochemical Sensors

The optimized LCNFs were investigated for their use in bioanalysis by studying their detection capabilities of three highly relevant (bio)analytes, i.e.  $\beta$ -nicotinamide adenine dinucleotide (NADH), hydrazine and dopamine (Figure 3.7). LCNFs were compared to screen-printed carbon (SPCE) and gold (SPGE) electrodes that are ubiquitously used in medical diagnostics. The LCNF electrode facilitates electrooxidation of NADH at a very low overpotential of only 170 mV in comparison to the SPCE and SPGE (550 mV and 800 mV, respectively), suggesting that the LCNFs possess an inherent catalytic effect towards NADH (Figure 3.7a). It is also remarkably lower than that of using electrospun palladium nanoparticles-loaded CNFs modified carbon paste electrode, with an oxidation potential at 500 mV.<sup>135</sup> We propose that this observed electrocatalytic effect can be in fact attributed to two features; (i) multiple edge sites in LCNFs where oxygen-containing groups are present,<sup>179–181</sup> and (ii) iron oxide formed in the LCNF,<sup>119</sup> which functions as nanocatalyst.<sup>182,183</sup>

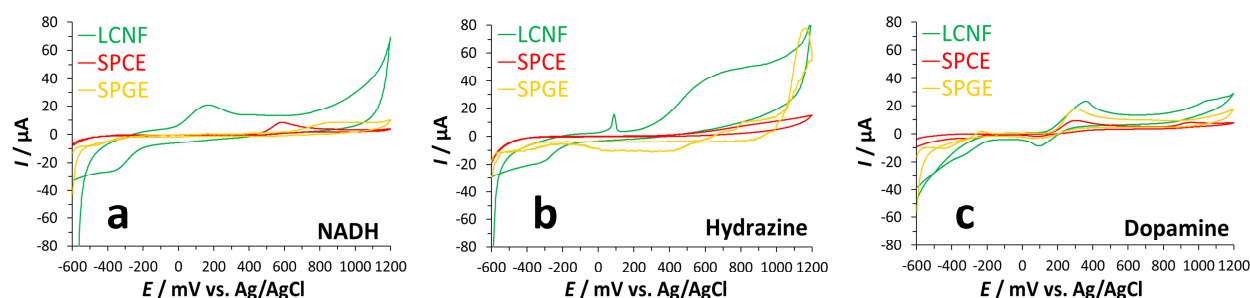


Figure 3.7: Electroanalytical performance of LCNF electrodes towards some model biomarkers compared with SPCE and SPGE electrodes for NADH (a), hydrazine (b) and dopamine (c). The analytes were prepared with 1 mM concentration in 0.1 M phosphate buffer (pH 7.0).

In the case of hydrazine (Figure 3.7b) the LCNF electrode exhibits an outstanding electrochemical behavior when compared to SPCE and SPGE. A well-defined oxidation peak of hydrazine can be observed only at LCNF electrode. The electrocatalytic oxidation is likely due to the embedded iron oxide in LCNF as previously demonstrated for iron oxide-carbon composite electrodes where the oxidation of hydrazine also occurred at 700 mV.<sup>184</sup> Supporting this hypothesis is the study by Jones *et al.*<sup>185</sup> They showed that multiwalled carbon nanotubes without metallic impurities do not exhibit

an electrochemical signal for hydrazine due to their sluggish heterogeneous charge-transfer kinetics.

Lastly, the LCNF electrode, SPCE and SPGE show similar oxidation and reduction potentials for dopamine detection (Figure 3.7c). However, the LCNF electrode yields a greater current intensity in comparison to the response of SPCE, which is likely due to a larger active electrode surface area (ESA). The ESA estimated from Randles-Sevcik equation (Table S3.2) shows that the ESA of the LCNF is about double that for the SPCE, which correlates to the about 2 times larger peak area obtained from dopamine analysis at LCNF.

In electroanalysis, electrode surfaces are frequently pretreated electrochemically, chemically or via plasma in order to improve their reactivity or render them more hydrophilic. We investigated UV/ozone treatment and found that exposure by 1 min rendered LCNFs to be electrochemically stable (Figure S3.7a), with better electron transfer capabilities (Table S3.2), are significantly more hydrophilic (Figure S3.7b-i+ii) and showed much better detection ability towards dopamine (~2 times higher peak current and a lower peak potential (Figure S3.7c and Table S3.2). The latter may be attributed to the introduction of oxygen-containing groups upon UV/ozone treatment,<sup>186,187</sup> promoting the adsorption of dopamine on LCNFs.<sup>188</sup> Other activation strategies, e.g. electrochemical pretreatment,<sup>188</sup> and plasma treatment,<sup>189</sup> will be studied in the future for other types of analytes.



### 3.5 Conclusion

In summary, we demonstrate feasibility of combining facile electrospinning and one-step laser irradiation to enable the *in situ* fabrication of carbon nanofibrous electrodes in ambient environments. The fabrication process lends itself towards scale-up, facile electrode patterning and is a low-cost procedure. Furthermore, it can be applied to low heat resistant substrates as thermal treatment using high temperature is not required. Controlling LCNF morphology and electrochemical activities can be obtained through manipulating electrospinning conditions, nanofiber composition, laser settings and electrode designs. The important effect of mat morphology on electrochemical behavior has been elucidated in this study. The study is very useful for developing carbon nanofibers-metal catalyst hybrids for use in non-enzymatic electrochemical sensors and energy storage. Taking it a step further, LCNFs can be modified in a simple process by adding molecules/particles either into the spinning solution or modifying the polymer chain. This will hence introduce new favorable functionalities into laser-carbonized nanofibers, advancing their applications into complex (bio)analytical, medical and energy storage fields. Furthermore, LCNFs prepared here represent a breathable substrate (in contrast to most electrodes being generated on solid support materials), which makes them desirable for all applications in which air flow is important such as air filtration, wound healing and face masks.



### 3.6 Supporting Information

#### Choice of Substrate

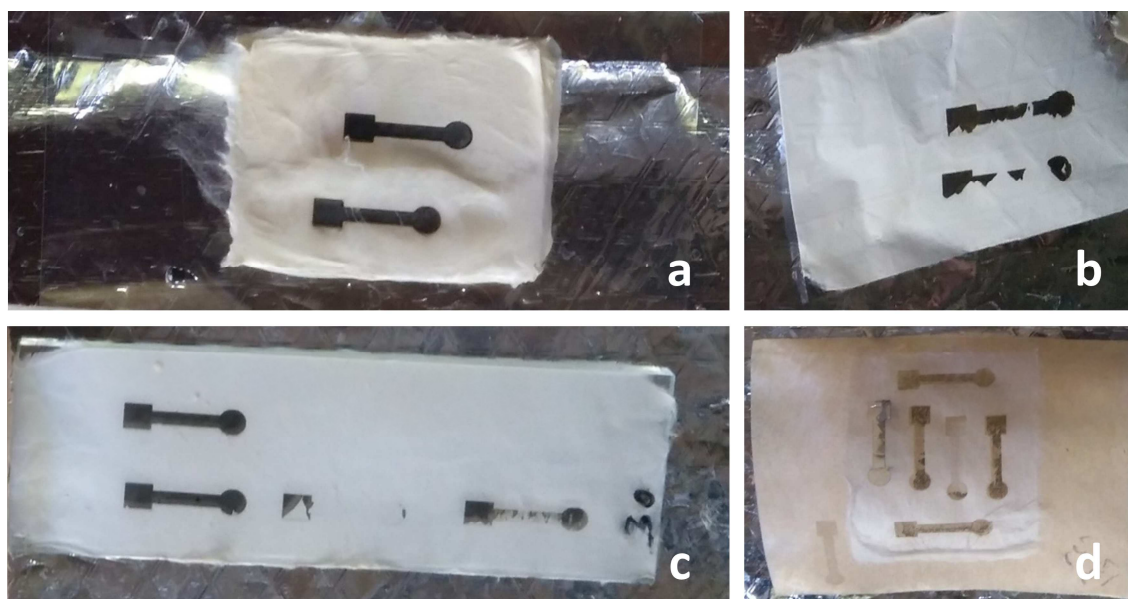


Figure S3.1: Preliminary investigation on finding out the proper substrate for collecting nanofibers. The photographs show the LCNF electrodes derived from Matrimid® nanofiber mat electrospun on ITO/PET sheet (a), aluminum foil (b), glass slide (c) and wax paper (d).

In comparison to the other substrates (Figure S3.1) such as glass slide, wax paper and aluminum foil, ITO yields the best electrode feature for unoptimized lasing conditions.

## Effect of Fiber Mat Density

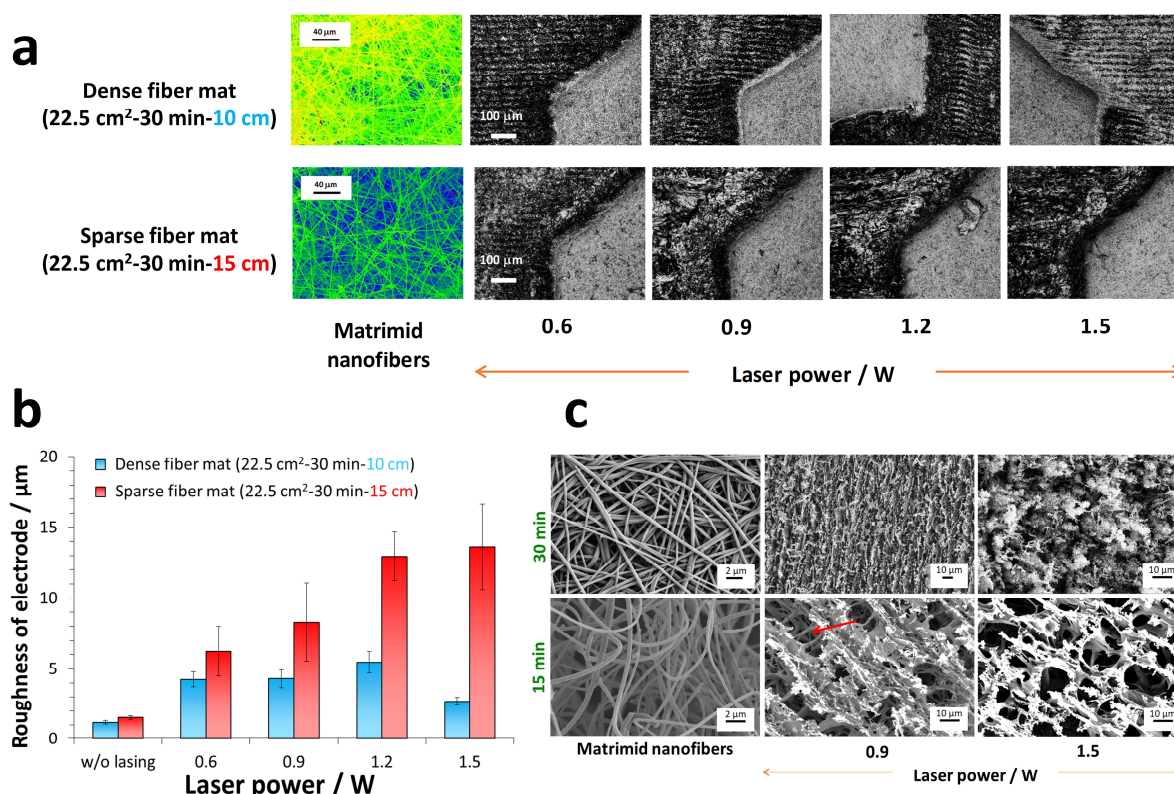


Figure S3.2: Effect of fiber mat density spun at various settings (area-time-TCD) on macroscopic morphologies of LCNF electrode at various laser powers (a). Quantification of the roughness of LCNFs (b). Effect of the electrospinning time on the microscopic fiber morphology (TCD = 10 cm). The red arrow indicates the obtained fiber structures after laser-induced carbonization (c).

The morphology of the electrospun nanofiber mat with respect to its density can be controlled by the tip-to-collector distance (TCD) and collecting time. While sparse fiber mats feature larger pore sizes when compared to dense fiber mats, we found that too thin and sparse fiber mats derived from collecting fibers on a large collecting area (22.5 cm<sup>2</sup>) and long TCD (15 cm) result in distorted and flaky electrodes as depicted in Figure S3.2a (lower panel). The electrode roughness increases with increasing laser power as determined by 3D-confocal laser microscopy (Figure S3.2b). In contrast, the roughness of the electrode derived from dense fiber mats (using 10 cm TCD, 30 min, 22.5 cm<sup>2</sup>) does not change significantly with varying laser power conditions and in fact is comparable to the density of non-scribed fibers. When fiber mats are spun too dense (30 min collecting time) SEM images reveal either a sheet-like structure or an irregular structure upon treatment with laser powers of 0.9 W and 1.5 W, respectively (Figure S3.2c-upper panel). Reducing the density (15 min collecting time) fibrous structures are retained (Figure S3.2c-lower panel). Hence, final electrode morphologies are easily tunable simply by controlling the electrospinning process, i.e. TCD, applied voltage, collecting area, feeding rate, etc.

## ESA for Different Lasing Powers

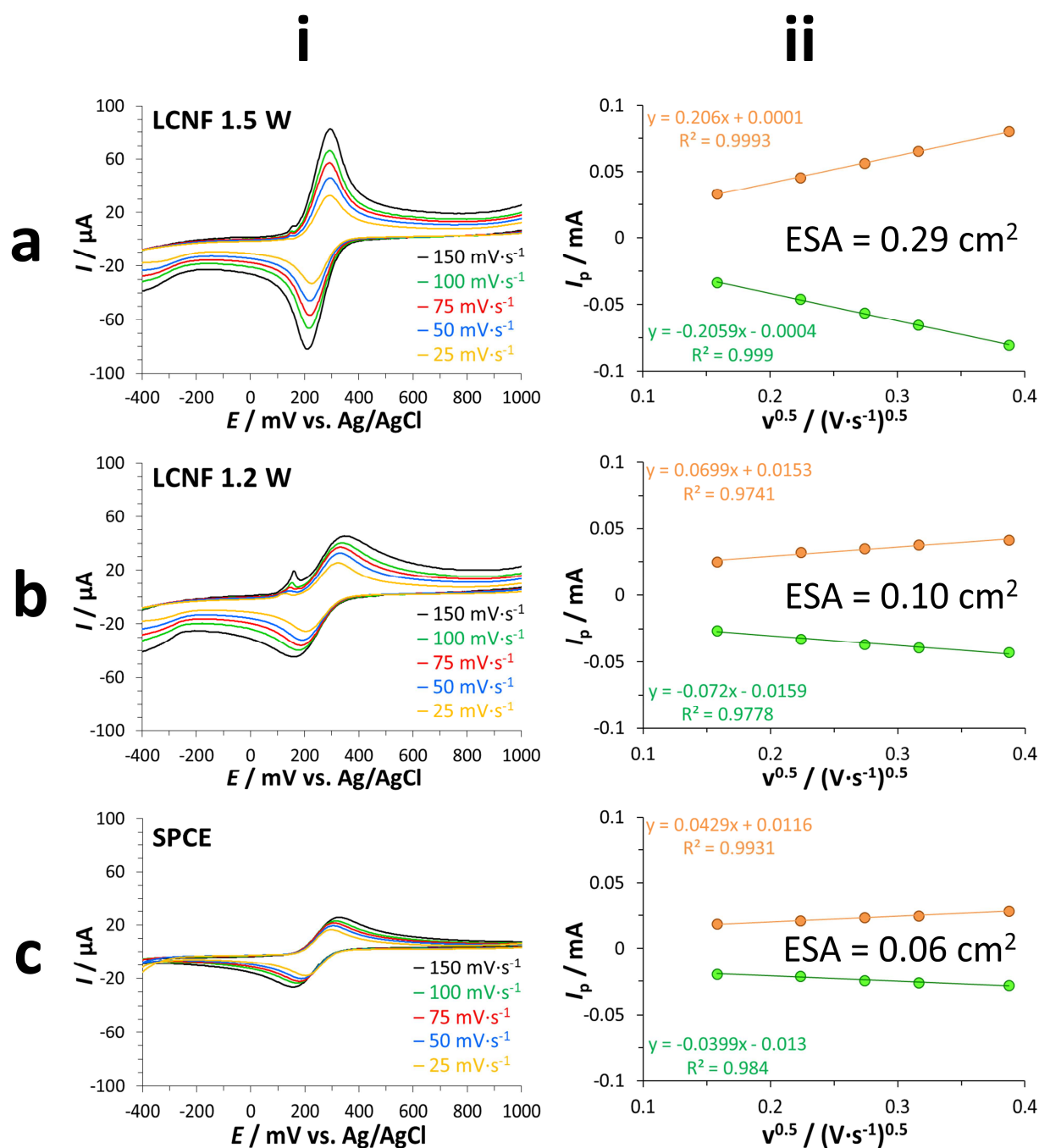


Figure S3.3: Panel (i): cyclic voltammograms at various scan rates for LCNF electrodes lased at 1.5 W (a), 1.2 W (b) and screen-printed carbon electrode (SPCE) (c) ran in 1 mM ferri/ferrocyanide (in 0.1 M phosphate buffer, pH 7.0, 0.1 M KCl). Panel (ii): Randles-Sevcik plots for the corresponding voltammograms in panel (i). The diameter of the electrodes was 3  $\text{mm}^2$ . The nanofibers contained 3 % iron.

## FTIR Spectra for LCNF

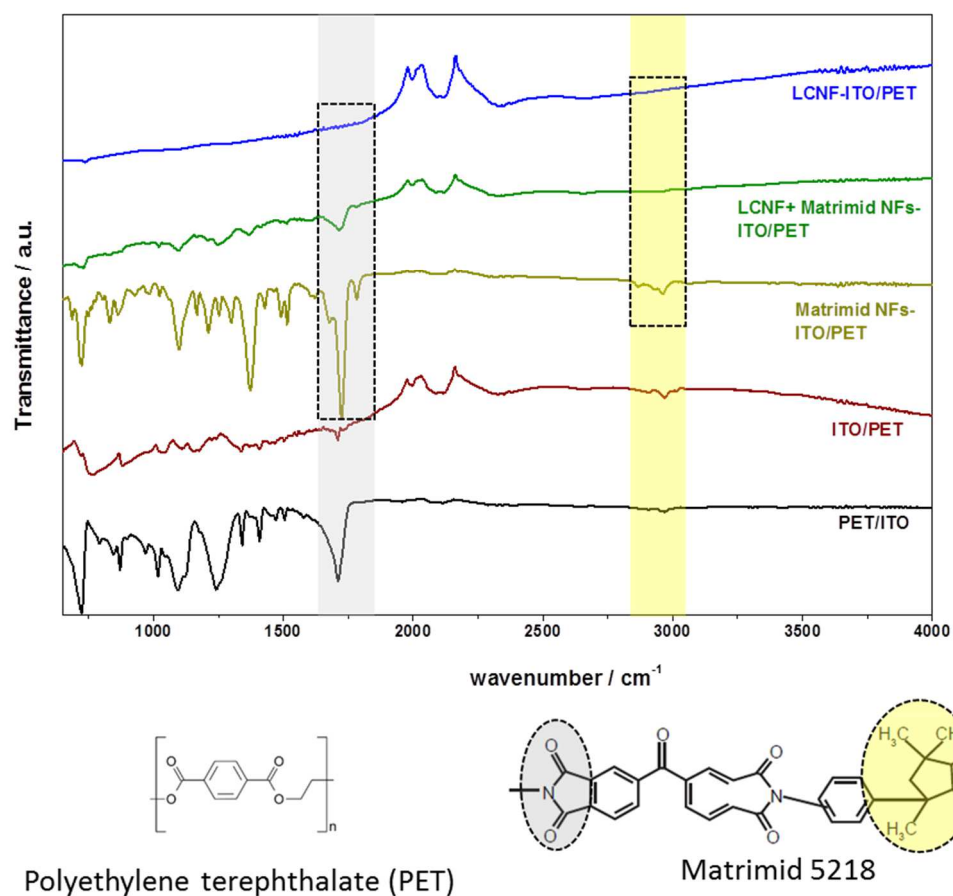


Figure S3.4: FTIR-ATR spectra of LCNF electrodes. LCNF + Matrimid<sup>®</sup> NFs-ITO/PET was prepared from applying the laser out of focus (-2 mm) 30 times.

## Elemental Analysis of Matrimid<sup>®</sup> Nanofibers vs. LCNFs

Table S3.1: Chemical compositions of Matrimid<sup>®</sup> nanofibers and LCNFs containing 5 % iron determined by elemental analysis (unless stated otherwise).

Sample	%				
	C	H	N	O	Fe
Matrimid <sup>®</sup> nanofibers	73.6 ± 0.4	4.6 ± 0.1	4.9 ± 0.1	16.1 ± 0.5	0.75*
LCNFs	89.3 ± 0.7	0.9 ± 0.1	0.7 ± 0.1	8.8. ± 0.6	0.65 ± 0.15**
% Change from initial content	↑ 21	↓ 80	↓ 85	↓ 45	-

\* calculated theoretical value; \*\* evaluated from three different LCNF electrodes by X-ray photoelectron spectroscopy (XPS)

## Variation of Lasing Power and Number of Electrodes per Row

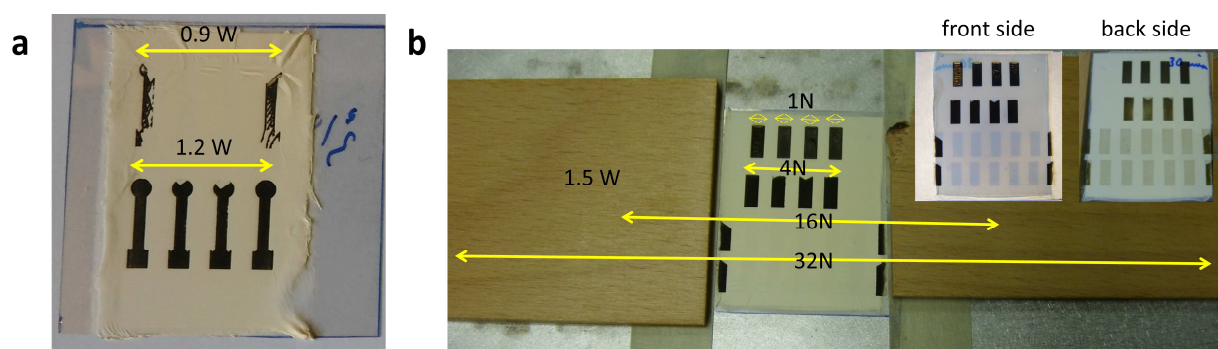


Figure S3.5: Effect of laser power on LCNF fabrication (15 min-fiber mat) (a). Setup for lasing a nanofiber mat with high number of electrodes in a row (30 min-fiber mat). The photographs (inset) show the LCNF electrodes after scribing on the front and back side (b). Matrimid® nanofibers in (a) and (b) contain 3 % and 5 % iron, respectively.

## LCNF Electrodes of Different Width

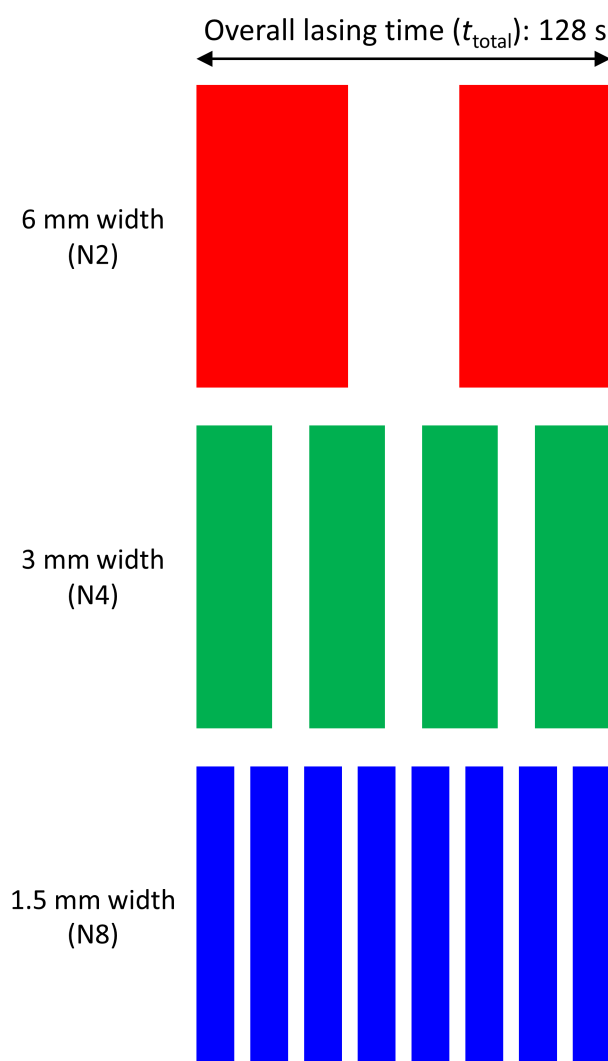


Figure S3.6: The  $t_{total}/t_{N(i)}$  of 15 per electrode was applied to the designs that consist of various electrode numbers and widths while maintaining  $t_{total}$ .  $t_{N(i)}$  for N2, N4 and N8 is ca. 1.08 s, 2.17 s and 4.34 s, respectively.



## Comparison Electrochemical Performance of LCNF vs. SPCE

Table S3.2: Evaluation of cyclic voltammograms for 1 mM dopamine using various carbon-based electrodes (LCNF contained 5 % iron).

Compared parameter	SPCE	LCNF	LCNF-UV/ozone
ESA / cm <sup>2</sup> (estimated from 1 mM ferrocyanide)	0.06	0.12	not determined
$E_{pa}$ / mV	298	356	210
$E_{pc}$ / mV	92	98	160
$\Delta E_p$ / mV	206	258	50
$I_{pa}$ / $\mu$ A	10.78	17.40	45.76
$I_{pc}$ / $\mu$ A	-3.612	-9.248	-17.43
$Ah_{anodic}$ / A·V	0.8540	1.625	1.917
$Ah_{cathodic}$ / A·V	0.4740	0.7812	0.7012

## Wettability and Cyclic Voltammetry of UV/Ozone Treated LCNFs

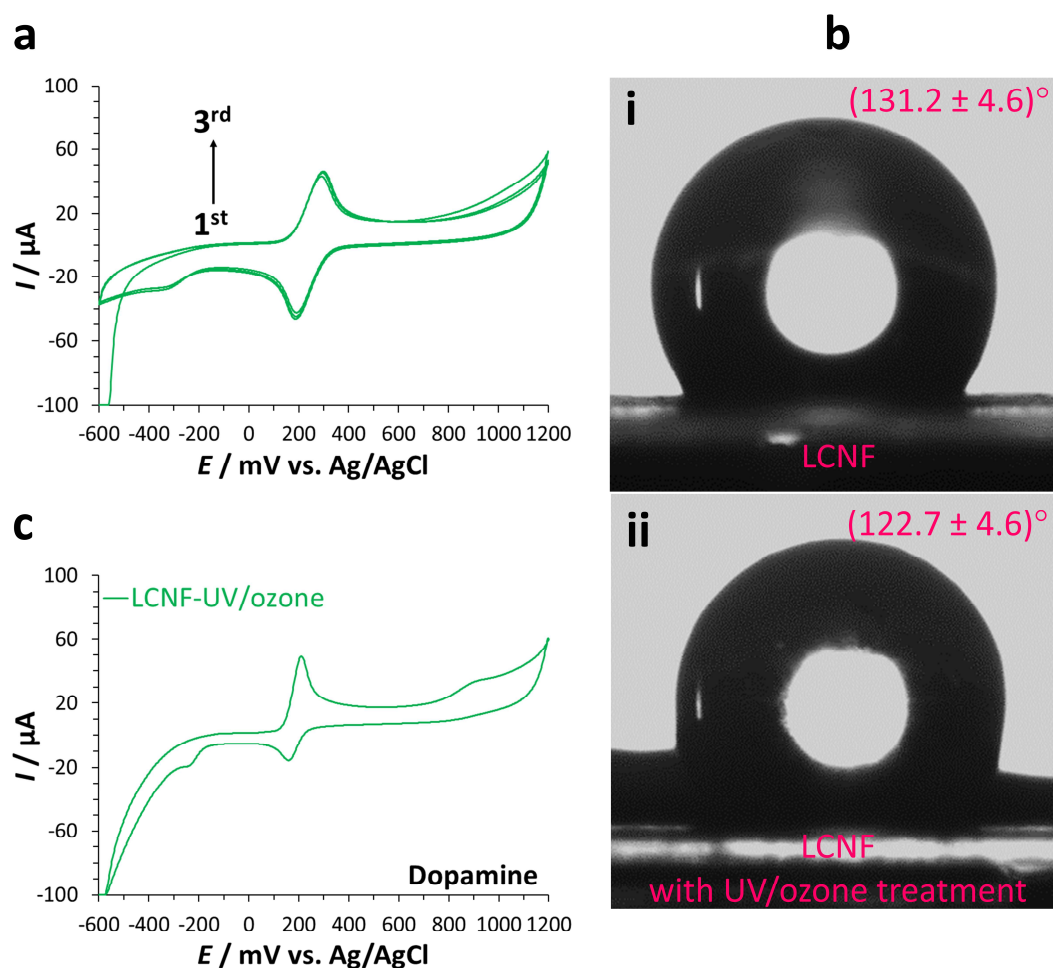


Figure S3.7: Three cycles of cyclic voltammograms of 1 mM ferri/ferrocyanide from LCNF electrode treated with 1 min UV/ozone. The LCNF electrode was prepared from 5 % iron nanofibers and lased at 1.5 W laser power with a speed of 762 mm·s<sup>-1</sup> (a). Contact angles of (i) LCNF electrode and (ii) UV/ozone-treated LCNF electrode (b). Cyclic voltammogram of 1 mM dopamine using UV/ozone-treated LCNF electrode (c).



## 4 Printable 3D Carbon Nanofiber Networks with Embedded Metal Nanocatalysts

### 4.1 Abstract

Carbon nanofiber (CNF) nanocatalyst hybrids hold great promise in fields such as energy storage, synthetic chemistry and sensors. Current strategies to generate such hybrids are laborious and utterly incompatible with miniaturization and large-scale production. Instead, this work demonstrates that Ni nanoparticles embedded in three-dimensional (3D) CNFs of any shape and design can be easily prepared using electrospinning, followed by laser carbonization under ambient conditions. Specifically, a solution of nickel acetylacetonate/polyimide is electrospun and subsequently a design is printed via CO<sub>2</sub>-laser (Ni-laser-induced carbon nanofibers (LCNFs)). This creates uniformly distributed small Ni nanoparticles (~8 nm) very tightly adhered to the CNF network. Morphological and performance characteristics can be directly influenced by metal content and lasing power and hence adapted for the desired application. Here, Ni-LCNFs are optimized for non-enzymatic electrochemical sensing of glucose with great sensitivity of 2,092  $\mu\text{A}\cdot\text{mM}^{-1}\cdot\text{cm}^{-2}$  and a detection limit down to 0.3  $\mu\text{M}$ . Its selectivity for glucose vs. interfering species (ascorbic and uric acid) is essentially governed by the Ni content. Most importantly, this strategy can be adapted to a whole range of metal precursors and hence provide opportunities for such 3D CNF-nanocatalyst hybrids in point-of-care applications where high-performance but also sustainable and low-cost fabrications are of utmost importance.

---

*This chapter has been published and formatted to fit this thesis:*

Simsek, M.; Hoecherl, K.; Schlosser, M.; Baeumner, A. J.; Wongkaew, N. Printable 3D Carbon Nanofiber Networks with Embedded Metal Nanocatalysts. *ACS Appl. Mater. Interfaces* **2020**, *12* (35), 39533–39540.

### *Author contributions*

The author and Dr. Nongnoot Wongkaew conceived the studies and wrote the manuscript. Prof. Dr. Antje J. Baeumner led the project administration and promoted manuscript preparation. The author performed the experiments. Dr. Marc Schlosser carried out EDX measurements. Kilian Hoecherl supported experiment implementation and validation.



## 4.2 Introduction

Carbon nanofiber (CNF)-metal nanocatalyst hybrids hold great promise in developing electrochemical devices for energy storage and conversion, e.g. batteries and supercapacitors, water splitting<sup>190</sup> and sensors.<sup>191</sup> Utilizing CNFs as support generally offers favorable features in promoting efficient electrocatalytic reactions.<sup>192</sup> In particular, three-dimensional (3D) architecture of CNF networks affords high surface area and porosity that significantly boost the internal mass transfer, thus facilitating efficient interactions between catalytic sites and electrolytes. Their good electrical conductivity, low material cost, chemical inertness and high stability under harsh conditions are additional advantages that make CNFs widely used as a support of metal nanocatalyst.

To generate metal-nanocatalyst-loaded CNFs, various strategies have been proposed, e.g. electrodeposition,<sup>193</sup> chemical anchoring by functional groups,<sup>194</sup> chemical vapor deposition<sup>195</sup> or microwave-assisted synthesis.<sup>196</sup> Chemical or electrochemical reduction of metal precursors on CNFs are among the most popular methods. Even though great electrocatalytic performance of the resulting hybrids is achievable, those techniques are considerably tedious and have poor reproducibility, thus hampering their applicability in large-scale manufacturing. The oxidation of CNFs prior to metal reduction is often needed to ensure sufficient hydrophilicity for efficient anchoring catalyst particles.<sup>192</sup> Such treatment may, however, introduce an adverse effect in terms of electrical conductivity. Besides, the reduction of metal precursors onto porous CNFs may suffer from the poor adhesion strength owing to high roughness and heterogeneity of the oxygenate groups at CNF's edge sites. Thus, the reduced metal nanocatalyst obtained via these approaches may not be a suitable candidate for long-term uses or under mechanical forces such as stirred/flow conditions.

Electrospinning has currently gained tremendous attention in producing CNFs, as it is highly compatible with industrial-scale production and cost-effective.<sup>133</sup> To produce CNFs, a solution of polymer precursor, e.g. polyacrylonitrile (PAN), is electrospun and subjected to a two-step heat treatment, i.e. stabilization and carbonization. The technique enables facile and efficient incorporation of metal precursor/s through just blending them with a solution of polymer where the applied electric field could potentially promote uniform distribution of the metal salts along the as-spun fibers. Upon two-step thermal treatment, the formation of CNFs and metal nanoparticles can be readily obtained. As shown in several studies,<sup>135,180,197–201</sup> highly uniform distribution and firm embedding of metal nanocatalysts within CNFs can be realized via this strategy, which undoubtedly leads to remarkable electrocatalytic performance as well as great

durability of the as-prepared hybrids that are successfully employed in various applications.

Growing demand for portable electrochemical devices in energy storage and conversion,<sup>202,203</sup> point-of-care diagnostics<sup>204</sup> and wearable sensors<sup>205</sup> has nowadays driven research efforts towards miniaturization and integration of functional nanomaterials. To meet this end, transfer-free, fully printed, customized electrode designs and roll-to-roll production feasibility are highly preferred. Metal-nanocatalyst-loaded CNFs prepared via conventional heat treatment still cannot fulfill these preferences, as they inevitably require laborious transfer and complicated integration approaches after their production.<sup>136,200,201</sup> Difficulty in maintaining 3D structures of the CNF networks remains an additional issue after device integration.

In contrast, laser-induced carbonization has become a promising technology to tackle those challenges. Various kinds and forms of substrates,<sup>205</sup> including electrospun nanofibers recently developed by our group,<sup>140</sup> have been laser-scribed into electrodes and their performances investigated both in energy-related fields and sensors. A study shown by Tour's group has revealed the possibility of CO<sub>2</sub>-laser in converting polyimide (PI) film containing metal precursor into metal oxide nanocrystals embedded in graphene.<sup>119</sup> The hybrids exhibited excellent electrocatalytic activity and high cycling stability in converting O<sub>2</sub> to OH<sup>-</sup>.

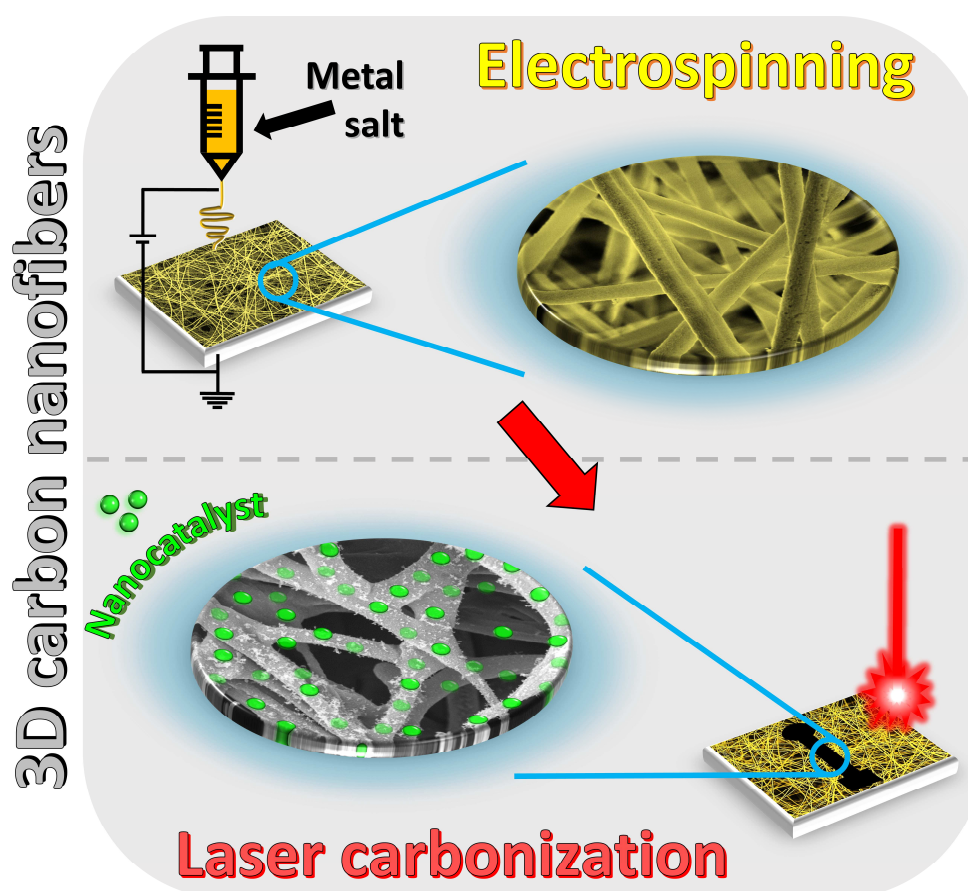


Figure 4.1: A simple approach of generating patternable 3D hybrids of laser-induced carbon nanofibers with embedded metal nanocatalyst.

This work presents 3D CNF networks embedded with metal nanocatalysts realized by one-step laser carbonization of electrospun PI nanofibers containing metal precursors (Figure 4.1). Here, solvent-soluble PI and a metal complex, nickel acetylacetonate ( $\text{Ni}(\text{acac})_2$ ) as an example, were blended and electrospun on an indium tin oxide (ITO) coated plastic sheet. The as-spun nanofibers were subsequently exposed to a  $\text{CO}_2$ -laser following the desired pattern of electrode design, termed as Ni-laser-induced carbon nanofibers (LCNFs). Ni content and lasing power were investigated to maximize the degree of metal loading while maintaining electrospinnability as well as intact fibrous morphology. The strategy not only enabled remarkable adhesion stability between Ni nanocatalysts and LCNFs but also provided the Ni-LCNF electrodes with excellent electrocatalytic activity towards non-enzymatic glucose sensing with minimum interfering effect from uric acid (UA) and ascorbic acid (AA).

## 4.3 Materials and Methods

### 4.3.1 Preparation of LCNF

Nanofiber mats were prepared by electrospinning of a solution containing 15 % (w/v) Matrimid® 5218 (Huntsman Advanced Materials BVBA, Belgium) and nickel(II) acetylacetonate (95 %, Sigma-Aldrich, Germany) or iron(III) acetylacetonate ( $\geq 99.9$  % trace metals basis, Sigma-Aldrich, Germany) dissolved in N,N-dimethylacetamide (Merck, Germany). The metal salt percentages reported here are relative to the dry mass of the polymer. It is abbreviated Ni(acac)<sub>2</sub> or Ni (or Fe) in the other sections. Spinning solutions were ultrasonicated for 30 min and stirred at least overnight before spinning. The electrospinning was conducted for 15 min per fiber mat at a  $10 \mu\text{l}\cdot\text{min}^{-1}$  flow rate with a 15 cm tip-to-collector distance. The applied voltage was adjusted in the range of 12-14 kV depending on the ambient temperature and humidity conditions. Indium tin oxide coated poly(ethylene terephthalate) (ITO/PET, sheet resistivity  $60 \Omega\cdot\text{sq}^{-1}$ , 1 ft  $\times$  1 ft  $\times$  5 mil, Sigma-Aldrich, Germany) that has been cut into 5 cm  $\times$  5 cm was used for nanofiber deposition. The as-cut ITO/PET piece was placed in the middle of a metal collector dish. An electrical connection between the ITO surface and the underneath metal collector was performed by taping two aluminum foil stripes at the rims of the ITO substrate at the opposite sides. This resulted in a final 4 cm  $\times$  5 cm collecting area. After electrospinning, conductive electrodes with the desired patterns of carbon nanofibers were generated by a CO<sub>2</sub>-laser (10.6  $\mu\text{m}$ , VLS 2.30, Universal Laser Systems, Polytech Systeme GmbH, Germany). The lasing speed was optimized in earlier studies to 60 % (of  $1,270 \text{ mm}\cdot\text{s}^{-1}$ ) and the image density was 1,000 DPI. The applied laser power (maximum power of 30 W) was set to 1.5 W if not mentioned otherwise.

### 4.3.2 Morphology Characterization

The morphology of nanofibers before and after carbonization was studied by scanning electron microscopy (Zeiss/LEO 1530, Germany) at 5.0 kV. The samples have been cut with a scissor and gold-sputtered for 30 s ( $\sim 7$  nm layer thickness) after placing them on specimen stubs. Scanning electron microscopy-energy-dispersive X-ray (SEM-EDX) (Zeiss EVO MA 15 with Bruker XFlash Detector 630M) at 15 kV was applied to demonstrate the elemental composition and distribution along samples. For transmission electron microscopy (TEM), the LCNF structure of one electrode was scratched off and dispersed in 100  $\mu\text{l}$  of water by ultrasonication for 30 s. Two microliters were dropped on a TEM grid (carbon film on 400 squares copper grid mesh) placed on a heating plate at 80 °C to enable fast evaporation. Microscopic imaging was performed with a JEOL 2100F with a 4k  $\times$  4k camera (UltraScan 4000; Gatan Inc.) at 200 kV.

### 4.3.3 Electrochemical Characterization

A CV-50W voltammetric analyzer (Bioanalytical Systems, USA) with a three-electrode system consisting of LCNF as the working electrode, Pt wire as the counter electrode and a Ag/AgCl reference electrode was utilized for all electrochemical measurements. The working area of the LCNF immersed into a measuring solution was defined as 2.8 mm × 3 mm and separated from the contacting part using candle wax. Cyclic voltammetry was performed from -0.6 to 1.2 V ( $50 \text{ mV} \cdot \text{s}^{-1}$ , unless stated otherwise) and amperometry was run at 0.55 V fixed potential. Glucose detection took place in 0.5 M NaOH under gentle stirring (ca. 100 rpm).

### 4.3.4 Mechanical Stability Test

Electrodeposition on laser-induced graphene (LIG) and Fe-LCNFs was performed at -1.0 V for 60 s in an aqueous solution of 0.1 M  $\text{NaNO}_3$  and 0.04 M  $\text{Ni}(\text{NO}_3)_2$ . One half of the samples was put into a Petri dish, filled with already tempered 0.1 M phosphate buffer (PB, pH 7) and incubated at 37 °C for 5 h while shaking (50 rpm) to simulate the application in biological media (VWR Incubating Orbital Shaker, Professional 3500). The other half was kept without incubation as a reference for Ni content.

## 4.4 Results and Discussion

### 4.4.1 Effect of Nickel Content on LCNF Morphology

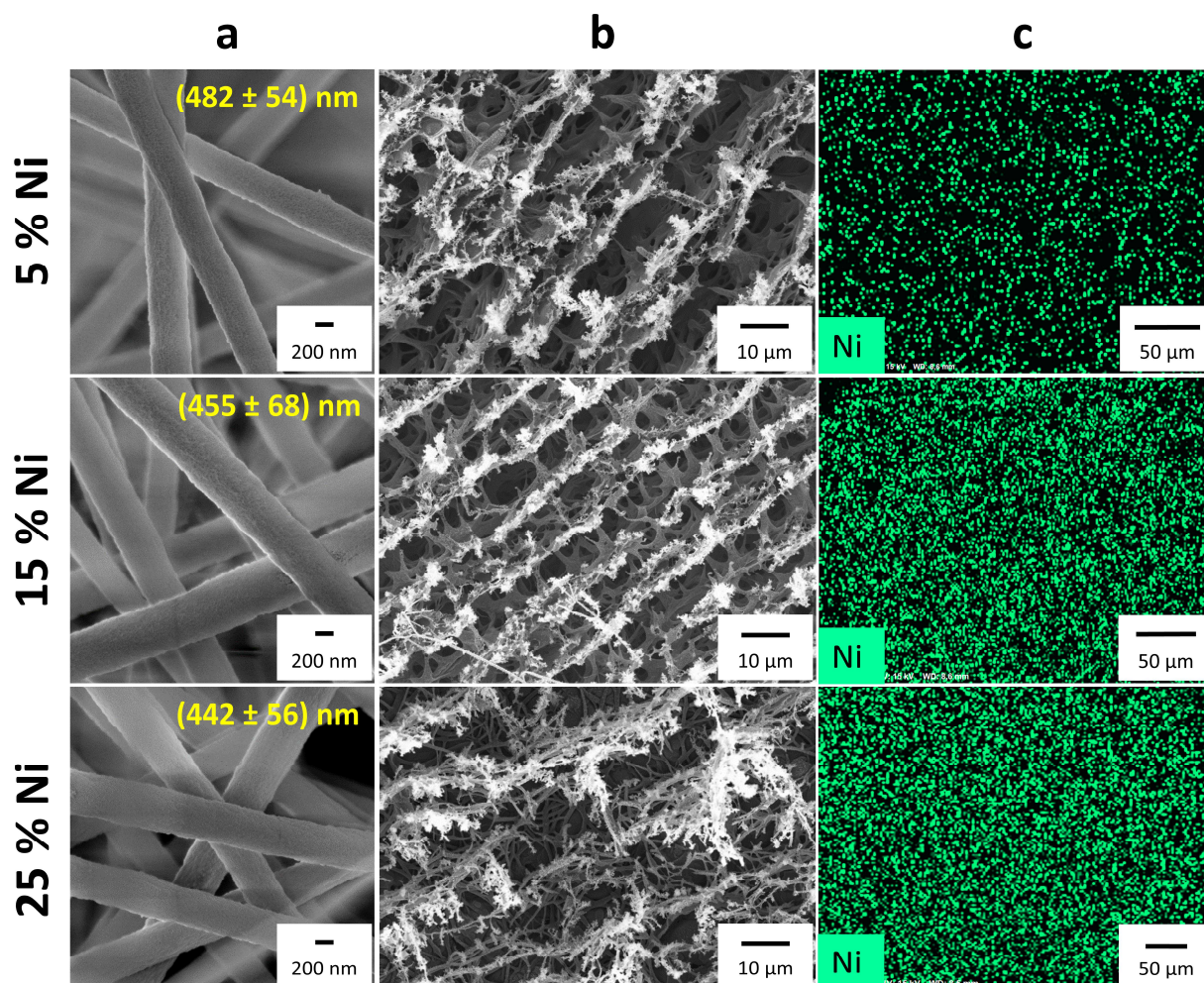


Figure 4.2: SEM images of the electrospun PI nanofibers (a) and LCNF after carbonization for different Ni salt contents (b). EDX elemental mapping showing the distribution of nickel molecules for LCNF (c). EDX was recorded with different samples compared to (b).

Introducing metal salt into spinning solutions leads to changes in the ionic conductivity, typically influencing electrospinnability and fiber morphology.<sup>206</sup> Moreover, nanofibers containing metal salt greatly affect optimal lasing conditions.<sup>140</sup> Therefore, the influence of Ni content in the spinning solution on the morphology of nanofibers (Figure 4.2a) and laser-carbonized nanofibers (Figure 4.2b) was investigated by SEM. Increasing nickel salt from 5 to 25 % did not show any profound effects on nanofiber mats and fiber diameter (Figure 4.2a). However, the LCNF electrodes after scribing with the same laser settings (1.5 W, 60 % lasing speed) provided differences in morphology (Figure 4.2b). The LCNFs with 25 % Ni showed rather intact homogeneous fibrous structures for most of the lasing area, while the majority of 5 and 15 %



Ni-LCNFs yielded flat/ribbon-like LCNFs with broader diameters compared with that of 25 % Ni, as can also be seen in Figure S4.1. Here, the diameters of 25 % LCNFs were evaluated and compared with those of 15 % LCNFs. The expansion of the LCNF diameters compared to those of the pristine electrospun nanofibers was approximately 20 and 160 % for 25 % Ni-LCNFs and 15 % Ni-LCNFs, respectively. This might be explained by the fact that increasing the metal content promotes greater heat distribution along the nanofibers during the lasing process, thus resulting in the preserved structure similar to the non-scribed nanofibers. We also observed the same heat-transfer behavior for LCNFs with varying Fe content in our previous work,<sup>140</sup> in which an increase in the Fe content from 3 up to 7 % led to greater fibrous structures and distortion at 10 % Fe. The LCNFs containing 5 % Fe shared similarity in their morphology as obtained from 15 % Ni-LCNF (Figure S4.2). This suggested that metal salts possess different heat-transfer capabilities that need to be taken into consideration in the lasing process.

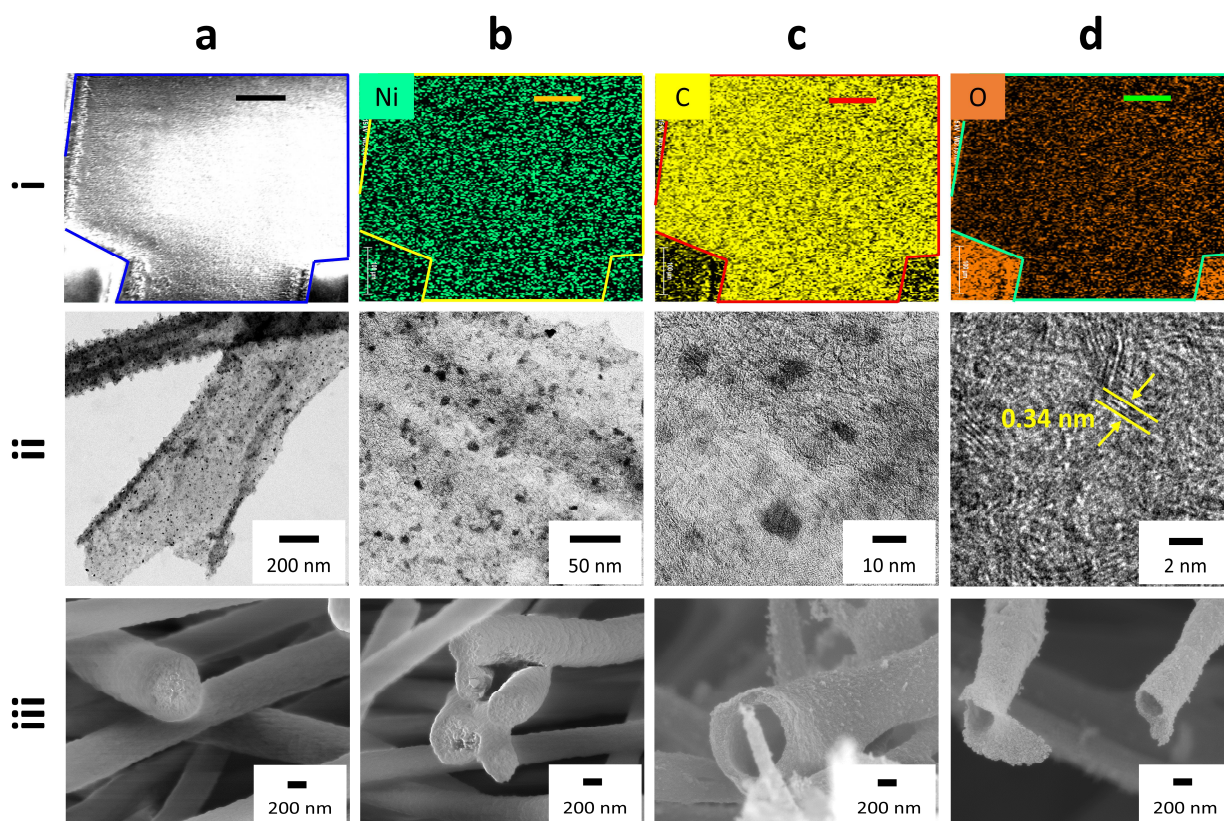


Figure 4.3: (i) SEM image of LCNF showing the selected field for EDX analysis (a). The lines enclose the carbonized part. Elemental mapping of nickel (b), carbon (c) and oxygen (d) demonstrating changes in non-scribed and scribed regions. Scale bars are 100  $\mu\text{m}$ . (ii) TEM images of Ni-LCNF at different magnifications. The lattice fringe spacing value of 0.34 nm was determined by TEM software. (iii) SEM images of electrospun solid Matrimid® nanofibers (a, b) and hollow LCNFs (c, d). All nanofibers displayed in this figure contained 25 % Ni.

The uniform distribution of nanocatalysts on the electrodes is favorable to enhance electrocatalytic

performance. Here, the energy-dispersive X-ray (EDX) mappings have proven that the nickel molecules are distributed evenly over the whole LCNF electrodes at all tested Ni concentrations (Figure 4.2c). It is likely that during the electrospinning process, Ni salt could be greatly distributed along the electrospun nanofibers, even at 25 % Ni content. Attempts to increase the Ni content higher than 25 % resulted in poor electrospinnability and beaded fibers that subsequently hindered the uniform carbonization of those nanofiber mats (Figure S4.3).

To demonstrate the changes in elemental components of scribed and non-scribed nanofibers, EDX characterization was performed. As illustrated in Figure 4.3i-b, high density of Ni was observed for both scribed and non-scribed areas. This could be anticipated because Ni should not be destroyed by CO<sub>2</sub>-laser but transformed into different Ni species. On the other hand, the laser-scribed area displayed higher carbon content (Figure 4.3i-c) and lower oxygen content (Figure 4.3i-d) than the non-scribed areas, indicating the successful conversion of electrospun PI fibers into CNFs. The data is well consistent with the elemental analysis carried out for Fe-LCNF in our previous study.<sup>140</sup>

Apart from EDX mapping, Ni particles embedded within LCNFs and their distribution was characterized by TEM. As can be seen in Figure 4.3ii, the particles are distributed evenly along the LCNFs. The Ni particles obtained by the lasing process had a mean diameter of  $(7.9 \pm 1.2)$  nm, which is considerably smaller than that of the particles obtained from thermal carbonization, as shown by Liu *et al.*<sup>136</sup> where approximately 50 nm Ni particles have been reported. The smaller Ni particles could lead to greater electrochemical sensitivity due to the higher surface area-to-volume ratio. The TEM images shown in Figure 4.3ii-a+b and Figure S4.4 also suggested that favorable distribution of the laser-generated Ni nanoparticles within LCNFs could be achieved from the proposed method. However, it should be noted that under suboptimal spinning conditions, electrospun PI nanofibers containing large agglomerated metal salts can be obtained. These typically result in LCNFs with defects and poor quality due to non-uniform heat dissipation during laser exposure. The lattice distance of 0.34 nm between the carbon layers shown in Figure 4.3ii-d confirmed the formation of graphitic structure in LCNF. The high-resolution TEM image (Figure 4.3ii-c) and X-ray diffraction (XRD) spectra (data not shown) suggested that the obtained Ni particles were present in the amorphous form.

Interestingly, further morphological characterizations of 25 % Ni-LCNFs with high-magnification SEM indicated that the laser carbonization process transformed the electrospun solid nanofibers containing 25 % Ni (Figure 4.3iii-a+b) into hollow-like structure (Figure 4.3iii-c+d) where TEM images shown in Figure S4.4 may also support this hypothesis. Even though the SEM and TEM



images indicated hollow-like structures of Ni-LCNFs at first glance, a thorough investigation via electron tomography<sup>207</sup> needs to be performed to elucidate whether the hollow structure is obtained in the full length or at least to a great extent of LCNFs. This would be of interest for further in-depth study, especially to reveal possible mechanisms and factors that enable hollow-like structure fiber, which is typically achieved by sophisticated methods such as core-shell electrospinning.<sup>208</sup> This hollow structure is highly beneficial for developing ultrasensitive sensors, especially for gas sensing, where interactions between analytes and nanocatalysts could take place at the surfaces of the outer and inner walls.<sup>209</sup> High-magnification SEM images in Figure 4.3iii-c+d and Figure S4.1 revealed that LCNF walls are nonporous to a large extent. The interconnected pore size of LCNFs estimated from SEM images was  $(4 \pm 3) \mu\text{m}$  and predominated within the 3D fibrous network. Such pore networks facilitate the accessibility of electroactive species towards the interface.

#### 4.4.2 Influence of Lasing Power on LCNF Morphology

The laser power plays a significant role in the carbonization process especially with nanofibers embedded with metal salt at various concentrations. Figure 4.4 reveals the impact of the laser power on the overall morphology of 25 % Ni-LCNF electrodes after carbonization. The LCNF electrodes scribed at 1.5 W displayed a fully scribed electrode feature and favorable fibrous structures with high porosity as shown in the top and side views of the respective SEM images. The laser power at 0.9 W was insufficient to completely carbonize the whole electrode area, while that at 1.8 W resulted in electrode burning. As illustrated in the SEM images, the remaining pristine electrospun nanofibers and sheet-like structure were obtained in case of insufficient- and over-carbonized electrodes, respectively. The dependence of lasing power on various Ni concentrations was also investigated (Figure S4.3). As expected, the higher Ni content required lower lasing power to obtain the desired features of LCNF electrodes and vice versa.

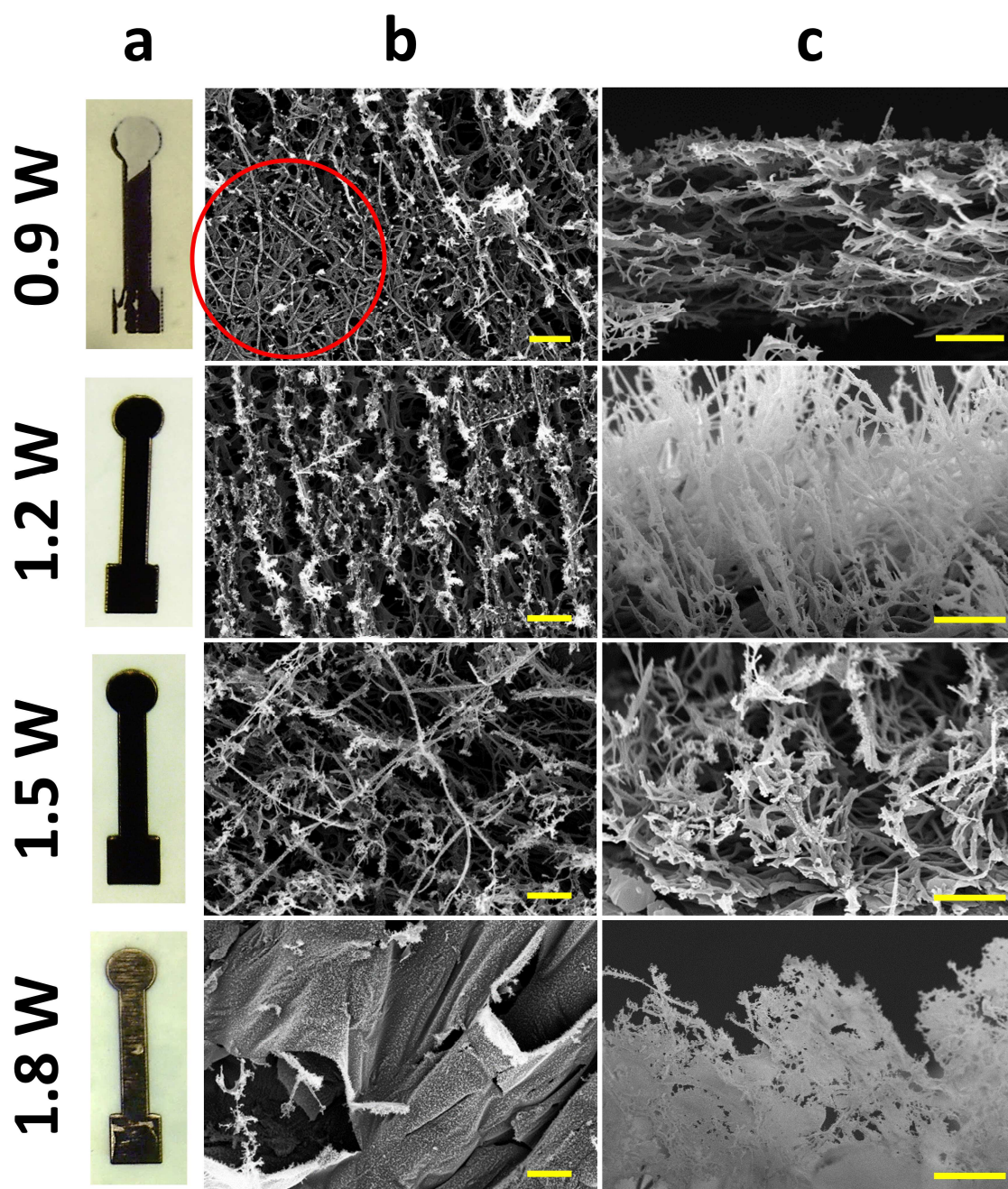


Figure 4.4: Microscopic images of LCNF electrodes containing 25 % Ni after scribing with 0.9, 1.2, 1.5 and 1.8 W laser power (a). Corresponding SEM images of the top view (b) and side view (c). The scale bars are 10  $\mu\text{m}$ . The red circle (at 0.9 W) indicates an area where fibers were incompletely carbonized.

#### 4.4.3 Mechanical Stability of Embedded Metal Nanocatalysts

In electroanalytical applications, the mechanical stability of the embedded nanocatalysts is of great importance as the transducers may encounter stirring conditions or solution flows to promote mass transport. This could subsequently cause the detachment of nanocatalysts from the LCNFs. Therefore, the mechanical stability of the Ni nanoparticles in the LCNFs was assessed by determining the change of Ni content after incubation in PB solution under shaking at 50 rpm for

5 h. The EDX data (Figure S4.5) and Table 4.1 reveal the high stability of Ni particles in LCNFs, which is greater than that of the electrodeposited Ni particles (eNi) on the laser-induced graphene (LIG; Kapton foil) and Fe-LCNFs. Here, Ni particles remained stable in the LCNF matrix after washing, whereas almost 100 % of electrodeposited Ni on LIG and Fe-LCNFs were detached from the electrode surfaces. The strong binding of Ni particles inside LCNFs could result from an efficient dispersion of Ni salt during electrospinning and great adhering capability of the Ni complex with PI matrix. In addition, the electrochemical measurement under the stirring condition as typically conducted in this work did not lead to any dramatic change in the overall morphology of Ni-LCNFs (Figure S4.6). Therefore, the strategy is highly suitable to generate CNF-nanocatalyst hybrids for electroanalytical applications, particularly when promoting mass transport through convection is required.

Table 4.1: Nickel content before and after shaking incubation for different electrodes determined by EDX.

Electrode	Ni content before	Ni content after
LIG w/ eNi	(39.61 ± 1.21) %	(0.83 ± 0.19) %
Fe-LCNF w/ eNi	(40.22 ± 1.19) %	(0.67 ± 0.14) %
Ni-LCNF	(6.43 ± 0.76) %	(6.85 ± 0.80) %

#### 4.4.4 Electrochemical Glucose Sensing

LCNF carrying Ni particles can be exploited in a wide application range. These include electrode material for fuel cells<sup>210</sup> or solar cells,<sup>211</sup> supercapacitors for energy storage<sup>212</sup> and organic catalysis.<sup>213</sup> Here, we demonstrate their capability in non-enzymatic sensing of glucose based on electrochemical detection. The electrocatalytic oxidation of glucose by Ni in the alkaline medium has been well-established with NaOH being the preferred electrolyte.<sup>214</sup> Figure S4.7 demonstrates the CV studies of the electrocatalytic mechanism by the as-prepared Ni-LCNFs in NaOH. In the absence of glucose (Figure S4.7a-i+iii), the anodic and cathodic peaks at ca. 500 and 300 mV, respectively, were present, indicating the formation of a redox couple, Ni(OH)<sub>2</sub>/NiO(OH), which typically occurs with Ni-based electrodes in an alkaline medium.<sup>214</sup> This led to the assumption that the laser exposure may induce the formation of NiO rather than the other oxide species, e.g. NiO<sub>2</sub> and Ni<sub>3</sub>O<sub>4</sub>. The change in one electron process (Ni<sup>2+</sup>/Ni<sup>3+</sup>) in the electrocatalytic reaction as described in Figure S4.7 may also support the formation of NiO, which differs from NiO<sub>2</sub> and Ni<sub>3</sub>O<sub>4</sub> where the changes in electron are 2 and 0.67, respectively. Apart from this evidence, the additional peak couples at 660 and 620 mV of Ni-LCNFs in ferri/ferrocyanide solution shown in

Figure S4.8 also postulated the formation of NiO during laser exposure, as  $\text{Ni}^{2+}$  generally participated in the generation of nickel hexacyanoferrate (NiHCF) complex ( $\text{Ni}^{2+} + \text{K}_3\text{Fe}(\text{CN})_6 \rightarrow \text{KNiFe}(\text{CN})_6 + 2 \text{K}^+$ ).<sup>215</sup> A further detailed discussion with respect to the formation of NiHCF can be found in the Supporting Information (Figure S4.8). Treating the electrode with 40 CV cycles resulted in the increased peak currents until they became saturated. This suggests that upon electrochemical treatment, the hydrophilicity of Ni-LCNF electrodes increased, enabling the accessibility of analytes inside the porous structure. The presence of glucose resulted in the increased oxidative peak and anodic shift towards 550 mV, attributed to the electrocatalytic oxidation of glucose to gluconolactone by NiO(OH) (Figure S4.7a-ii). The generated anodic peaks were proportional to the concentrations of glucose (Figure S4.7b). The linearity between the peak currents and square root of scan rates revealed that the diffusion-based reaction of NaOH and glucose occurred at the Ni-LCNFs. These results are consistent with those reported in the literature,<sup>216–218</sup> suggesting that the expected electrocatalytic behavior can be realized from the laser-generated Ni hybrid. The sensing mechanism is detailed in the Supporting Information (Figure S4.7).

The effects of Ni content in the electrospun PI nanofibers on the electrochemical performance of glucose sensing were investigated by amperometry at 550 mV. As expected, the higher amount of Ni content facilitated a greater sensitivity for glucose sensing (Figure 4.5a). It is assumed that the 25 % Ni content promoted a larger number of laser-generated nanocatalysts exposed to the LCNF surface than that of 15 and 5 %. It is also possible that the remarkable current response obtained from 25 % Ni-LCNFs might be also attributed to the enhanced electroactive surface area (ESA) offered by the intact fibrous feature (Figure 4.2b, 25 % Ni). As can be seen in Figure S4.8, the 25 % Ni-LCNF electrodes possessed an ESA that was approximately 1.3 times and 3.1 times higher than those of 15 % Ni-LCNFs and 5 % Ni-LCNFs, respectively. The result implies that high Ni content loaded in LCNFs plays a more important role in the enhanced sensitivity than the increased ESA, as the sensitivity of glucose sensing offered by 25 % Ni-LCNF electrodes was ca. 4.7 times and 9.9 times higher than those of 15 % Ni-LCNF and 5 % Ni-LCNF, respectively. However, we believe that the fiber-like morphology obtained from 25 % Ni-LCNF not only contributed to higher collision rates between Ni nanoparticles and glucose but also facilitated the fast response time as can be seen from rapid signal rising within 5 s after glucose injection. In summary, the combination of a high content of nanocatalysts with the obtained fiber-like structures leads to a large surface area with exposed functional nanocatalysts, which is thought to be the main reason for the significant boost in electrochemical performance of 25 % Ni-LCNF compared to 5 and 15 %. In addition, the inset of Figure 4.5a clearly indicates that the electrocatalytic oxidation

of glucose specifically resulted from Ni nanoparticles as LCNFs carrying 5 % Fe did not provide any significant signal response upon glucose injection. Furthermore, we found that various lasing powers not only generate 25 % Ni-LCNFs with distinct morphological structures but also greatly affect the sensitivity of glucose sensing, as shown in Figure S4.9. Here, lasing the nanofibers with 1.5 W enabled the maximum signal current of glucose sensing, which could also be attributed to the obtained intact fibrous LCNFs (Figure 4.4).

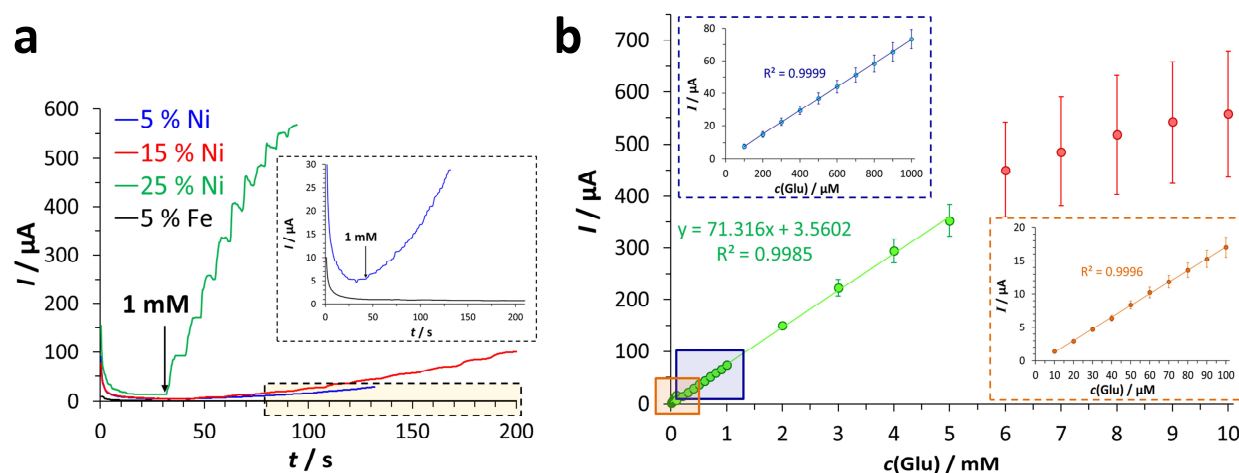


Figure 4.5: Amperometric response of LCNF containing different concentrations of Ni (5, 15 and 25 %) and 5 % Fe as control towards glucose injection (a). One injection step equals 1 mM glucose. Dose response upon glucose injection in 10  $\mu\text{M}$  steps (0-100  $\mu\text{M}$ , orange box), 100  $\mu\text{M}$  steps (100-1,000  $\mu\text{M}$ , blue box) and 1,000  $\mu\text{M}$  steps (1,000-10,000  $\mu\text{M}$ ) ( $n \geq 3$ ) (b). The potential was fixed at 0.55 V and the detection matrix consisted of 0.5 M NaOH.

The sensitivity of 25 % Ni-LCNF electrodes was further investigated as shown in Figure 4.5b. The sensitivity towards glucose reached up to 2,092 and 857  $\mu\text{A} \cdot \text{mM}^{-1} \cdot \text{cm}^{-2}$  for the linear range of 10-100  $\mu\text{M}$  and 100  $\mu\text{M}$  to 5 mM, respectively. A limit of detection (LOD) as low as 0.3  $\mu\text{M}$  could be achieved. The obtained large dynamic range covers the range of glucose in several human body fluids (ocular fluid, urine, saliva and sweat).<sup>89,219</sup> Electrode poisoning by halides, e.g.  $\text{Cl}^-$ , is a major problem in non-enzymatic electrochemical sensors based on glucose detection.<sup>214,220,221</sup> However, as shown in Figure S4.10, the presence of  $\text{Cl}^-$  in the detection medium even up to 250 mM did not notably interfere with the sensing performance. A comparison of glucose sensing of our material with that of other existing composites that are also based on nickel-carbon composites is given in Table 4.2. Our LCNF-Ni electrode not only provides excellent analytical performance that is highly comparable to other reports but also possesses superior characteristics, especially, in terms of its simplicity, flexibility, affordability and mass-production capability.

Table 4.2: Comparison of the analytical performance of most recent nickel-carbon hybrid materials towards non-enzymatic glucose sensing.

Material	Linear range / $\mu\text{M}$	LOD / $\mu\text{M}$	Sensitivity / $\mu\text{A}\cdot\text{mM}^{-1}\cdot\text{cm}^{-2}$	Reference
Nano NiO processed by	1-10	0.16	66.0	222
potential scan	1-110		55.9	
NiNP/SMWNTs	1-1,000	0.5	1,438	223
Ni(OH) <sub>2</sub> -graphene	1-10	0.6	494	224
	10-1,000		328	
NiO/OMC/GCE	2-1,000	0.65	834.8	225
CNT-Ni nanocomposite	5-2,000	2	1,384.1	226
NiONP/PANINW/GO/GCE	2-960	0.5	376.22	227
	960-5,560			
NiNPs/ATP/RGO	1-710	0.37	1,414.4	228
3D/Ni-Fe nanosheets	0.05-200	0.031	7.90	229
NiO-HAC	10-3,300	1	199.86	230
Ni(OH) <sub>2</sub> /CNT fiber microelectrodes	20-10,500	0.645	12,200	231
PF/Ni30	20-500	8	670	232
Ni-Pd@AC/GCE	10-1,000	0.014	90,000	233
Ni/NC-800	2-4,658	0.12	660.3	234
Ni-LCNF	10-100	0.3	2,092	this work
	100-5,000		857	

Apart from sensitivity, different Ni contents in LCNFs also affect the selectivity of glucose sensing. As can be seen from Figure 4.6a+c, 25 % Ni was high enough to selectively enable the electrocatalytic response of glucose for both 1 mM and 100  $\mu\text{M}$  without interfering effects from uric acid (UA) and ascorbic acid (AA). On the other hand, the current responses of interferent species obtained from 5 and 15 % Ni are non-negligible when compared to that of glucose (Figure 4.6b+d). It is possible that the oxidations of UA and AA were prone to take place at the carbon surface, generating a high signal response, especially at 5 % Ni (Figure 4.6d). It should be



noted that the higher concentrations of UA and AA may possibly interfere with the sensing performance of Ni-LCNFs, which is considered as an inherent problem for the general non-enzymatic electrochemical sensors. However, other studies demonstrated a viable solution to this problem, e.g. using a semipermeable membrane as a protective layer.<sup>16,235</sup>

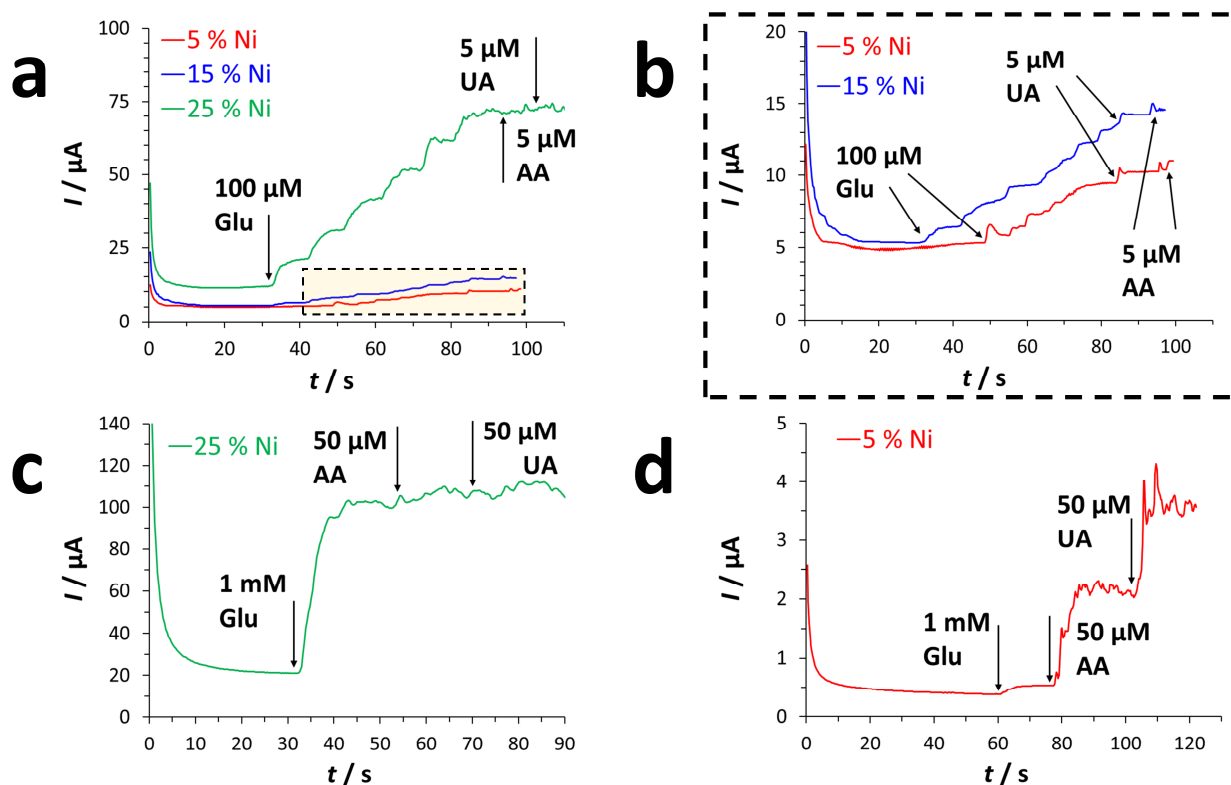


Figure 4.6: Amperometric response of LCNF containing different percentages of Ni towards successive 100  $\mu$ M glucose (Glu) addition and final addition of potential interferents ascorbic acid (AA) and uric acid (UA) (both 5  $\mu$ M) ( $n = 3$ ) (a). Zoom-in of the amperograms for 5/15 % Ni content with noticeable steps after the addition of interferents (b). Amperometric response of LCNF containing 25 % Ni (c) and 5 % Ni (d) after the addition of 1 mM Glu and 50  $\mu$ M of AA and UA each. For 5 % Ni, the signals of both interferents are significantly higher than that of glucose, whereas for the 25 % Ni only glucose leads to an obvious signal response. The potential was fixed at 0.55 V and the detection matrix consisted of 0.5 M NaOH. In the case of fluctuating signals, the mean value was taken for evaluation.

## 4.5 Conclusion

Generating carbon nanofibers with embedded metal nanocatalysts can be easily achieved by one-step laser-induced carbonization of electrospun nanofibers containing metal complex. Our strategy provides a 3D architecture of carbon nanofiber networks with embedded ultrasmall and uniform distribution of metal nanoparticles. The nanoparticles adhere firmly within the carbon nanofibers. Undoubtedly, the as-prepared hybrids exhibit excellent performance for non-enzymatic glucose sensing, especially in terms of sensitivity and selectivity. By changing the metal complex, carbon nanofibers with a variety of metal nanocatalysts can be created. Apart from favorable electrocatalytic performance, extremely low material cost (\$0.07 per electrode), fast manufacturing process and high flexibility in terms of electrode designs and type of incorporated metal nanocatalysts are additional characteristics that make this strategy ideal for large-scale production and commercialization. This opens up an opportunity to efficiently miniaturize and integrate electrochemical devices with nanocatalysts useful for many relevant applications, especially in domains of (bio)sensing, energy storage, synthetic chemistry or (bio)medicine.



## 4.6 Supporting Information

### Morphology of Ni-LCNFs with Varying Nickel Content

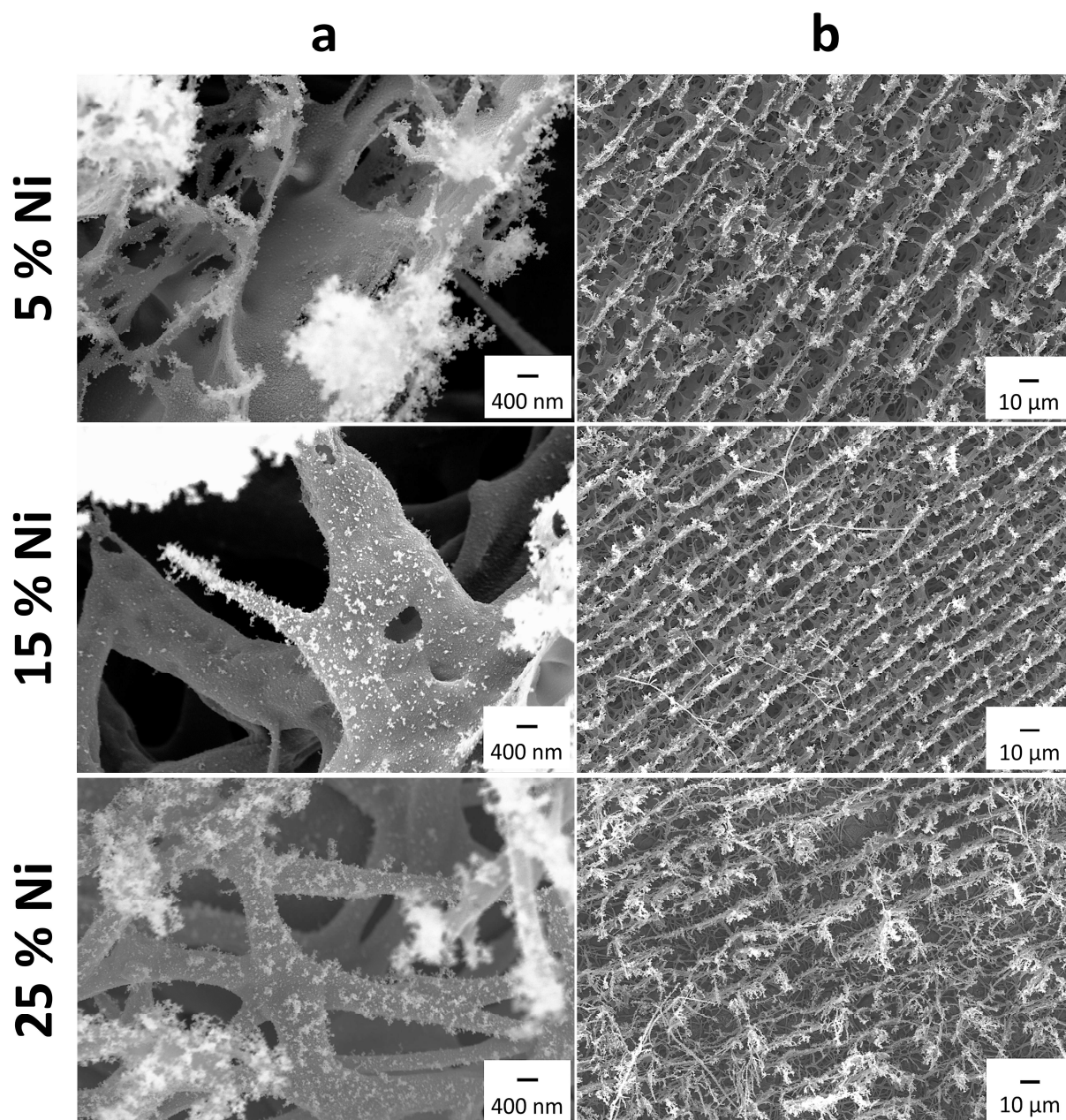


Figure S4.1: SEM images of LCNFs for different Ni salt contents at high magnification showing significantly more pronounced fibrous structures of 25 % Ni compared to 5 % and 15 % (a) and low magnification demonstrating homogenous overall morphology (b).

### Morphology of Ni-LCNFs vs. Fe-LCNFs

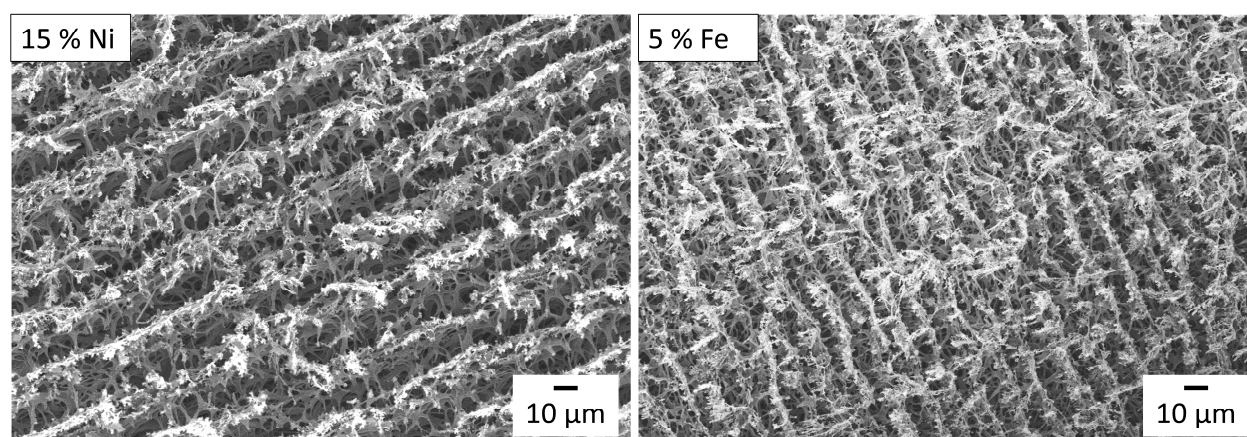


Figure S4.2: SEM images of LCNF containing 15 % Ni and 5 % Fe demonstrating morphological similarities.

### Lasing Power and Nickel Content Variation

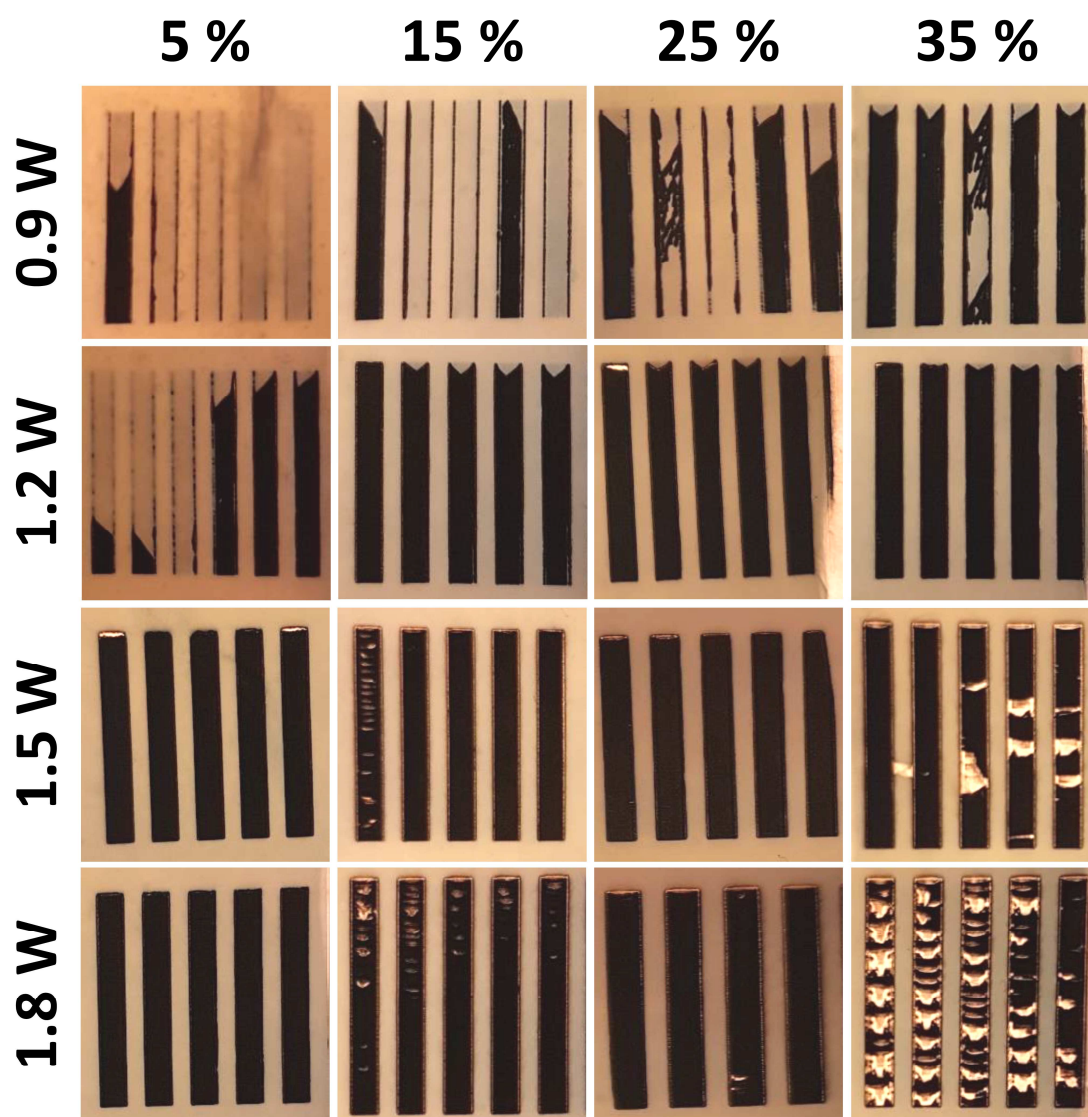


Figure S4.3: Photographs of LCNF (1.5 mm x 14 mm) observed for Ni content variation (5 %, 15 %, 25 %, 35 %) in combination with laser power variation (0.9 W, 1.2 W, 1.5 W, 1.8 W).



## TEM Images of 25 % Ni-LCNFs

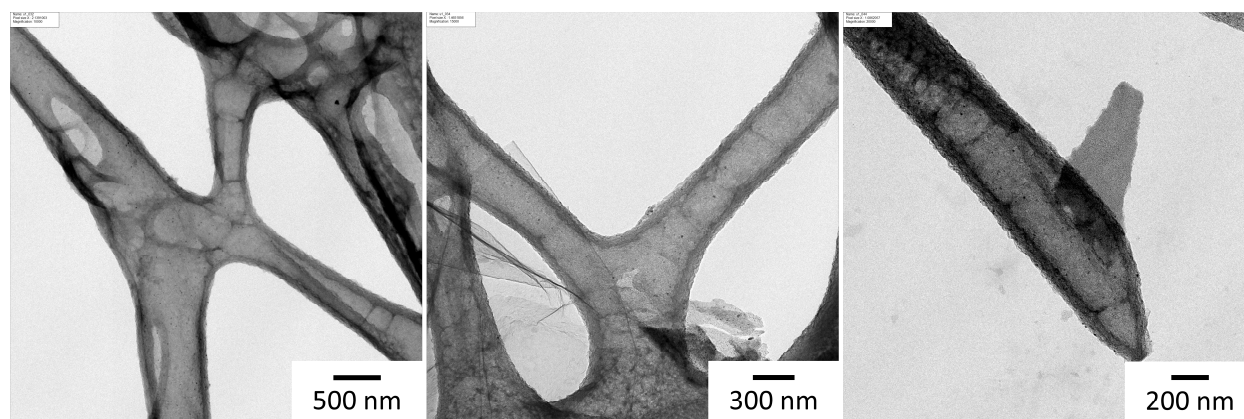


Figure S4.4: TEM images of different 25 % Ni-LCNFs at different magnifications. The lighter grey color of the inner part of LCNF compared to the rims indicates that fewer atoms are present inside. This could point to hollow-like structure of carbon nanofibers.

## EDX Spectra for Mechanical Stability Experiment

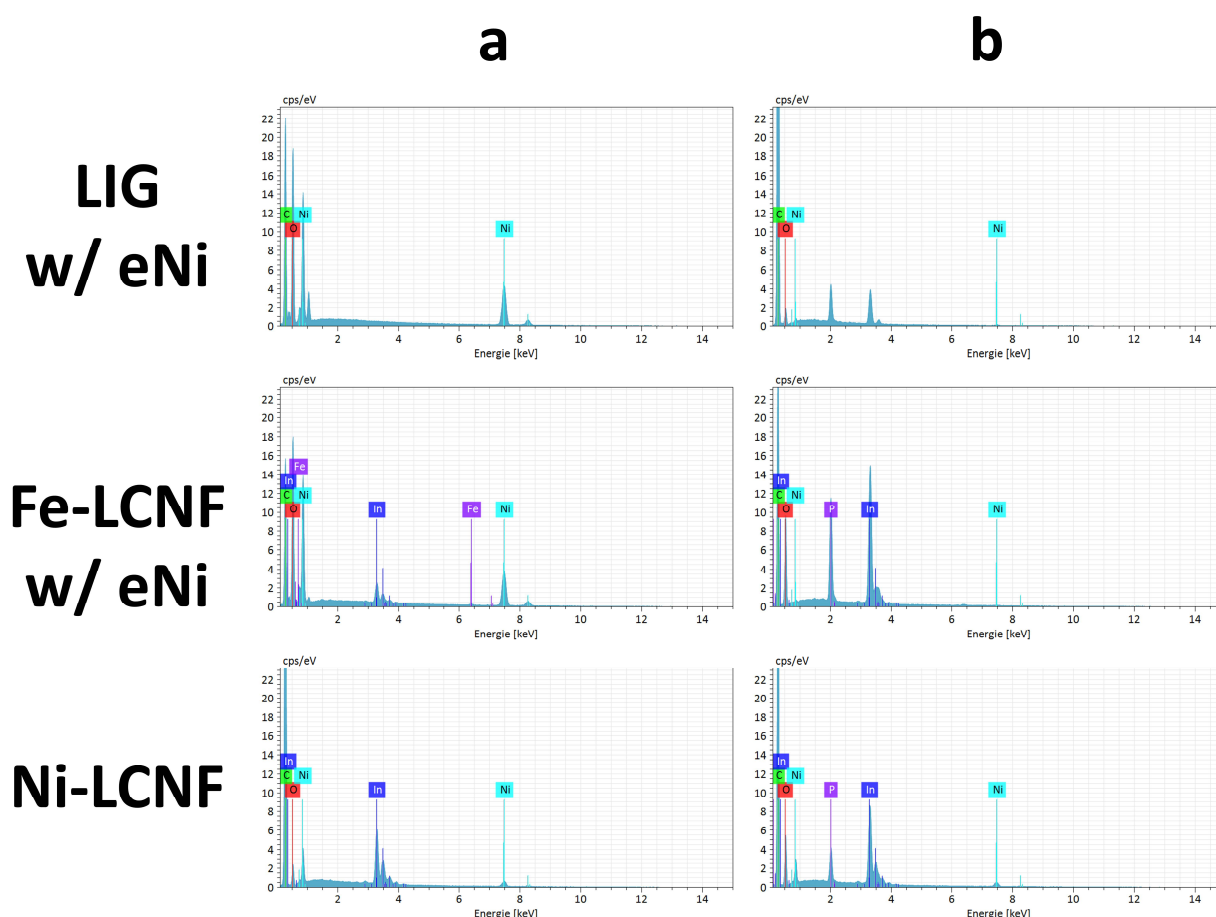


Figure S4.5: EDX spectra before (a) and after (b) incubation in PB for LIG (laser-induced graphene on Kapton foil) and Fe-LCNF with electrodeposited Ni (eNi) and Ni-LCNF. The incubation was conducted by a shaking incubator (VWR Incubating Orbital Shaker, Professional 3500) for 5 h (50 rpm) at 37 °C with the samples burdened on the ground of a Petri dish that was filled with PB. LIG and Fe-LCNF loose almost the complete Ni during incubation while LCNF with Ni that was embedded during electrospinning shows no loss.

## Mechanical Stability of Ni-LCNFs after Electrochemical Measurement under Stirring Condition

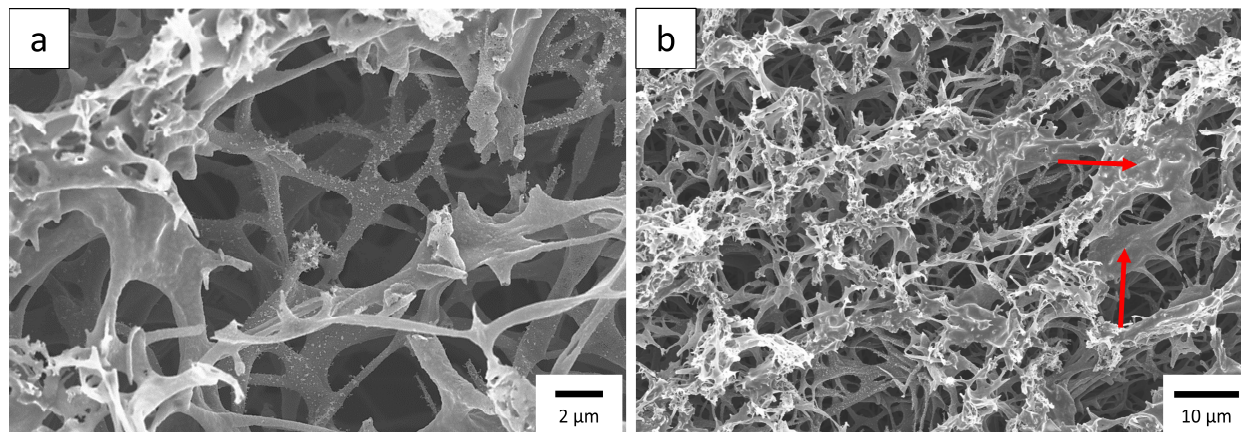


Figure S4.6: SEM images of 25 % Ni-LCNFs at high (a) and low magnification (b). The LCNF electrode has been used for electrochemical glucose detection at 0.55 V with several consecutive glucose injections under stirred condition as commonly done in this study. Afterwards, the electrode was blow-dried with nitrogen stream prior to SEM imaging. Fibrous structure is still maintained indicating favorable mechanical stability for electroanalytical applications. The red arrows point out the area that is covered with the solution residues from the measurement.

## Cyclic Voltammetry Glucose Mechanism Study

CV studies reveal the sensing mechanism of the Ni-LCNF hybrid with glucose. In the absence of glucose (Figure S4.7a-i+iii), the anodic and cathodic peaks at 500 mV and 300 mV, respectively, indicate the following redox reactions:



When glucose is present (Figure S4.7a-ii), the strong oxidizer, NiO(OH) induces the oxidation of glucose as following:



Here, upon addition of glucose the oxidative peak not only increased but also shifted anodically while the cathodic peak remained unchanged for its magnitude and peak potential. The latter indicated the reduction of the as-generated Ni(OH)<sub>2</sub> from reaction (S4.2). The irreversible reaction in (S4.2) resulted in the decrease in peak intensities from cycle to cycle (Figure S4.7a-ii).

Considering the first CV cycle, increasing glucose concentration led to obvious anodic shift of oxidative peak (Figure S4.7b) as adsorption of glucose took place at the interface. Consequently, such phenomenon experienced less number of active NiO(OH) for electrocatalytic oxidation of glucose as can be seen from lowest cathodic peak intensity for high glucose concentration.

In contrast, the oxidative peaks at the last CV cycles appeared at similar peak potential for all glucose concentrations (Figure S4.7c-iv) while the peak intensities decreased at high glucose concentration. As the glucose reaction occurs at ca. 550 mV for higher glucose concentration, this potential was chosen for the amperometric glucose detection.

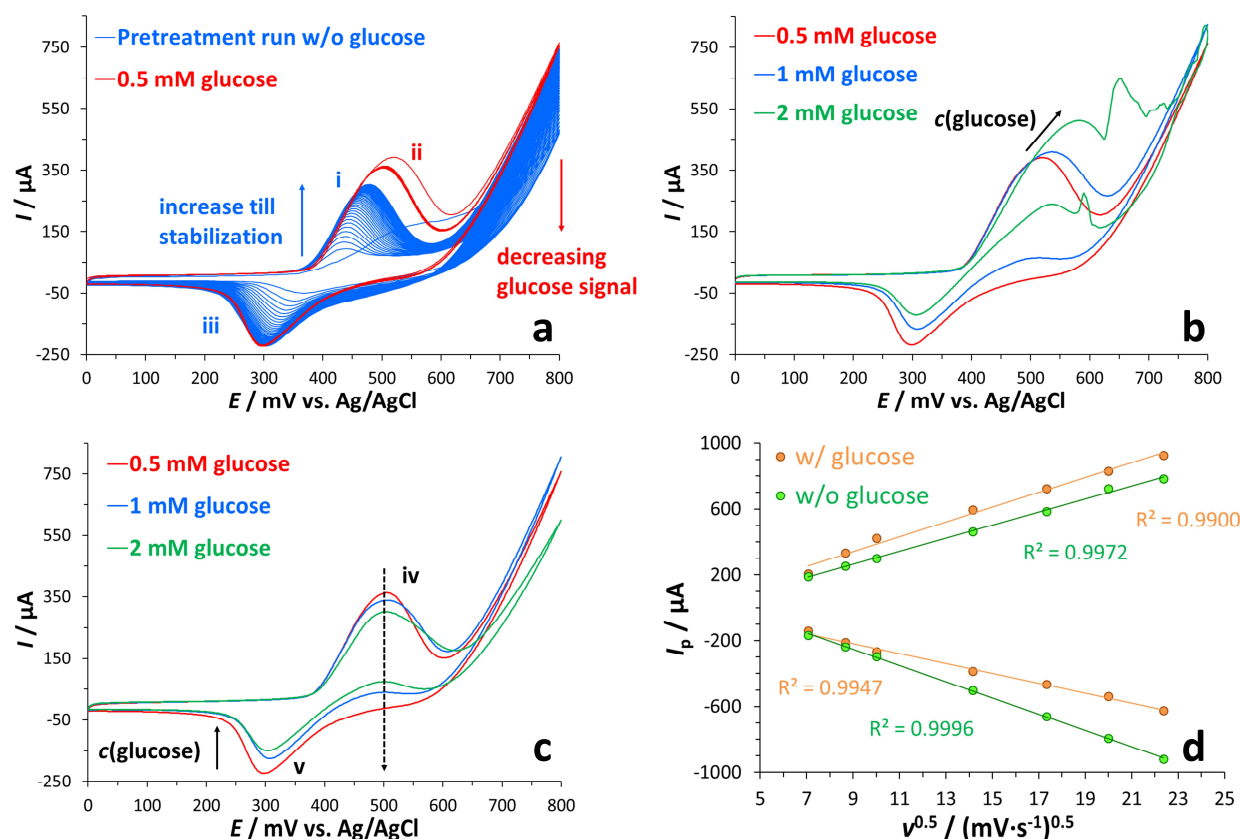


Figure S4.7: Cyclic voltammograms of LCNF in 0.5 M NaOH w/o glucose (40 cycles) and subsequent run (10 cycles) w/ 0.5 mM glucose (a). First cycle (b) and last cycle (10th) (c) w/ 0.5, 1 and 2 mM glucose. Oxidation and reduction peak currents, observed after scan rate variation, plotted against the square root of the scan rate (d). The associated measurements were performed in 0.5 M NaOH w/ and w/o 1 mM glucose.

## Electrochemical Surface Area at Varying Nickel Content

The electrochemical surface area of Ni-LCNF electrodes containing different contents of Ni salt was studied by cyclic voltammetry with ferri/ferrocyanide as redox marker. Alongside the results discussed in the main research article, it was found that a peak couple additional to the ferri/ferrocyanide redox couple appeared at 660 mV and 620 mV for the oxidation and reduction reaction respectively (Figure S4.8-i). This peak couple showed a current signal increase with increasing amount of Ni in the LCNF electrodes. It is known that metal hexacyanoferrate complexes can form during cyclic voltammetry with ferri-, ferrocyanide or ferri/ferrocyanide mixture solutions containing transition metal salts.<sup>236–238</sup> In addition to liquid/liquid reaction, a recent study by Oliveira *et al.* has shown that the generation of nickel hexacyanoferrate (NiHCF)

could be carried out through voltammetric cycling of Ni nanoparticles modified electrode in ferricyanide solution.<sup>239</sup> Their cyclic voltammogram revealed that the redox process of NiHCF complex took place at 630/580 mV which is highly consistent to our study.

Thus, our results shown here suggest an additional potential functionality of Ni-LCNFs, opening opportunities for further analytical applications.<sup>240</sup> Thorough investigations towards NiHCF generation using the Ni-LCNF hybrids and their potential applicability are our ongoing work.

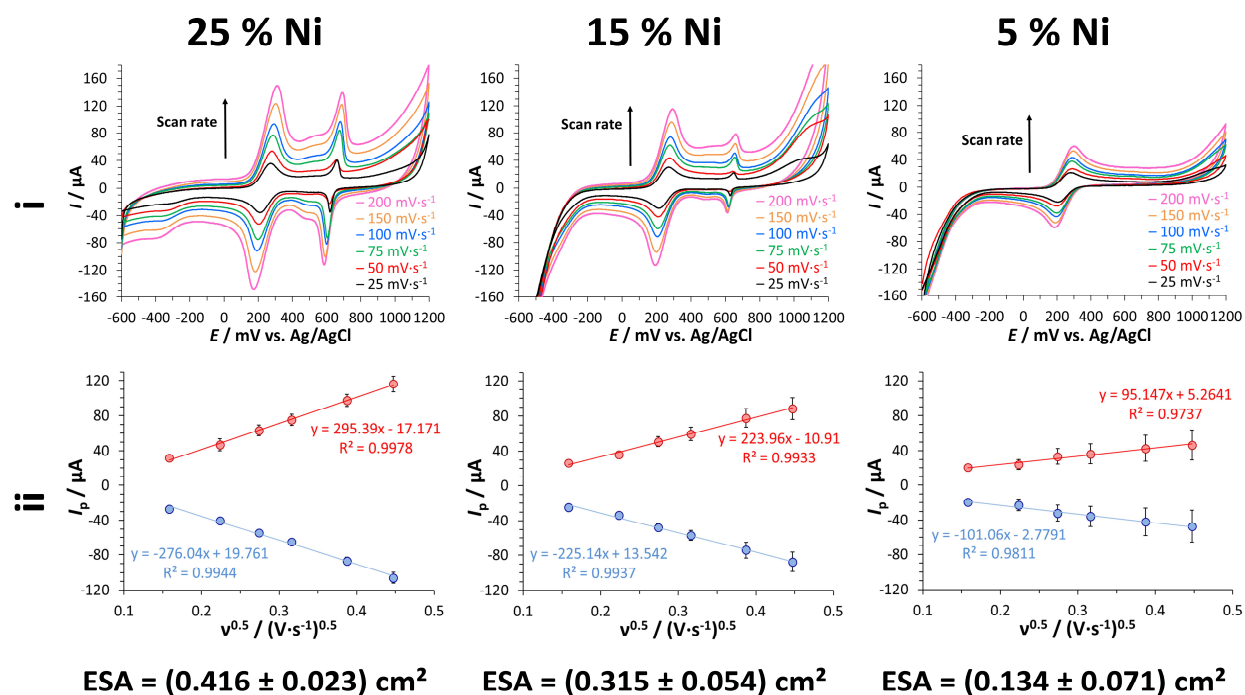


Figure S4.8: Cyclic voltammograms at various scan rates for Ni-LCNF with different Ni content (i). Randles-Sevcik plots for the corresponding cyclic voltammograms ( $n = 4$ ). For evaluation the ferri/ferrocyanide peak couple at lower potential (ca. 280/210 mV) was taken (ii). The peak couple at 660/620 mV relates to the formation of nickel hexacyanoferrate (NiHCF) species. The measurements were performed with 1 mM ferri/ferrocyanide in 0.1 M phosphate buffer (0.1 M KCl, pH 7.0).

In principle, the formation of NiHCF complex can be achieved only from Ni(II)-salts. Thus, the results could imply that the laser process tends to convert  $\text{Ni}(\text{acac})_2$  into NiO rather than other forms, e.g.  $\text{NiO}_2$  and  $\text{Ni}_3\text{O}_4$ . Moreover, the electrocatalytic mechanism of glucose sensing described in the main part where  $\text{Ni}(\text{OH})_2$  is required in the reaction could also well support the aforementioned statement.

### Glucose Response for Ni-LCNF Prepared with Varying Lasing Power

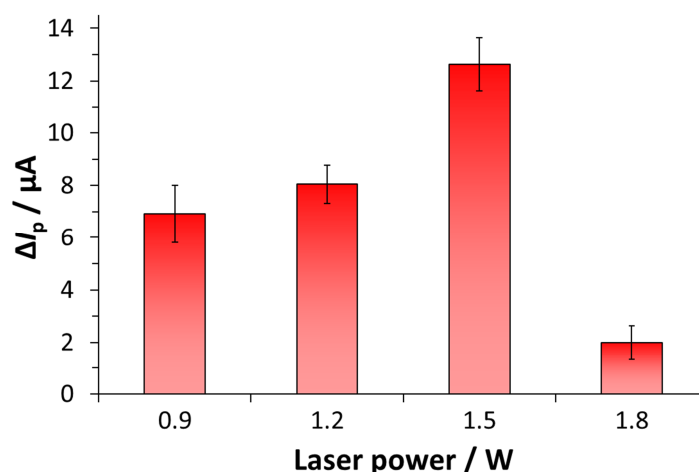


Figure S4.9: Amperometric response of LCNF generated at 0.9 W, 1.2 W, 1.5 W and 1.8 W towards 100  $\mu$ M glucose (Glu) ( $n = 3$ ). The average working area of the not-fully carbonized electrodes for 0.9 W laser power was determined by ImageJ using microscopic pictures and the current was normalized to the same area as for the other lasing settings.

### Glucose Response for Ni-LCNF in NaOH w/ and w/o NaCl

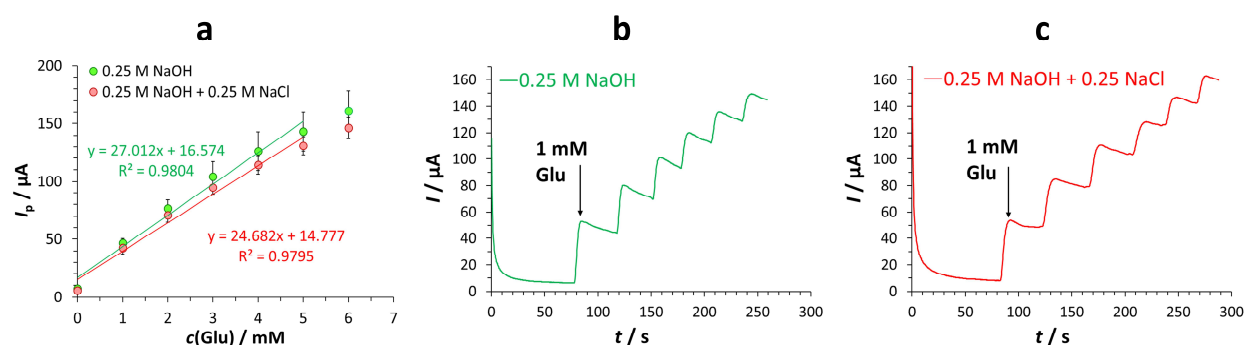


Figure S4.10: Dose-response curve ( $n \geq 3$ ) for 25 % Ni-LCNF towards successive glucose addition into 0.25 M NaOH matrix w/ and w/o 0.25 M NaCl (a). Respective amperograms in 0.25 M NaOH matrix w/o (b) and w/ 0.25 M NaCl (c). The detection potential was fixed at 0.55 V. To keep the total molarity at the same level as for the presented glucose detection experiments (0.5 M NaOH) and to have a ratio of 1:1 (NaOH:NaCl) the NaOH concentration was decreased to 0.25 M.



## 5 Non-Enzymatic Detection of Hydrogen Peroxide via Laser-Induced Carbon Nanofiber Hybrids

### 5.1 Abstract

Hydrogen peroxide is an important molecule with key functionalities during wound healing. Thus, monitoring the respective levels can give direct insights in the course of the healing process. As electroactive species,  $\text{H}_2\text{O}_2$  can be detected with electroanalytical methods in a fast and sensitive manner. Unfortunately, there is still a lack of wearable electrochemical sensors for direct monitoring of hydrogen peroxide secreted in wound fluids. Carbon nanofiber networks offer fascinating electrochemical properties and large numbers of surface interaction sites making them well suited for electroanalytical sensors. In this work, the fabrication of laser-induced carbon nanofibers (LCNFs) with embedded iron, palladium and a blend of both is investigated towards amperometric detection of hydrogen peroxide. After initial optimization with respect to electrospinnability and carbonizability, the electrochemical sensing abilities of metal-LCNFs were evaluated where a signal response down to  $100\text{ }\mu\text{M}$   $\text{H}_2\text{O}_2$  was achieved. Electrochemical treatment and chemical reduction of Pd and Fe nanoparticles in LCNFs turned out as feasible strategies to improve the  $\text{H}_2\text{O}_2$  reduction abilities. Further, enhanced electrocatalytic characteristics of bimetallic LCNF electrodes over their monometallic counterparts was indicated by a significant shift of the detection potential down to  $-0.25\text{ V}$ . This opens up a large field of LCNFs containing different metal combinations tunable towards desired catalysis related applications.

---

*This chapter has not been published.*

#### *Author contributions*

All experiments were performed by the author. The author wrote this chapter and Dr. Nongnoot Wongkaew contributed with strategic discussions on the finalization. Prof. Dr. Antje J. Baeumner was the leader of this project.



## 5.2 Introduction

In living organisms hydrogen peroxide performs many key functions. It is known to cause oxidative stress as it belongs to the reactive oxygen species (ROS) but can also act as signaling agent or be part of host defense mechanisms.<sup>241</sup>  $\text{H}_2\text{O}_2$  plays diverse roles in one of its area of appearance which is wound healing. Preventing infection of the wound by killing bacteria or inhibiting their growth is a benefit of cell-related  $\text{H}_2\text{O}_2$  secretion.<sup>242</sup> A main function of hydrogen peroxide is the support of the course of the different healing stages as described in the following. The molecular mechanisms after wound generation were studied in several species such as mice<sup>243</sup> or zebrafish and it was found that enzymes with NADPH oxidase function in cells adjacent to the wound tissue are the main source of  $\text{H}_2\text{O}_2$ . Increased local concentration of hydrogen peroxide causes an immune response in form of leukocyte recruitment.<sup>244</sup> Also,  $\text{H}_2\text{O}_2$  promotes wound healing by stimulating the proliferation of fibroblasts and vascular endothelial cells.<sup>245</sup> Neutrophils, that are belonging to the group of leukocytes, are able to control  $\text{H}_2\text{O}_2$  concentrations in both ways, either by consuming it or producing it and, therefore, keep antiseptic properties and indirectly control inflammation.<sup>246</sup> Malfunctions of those inflammatory cells and hence abnormal hydrogen peroxide levels can result in tissue degeneration or overexpression. On this account, the determination of  $\text{H}_2\text{O}_2$  values is of high interest to monitor wound healing.

Beneath several optical detection strategies such as luminescence,<sup>247</sup> colorimetry<sup>248</sup> and fluorescence,<sup>249</sup> electrochemical approaches are the most popular for  $\text{H}_2\text{O}_2$  sensing. This is due to the benefits of electrochemistry which are the fast and sensitive measurements while working with highly affordable equipment and the possibility of label-free detection. Nowadays, the classical enzyme-based sensor is desired to be substituted by non-enzymatic counterparts as those are more stable, cost-effective and easier available. Hereby, it was found that many metal nanomaterials such iron compounds (e.g. Prussian blue<sup>250</sup> or  $\text{Fe}_3\text{O}_4$ <sup>251</sup>), platinum,<sup>252–256</sup> gold,<sup>257–259</sup> silver<sup>260–262</sup> or palladium<sup>263–265</sup> possess catalytic or enzyme-like activity towards  $\text{H}_2\text{O}_2$  respectively.

Carbon nanofibers (CNFs) own many exciting features including large surface-to-volume ratio, excellent conductivity, chemical resistance and high mechanical stability which leads to a great demand in (bio)sensor development. To prepare them mainly two techniques are established. One is the growth by chemical vapor deposition (CVD) and the other comprises electrospinning of nanofibers (commonly polyacrylonitrile) with subsequent thermal stabilization and carbonization treatment steps.<sup>266</sup> The selectivity of CNFs, with respect to electrochemical analyte detection, is conventionally improved by preparing hybrid composites, either by incorporation during synthesis or decoration afterwards. Both is gladly done with metal compounds due to the already mentioned

catalytic features and easy processability.<sup>267,268</sup>

Previously, we reported a facile strategy to fabricate CNFs by electrospinning with following carbonization by CO<sub>2</sub>-laser.<sup>140,141</sup> This method enables to pattern laser-induced carbon nanofibers (LCNFs) into highly conductive electrodes with any desired design set with PC software before. Compared to as-mentioned CVD and thermal carbonization, the total process is accomplished in much faster manner (seconds to minutes depending on the electrode size) and with no need of post-fabrication steps such as shortening and binding CNF on a proper substrate. We found that LCNF hybrids with iron or nickel salts provide superior electron transfer abilities and catalytic properties e.g. for the rapid and sensitive detection of glucose. The embedding of metal particles in nanofibers by simply mixing electrospinning solutions with metal powder further leads to enhanced stability of the metal in the matrix, preventing leaching during operation in aqueous environment.<sup>141</sup> This is an important requirement for potential sensing application in- and on-body where detachment of metal with uptake into metabolism could result in toxic impacts.

In this work, the aim is to prepare LCNFs with electrocatalytic functionalities towards H<sub>2</sub>O<sub>2</sub> detection. Palladium and iron were chosen as metal compounds due to their already mentioned catalytic abilities. The content and type of metal salt incorporated in nanofibers were studied with respect to electrospinnability and laser carbonization behavior. The hydrogen peroxide sensing abilities of metal-containing LCNF electrodes was investigated by electrochemical methods, namely cyclic voltammetry and amperometry. Different strategies (electrochemical and chemical) to enhance the signal response were investigated and electrocatalytic characteristic of bimetallic hybrids with both metals embedded are studied for the first time in LCNF.

## 5.3 Materials and Methods

### 5.3.1 Fabrication of LCNF Electrodes

Nanofiber mats were prepared by electrospinning of a solution containing 15 % (w/v) Matrimid® 5218 (Huntsman Advanced Materials BVBA, Belgium) and palladium(II) acetylacetonate (99 %, Sigma-Aldrich, Germany), palladium(II) chloride or iron(III) acetylacetonate ( $\geq 99.9$  % trace metals basis, Sigma-Aldrich, Germany) dissolved in N,N-dimethylacetamide (Merck, Germany). The metal salt percentages reported here are relative to the dry mass of the polymer. It is abbreviated Pd(acac)<sub>2</sub>/Fe(acac)<sub>3</sub> or Pd/Fe in the other sections. Spinning solutions were ultrasonicated for 30 min and stirred at least overnight before spinning. The electrospinning was conducted for 15 min per fiber mat at a 10  $\mu\text{L}\cdot\text{min}^{-1}$  flow rate with a 15 cm tip-to-collector distance. The applied voltage was adjusted in the range of 12-15 kV depending on the ambient temperature and humidity conditions. Indium tin oxide coated poly(ethylene terephthalate) (ITO/PET, sheet resistivity 60  $\Omega\cdot\text{sq}^{-1}$ , 1 ft  $\times$  1 ft  $\times$  5 mil, Sigma-Aldrich, Germany) that has been cut into 5 cm  $\times$  5 cm was used for nanofiber deposition. The as-cut ITO/PET piece was placed in the middle of a metal collector dish. An electrical connection between the ITO surface and the underneath metal collector was performed by taping two aluminum foil stripes at the rims of the ITO substrate at the opposite sides. This resulted in a final 4 cm  $\times$  5 cm collecting area. After electrospinning, conductive electrodes with the desired patterns of carbon nanofibers were generated by a CO<sub>2</sub>-laser (10.6  $\mu\text{m}$ , VLS 2.30, Universal Laser Systems, Polytech Systeme GmbH, Germany). The lasing speed was optimized in earlier studies to 60 % (of 1,270  $\text{mm}\cdot\text{s}^{-1}$ ) and the image density was set to 1,000 DPI.

### 5.3.2 Electrochemical Characterization

A CV-50W voltammetric analyzer (Bioanalytical Systems, USA) with a three-electrode system consisting of LCNF as the working electrode, Pt wire as the counter electrode and a Ag/AgCl reference electrode was utilized for all electrochemical measurements. The working area of the LCNF immersed into a measuring solution was defined as 2.8 mm  $\times$  3 mm and separated from the contacting part using candle wax. PB solutions were purged with N<sub>2</sub> gas for at least 10 min prior to H<sub>2</sub>O<sub>2</sub> injection and measurement.

### 5.3.3 Chemical Reduction

Sodium borohydride solutions were prepared by carefully dissolving 0.2 % (w/v) NaBH<sub>4</sub> (ReagentPlus®, 99 %, Sigma-Aldrich, Germany) in deionized water. LCNFs electrodes have been

cut out with scissors prior to placing them into Eppendorftubes. Subsequently, chemical reduction of metal compounds in LCNFs was executed by pipetting the prepared  $\text{NaBH}_4$  solution into the Eppendorftubes. The volume (ca. 500  $\mu\text{l}$ ) was chosen to immerse the whole working area of LCNF electrodes. Incubation was carried out for 3/24 hours with closed lids and electrodes were rinsed with deionized water and blow-dried with nitrogen afterwards.

## 5.4 Results and Discussion

### 5.4.1 Effect of Varying Palladium Salts and Content

As each type of metal and metal salt owns different (ionic) conductivity, charging and solubility, their behavior during electrospinning varies significantly. Thus the respective content in the spinning solution needs to be optimized. It was demonstrated before that polymer mixtures with  $\text{PdCl}_2$ <sup>269</sup> and  $\text{Pd}(\text{acac})_2$ <sup>197</sup> can be electrospun into nanofibers. For fabricating palladium-containing LCNF electrodes (termed Pd-LCNF) the electrospinnability of both mentioned Pd salts with Matrimid® needed to be checked initially. As can be seen in Figure 5.1a, the well-dispersion of Pd salt in Matrimid® solutions was achieved at 15 % and 25 % content while 35 % Pd led to a precipitation of the metal salt as indicated by the red arrow. To keep the molar amount of Pd the same as for 25 %  $\text{Pd}(\text{acac})_2$ ,  $\text{PdCl}_2$  content was set to 15 % in the respective solution.

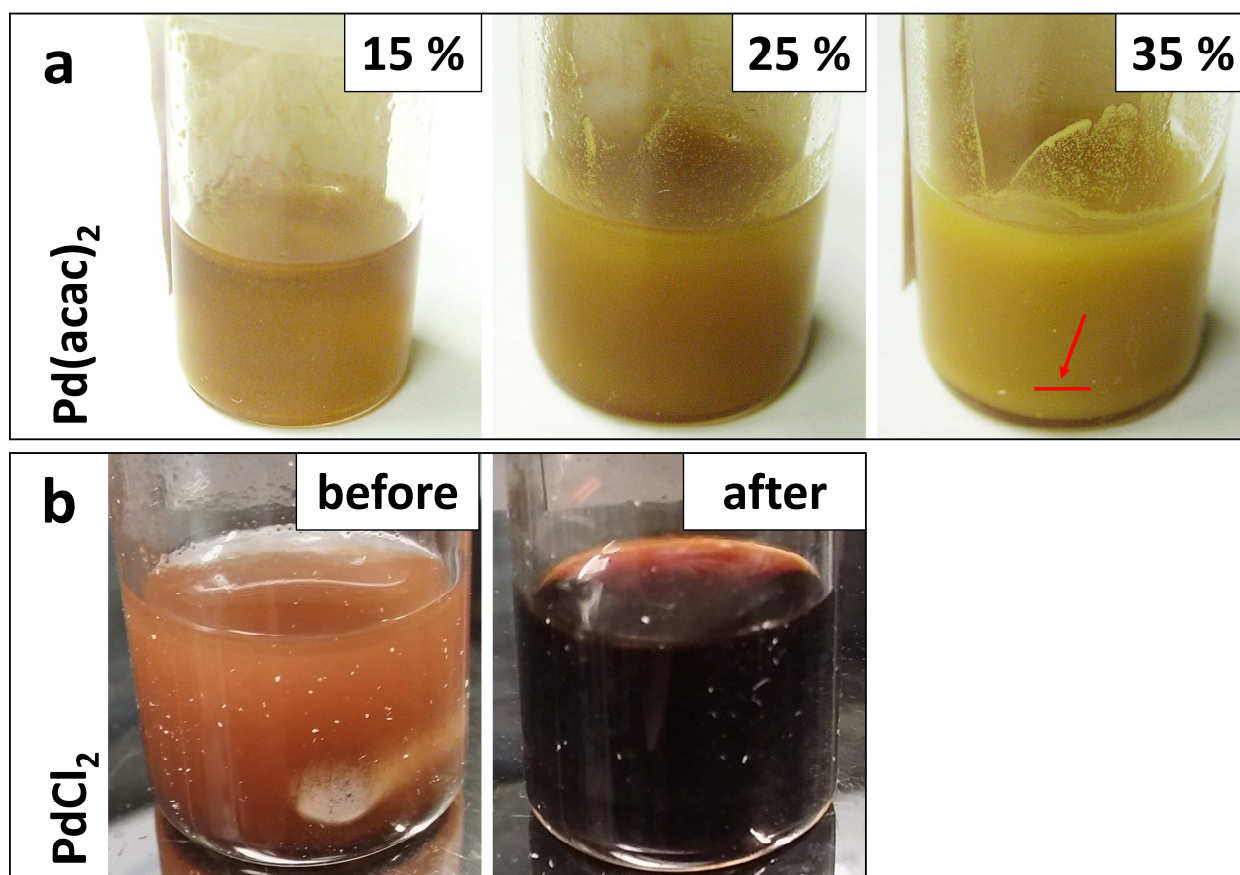


Figure 5.1: Spinning solutions containing 15 % (w/v) Matrimid® and 15/25/35 %  $\text{Pd}(\text{acac})_2$  (a) or 15 %  $\text{PdCl}_2$  (b). The red arrow at 35 %  $\text{Pd}(\text{acac})_2$  solution indicates precipitating metal salt. The  $\text{PdCl}_2$  solution was mixed with NaCl (molar ratio of 2:1 to  $\text{PdCl}_2$ ) and the pictures show the change after heating on a hot plate at 70 °C compared to before.

As  $\text{PdCl}_2$  is only soluble in complexing solvents e.g. alcohols (Matrimid® is insoluble in alcohol) or in the presence of chloride ions (formation of Pd complex  $[\text{PdCl}_4]^{2-}$ ),<sup>270</sup> NaCl in a molar ratio

of 2:1 to  $\text{PdCl}_2$  has been added. Stirring overnight still did not lead to clear solutions and, therefore, the spinning solution was heated on a hot plate at  $70^\circ\text{C}$  while stirring. After some minutes a clear dark red spinning solution was obtained (Figure 5.1b). However, spinning those solutions resulted in strong flash formation between the voltage supply and syringe and poor fiber deposition. Further tests with as low as 5 %  $\text{PdCl}_2$  showed the same behavior. A reason for that could lie in too high ionic conductivity. It is assumed that the different polymer mixtures, e.g. copolymer of polyacrylonitrile with acrylic acid or poly(vinyl pyrrolidone) with tetraethyl orthosilicate, used by other work groups are able to compensate the charge contributed by  $\text{PdCl}_2$  in contrast to Matrimid<sup>®</sup> and, therefore, enable electrospinning.<sup>269,271</sup>

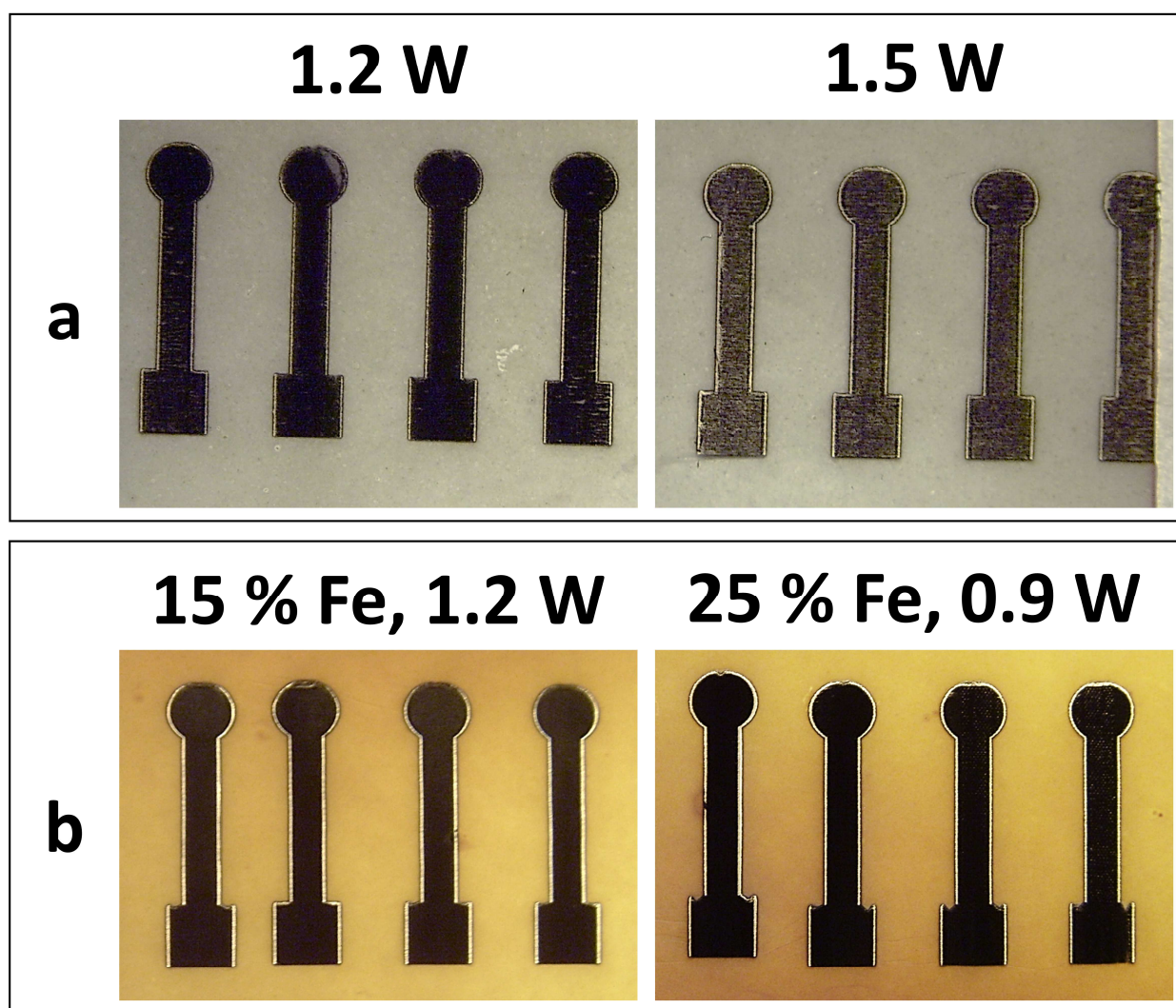


Figure 5.2: Photographs of Pd-LCNF containing 25 %  $\text{Pd}(\text{acac})_3$  obtained from 1.2 W and 1.5 W laser power (a) and Fe-LCNF containing 15/25 %  $\text{Fe}(\text{acac})_3$  obtained from 1.2 W and 0.9 W laser power respectively (b).

The laser-carbonization of 25 %  $\text{Pd}(\text{acac})_2$  containing nanofibers was further investigated. A laser power of 1.2 W was sufficient to obtain fully carbonized electrodes (Figure 5.2a). In contrast to 25 %  $\text{Ni}(\text{acac})_2$  in our previous studies (compare Figure 4.4), 1.5 W did not lead to even blackish

structures but distortions. Obviously, the heat conduction and absorption properties of Pd during lasing process differ from the ones of Ni, making it important to carry out initial studies of lasing parameters when switching the metal salt in electrospun polyimide nanofibers. The influence of laser power on carbonization behavior was further compared to Fe-LCNF (Figure 5.2b) and it was found that even less power (0.9 W) is required to homogeneously carbonize nanofibers with similar metal content (25 %). With decreasing Fe content (15 %) the lasing power needs to be increased (1.2 W) in order to obtain LCNFs with equal quality. Concluding, the heat conduction ability rises from nickel to palladium to iron which necessitates lowering the laser power in the same order (when keeping the metal content the same relative to the polymer).

#### 5.4.2 Non-Enzymatic H<sub>2</sub>O<sub>2</sub> Sensing

There are several potential mechanisms of electrocatalytic H<sub>2</sub>O<sub>2</sub> decomposition at metal catalysts discussed in literature. The reduction in media with acidic to neutral conditions takes place in two steps<sup>272</sup> involving the adsorption of hydroxide species on the surface of the catalyst:



However, catalytic decomposition of H<sub>2</sub>O<sub>2</sub> to water through O<sub>2</sub> intermediates (5.3-5.5) or direct reduction (5.5)<sup>273</sup> without adsorbed hydroxide ions are also reported:



To study the electrocatalytic mechanism of hydrogen peroxide with 25 % Pd-LCNFs, cyclic voltammetry (CV) was performed. It can be seen in Figure 5.3a that the CV in presence of 10 mM H<sub>2</sub>O<sub>2</sub> did not lead to observable peaks compared to the control. It is assumed that the oxidative lasing process results in oxidized species present in LCNF. As already discussed with equations (5.1-5.5) the catalytic decomposition is a reduction process. Therefore, the catalyst should perform better when present in lower oxidation state compared to high oxidation state where further oxidation, which comes simultaneously with H<sub>2</sub>O<sub>2</sub> reduction, is prevented. Picking up on this hypothesis, Pd-LCNF electrodes were electrochemically (EC) treated by applying high negative potential for certain time (-1 V for 3 min) to enhance their catalytic abilities. Figure 5.3b shows that electrodes with EC pretreatment display a peak at ca. -600 mV that derives from hydrogen peroxide in contrast the control. It was found that EC pretreatment can also be achieved by multiple



cycling with CV technique where a reduction peak at ca. -450 mV was observed at subsequent CV with hydrogen peroxide. However, while the cathodic peak decreases with ongoing cycling the anodic peak increases (Figure 5.3c+d). This could indicate the simultaneous oxidation (electron donation) of the metal nanocatalysts in LCNFs due to the reduction of  $\text{H}_2\text{O}_2$  (electron uptake). A variation of the added hydrogen peroxide concentration could possibly prove this assumption by proportional peak height changes of the oxidation and reduction peaks. Pretreatment in 0.5 M NaOH vs. 0.1 M PB did not result in observable difference in  $\text{H}_2\text{O}_2$  sensitivity (data not shown). However, for CV pretreatment only both peaks (cathodic and anodic) appeared in subsequent CV with hydrogen peroxide, whereas it did not for pretreatment by constant potential. For further investigations, CV cycling was chosen as pretreatment method due to the lower reduction potential peak compared to pretreatment by constant potential (-0.45 V vs. -0.6 V). Additionally, electrodes pretreated with constant potential did not display an observable CV peak at lower  $\text{H}_2\text{O}_2$  concentrations (100  $\mu\text{M}$  tested as for CV pretreated electrodes, data not shown).

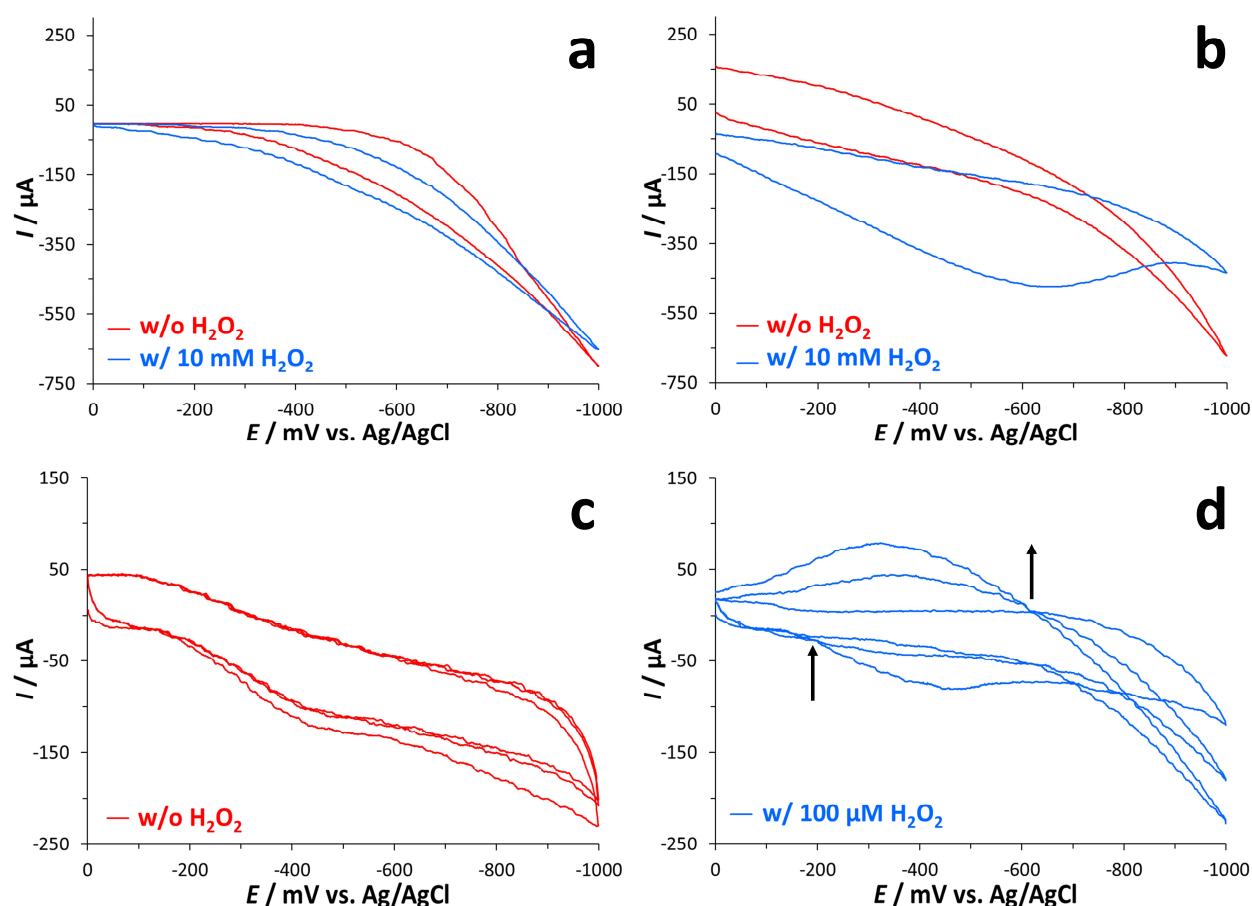


Figure 5.3: Cyclic voltammograms of 25 % Pd-LCNF in 0.1 M PB 10 mM  $\text{H}_2\text{O}_2$  w/o EC pretreatment (a) and w/ pretreatment at -1 V for 3 min for control and 10 mM  $\text{H}_2\text{O}_2$  (b). Cyclic voltammograms (three cycles) w/o  $\text{H}_2\text{O}_2$  (c) and w/ 100  $\mu\text{M}$   $\text{H}_2\text{O}_2$  (d) after pretreatment by 20 CV cycles from -0.8 V to 1 V in 0.5 M NaOH. The arrows in (d) describe the changes in heights of anodic and cathodic peak with ongoing cycling.



Hydrogen peroxide is widely present in human body with varying concentration. Hereby, the concentration ranges from sub-micromolar to roughly 100  $\mu\text{M}$ .<sup>274–276</sup> In wound fluids micromolar levels (e.g. 0.5–50  $\mu\text{M}$  found in zebrafish) of  $\text{H}_2\text{O}_2$  are common as well.<sup>245,277</sup> Therefore, metal-containing LCNF ideally should possess a dynamic detection range covering these levels. For testing the sensing ability of Pd-LCNFs, amperometry was carried out with electrodes EC pretreated with CV. A detection potential of -0.5 V was set due to the appearance of a hydrogen peroxide peak at approximately this potential at previous mentioned CV studies (Figure 5.3b+d). This detection potential has shown up to be also ideal for Fe-LCNFs due to the appearance of a small peak from hydrogen peroxide compared to the control (data not shown).

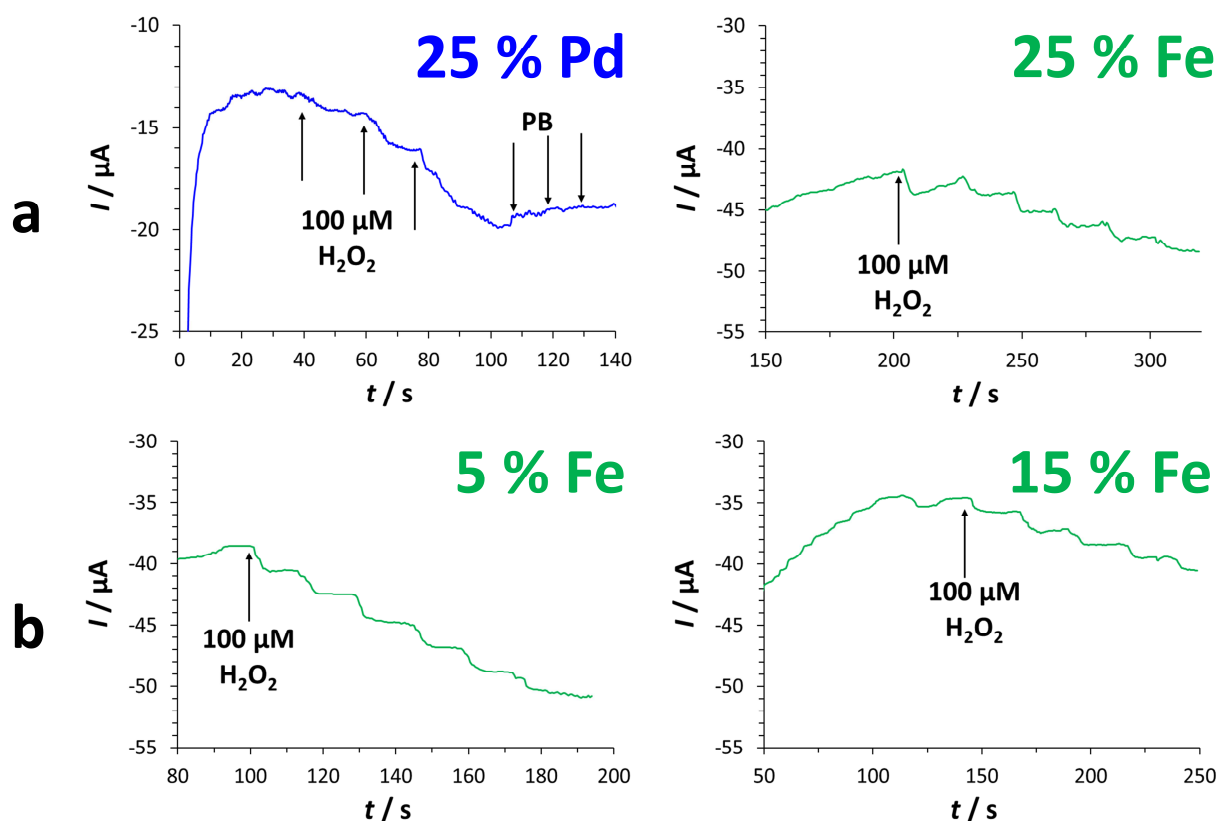


Figure 5.4: Amperometric response of LCNF containing 25 % Pd, 25 % Fe (a), 5 % and 15 % Fe (b) towards successive 100  $\mu\text{M}$   $\text{H}_2\text{O}_2$  addition. The potential was fixed at -0.5 V and the detection matrix consisted of 0.1 M PB.

As presented in Figure 5.4a, the electrochemical signal towards multiple  $\text{H}_2\text{O}_2$  injections is very low but differentiable from phosphate buffer (PB), which did not result in significant signal change. Compared to 25 % Fe-LCNF, the signal height is in the similar range (1–2  $\mu\text{A}$  per 100  $\mu\text{M}$   $\text{H}_2\text{O}_2$  injection), which indicates, that the sensitivity of 25 % Pd did not get significantly enhanced after EC pretreatment even after peak appearance at cyclic voltammetry. Additionally, the amperometric responses does not seem to essentially change with varying metal concentration in LCNF as demonstrated by the amperograms of 5/15 % Fe (Figure 5.4b). This implies that both

metals could still not be present in the proper oxidation state for hydrogen peroxide reduction or that the metal particles are not accessible for analyte molecules.

### 5.4.3 Chemical Reduction of Metal Compounds in LCNF

It is commonly known that the reduction of a variety of metal salts can be achieved by sodium borohydride.<sup>278</sup> Thus, to study if electrochemical sensitivity of Fe- or Pd-LCNF is prevented by the oxidation state of the respective metal, chemical reduction was carried out by incubating LCNF electrodes in NaBH<sub>4</sub> solutions for 3 hours and 24 hours. It was observed that Fe-LCNFs provide no difference in signal response towards 100  $\mu$ M hydrogen peroxide injection after NaBH<sub>4</sub> treatment (Figure 5.5). For Pd-LCNF the signal increases for electrodes incubated for 3 h in NaBH<sub>4</sub> and decreases to lower values for 24 h compared to untreated ones. This leads to the possibilities that iron is not available for reduction (embedded in the matrix) or already in low oxidation state and palladium is getting reduced. For Pd-LCNFs with longer incubation times seem to negatively affect the electrocatalytic ability. It is, therefore, suggested to validate the magnitude of reduction by studying more incubation times between 3 h to 24 h. Mechanism studies including further electrochemical experiments could promote the elucidation of oxidation states.

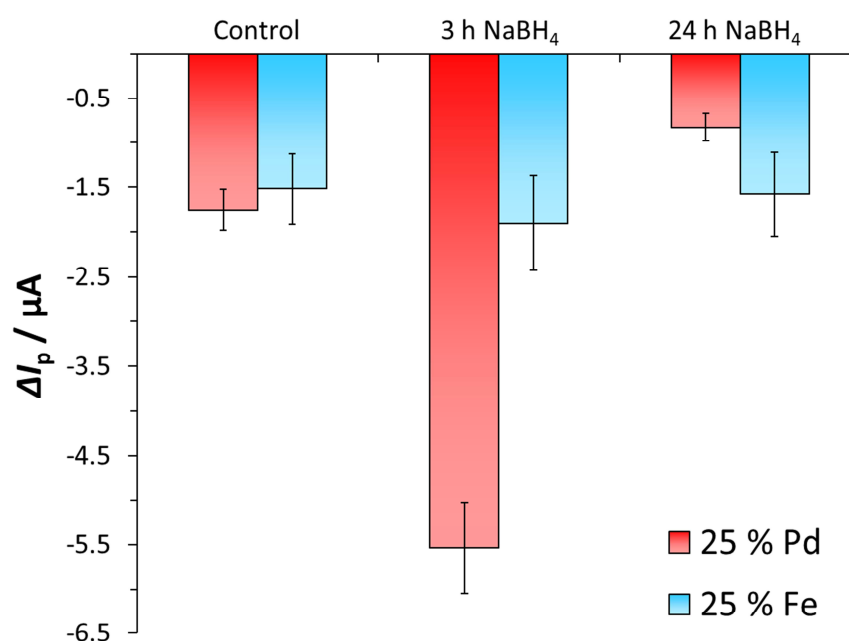


Figure 5.5: Amperometric response of LCNF electrodes containing 25 % Pd or Fe towards 100  $\mu$ M H<sub>2</sub>O<sub>2</sub> ( $n \geq 3$ ) after incubation 3 h and 24 h and without incubation.

### 5.4.4 Bimetallic LCNF hybrids

Bimetallic nanoparticle hybrids step into the focus because of their outstanding electrocatalytic characteristics derived from synergistic effects. Those make them surpass the monometallic counterparts in terms of analyte sensitivity/selectivity and higher stability against

deactivation.<sup>13,279</sup> Composites containing palladium and iron such as core-shell type<sup>280</sup> or alloy<sup>281</sup> have successfully been developed towards  $\text{H}_2\text{O}_2$  detection. Thus, Pd/Fe-LCNFs with mixed monometallic nanoparticles have been fabricated in order to improve sensing abilities and reach sensitivity levels required for real application. As the electrospinnability and carbonization ability of  $\text{Pd}(\text{acac})_2$  and  $\text{Fe}(\text{acac})_3$  containing nanofibers can still be achieved till 25 % content relative to the polymer mass, spinning solutions with 12.5 % content of each metal salt have been mixed and investigated.

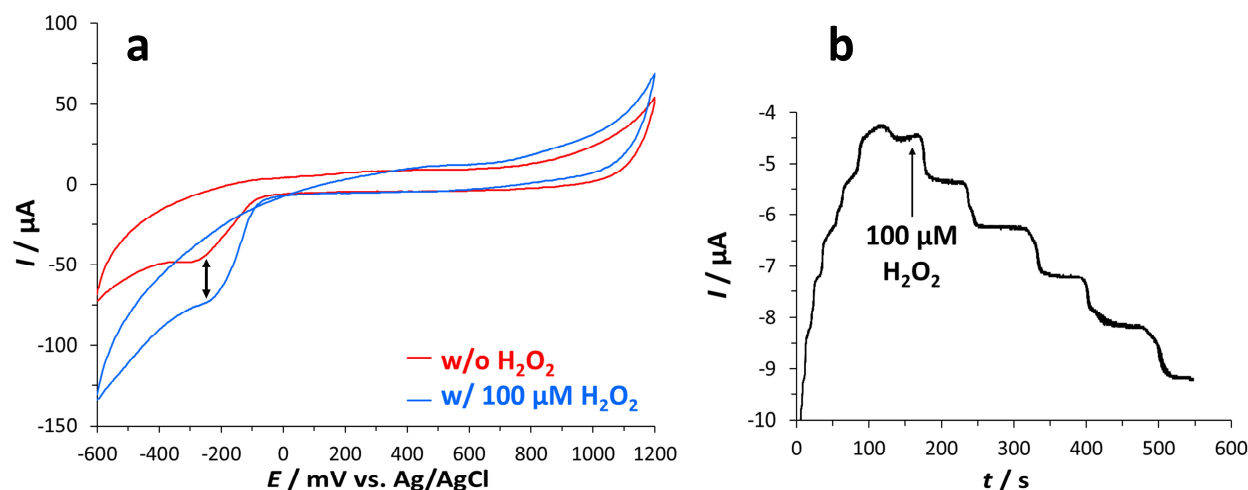


Figure 5.6: Cyclic voltammograms of Pd/Fe-LCNF electrodes containing 12.5 % of each metal salt in 0.1 M PB w/o and w/ 100  $\mu\text{M}$   $\text{H}_2\text{O}_2$  (a). The arrow indicates a current signal difference that can be linked to  $\text{H}_2\text{O}_2$ . Amperogram for 100  $\mu\text{M}$   $\text{H}_2\text{O}_2$  injections (b). The potential was fixed at -0.25 V and the detection matrix consisted of 0.1 M PB.

Electrospinning of solutions with Pd/Fe salts was not noticeably negatively affected by the presence of two metals and carbonization could successfully be carried out at 1.2 W laser power (data not shown). The catalytic abilities of Pd/Fe-LCNF electrodes were further evaluated with cyclic voltammetry where a current intensity difference for 100  $\mu\text{M}$   $\text{H}_2\text{O}_2$  compared to the control could be observed (Figure 5.6a, arrow). This indicates that the reduction peak potential for hydrogen peroxide can be decreased to ca. -250 mV compared to the range of ca. -600 mV to -450 mV (depending on the pretreatment method) for monometallic Pd- and Fe-LCNFs, respectively (Figure 5.3). A shift of the detection potential to lower relative values generally points to better electron transfer properties. This could point to a synergistic effect that is derived from close proximity of Pd and Fe, which results in a change of *d*-band structure that leads to overall better electrocatalytic performance.<sup>55,56</sup> The hydrogen peroxide detection ability was thus verified by amperometry at -0.25 V fixed potential. In Figure 5.6b it can be seen that Pd/Fe-LCNF exhibit a signal response towards 100  $\mu\text{M}$   $\text{H}_2\text{O}_2$  injections which cannot be achieved at relative potentials lower than -0.5 V by LCNFs containing just one of the metal salts (data not shown). However, the

ability to detect hydrogen peroxide at concentrations lower than 100  $\mu\text{M}$  is still not given after using two nanocatalysts, Pd and Fe, in LCNFs. Further studies such as investigating different metal combinations are necessary to improve the sensitivity of bimetallic LCNF hybrids.

## 5.5 Conclusion

The fabrication of carbon nanofibers by electrospinning with subsequent laser-induced carbonization was successfully implemented for nanofibers containing up to 25 % palladium and iron salt, respectively. Electrochemical pretreatment, either by applying constant potential or cyclic voltammetry cycling, could enhance the electrochemical sensing performance of LCNF electrodes towards  $\text{H}_2\text{O}_2$  detection. Further improvement could be achieved by chemical reduction of Pd-LCNFs but not for Fe-LCNFs. By preparation of bimetallic Pd/Fe-LCNF hybrids a synergistic effect is indicated by lower detection potential possibility compared to Pd alone (-0.25 V vs. -0.5 V). Unfortunately, LCNFs containing Fe, Pd or both so far are not able to detect  $\text{H}_2\text{O}_2$  at concentrations lower than 100  $\mu\text{M}$ , which is the crucial criteria for final sensor development that are supposed to apply for wound healing. Therefore, the sensitivity needs to be further improved. After this first goal has been achieved, the fabrication of free-standing LCNFs is desired. Those allow making sensor array patches with independent single array spots that would otherwise on ITO/PET substrate be electrically connected (short circuit). Additionally, the transfer on flexible and biocompatible material is easier possible for application as wearable. The single array spots are intend to recognize local  $\text{H}_2\text{O}_2$  changes, which would have then a high potential for healthcare purposes.

## 6 Conclusion and Future Perspectives

Nowadays, analytical biosensors must fulfill many requirements as they should be reliable, sensitive and easy to use on the one hand but also be long-time storable and affordable for everyone who is in need (i.e. sensors should be cheap) on the other hand. Regarding the detection of body metabolites whose unusual concentration values can indicate or result in disease development, conventional enzymatic approaches can only offer good selectivity and sensitivity but not the other mentioned aspects. Therefore, it draws the attention of many researchers to replace them with non-enzymatic materials acting as biorecognition element. Hereby, metal-based nanocatalysts are ideal candidates because of their magnificent conducting properties and electroanalytical sensitivity, depending on the choice of metal group (noble, non-noble, alloy or composite) and element. Regarding electrochemical sensing techniques, several advantages such as affordable equipment, fast and simple measurement procedures and the ability of detecting small response changes, make them attractive to meet the requirements. Carbon nanomaterials reached significant popularity as transducers as of their high electron transfer rates, mostly low production costs and easy processing. They offer several modification possibilities during or after synthesis and thus they are often utilized as matrix for anchoring or embedding nanocatalyst particles. Laser-induced carbonization gained large attention as method to generate conductive carbon nanomaterials at mass-scale with design flexibility of received electrodes. Many material precursors can be turned into carbonaceous structures but most often polyimide foils are employed.<sup>110,116,117</sup> It has been demonstrated that polyimide solutions can be doped with metal salts prior to drop-casting on foils and laser irradiation to receive laser-induced graphene (LIG) with incorporated metal nanoparticles.<sup>119</sup>

Chemical vapor deposition or electrospinning of nanofibers with subsequent thermal treatment steps have been established as two main routes to generate carbon nanofibers.<sup>133</sup> Both are laborious and require several rather slow heating steps. The equipment for those is relatively expensive due to the high-temperatures and vacuum conditions. Additionally, post processing to receive electrodes from as-prepared carbon nanofibers hinders scalability. Therefore, the aim of this work was to prepare carbon nanofibers by a completely new method. Here, the strategy of electrospinning polyimide nanofibers as carbon precursor with ensuing carbonization by CO<sub>2</sub>-laser was demonstrated.

First, parameters of the generation of electrospun nanofiber precursor were optimized. The respective thickness and density strongly correlates with the electrochemical properties obtained after laser scribing due to differences in porosity and, therefore, electroactive surface area. A

4 times increase compared to the geometric area of the electrode was achieved for the latter. The complete carbonization was confirmed by Raman spectroscopy by the presence of typical G, D and 2D bands and FTIR-ATR spectroscopy by the disappearance of peaks, originating from organic groups of the polymer, after lasing. Additionally, the morphology of laser-induced carbon nanofibers (LCNFs) can be tuned by varying the metal salt content, introduced during electrospinning by doping the polymer solution. It is assumed that the metal, here iron, contributes to the carbonization process by promoting heat transfer or adsorption. From the lasing parameters side, the energy input can, among others, be controlled by either lasing power and speed or changing the scribing strategy. During continuous scribing of several electrodes in one row the laser sweeps a line across a large range of all electrodes before moving to next line and, therefore, the starting point of the first electrode. When scribing discontinuously (just one electrode prior to the next), the sweeping lines are obviously shorter and hence the local heat input takes place in a shorter period. After optimization, LCNFs with outstanding electron transfer properties could be reliably generated. The reaction rate constant for redox marker and analyte (dopamine) was roughly one order of magnitude higher than those reported for CNFs fabricated by thermal treatment. A determined pore size of  $(4 \pm 1) \mu\text{m}$  for Fe-LCNFs is also one order of magnitude lower than for commercial graphene foam<sup>1</sup> resulting in significant more interaction sites. This makes LCNFs very promising as biosensing material as further evinced by model analytes NADH, hydrazine and dopamine whose detection was feasible with higher response and/or at lower potentials compared to commercial screen-printed carbon and gold electrodes.

Concrete biosensing abilities of LCNFs were thus further studied with focus on non-enzymatic catalysis. To achieve this goal, nickel salt was introduced into LCNF because of its well-known electrocatalytic glucose sensing mechanism<sup>216–218</sup> and due to the high relevance of glucose detection because of fast raising number of diabetic patients. Studying the morphology of LCNFs with varying metal content, similar heat distribution abilities as previously found for iron could be observed. Here, the morphology from 15 % Ni-containing LCNFs equaled those of 5 % Fe which suggests that different types of metal are able to transfer the generated heat during lasing to different extend. While the nickel content does not influence the electrospun nanofiber diameter noticeably, the expansion during carbonization is indeed affected. The highest spinnable metal content of 25 % Ni provided an increase of the fiber diameter by only 20 % compared to 160 % for 15 % Ni-containing LCNFs. By EDX mapping experiments it was proven that the molecular nickel distribution does not change after lasing process in contrast to carbon and oxygen, whose content increased and decreased, respectively. It was further confirmed with TEM images that the Ni nanoparticles did not agglomerate and were evenly dispersed with low particle diameters of

( $7.9 \pm 1.2$ ) nm within the LCNFs. Compared to carbon nanofibers gained by thermal carbonization (50 nm),<sup>136</sup> the diameter is significantly smaller which contributes to powerful catalytic properties. TEM images additionally gave a hint that solid electrospun nanofibers turn to hollow-like LCNFs during laser irradiation, which is a highly desirable feature due to more interaction sites also at the inside walls of nanofibers. The necessary investigations via electron tomography<sup>207</sup> have to be performed in order to confirm this assumption. As a crystal lattice of nickel nanoparticles could not be observed by TEM, and XRD measurements could not resolve a crystal structure (data not shown), it is assumed by now that the metal is present in amorphous structure which is in contrast to the results of Ye *et al.* who also embedded different metal acetylacetonates but in LIG.<sup>119</sup> Carrying out additional XRD experiments is recommended to possibly answer this question and also to prove the oxidation state of the metal after lasing.

For potential application *in situ*, it must be ensured that metal particles, which could cause toxic effects when entering the human metabolism, do not detach from the sensor matrix. Hence, the stable adhesion of nickel nanoparticles to LCNFs was tested by EDX measurements of the metal content before and after shaking incubation of electrodes. In contrast to electrodeposited nickel, which almost completely detached, the nickel content in LCNFs introduced during electrospinning did remain unchanged after shaking in phosphate buffer at 37 °C for five hours. The LCNF network itself possesses adequate mechanical stability, as observed from SEM images that indicate no obvious change in morphology after electrochemical measurement at stirred conditions. These results are very promising for realizing application of metal nanocatalyst containing LCNFs at real biological conditions. By cyclic voltammetry studies the sensing mechanism of glucose was revealed and amperometric detection of glucose was successfully carried out. The sensitivity enhancement with increasing nickel concentrations in LCNFs is way higher than the respective rise in electroactive surface area. This suggests that not only the better fibrosity obtained for 25 % nickel-containing LCNFs but also the catalytic ability derived from metal nanoparticles are responsible for analyte sensitivity. With electrodes containing 25 % nickel an excellent sensitivity up to  $2,092 \mu\text{A} \cdot \text{mM}^{-1} \cdot \text{cm}^{-2}$  and a limit of detection of  $0.3 \mu\text{M}$  was reached for the linear ranges of 10-100  $\mu\text{M}$  and 100  $\mu\text{M}$  to 5 mM, which covers the levels of glucose in human body fluids such as blood. Possible interferents that are normally present in real matrices, e.g. uric acid and ascorbic acid, did not lead to a significant electrochemical signal at their relevant concentrations. Also, high salt concentrations of 250 mM NaCl, which are often an issue for non-enzymatic electrochemical sensors,<sup>214,220,221</sup> did not poison the LCNF electrodes.

The concept of generating LCNFs with different catalytic functionalities was further taken up by studies towards hydrogen peroxide sensing. The final goal here was the development of a sensor



array patch that can be mounted on wounded human body parts and monitor local  $\text{H}_2\text{O}_2$  concentrations, as the molecule plays an important role in wound healing. Palladium and iron have been chosen as metal salts due to their well-known catalytic abilities towards  $\text{H}_2\text{O}_2$  detection.<sup>251,263–265</sup> With the expertise gained from previous studies, the carbonization of LCNFs containing up to 25 % palladium or iron could be achieved. It was found that the electrochemical sensing performance of palladium-containing LCNFs could be enhanced by either application of a negative constant potential for a certain time (-1 V for 3 min) or multiple cyclic voltammetry runs prior to amperometric  $\text{H}_2\text{O}_2$  measurements. As the sensitivity was still not satisfying, it was assumed that the metal needs to be completely chemically reduced to enable hydrogen peroxide reduction. Therefore, palladium- and iron-containing LCNF electrodes were incubated in  $\text{NaBH}_4$  (reducing agent) solutions. The amperometric response of Fe-LCNFs towards  $\text{H}_2\text{O}_2$  did not change after 3 and 24 hours incubation, whereas for Pd-LCNFs it did increase for 3 h and then decrease again for 24 h incubation. These results could indicate that iron is already present at lowest oxidation state while palladium is not. XRD measurements could be helpful to resolve the molecular structure and, therefore, draw conclusions on the oxidation state. The incubation time between 3-24 h for Pd-LCNFs should be also further evaluated and optimized to maximize the reduction degree.

Combining Pd and Fe salts in LCNFs did result in decreased detection potential which could be a first hint that a synergistic effect between both metals arose. Still, the lowest detectable concentration of 100  $\mu\text{M}$   $\text{H}_2\text{O}_2$  could not be undercut. Before generation of sensor arrays, LCNFs should be further improved to facilitate detection between low micromolar and 100  $\mu\text{M}$  which are the levels commonly present in wounds.<sup>245,277</sup> In the next steps, electron microscopy should be performed to compare morphological differences that could be linked to electrochemical behavior. Hereby, it is suggested to compare electrodes that offered good hydrogen peroxide response with poor ones after prior electrochemical experiments. Additionally, the morphology of Ni-LCNFs that already own excellent catalytic properties could serve as reference. With respect to nanocatalyst particles, TEM imaging in combination with tomography could enlighten if those are freely available on the surface or hidden in the carbon matrix which would negatively affect electrocatalytic behavior. Also, the distribution, in particular agglomeration, is an aspect that needs to be clarified. Strategies that potentially change metal dispersion or allow the directed settling of nanoparticles on nanofiber surfaces include the change of spinning composition (e.g. other carbon precursor polymer or switching solvent) and core-shell electrospinning, respectively. A feasible synergistic effect by creating bimetallic LCNFs necessitates more investigation. Here, several metal combinations with platinum, gold or silver could be tested as those offer catalytic activity

towards  $\text{H}_2\text{O}_2$  as well.<sup>252–261</sup> Likewise, the ratio of different metal catalysts could have an impact on electrospinning leading to changes in nanofiber morphology but also agglomeration and non-homogeneous distribution of the nanoparticles in the nanofibers. Additionally, the electronic *d*-band structures, and hence catalytic abilities, might significantly change in dependency of the types and ratios of metals unified in LCNFs.<sup>55,56</sup> As a consequence, additional comprehensive studies would need to be carried out. Nickel hexacyanoferrate, a Prussian blue analogue, offers redox mediator characteristics and catalytic reduction ability towards hydrogen peroxide, while being significantly more chemically stable compared to Prussian blue which is attributed to the replacement of some  $\text{Fe}^{3+}$  ions by  $\text{Ni}^{2+}$ .<sup>282–284</sup> As demonstrated in chapter 4, nickel hexacyanoferrate can be formed on Ni-LCNFs by cyclic voltammetry cycling with solutions containing  $[\text{Fe}(\text{CN})_6]^{4-/3-}$ . The as-prepared composite could further be investigated towards electroanalytical hydrogen peroxide sensitivity as well.

The overall investigations lead to the conclusion that carbon nanofibers containing different catalytic functionalities can be fabricated in a facile and cheap (\$0.07 material costs per electrode) manner by laser-induced carbonization of electrospun polyimide nanofibers doped with metal salts. Design flexibility of electrodes, simple miniaturization ability and large-scale production are key benefits over traditional CNF synthesis methods CVD and thermal carbonization. Therefore, besides electrochemical sensing, the developed strategy is also appropriate for creating materials applicable for catalytic synthesis or energy storage. For the future, besides wearable patches of free-standing LCNFS, several application possibilities are proposed e.g. gas sensing in industry or breath analysis, which is conceivable due to the highly porous nature of LCNFs. The already proven ability of cells to grow on laser-induced carbon<sup>142</sup> facilitates the fabrication of cellular assays or the utilization as scaffolds in (bio)medicine. Further, already derived projects including the fabrication of LCNF-based microfluidic chips have great potential for the development of miniaturized point-of-care sensors.



## 7 Summary

The development of electrochemical sensors utilizing non-enzymatic detection strategies is a topic of high interest for many researchers in order to replace classic expensive and less stable enzymatic approaches. In this thesis, recent developments in non-enzymatic sensing were reviewed. The general principles of (nano)catalysis and preparation of nanomaterials were discussed focusing on carbon materials and metal-based catalysts. Carbon nanomaterials stand out for their great electron transfer properties and, especially for nanofibers, high surface-to-volume ratio with multiple analyte interaction sites. Doping carbon nanofibers with heteroatoms or metal nanoparticles further introduces nanocatalytic functionalities. Hereby, the type of atom and metal, respectively, determines the selectivity as well as sensitivity of the generated composite. The fabrication of laser-induced carbon materials was quite recently found to be a simple and effective way to receive such hybrids. In this regard, several substrates are suitable for being carbonized e.g. polymer films containing metal salts. Already constructed non-enzymatic platforms, based on laser-induced graphene, for sensing in aqueous solution but also with gaseous analytes were presented. The current achievements in wearables were emphasized which guide the prospective trends. Concluding, the key aspects were summarized and thoughts on improvements and suggestion for future evolvments were shared.

In this thesis the strategy of one-step laser-carbonization of electrospun nanofibers to obtain carbon nanofibers was developed as a superior process over traditional chemical vapor deposition and thermal carbonization of electrospun nanofibers which are laborious, time-consuming and inflexible. Polyimide, more precisely Matrimid<sup>®</sup> 5218, served as carbon precursor and polymer solutions of it were electrospun into nanofiber mats. Afterwards, carbon nanofibers were prepared in a facile manner via direct lasing on as-spun mats at ambient conditions with a CO<sub>2</sub>-laser. This method allows the generation of electrodes with any design and shape controlled by PC software. Compared to both mentioned conventional procedures, large-scale production of carbon nanofibers at affordable costs is possible in a short time.

The morphology of laser-induced carbon nanofibers (LCNFs) can not only be controlled by lasing parameters such as laser power and speed. During electrospinning, metal nanoparticles can be incorporated into nanofibers by simply doping the spinning solutions with metal salt e.g. iron(III) acetylacetonate before. This metal, as studied for iron, additionally contributes to the homogeneous carbonization during lasing process by a kind of heat transfer ability. Therefore, the respective metal content relative to the polymer also enables tuning of the obtained LCNF morphology. Continuously scribing of several electrodes in a row vs. discontinuously i.e. one

electrode prior to the next also has a huge impact on the heat input because of different durations of scribing one line. It was demonstrated that the electrochemical properties of LCNF electrodes can be optimized due to the direct link to the morphology or rather electrochemical surface area. The latter was found to be much greater than the geometric area. The 3D porous network structure of LCNFs with an average pore size in low micrometer range facilitates interaction with molecules in aqueous solution and hence allows high electron transfer rates, which was displayed by very low peak-to-peak separations, as studied with  $[\text{Fe}(\text{CN})_6]^{4-/3-}$  redox marker.

The type of metal salt incorporated in LCNFs defines its catalytic properties. Nickel salt can be evenly embedded into carbon matrix with low nanometer nanoparticle size. The electrospun nanofiber diameter does not change with varying nickel content. However, it was shown that the expansion of nanofibers during carbonization is influenced assumedly by the mentioned heat transfer ability. A significant smaller increase of LCNF diameter compared to electrospun nanofibers was achieved with increasing the nickel content, which resulted in better fibrosity. In contrast to electrodeposited nickel particles, it was evinced that nickel in LCNFs is stably adhered to the carbon and does not leach out during several hours of shaking incubation in phosphate buffer at body temperature. Prevented desorption of potential toxic metals brings the application of LCNFs *in vivo* one step closer. With its catalytic behavior towards glucose, Ni-LCNF was utilized for amperometric glucose sensing. The electroanalytical performance with a high sensitivity and a low limit of detection turned out to be excellent and the linear range covers the real glucose levels in blood. Further, ascorbic acid and uric acid did not produce interference at their relevant levels. Those great electrochemical characteristics are attributed to derive from nickel nanocatalyst on the one hand and 3D fibrosity on the other hand. Electron microscopic images gave a hint that LCNFs could be hollow which additionally could increase the interaction of catalyst nanoparticles with analytes in solution but also gaseous molecule samples.

With focus on catalysis, LCNFs with several different metals can be created to enable a variety of application possibilities. Palladium-containing LCNFs were furthermore prepared in order to electrochemically detect hydrogen peroxide. In this experiments, the amperometric sensitivity towards  $\text{H}_2\text{O}_2$  was enhanced by improving the electrochemical properties of Pd-LCNF either electrochemically by cyclic voltammetry cycling, application of a constant negative potential or chemically by reduction during incubating Pd-LCNF electrodes in  $\text{NaBH}_4$  solutions for some hours. By fabrication of bimetallic Pd/Fe-LCNF hybrids, the detection potential of  $\text{H}_2\text{O}_2$  could be significantly reduced which gives a first hint on successful achievement of a synergistic effect. As these investigations were only preliminary ones, further optimizations to reach low micromolar limit of detection prior to final sensor development have to be carried out.

## 8 Zusammenfassung

Die Entwicklung elektrochemischer Sensoren unter Verwendung nichtenzymatischer Nachweisstrategien ist für viele Forscher ein Thema von großem Interesse, um klassische teure und weniger stabile enzymatische Ansätze zu ersetzen. In dieser Dissertation wurden aktuelle Entwicklungen in der nichtenzymatischen Sensorik rezensiert. Die allgemeinen Prinzipien der (Nano-)Katalyse und Herstellung von Nanomaterialien wurden diskutiert, wobei der Schwerpunkt auf Kohlenstoffmaterialien und Katalysatoren auf Metallbasis lag. Kohlenstoffnanomaterialien zeichnen sich durch ihre hervorragenden Elektronentransfereigenschaften und, insbesondere bei Nanofasern, ein hohes Verhältnis von Oberfläche zu Volumen mit mehreren Analytwechselwirkungsstellen aus. Das Dotieren von Kohlenstoffnanofasern mit Heteroatomen oder Metallnanopartikeln führt ferner nanokatalytische Funktionalitäten ein. Hierbei bestimmt die Art des Atoms bzw. des Metalls die Selektivität sowie die Empfindlichkeit des erzeugten Verbundstoffs. Die Herstellung von laserinduzierten Kohlenstoffmaterialien hat sich vor kurzem als einfacher und effektiver Weg erwiesen solche Hybride zu erhalten. In dieser Hinsicht eignen sich mehrere Substrate zum Karbonisieren, z. B. Polymerfilme, die Metallsalze enthalten. Es wurden bereits entwickelte nichtenzymatische Plattformen auf Basis von laserinduziertem Graphen für Messungen in wässriger Lösung, aber auch mit gasförmigen Analyten vorgestellt. Hervorgehoben wurden die aktuellen Erfolge bei Sensoren die am Körper getragen werden und die die voraussichtlichen Trends bestimmen. Abschließend wurden die wichtigsten Aspekte zusammengefasst und Gedanken zu Verbesserungen sowie Vorschläge für zukünftige Entwicklungen geteilt.

In dieser Arbeit wurde die Strategie der einstufigen Laserkarbonisierung von elektrogesponnenen Nanofasern zur Gewinnung von Kohlenstoffnanofasern als überlegenes Verfahren gegenüber der herkömmlichen chemischen Gasphasenabscheidung und thermischen Karbonisierung von elektrogesponnenen Nanofasern entwickelt, welche mühsam, zeitaufwendig und unflexibel sind. Polyimid, genauer gesagt Matrimid® 5218, diente als Kohlenstoffvorläufer und Polymerlösungen davon wurden zu Nanofasermatten elektrogesponnen. Anschließend wurden Kohlenstoffnanofasern auf einfache Weise, durch direktes Lasern auf gesponnenen Matten bei Umgebungsbedingungen, mit einem CO<sub>2</sub>-Laser hergestellt. Diese Methode ermöglicht die Erzeugung von Elektroden in jedem Design und jeder Form, die durch PC-Software gesteuert werden können. Im Vergleich zu beiden genannten konventionellen Verfahren ist eine großtechnische Herstellung von Kohlenstoffnanofasern zu erschwinglichen Kosten in kurzer Zeit möglich.

Die Morphologie von laserinduzierten Kohlenstoffnanofasern (LCNFs) kann nicht nur durch Laserparameter wie Laserleistung und Geschwindigkeit gesteuert werden. Während des Elektrosinnens können Metallnanopartikel in Nanofasern eingebaut werden, indem die Spinnlösungen einfach mit Metallsalz, z.B. Eisen(III)-acetylacetonat, zuvor dotiert werden. Dieses Metall, wie es für Eisen untersucht wurde, trägt zusätzlich zur homogenen Karbonisierung während des Laserprozesses durch eine Art Wärmeübertragungsfähigkeit bei. Daher ermöglicht der jeweilige Metallgehalt relativ zum Polymer auch die Abstimmung der erhaltenen LCNF-Morphologie. Das kontinuierliche Schreiben mehrerer Elektroden in einer Reihe gegenüber dem diskontinuierlichen Schreiben, d.h. eine Elektrode vor der nächsten, hat aufgrund der unterschiedlichen Dauer des Schreibens einer Linie ebenfalls einen großen Einfluss auf den Wärmeeintrag. Es wurde gezeigt, dass die elektrochemischen Eigenschaften von LCNF-Elektroden aufgrund der direkten Verbindung zur Morphologie, oder vielmehr zur elektrochemischen Oberfläche, optimiert werden können. Letztere erwies sich als viel größer als die geometrische Fläche. Die poröse 3D-Netzwerkstruktur von LCNFs mit einer durchschnittlichen Porengröße im niedrigen Mikrometerbereich erleichtert die Wechselwirkung mit Molekülen in wässriger Lösung und ermöglicht daher hohe Elektronentransferraten, was durch sehr niedrige Peak-zu-Peak-Abstände für  $[\text{Fe}(\text{CN})_6]^{4-/3-}$  Redoxmarker gezeigt wurde.

Die Art des, in LCNFs enthaltenen, Metallsalzes definiert deren katalytischen Eigenschaften. Nickelsalz kann mit einer Nanopartikelgröße in niedrigen Nanometerbereich gleichmäßig in eine Kohlenstoffmatrix eingebettet werden. Der elektrogewonnene Nanofaserdurchmesser ändert sich nicht mit variierendem Nickelgehalt. Es wurde jedoch gezeigt, dass die Expansion von Nanofasern während der Karbonisierung, vermutlich durch die erwähnte Wärmeübertragungsfähigkeit, beeinflusst wird. Eine signifikant geringe Zunahme des LCNF-Durchmessers im Vergleich zu elektrogewonnenen Nanofasern wurde mit zunehmendem Nickelgehalt erreicht, was zu besserer Faserigkeit führte. Im Gegensatz zu galvanisch abgeschiedenen Nickelpartikeln wurde gezeigt, dass Nickel in LCNFs stabil am Kohlenstoff haftet und während mehrerer Stunden Schüttelinkubation in Phosphatpuffer bei Körpertemperatur nicht auslaugt. Die verhinderte Desorption potenziell toxischer Metalle bringt die Anwendung von LCNFs *in vivo* einen Schritt näher. Aufgrund seines katalytischen Verhaltens gegenüber Glukose wurde Ni-LCNF zur amperometrischen Glukosemessung verwendet. Die elektroanalytische Leistung mit einer hohen Empfindlichkeit und einer niedrigen Nachweisgrenze erwies sich als exzellent und der lineare Bereich deckt den tatsächlichen Glukosespiegel im Blut ab. Ferner erzeugten Ascorbinsäure und Harnsäure in ihren relevanten Mengen keine Störsignale. Diese großartigen elektrochemischen Eigenschaften werden einerseits auf den Nickel-Nanokatalysator und andererseits auf die 3D-

Faserigkeit zurückgeführt. Elektronenmikroskopische Bilder gaben einen Hinweis darauf, dass LNCFs hohl sein könnten, was zusätzlich die Wechselwirkung von Katalysator-Nanopartikeln mit Analyten in Lösung, aber auch gasförmigen Molekülproben erhöhen könnte.

Mit Schwerpunkt auf der Katalyse können LCNFs mit mehreren verschiedenen Metallen erstellt werden, um eine Vielzahl von Anwendungsmöglichkeiten zu ermöglichen. Palladiumhaltige LCNFs wurden ferner präpariert, um Wasserstoffperoxid elektrochemisch nachzuweisen. In diesen Experimenten wurde die amperometrische Empfindlichkeit gegenüber  $\text{H}_2\text{O}_2$  erhöht, indem die elektrochemischen Eigenschaften von Pd-LCNF entweder elektrochemisch durch Cyclovoltammetriezyklen, Anlegen eines konstanten negativen Potentials oder chemisch durch Reduktion während der Inkubation von Pd-LCNF-Elektroden in  $\text{NaBH}_4$ -Lösungen für einige Stunden, verbessert wurden. Durch die Herstellung von Bimetall-Pd/Fe-LCNF-Hybriden konnte das Nachweispotential von  $\text{H}_2\text{O}_2$  signifikant reduziert werden, was einen ersten Hinweis auf die erfolgreiche Erzielung eines synergistischen Effekts gibt. Da es sich bei diesen Untersuchungen nur um vorläufige handelt, müssen weitere Optimierungen durchgeführt werden, um die untere mikromolare Nachweisgrenze vor der endgültigen Sensorentwicklung zu erreichen.





## 9 References

- (1) Dong, X.; Wang, X.; Wang, L.; Song, H.; Zhang, H.; Huang, W.; Chen, P. 3D Graphene Foam as a Monolithic and Macroporous Carbon Electrode for Electrochemical Sensing. *ACS Appl. Mater. Interfaces* **2012**, 4 (6), 3129–3133.
- (2) Wongkaew, N.; Simsek, M.; Griesche, C.; Baeumner, A. J. Functional Nanomaterials and Nanostructures Enhancing Electrochemical Biosensors and Lab-on-a-Chip Performances: Recent Progress, Applications, and Future Perspective. *Chem. Rev.* **2018**, 119, 120–194.
- (3) Inzelt, G.; Lewenstam, A.; Scholz, F. *Handbook of Reference Electrodes*; Springer Berlin Heidelberg, 2013.
- (4) Benck, J. D.; Pinaud, B. A.; Gorlin, Y.; Jaramillo, T. F. Substrate Selection for Fundamental Studies of Electrocatalysts and Photoelectrodes: Inert Potential Windows in Acidic, Neutral, and Basic Electrolyte. *PLoS One* **2014**, 9 (10).
- (5) Wang, K.; Wu, H.; Meng, Y.; Zhang, Y.; Wei, Z. Integrated Energy Storage and Electrochromic Function in One Flexible Device: An Energy Storage Smart Window. *Energy Environ. Sci.* **2012**, 5 (8), 8384–8389.
- (6) Pravda, M. Analytical Methods | Electrochemical Analysis. In *Encyclopedia of Dairy Sciences*; Fuquay, J. W., Ed.; Academic Press: San Diego, 2011; pp 193–197.
- (7) Kimmel, D. W.; LeBlanc, G.; Meschievitz, M. E.; Cliffel, D. E. Electrochemical Sensors and Biosensors. *Anal. Chem.* **2012**, 84 (2), 685–707.
- (8) Amine, A.; Mohammadi, H. Amperometry☆. In *Encyclopedia of Analytical Science*; Worsfold, P., Poole, C., Townshend, A., Miró, M., Eds.; Academic Press: Oxford, 2019; pp 85–98.
- (9) Elgrishi, N.; Rountree, K. J.; McCarthy, B. D.; Rountree, E. S.; Eisenhart, T. T.; Dempsey, J. L. A Practical Beginner's Guide to Cyclic Voltammetry. *J. Chem. Educ.* **2018**, 95 (2), 197–206.
- (10) Kounaves, S. P. Voltammetric Techniques. In *Handbook of Instrumental Techniques for Analytical Chemistry*; Prentice Hall, Upper Saddle River, NJ, 1997; pp 709–726.
- (11) Shadlaghani, A.; Farzaneh, M.; Kinser, D.; Reid, C. R. Direct Electrochemical Detection of Glutamate, Acetylcholine, Choline, and Adenosine Using Non-Enzymatic Electrodes. *Sensors* **2019**, 19 (3), 447.

- (12) Hwang, D.-W.; Lee, S.; Seo, M.; Chung, T. D. Recent Advances in Electrochemical Non-Enzymatic Glucose Sensors – A Review. *Anal. Chim. Acta* **2018**, *1033*, 1–34.
- (13) Dhara, K.; Mahapatra, D. R. Recent Advances in Electrochemical Nonenzymatic Hydrogen Peroxide Sensors Based on Nanomaterials: A Review. *J. Mater. Sci.* **2019**, *54* (19), 12319–12357.
- (14) Tang, J.; Tang, D. Non-Enzymatic Electrochemical Immunoassay Using Noble Metal Nanoparticles: A Review. *Microchim. Acta* **2015**, *182* (13), 2077–2089.
- (15) Zhu, H.; Li, L.; Zhou, W.; Shao, Z.; Chen, X. Advances in Non-Enzymatic Glucose Sensors Based on Metal Oxides. *J. Mater. Chem. B* **2016**, *4*, 7333–7349.
- (16) Park, S.; Jeong, R.-A.; Boo, H.; Park, J.; Kim, H. C.; Chung, T. D. Nonenzymatic Continuous Glucose Monitoring in Human Whole Blood Using Electrified Nanoporous Pt. *Biosens. Bioelectron.* **2012**, *31*, 284–291.
- (17) Zhu, X.; Ju, Y.; Chen, J.; Liu, D.; Liu, H. Nonenzymatic Wearable Sensor for Electrochemical Analysis of Perspiration Glucose. *ACS Sensors* **2018**, *3*, 1135–1141.
- (18) An, K.; Somorjai, G. A. Size and Shape Control of Metal Nanoparticles for Reaction Selectivity in Catalysis. *ChemCatChem* **2012**, *4* (10), 1512–1524.
- (19) Thiruvengadathan, R.; Korampally, V.; Ghosh, A.; Chanda, N.; Gangopadhyay, K.; Gangopadhyay, S. Nanomaterial Processing Using Self-Assembly-Bottom-up Chemical and Biological Approaches. *Reports Prog. Phys.* **2013**, *76* (6), 066501.
- (20) Sattler, K. D. *Handbook of Nanophysics: Nanoparticles and Quantum Dots*; Handbook of Nanophysics; CRC Press, 2016.
- (21) Zaidi, S. A.; Shin, J. H. Recent Developments in Nanostructure Based Electrochemical Glucose Sensors. *Talanta* **2016**, *149*, 30–42.
- (22) Cao, S.; Tao, F. (Feng); Tang, Y.; Li, Y.; Yu, J. Size- and Shape-Dependent Catalytic Performances of Oxidation and Reduction Reactions on Nanocatalysts. *Chem. Soc. Rev.* **2016**, *45* (17), 4747–4765.
- (23) Haruta, M. When Gold Is Not Noble: Catalysis by Nanoparticles. *Chem. Rec.* **2003**, *3* (2), 75–87.
- (24) Kang, Y.; Yang, P.; Markovic, N. M.; Stamenkovic, V. R. Shaping Electrocatalysis through Tailored Nanomaterials. *Nano Today* **2016**, *11* (5), 587–600.

- (25) Sánchez-Sánchez, C. M.; Solla-Gullón, J.; Vidal-Iglesias, F. J.; Aldaz, A.; Montiel, V.; Herrero, E. Imaging Structure Sensitive Catalysis on Different Shape-Controlled Platinum Nanoparticles. *J. Am. Chem. Soc.* **2010**, *132* (16), 5622–5624.
- (26) Solla-Gullón, J.; Vidal-Iglesias, F. J.; Feliu, J. M. Shape Dependent Electrocatalysis. *Annu. Rep. Prog. Chem., Sect. C* **2011**, *107*, 263–297.
- (27) Rao, C. N. R.; Kulkarni, G. U.; Thomas, P. J.; Edwards, P. P. Metal Nanoparticles and Their Assemblies. *Chem. Soc. Rev.* **2000**, *29*, 27–35.
- (28) Thota, S.; Crans, D. C. *Metal Nanoparticles: Synthesis and Applications in Pharmaceutical Sciences*; Wiley, 2018.
- (29) Wang, Z.; Hu, T.; Liang, R.; Wei, M. Application of Zero-Dimensional Nanomaterials in Biosensing. *Front. Chem.* **2020**, *8*, 320.
- (30) Singh, S.; Kumar, N.; Kumar, M.; Jyoti; Agarwal, A.; Mizaikoff, B. Electrochemical Sensing and Remediation of 4-Nitrophenol Using Bio-Synthesized Copper Oxide Nanoparticles. *Chem. Eng. J.* **2017**, *313*, 283–292.
- (31) Xi, J.; Xie, C.; Zhang, Y.; Wang, L.; Xiao, J.; Duan, X.; Ren, J.; Xiao, F.; Wang, S. Pd Nanoparticles Decorated N-Doped Graphene Quantum Dots@N-Doped Carbon Hollow Nanospheres with High Electrochemical Sensing Performance in Cancer Detection. *ACS Appl. Mater. Interfaces* **2016**, *8* (34), 22563–22573.
- (32) Jaroenapibal, P.; Boonma, P.; Saksilaporn, N.; Horprathum, M.; Amornkitbamrung, V.; Triroj, N. Improved NO<sub>2</sub> Sensing Performance of Electrospun WO<sub>3</sub> Nanofibers with Silver Doping. *Sensors Actuators B Chem.* **2018**, *255*, 1831–1840.
- (33) Sekar, A. D.; Kumar, V.; Muthukumar, H.; Gopinath, P.; Matheswaran, M. Electrospinning of Fe-Doped ZnO Nanoparticles Incorporated Polyvinyl Alcohol Nanofibers for Its Antibacterial Treatment and Cytotoxic Studies. *Eur. Polym. J.* **2019**, *118*, 27–35.
- (34) Bagheri, H.; Hajian, A.; Rezaei, M.; Shirzadmehr, A. Composite of Cu Metal Nanoparticles-Multiwall Carbon Nanotubes-Reduced Graphene Oxide as a Novel and High Performance Platform of the Electrochemical Sensor for Simultaneous Determination of Nitrite and Nitrate. *J. Hazard. Mater.* **2017**, *324*, 762–772.

- (35) Arvand, M.; Sayyar Ardaki, M. Poly-L-Cysteine/Electrospun Copper Oxide Nanofibers-Zinc Oxide Nanoparticles Nanocomposite as Sensing Element of an Electrochemical Sensor for Simultaneous Determination of Adenine and Guanine in Biological Samples and Evaluation of Damage to DsDNA and DNA purine bases by UV radiation. *Anal. Chim. Acta* **2017**, *986*, 25–41.
- (36) Zhou, W.-H.; Wang, H.-H.; Li, W.-T.; Guo, X.-C.; Kou, D.-X.; Zhou, Z.-J.; Meng, Y.-N.; Tian, Q.-W.; Wu, S.-X. Gold Nanoparticles Sensitized ZnO Nanorods Arrays for Dopamine Electrochemical Sensing. *J. Electrochem. Soc.* **2018**, *165* (12), G3001–G3007.
- (37) Wang, N.; Lin, M.; Dai, H.; Ma, H. Functionalized Gold Nanoparticles/Reduced Graphene Oxide Nanocomposites for Ultrasensitive Electrochemical Sensing of Mercury Ions Based on Thymine–Mercury–Thymine Structure. *Biosens. Bioelectron.* **2016**, *79*, 320–326.
- (38) Sapountzi, E.; Braiek, M.; Vocanson, F.; Chateaux, J.-F.; Jaffrezic-Renault, N.; Lagarde, F. Gold Nanoparticles Assembly on Electrospun Poly(Vinyl Alcohol)/Poly(Ethyleneimine)/Glucose Oxidase Nanofibers for Ultrasensitive Electrochemical Glucose Biosensing. *Sensors Actuators B Chem.* **2017**, *238*, 392–401.
- (39) Guler, M.; Turkoglu, V.; Bulut, A.; Zahmakiran, M. Electrochemical Sensing of Hydrogen Peroxide Using Pd@Ag Bimetallic Nanoparticles Decorated Functionalized Reduced Graphene Oxide. *Electrochim. Acta* **2018**, *263*, 118–126.
- (40) Li, X.; Du, X. Molybdenum Disulfide Nanosheets Supported Au-Pd Bimetallic Nanoparticles for Non-Enzymatic Electrochemical Sensing of Hydrogen Peroxide and Glucose. *Sensors Actuators B Chem.* **2017**, *239*, 536–543.
- (41) Xue, Y.; Maduraiveeran, G.; Wang, M.; Zheng, S.; Zhang, Y.; Jin, W. Hierarchical Oxygen-Implanted MoS<sub>2</sub> Nanoparticle Decorated Graphene for the Non-Enzymatic Electrochemical Sensing of Hydrogen Peroxide in Alkaline Media. *Talanta* **2018**, *176*, 397–405.
- (42) Durán, N.; Marcato, P. D.; Durán, M.; Yadav, A.; Gade, A.; Rai, M. Mechanistic Aspects in the Biogenic Synthesis of Extracellular Metal Nanoparticles by Peptides, Bacteria, Fungi, and Plants. *Appl. Microbiol. Biotechnol.* **2011**, *90* (5), 1609–1624.
- (43) Palomo, J. M.; Filice, M. Biosynthesis of Metal Nanoparticles: Novel Efficient Heterogeneous Nanocatalysts. *Nanomater. (Basel, Switzerland)* **2016**, *6* (5), 84.
- (44) Buzea, C.; Pacheco, I. Electrical Properties of Nanowires and Nanofibers BT - Handbook of Nanofibers. In *Handbook of Nanofibers*; Barhoum, A., Bechelany, M., Makhoul, A., Eds.; Springer International Publishing: Cham, 2018; pp 1–62.

- (45) Xia, Y.; Yang, P.; Sun, Y.; Wu, Y.; Mayers, B.; Gates, B.; Yin, Y.; Kim, F.; Yan, H. One-Dimensional Nanostructures: Synthesis, Characterization, and Applications. *Adv. Mater.* **2003**, *15* (5), 353–389.
- (46) Ramakrishna, S.; Fujihara, K.; Teo, W.-E.; Lim, T.-C.; Ma, Z. *An Introduction to Electrospinning and Nanofibers*; World Scientific, 2005.
- (47) Bagherzadeh, R.; Gorji, M.; Sorayani Bafgi, M. S.; Saveh-Shemshaki, N. 18 - Electrospun Conductive Nanofibers for Electronics. In *Woodhead Publishing Series in Textiles*; Afshari, M., Ed.; Woodhead Publishing, 2017; pp 467–519.
- (48) Jin, H.; Guo, C.; Liu, X.; Liu, J.; Vasileff, A.; Jiao, Y.; Zheng, Y.; Qiao, S.-Z. Emerging Two-Dimensional Nanomaterials for Electrocatalysis. *Chem. Rev.* **2018**, *118* (13), 6337–6408.
- (49) Bhuyan, M. S. A.; Uddin, M. N.; Islam, M. M.; Bipasha, F. A.; Hossain, S. S. Synthesis of Graphene. *Int. Nano Lett.* **2016**, *6* (2), 65–83.
- (50) Grimaldi, N.; Andrade, F.; Segovia, N.; Ferrer-Tasies, L.; Sala, S.; Veciana, J.; Ventosa, N. Lipid-Based Nanovesicles for Nanomedicine. *Chem. Soc. Rev.* **2016**, *45*, 6520–6545.
- (51) George, J. M.; Antony, A.; Mathew, B. Metal Oxide Nanoparticles in Electrochemical Sensing and Biosensing: A Review. *Microchim. Acta* **2018**, *185*, 358.
- (52) Girigoswami, K. Toxicity of Metal Oxide Nanoparticles. In *Cellular and Molecular Toxicology of Nanoparticles*; Saquib, Q., Faisal, M., Al-Khedhairi, A. A., Alatar, A. A., Eds.; Springer International Publishing: Cham, 2018; pp 99–122.
- (53) Cañas-Carrell, J. E.; Li, S.; Parra, A. M.; Shrestha, B. 10 - Metal Oxide Nanomaterials: Health and Environmental Effects. In *Health and Environmental Safety of Nanomaterials*; Njuguna, J., Pielichowski, K., Zhu, H., Eds.; Woodhead Publishing, 2014; pp 200–221.
- (54) Karlsson, H. L.; Toprak, M. S.; Fadeel, B. Chapter 4 - Toxicity of Metal and Metal Oxide Nanoparticles. In *Handbook on the Toxicology of Metals*; Nordberg, G. F., Fowler, B. A., Nordberg, M., Eds.; Academic Press: San Diego, 2015; pp 75–112.
- (55) Xin, H.; Vojvodic, A.; Voss, J.; Nørskov, J. K.; Abild-Pedersen, F. Effects of *d*-Band Shape on the Surface Reactivity of Transition-Metal Alloys. *Phys. Rev. B* **2014**, *89* (11), 115114.
- (56) Nørskov, J. K.; Abild-Pedersen, F.; Studt, F.; Bligaard, T. Density Functional Theory in Surface Chemistry and Catalysis. *Proc. Natl. Acad. Sci.* **2011**, *108* (3), 937–943.

- (57) Gorzkowski, M. T.; Lewera, A. Probing the Limits of D-Band Center Theory: Electronic and Electrocatalytic Properties of Pd-Shell–Pt-Core Nanoparticles. *J. Phys. Chem. C* **2015**, *119* (32), 18389–18395.
- (58) McCreery, R. L. Advanced Carbon Electrode Materials for Molecular Electrochemistry. *Chem. Rev.* **2008**, *108* (7), 2646–2687.
- (59) Gu, W.; Yushin, G. Review of Nanostructured Carbon Materials for Electrochemical Capacitor Applications: Advantages and Limitations of Activated Carbon, Carbide-Derived Carbon, Zeolite-Templated Carbon, Carbon Aerogels, Carbon Nanotubes, Onion-like Carbon, and Graphene. *WIREs Energy Environ.* **2014**, *3* (5), 424–473.
- (60) Yang, C.; Denno, M. E.; Pyakurel, P.; Venton, B. J. Recent Trends in Carbon Nanomaterial-Based Electrochemical Sensors for Biomolecules: A Review. *Anal. Chim. Acta* **2015**, *887*, 17–37.
- (61) Wang, L.; Pumera, M. Electrochemical Catalysis at Low Dimensional Carbons: Graphene, Carbon Nanotubes and beyond – A Review. *Appl. Mater. Today* **2016**, *5*, 134–141.
- (62) Zhu, G.; Sun, H.; Zou, B.; Liu, Z.; Sun, N.; Yi, Y.; Wong, K. Electrochemical Sensing of 4-Nitrochlorobenzene Based on Carbon Nanohorns/Graphene Oxide Nanohybrids. *Biosens. Bioelectron.* **2018**, *106*, 136–141.
- (63) Zhu, W.; Zhang, Y.; Gong, J.; Ma, Y.; Sun, J.; Li, T.; Wang, J. Surface Engineering of Carbon Fiber Paper toward Exceptionally High-Performance and Stable Electrochemical Nitrite Sensing. *ACS Sensors* **2019**, *4* (11), 2980–2987.
- (64) Vishnu, N.; Gandhi, M.; Rajagopal, D.; Kumar, A. S. Pencil Graphite as an Elegant Electrochemical Sensor for Separation-Free and Simultaneous Sensing of Hypoxanthine, Xanthine and Uric Acid in Fish Samples. *Anal. Methods* **2017**, *9* (15), 2265–2274.
- (65) Tian, Y.; Wei, Z.; Zhang, K.; Peng, S.; Zhang, X.; Liu, W.; Chu, K. Three-Dimensional Phosphorus-Doped Graphene as an Efficient Metal-Free Electrocatalyst for Electrochemical Sensing. *Sensors Actuators B Chem.* **2017**, *241*, 584–591.
- (66) Chu, K.; Wang, F.; Tian, Y.; Wei, Z. Phosphorus Doped and Defects Engineered Graphene for Improved Electrochemical Sensing: Synergistic Effect of Dopants and Defects. *Electrochim. Acta* **2017**, *231*, 557–564.

- (67) Liu, D.; Zhang, X.; Sun, Z.; You, T. Free-Standing Nitrogen-Doped Carbon Nanofiber Films as Highly Efficient Electrocatalysts for Oxygen Reduction. *Nanoscale* **2013**, *5* (20), 9528–9531.
- (68) Cui, R.; Xu, D.; Xie, X.; Yi, Y.; Quan, Y.; Zhou, M.; Gong, J.; Han, Z.; Zhang, G. Phosphorus-Doped Helical Carbon Nanofibers as Enhanced Sensing Platform for Electrochemical Detection of Carbendazim. *Food Chem.* **2017**, *221*, 457–463.
- (69) Sun, J.; Li, L.; Zhang, X.; Liu, D.; Lv, S.; Zhu, D.; Wu, T.; You, T. Simultaneous Determination of Ascorbic Acid, Dopamine and Uric Acid at a Nitrogen-Doped Carbon Nanofiber Modified Electrode. *RSC Adv.* **2015**, *5*, 11925–11932.
- (70) Chu, K.; Wang, F.; Zhao, X.; Wang, X.; Tian, Y. Electrochemical Dopamine Sensor Based on P-Doped Graphene: Highly Active Metal-Free Catalyst and Metal Catalyst Support. *Mater. Sci. Eng. C* **2017**, *81*, 452–458.
- (71) Mutyala, S.; Mathiyarasu, J. A Reagentless Non-Enzymatic Hydrogen Peroxide Sensor Presented Using Electrochemically Reduced Graphene Oxide Modified Glassy Carbon Electrode. *Mater. Sci. Eng. C* **2016**, *69*, 398–406.
- (72) Rahsepar, M.; Foroughi, F.; Kim, H. A New Enzyme-Free Biosensor Based on Nitrogen-Doped Graphene with High Sensing Performance for Electrochemical Detection of Glucose at Biological pH Value. *Sensors Actuators B Chem.* **2019**, *282*, 322–330.
- (73) Foroughi, F.; Rahsepar, M.; Kim, H. A Highly Sensitive and Selective Biosensor Based on Nitrogen-Doped Graphene for Non-Enzymatic Detection of Uric Acid and Dopamine at Biological PH Value. *J. Electroanal. Chem.* **2018**, *827*, 34–41.
- (74) Jiang, Y.; Wang, B.; Meng, F.; Cheng, Y.; Zhu, C. Microwave-Assisted Preparation of N-Doped Carbon Dots as a Biosensor for Electrochemical Dopamine Detection. *J. Colloid Interface Sci.* **2015**, *452*, 199–202.
- (75) Liu, Y.; Ma, Y.; Jin, Y.; Chen, G.; Zhang, X. Microwave-Assisted Solvothermal Synthesis of Sulfur-Doped Graphene for Electrochemical Sensing. *J. Electroanal. Chem.* **2015**, *739*, 172–177.
- (76) Wang, Y.; Shao, Y.; Matson, D. W.; Li, J.; Lin, Y. Nitrogen-Doped Graphene and Its Application in Electrochemical Biosensing. *ACS Nano* **2010**, *4*, 1790–1798.



- (77) Li, O. L.; Chiba, S.; Wada, Y.; Panomsuwan, G.; Ishizaki, T. Synthesis of Graphitic-N and Amino-N in Nitrogen-Doped Carbon via a Solution Plasma Process and Exploration of Their Synergic Effect for Advanced Oxygen Reduction Reaction. *J. Mater. Chem. A* **2017**, 5 (5), 2073–2082.
- (78) Ouyang, B.; Zhang, Y.; Wang, Y.; Zhang, Z.; Fan, H. J.; Rawat, R. S. Plasma Surface Functionalization Induces Nanostructuring and Nitrogen-Doping in Carbon Cloth with Enhanced Energy Storage Performance. *J. Mater. Chem. A* **2016**, 4 (45), 17801–17808.
- (79) Zhu, C.; Li, H.; Fu, S.; Du, D.; Lin, Y. Highly Efficient Nonprecious Metal Catalysts towards Oxygen Reduction Reaction Based on Three-Dimensional Porous Carbon Nanostructures. *Chem. Soc. Rev.* **2016**, 45 (3), 517–531.
- (80) Gao, K.; Wang, B.; Tao, L.; Cunnings, B. V.; Zhang, Z.; Wang, S.; Ruoff, R. S.; Qu, L. Efficient Metal-Free Electrocatalysts from N-Doped Carbon Nanomaterials: Mono-Doping and Co-Doping. *Adv. Mater.* **2019**, 31 (13), 1805121.
- (81) Tajik, S.; Dourandish, Z.; Zhang, K.; Beitollahi, H.; Le, Q. Van; Jang, H. W.; Shokouhimehr, M. Carbon and Graphene Quantum Dots: A Review on Syntheses, Characterization, Biological and Sensing Applications for Neurotransmitter Determination. *RSC Adv.* **2020**, 10 (26), 15406–15429.
- (82) Campuzano, S.; Yáñez-Sedeño, P.; Pingarrón, J. M. Carbon Dots and Graphene Quantum Dots in Electrochemical Biosensing. *Nanomaterials* **2019**, 9, 634.
- (83) Li, Y.; Zhao, Y.; Cheng, H.; Hu, Y.; Shi, G.; Dai, L.; Qu, L. Nitrogen-Doped Graphene Quantum Dots with Oxygen-Rich Functional Groups. *J. Am. Chem. Soc.* **2012**, 134, 15–18.
- (84) Huang, J.; Liu, Y.; You, T. Carbon Nanofiber Based Electrochemical Biosensors: A Review. *Anal. Methods* **2010**, 2 (3), 202–211.
- (85) Kour, R.; Arya, S.; Young, S.-J.; Gupta, V.; Bandharia, P.; Khosla, A. Review—Recent Advances in Carbon Nanomaterials as Electrochemical Biosensors. *J. Electrochem. Soc.* **2020**, 167 (3), 037555.
- (86) Jacobs, C. B.; Peairs, M. J.; Venton, B. J. Review: Carbon Nanotube Based Electrochemical Sensors for Biomolecules. *Anal. Chim. Acta* **2010**, 662 (2), 105–127.
- (87) Tee, S. Y.; Teng, C. P.; Ye, E. Metal Nanostructures for Non-Enzymatic Glucose Sensing. *Mater. Sci. Eng. C* **2017**, 70, 1018–1030.

- (88) Niu, X.; Li, X.; Pan, J.; He, Y.; Qiu, F.; Yan, Y. Recent Advances in Non-Enzymatic Electrochemical Glucose Sensors Based on Non-Precious Transition Metal Materials: Opportunities and Challenges. *RSC Adv.* **2016**, *6* (88), 84893–84905.
- (89) Bruen, D.; Delaney, C.; Florea, L.; Diamond, D. Glucose Sensing for Diabetes Monitoring: Recent Developments. *Sensors* **2017**, *17* (8), 1866.
- (90) Bae, C. W.; Toi, P. T.; Kim, B. Y.; Lee, W. Il; Lee, H. B.; Hanif, A.; Lee, E. H.; Lee, N.-E. Fully Stretchable Capillary Microfluidics-Integrated Nanoporous Gold Electrochemical Sensor for Wearable Continuous Glucose Monitoring. *ACS Appl. Mater. Interfaces* **2019**, *11* (16), 14567–14575.
- (91) Yao, H.; Liao, Y.; Lingley, A. R.; Afanasiev, A.; Lähdesmäki, I.; Otis, B. P.; Parviz, B. A. A Contact Lens with Integrated Telecommunication Circuit and Sensors for Wireless and Continuous Tear Glucose Monitoring. *J. Micromechanics Microengineering* **2012**, *22* (7), 075007.
- (92) Kim, J.; Valdés-Ramírez, G.; Bandodkar, A. J.; Jia, W.; Martinez, A. G.; Ramírez, J.; Mercier, P.; Wang, J. Non-Invasive Mouthguard Biosensor for Continuous Salivary Monitoring of Metabolites. *Analyst* **2014**, *139* (7), 1632–1636.
- (93) Mannoor, M. S.; Tao, H.; Clayton, J. D.; Sengupta, A.; Kaplan, D. L.; Naik, R. R.; Verma, N.; Omenetto, F. G.; McAlpine, M. C. Graphene-Based Wireless Bacteria Detection on Tooth Enamel. *Nat. Commun.* **2012**, *3* (1), 763.
- (94) Frew, J. E.; Harmer, M. A.; O. Hill, H. A.; Libor, S. I. A Method for Estimation of Hydrogen Peroxide Based on Mediated Electron Transfer Reactions of Peroxidases at Electrodes. *J. Electroanal. Chem. Interfacial Electrochem.* **1986**, *201* (1), 1–10.
- (95) Shamkhalichenar, H.; Choi, J.-W. Review—Non-Enzymatic Hydrogen Peroxide Electrochemical Sensors Based on Reduced Graphene Oxide. *J. Electrochem. Soc.* **2020**, *167* (3), 037531.
- (96) Mollarasouli, F.; Asadpour-Zeynali, K.; Campuzano, S.; Yáñez-Sedeño, P.; Pingarrón, J. M. Non-Enzymatic Hydrogen Peroxide Sensor Based on Graphene Quantum Dots-Chitosan/Methylene Blue Hybrid Nanostructures. *Electrochim. Acta* **2017**, *246*, 303–314.
- (97) Kogularasu, S.; Govindasamy, M.; Chen, S.-M.; Akilarasan, M.; Mani, V. 3D Graphene Oxide-Cobalt Oxide Polyhedrons for Highly Sensitive Non-Enzymatic Electrochemical Determination of Hydrogen Peroxide. *Sensors Actuators B Chem.* **2017**, *253*, 773–783.

- (98) Bai, Z.; Li, G.; Liang, J.; Su, J.; Zhang, Y.; Chen, H.; Huang, Y.; Sui, W.; Zhao, Y. Non-Enzymatic Electrochemical Biosensor Based on Pt NPs/RGO-CS-Fc Nano-Hybrids for the Detection of Hydrogen Peroxide in Living Cells. *Biosens. Bioelectron.* **2016**, *82*, 185–194.
- (99) Khairy, M.; Mahmoud, B. G.; Banks, C. E. Simultaneous Determination of Codeine and Its Co-Formulated Drugs Acetaminophen and Caffeine by Utilising Cerium Oxide Nanoparticles Modified Screen-Printed Electrodes. *Sensors Actuators B Chem.* **2018**, *259*, 142–154.
- (100) K. B., A.; Bhat, V. S.; Varghese, A.; George, L.; Hegde, G. Non-Enzymatic Electrochemical Determination of Progesterone Using Carbon Nanospheres from Onion Peels Coated on Carbon Fiber Paper. *J. Electrochem. Soc.* **2019**, *166* (13), B1097–B1106.
- (101) Li, J.; Jiang, J.; Zhao, D.; Xu, Z.; Liu, M.; Deng, P.; Liu, X.; Yang, C.; Qian, D.; Xie, H. Facile Synthesis of Pd/N-Doped Reduced Graphene Oxide via a Moderate Wet-Chemical Route for Non-Enzymatic Electrochemical Detection of Estradiol. *J. Alloys Compd.* **2018**, *769*, 566–575.
- (102) Liu, W.; Ma, Y.; Sun, G.; Wang, S.; Deng, J.; Wei, H. Molecularly Imprinted Polymers on Graphene Oxide Surface for EIS Sensing of Testosterone. *Biosens. Bioelectron.* **2017**, *92*, 305–312.
- (103) Wierzbicka, E.; Sulka, G. D. Fabrication of Highly Ordered Nanoporous Thin Au Films and Their Application for Electrochemical Determination of Epinephrine. *Sensors Actuators B Chem.* **2016**, *222*, 270–279.
- (104) Keerthi, M.; Boopathy, G.; Chen, S.-M.; Chen, T.-W.; Lou, B.-S. A Core-Shell Molybdenum Nanoparticles Entrapped *f*-MWCNTs Hybrid Nanostructured Material Based Non-Enzymatic Biosensor for Electrochemical Detection of Dopamine Neurotransmitter in Biological Samples. *Sci. Rep.* **2019**, *9* (1), 13075.
- (105) Hussain, M. M.; Rahman, M. M.; Asiri, A. M.; Awual, M. R. Non-Enzymatic Simultaneous Detection of L-Glutamic Acid and Uric Acid Using Mesoporous Co<sub>3</sub>O<sub>4</sub> Nanosheets. *RSC Adv.* **2016**, *6* (84), 80511–80521.
- (106) Wang, L.; Chen, X.; Liu, C.; Yang, W. Non-Enzymatic Acetylcholine Electrochemical Biosensor Based on Flower-like NiAl Layered Double Hydroxides Decorated with Carbon Dots. *Sensors Actuators B Chem.* **2016**, *233*, 199–205.

- (107) Agnihotri, N.; Chowdhury, A. D.; De, A. Non-Enzymatic Electrochemical Detection of Cholesterol Using  $\beta$ -Cyclodextrin Functionalized Graphene. *Biosens. Bioelectron.* **2015**, *63*, 212–217.
- (108) Boopathy, G.; Keerthi, M.; Chen, S.-M.; Umapathy, M. J.; Govindasamy, M.; Chen, T.-W.; Ali, M. A.; Al-Hemaid, F. M. A.; Elshikh, M. S. Graphene Oxide/ $\alpha$ -MnO<sub>2</sub> Binary Nanosheets Based Non-Enzymatic Biosensor for Pico-Molar Level Electrochemical Detection of Biomarker (Guanine) in DNA Sample. *J. Electrochem. Soc.* **2018**, *165* (14), B651–B658.
- (109) Martinkova, P.; Kostelnik, A.; Pohanka, M. Nanomaterials as Pseudocatalysts in the Construction of Electrochemical Nonenzymatic Sensors for Healthcare: A Review. *Anal. Lett.* **2019**, *52* (9), 1396–1417.
- (110) Lin, J.; Peng, Z.; Liu, Y.; Ruiz-Zepeda, F.; Ye, R.; Samuel, E. L. G.; Yacaman, M. J.; Yakobson, B. I.; Tour, J. M. Laser-Induced Porous Graphene Films from Commercial Polymers. *Nat. Commun.* **2014**, *5*, 5714.
- (111) Wang, F.; Wang, K.; Zheng, B.; Dong, X.; Mei, X.; Lv, J.; Duan, W.; Wang, W. Laser-Induced Graphene: Preparation, Functionalization and Applications. *Mater. Technol.* **2018**, *33* (5).
- (112) Ye, R.; Chyan, Y.; Zhang, J.; Li, Y.; Han, X.; Kittrell, C.; Tour, J. M. Laser-Induced Graphene Formation on Wood. *Adv. Mater.* **2017**, *29* (37), 1702211.
- (113) Chyan, Y.; Ye, R.; Li, Y.; Singh, S. P.; Arnusch, C. J.; Tour, J. M. Laser-Induced Graphene by Multiple Lasing: Toward Electronics on Cloth, Paper, and Food. *ACS Nano* **2018**, *12*, 2176–2183.
- (114) Wang, H.; Wang, H.; Wang, Y.; Su, X.; Wang, C.; Zhang, M.; Jian, M.; Xia, K.; Liang, X.; Lu, H.; et al. Laser Writing of Janus Graphene/Kevlar Textile for Intelligent Protective Clothing. *ACS Nano* **2020**, *14* (3), 3219–3226.
- (115) Ruan, X.; Wang, R.; Luo, J.; Yao, Y.; Liu, T. Experimental and Modeling Study of CO<sub>2</sub> Laser Writing Induced Polyimide Carbonization Process. *Mater. Des.* **2018**, *160*, 1168–1177.
- (116) Li, Y.; Luong, D. X.; Zhang, J.; Tarkunde, Y. R.; Kittrell, C.; Sargunraj, F.; Ji, Y.; Arnusch, C. J.; Tour, J. M. Laser-Induced Graphene in Controlled Atmospheres: From Superhydrophilic to Superhydrophobic Surfaces. *Adv. Mater.* **2017**, *29* (27), 1700496.

- (117) Lin, S.; Feng, W.; Miao, X.; Zhang, X.; Chen, S.; Chen, Y.; Wang, W.; Zhang, Y. A Flexible and Highly Sensitive Nonenzymatic Glucose Sensor Based on DVD-Laser Scribed Graphene Substrate. *Biosens. Bioelectron.* **2018**, *110*, 89–96.
- (118) Nayak, P.; Kurra, N.; Xia, C.; Alshareef, H. N. Highly Efficient Laser Scribed Graphene Electrodes for On-Chip Electrochemical Sensing Applications. *Adv. Electron. Mater.* **2016**, *2* (10), 1600185.
- (119) Ye, R.; Peng, Z.; Wang, T.; Xu, Y.; Zhang, J.; Li, Y.; Nilewski, L. G.; Lin, J.; Tour, J. M. *In Situ* Formation of Metal Oxide Nanocrystals Embedded in Laser-Induced Graphene. *ACS Nano* **2015**, *9* (9), 9244–9251.
- (120) Deng, H.; Zhang, C.; Xie, Y.; Tumlin, T.; Giri, L.; Karna, S. P.; Lin, J. Laser Induced MoS<sub>2</sub>/Carbon Hybrids for Hydrogen Evolution Reaction Catalysts. *J. Mater. Chem. A* **2016**, *4* (18), 6824–6830.
- (121) Clerici, F.; Fontana, M.; Bianco, S.; Serrapede, M.; Perrucci, F.; Ferrero, S.; Tresso, E.; Lamberti, A. *In Situ* MoS<sub>2</sub> Decoration of Laser-Induced Graphene as Flexible Supercapacitor Electrodes. *ACS Appl. Mater. Interfaces* **2016**, *8* (16), 10459–10465.
- (122) Ge, L.; Hong, Q.; Li, H.; Li, F. A Laser-Induced TiO<sub>2</sub>-Decorated Graphene Photoelectrode for Sensitive Photoelectrochemical Biosensing. *Chem. Commun.* **2019**, *55* (34), 4945–4948.
- (123) Rodrigues, J.; Zanoni, J.; Gaspar, G.; Fernandes, A. J. S.; Carvalho, A. F.; Santos, N. F.; Monteiro, T.; Costa, F. M. ZnO Decorated Laser-Induced Graphene Produced by Direct Laser Scribing. *Nanoscale Adv.* **2019**, *1* (8), 3252–3268.
- (124) You, Z.; Qiu, Q.; Chen, H.; Feng, Y.; Wang, X.; Wang, Y.; Ying, Y. Laser-Induced Noble Metal Nanoparticle-Graphene Composites Enabled Flexible Biosensor for Pathogen Detection. *Biosens. Bioelectron.* **2020**, *150*, 111896.
- (125) Hirose, A.; Kobayashi, K. F. Surface Alloying of Copper with Chromium by CO<sub>2</sub> Laser. *Mater. Sci. Eng. A* **1994**, *174* (2), 199–206.
- (126) Abboud, J. H.; West, D. R. F. Laser Surface Alloying of Titanium with Aluminium. *J. Mater. Sci. Lett.* **1990**, *9* (3), 308–310.
- (127) Peng, Z.; Ye, R.; Mann, J. A.; Zakhidov, D.; Li, Y.; Smalley, P. R.; Lin, J.; Tour, J. M. Flexible Boron-Doped Laser-Induced Graphene Microsupercapacitors. *ACS Nano* **2015**, *9* (6), 5868–5875.

- (128) Zhang, F.; Alhajji, E.; Lei, Y.; Kurra, N.; Alshareef, H. N. Highly Doped 3D Graphene Na-Ion Battery Anode by Laser Scribing Polyimide Films in Nitrogen Ambient. *Adv. Energy Mater.* **2018**, *8* (23), 1800353.
- (129) Kim, K. Y.; Choi, H.; Tran, C. Van; In, J. Bin. Simultaneous Densification and Nitrogen Doping of Laser-Induced Graphene by Duplicated Pyrolysis for Supercapacitor Applications. *J. Power Sources* **2019**, *441*, 227199.
- (130) Lamberti, A.; Serrapede, M.; Ferraro, G.; Fontana, M.; Perrucci, F.; Bianco, S.; Chiolerio, A.; Bocchini, S. All-SPEEK Flexible Supercapacitor Exploiting Laser-Induced Graphenization. *2D Mater.* **2017**, *4* (3), 035012.
- (131) Che, G.; Lakshmi, B. B.; Martin, C. R.; Fisher, E. R.; Ruoff, R. S. Chemical Vapor Deposition Based Synthesis of Carbon Nanotubes and Nanofibers Using a Template Method. *Chem. Mater.* **1998**, *10* (1), 260–267.
- (132) Zheng, G.-B.; Kouda, K.; Sano, H.; Uchiyama, Y.; Shi, Y.-F.; Quan, H.-J. A Model for the Structure and Growth of Carbon Nanofibers Synthesized by the CVD Method Using Nickel as a Catalyst. *Carbon N. Y.* **2004**, *42* (3), 635–640.
- (133) Inagaki, M.; Yang, Y.; Kang, F. Carbon Nanofibers Prepared via Electrospinning. *Adv. Mater.* **2012**, *24* (19), 2547–2566.
- (134) Liu, C.-K.; Lai, K.; Liu, W.; Yao, M.; Sun, R.-J. Preparation of Carbon Nanofibres through Electrospinning and Thermal Treatment. *Polym. Int.* **2009**, *58* (12), 1341–1349.
- (135) Huang, J.; Wang, D.; Hou, H.; You, T. Electrospun Palladium Nanoparticle-Loaded Carbon Nanofibers and Their Electrocatalytic Activities towards Hydrogen Peroxide and NADH. *Adv. Funct. Mater.* **2008**, *18* (3), 441–448.
- (136) Liu, Y.; Teng, H.; Hou, H.; You, T. Nonenzymatic Glucose Sensor Based on Renewable Electrospun Ni Nanoparticle-Loaded Carbon Nanofiber Paste Electrode. *Biosens. Bioelectron.* **2009**, *24* (11), 3329–3334.
- (137) Zhang, H.; Huang, J.; Hou, H.; You, T. Electrochemical Detection of Hydrazine Based on Electrospun Palladium Nanoparticle/Carbon Nanofibers. *Electroanalysis* **2009**, *21*, 1869–1874.
- (138) Tang, X.; Liu, Y.; Hou, H.; You, T. Electrochemical Determination of L-Tryptophan, L-Tyrosine and L-Cysteine Using Electrospun Carbon Nanofibers Modified Electrode. *Talanta* **2010**, *80* (5), 2182–2186.

- (139) Fu, J.; Qiao, H.; Li, D.; Luo, L.; Chen, K.; Wei, Q. Laccase Biosensor Based on Electrospun Copper/Carbon Composite Nanofibers for Catechol Detection. *Sensors (Basel)*. **2014**, *14* (2), 3543–3556.
- (140) Wongkaew, N.; Simsek, M.; Arumugam, P.; Behrent, A.; Berchmans, S.; Baeumner, A. J. A Robust Strategy Enabling Addressable Porous 3D Carbon-Based Functional Nanomaterials in Miniaturized Systems. *Nanoscale* **2019**, *11*, 3674–3680.
- (141) Simsek, M.; Hoecherl, K.; Schlosser, M.; Baeumner, A. J.; Wongkaew, N. Printable 3D Carbon Nanofiber Networks with Embedded Metal Nanocatalysts. *ACS Appl. Mater. Interfaces* **2020**, *12* (35), 39533–39540.
- (142) Puetz, P.; Behrent, A.; Baeumner, A. J.; Wegener, J. Laser-Scribed Graphene (LSG) as New Electrode Material for Impedance-Based Cellular Assays. *Sensors Actuators B Chem.* **2020**, *321*, 128443.
- (143) d'Amora, M.; Lamberti, A.; Fontana, M.; Giordani, S. Toxicity Assessment of Laser-Induced Graphene by Zebrafish during Development. *J. Phys. Mater.* **2020**, *3* (3), 034008.
- (144) Peng, Z.; Lin, J.; Ye, R.; Samuel, E. L. G.; Tour, J. M. Flexible and Stackable Laser-Induced Graphene Supercapacitors. *ACS Appl. Mater. Interfaces* **2015**, *7* (5), 3414–3419.
- (145) Peng, Z.; Ye, R.; Mann, J. A.; Zakhidov, D.; Li, Y.; Smalley, P. R.; Lin, J.; Tour, J. M. Flexible Boron-Doped Laser-Induced Graphene Microsupercapacitors. *ACS Nano* **2015**, *9* (6), 5868–5875.
- (146) Li, G.; Meng, Z.; Qian, J.; Ho, C.-L.; Lau, S. P.; Wong, W.-Y.; Yan, F. Inkjet Printed Pseudocapacitive Electrodes on Laser-Induced Graphene for Electrochemical Energy Storage. *Mater. Today Energy* **2019**, *12*, 155–160.
- (147) Singh, S. P.; Li, Y.; Be'er, A.; Oren, Y.; Tour, J. M.; Arnusch, C. J. Laser-Induced Graphene Layers and Electrodes Prevents Microbial Fouling and Exerts Antimicrobial Action. *ACS Appl. Mater. Interfaces* **2017**, *9* (21), 18238–18247.
- (148) Huang, L.; Xu, S.; Wang, Z.; Xue, K.; Su, J.; Song, Y.; Chen, S.; Zhu, C.; Tang, B. Z.; Ye, R. Self-Reporting and Photothermally Enhanced Rapid Bacterial Killing on a Laser-Induced Graphene Mask. *ACS Nano* **2020**, *14* (9), 12045–12053.
- (149) Tittle, C. M.; Yilman, D.; Pope, M. A.; Backhouse, C. J. Robust Superhydrophobic Laser-Induced Graphene for Desalination Applications. *Adv. Mater. Technol.* **2018**, *3* (2), 1700207.

- (150) Zhang, Y.; Li, N.; Xiang, Y.; Wang, D.; Zhang, P.; Wang, Y.; Lu, S.; Xu, R.; Zhao, J. A Flexible Non-Enzymatic Glucose Sensor Based on Copper Nanoparticles Anchored on Laser-Induced Graphene. *Carbon N. Y.* **2020**, *156*, 506–513.
- (151) Zhang, Y.; Zhu, H.; Sun, P.; Sun, C.-K.; Huang, H.; Guan, S.; Liu, H.; Zhang, H.; Zhang, C.; Qin, K.-R. Laser-Induced Graphene-Based Non-Enzymatic Sensor for Detection of Hydrogen Peroxide. *Electroanalysis* **2019**, *31* (7), 1334–1341.
- (152) Aparicio-Martínez, E.; Ibarra, A.; Estrada-Moreno, I. A.; Osuna, V.; Dominguez, R. B. Flexible Electrochemical Sensor Based on Laser Scribed Graphene/Ag Nanoparticles for Non-Enzymatic Hydrogen Peroxide Detection. *Sensors Actuators B Chem.* **2019**, *301*, 127101.
- (153) Vanegas, D. C.; Patiño, L.; Mendez, C.; Oliveira, D. A. de; Torres, A. M.; Gomes, C. L.; McLamore, E. S. Laser Scribed Graphene Biosensor for Detection of Biogenic Amines in Food Samples Using Locally Sourced Materials. *Biosensors* **2018**, *8* (2), 42.
- (154) Yu, Y.; Joshi, P. C.; Wu, J.; Hu, A. Laser-Induced Carbon-Based Smart Flexible Sensor Array for Multiflavors Detection. *ACS Appl. Mater. Interfaces* **2018**, *10* (40), 34005–34012.
- (155) Stanford, M. G.; Yang, K.; Chyan, Y.; Kittrell, C.; Tour, J. M. Laser-Induced Graphene for Flexible and Embeddable Gas Sensors. *ACS Nano* **2019**, *13* (3), 3474–3482.
- (156) Yang, L.; Yi, N.; Zhu, J.; Cheng, Z.; Yin, X.; Zhang, X.; Zhu, H.; Cheng, H. Novel Gas Sensing Platform Based on a Stretchable Laser-Induced Graphene Pattern with Self-Heating Capabilities. *J. Mater. Chem. A* **2020**, *8* (14), 6487–6500.
- (157) Zhu, J.; Cho, M.; Li, Y.; Cho, I.; Suh, J.-H.; Orbe, D. Del; Jeong, Y.; Ren, T.-L.; Park, I. Biomimetic Turbinate-like Artificial Nose for Hydrogen Detection Based on 3D Porous Laser-Induced Graphene. *ACS Appl. Mater. Interfaces* **2019**, *11* (27), 24386–24394.
- (158) Lan, L.; Le, X.; Dong, H.; Xie, J.; Ying, Y.; Ping, J. One-Step and Large-Scale Fabrication of Flexible and Wearable Humidity Sensor Based on Laser-Induced Graphene for Real-Time Tracking of Plant Transpiration at Bio-Interface. *Biosens. Bioelectron.* **2020**, *165*, 112360.
- (159) Zhu, C.; Tao, L.-Q.; Wang, Y.; Zheng, K.; Yu, J.; L, X.; Chen, X.; Huang, Y. Graphene Oxide Humidity Sensor with Laser-Induced Graphene Porous Electrodes. *Sensors Actuators B Chem.* **2020**, *325*, 128790.



- (160) Tao, L.-Q.; Tian, H.; Liu, Y.; Ju, Z.-Y.; Pang, Y.; Chen, Y.-Q.; Wang, D.-Y.; Tian, X.-G.; Yan, J.-C.; Deng, N.-Q.; et al. An Intelligent Artificial Throat with Sound-Sensing Ability Based on Laser Induced Graphene. *Nat. Commun.* **2017**, 8 (1), 14579.
- (161) Yang, Y.; Song, Y.; Bo, X.; Min, J.; Pak, O. S.; Zhu, L.; Wang, M.; Tu, J.; Kogan, A.; Zhang, H.; et al. A Laser-Engraved Wearable Sensor for Sensitive Detection of Uric Acid and Tyrosine in Sweat. *Nat. Biotechnol.* **2020**, 38 (2), 217–224.
- (162) Lamberti, A.; Clerici, F.; Fontana, M.; Scaltrito, L. A Highly Stretchable Supercapacitor Using Laser-Induced Graphene Electrodes onto Elastomeric Substrate. *Adv. Energy Mater.* **2016**, 6 (10), 1600050.
- (163) Xuan, X.; Kim, J. Y.; Hui, X.; Das, P. S.; Yoon, H. S.; Park, J.-Y. A Highly Stretchable and Conductive 3D Porous Graphene Metal Nanocomposite Based Electrochemical-Physiological Hybrid Biosensor. *Biosens. Bioelectron.* **2018**, 120, 160–167.
- (164) Prabhakaran, A.; Nayak, P. Surface Engineering of Laser-Scribed Graphene Sensor Enables Non-Enzymatic Glucose Detection in Human Body Fluids. *ACS Appl. Nano Mater.* **2020**, 3 (1), 391–398.
- (165) Sun, B.; McCay, R. N.; Goswami, S.; Xu, Y.; Zhang, C.; Ling, Y.; Lin, J.; Yan, Z. Gas-Permeable, Multifunctional On-Skin Electronics Based on Laser-Induced Porous Graphene and Sugar-Templated Elastomer Sponges. *Adv. Mater.* **2018**, 30 (50), 1804327.
- (166) Chhetry, A.; Sharifuzzaman, M.; Yoon, H.; Sharma, S.; Xuan, X.; Park, J. Y. MoS<sub>2</sub>-Decorated Laser-Induced Graphene for a Highly Sensitive, Hysteresis-Free, and Reliable Piezoresistive Strain Sensor. *ACS Appl. Mater. Interfaces* **2019**, 11 (25), 22531–22542.
- (167) Ling, Y.; Pang, W.; Li, X.; Goswami, S.; Xu, Z.; Stroman, D.; Liu, Y.; Fei, Q.; Xu, Y.; Zhao, G.; et al. Laser-Induced Graphene for Electrothermally Controlled, Mechanically Guided, 3D Assembly and Human–Soft Actuators Interaction. *Adv. Mater.* **2020**, 32 (17), 1908475.
- (168) Mao, X.; Tian, W.; Hatton, T. A.; Rutledge, G. C. Advances in Electrospun Carbon Fiber-Based Electrochemical Sensing Platforms for Bioanalytical Applications. *Anal. Bioanal. Chem.* **2016**, 408 (5), 1307–1326.
- (169) Zhao, D.; Wang, T.; Han, D.; Rusinek, C.; Steckl, A. J.; Heineman, W. R. Electrospun Carbon Nanofiber Modified Electrodes for Stripping Voltammetry. *Anal. Chem.* **2015**, 87 (18), 9315–9321.

- (170) Ye, R.; James, D. K.; Tour, J. M. Laser-Induced Graphene. *Acc. Chem. Res.* **2018**, *51* (7), 1609–1620.
- (171) Luong, D. X.; Subramanian, A. K.; Silva, G. A. L.; Yoon, J.; Cofer, S.; Yang, K.; Owuor, P. S.; Wang, T.; Wang, Z.; Lou, J.; et al. Laminated Object Manufacturing of 3D-Printed Laser-Induced Graphene Foams. *Adv. Mater.* **2018**, *30* (28), 1707416.
- (172) Go, D.; Lott, P.; Stollenwerk, J.; Thomas, H.; Möller, M.; Kuehne, A. J. C. Laser Carbonization of PAN-Nanofiber Mats with Enhanced Surface Area and Porosity. *ACS Appl. Mater. Interfaces* **2016**, *8* (42), 28412–28417.
- (173) Go, D.; Opitz, M.; Lott, P.; Rahimi, K.; Stollenwerk, J.; Thomas, H.; Möller, M.; Roling, B.; Kuehne, A. J. C. Electrochemical Characterization of Laser-Carbonized Polyacrylonitrile Nanofiber Nonwovens. *J. Appl. Polym. Sci.* **2018**, *135* (25), 46398.
- (174) Chung, G. S.; Jo, S. M.; Kim, B. C. Properties of Carbon Nanofibers Prepared from Electrospun Polyimide. *J. Appl. Polym. Sci.* **2005**, *97* (1), 165–170.
- (175) Mao, X.; Yang, X.; Rutledge, G. C.; Alan Hatton, T. Ultra-Wide-Range Electrochemical Sensing Using Continuous Electrospun Carbon Nanofibers with High Densities of States. *ACS Appl. Mater. Interfaces* **2014**, *6* (5), 3394–3405.
- (176) Guadagno, L.; Raimondo, M.; Vittoria, V.; Vertuccio, L.; Lafdi, K.; De Vivo, B.; Lamberti, P.; Spinelli, G.; Tucci, V. The Role of Carbon Nanofiber Defects on the Electrical and Mechanical Properties of CNF-Based Resins. *Nanotechnology* **2013**, *24* (30), 305704.
- (177) Xiao, Y.; Dai, Y.; Chung, T.-S.; Guiver, M. D. Effects of Brominating Matrimid Polyimide on the Physical and Gas Transport Properties of Derived Carbon Membranes. *Macromolecules* **2005**, *38* (24), 10042–10049.
- (178) Mao, X.; Simeon, F.; Rutledge, G. C.; Hatton, T. A. Electrospun Carbon Nanofiber Webs with Controlled Density of States for Sensor Applications. *Adv. Mater.* **2013**, *25* (9), 1309–1314.
- (179) Yuan, W.; Zhou, Y.; Li, Y.; Li, C.; Peng, H.; Zhang, J.; Liu, Z.; Dai, L.; Shi, G. The Edge- and Basal-Plane-Specific Electrochemistry of a Single-Layer Graphene Sheet. *Sci. Rep.* **2013**, *3* (1), 2248.
- (180) Liu, Y.; Hou, H.; You, T. Synthesis of Carbon Nanofibers for Mediatorless Sensitive Detection of NADH. *Electroanalysis* **2008**, *20* (15), 1708–1713.

- (181) Wu, L.; Zhang, X.; Ju, H. Detection of NADH and Ethanol Based on Catalytic Activity of Soluble Carbon Nanofiber with Low Overpotential. *Anal. Chem.* **2007**, *79* (2), 453–458.
- (182) Teymourian, H.; Salimi, A.; Hallaj, R. Low Potential Detection of NADH Based on Fe<sub>3</sub>O<sub>4</sub> Nanoparticles/Multiwalled Carbon Nanotubes Composite: Fabrication of Integrated Dehydrogenase-Based Lactate Biosensor. *Biosens. Bioelectron.* **2012**, *33* (1), 60–68.
- (183) Kim, Y. H.; Kim, T.; Ryu, J. H.; Yoo, Y. J. Iron Oxide/Carbon Black (Fe<sub>2</sub>O<sub>3</sub>/CB) Composite Electrode for the Detection of Reduced Nicotinamide Cofactors Using an Amperometric Method under a Low Overpotential. *Biosens. Bioelectron.* **2010**, *25* (5), 1160–1165.
- (184) Šljukić, B.; Banks, C. E.; Crossley, A.; Compton, R. G. Iron(III) Oxide Graphite Composite Electrodes: Application to the Electroanalytical Detection of Hydrazine and Hydrogen Peroxide. *Electroanalysis* **2006**, *18* (18), 1757–1762.
- (185) Jones, C. P.; Jurkschat, K.; Crossley, A.; Compton, R. G.; Riehl, B. L.; Banks, C. E. Use of High-Purity Metal-Catalyst-Free Multiwalled Carbon Nanotubes To Avoid Potential Experimental Misinterpretations. *Langmuir* **2007**, *23* (18), 9501–9504.
- (186) Xue, Q.; Kato, D.; Kamata, T.; Guo, Q.; You, T.; Niwa, O. Improved Direct Electrochemistry for Proteins Adsorbed on a UV/Ozone-Treated Carbon Nanofiber Electrode. *Anal. Sci.* **2013**, *29* (6), 611–618.
- (187) Sham, M. L.; Kim, J.-K. Surface Functionalities of Multi-Wall Carbon Nanotubes after UV/Ozone and TETA Treatments. *Carbon N. Y.* **2006**, *44*, 768–777.
- (188) Roberts, J. G.; Moody, B. P.; McCarty, G. S.; Sombers, L. A. Specific Oxygen-Containing Functional Groups on the Carbon Surface Underlie an Enhanced Sensitivity to Dopamine at Electrochemically Pretreated Carbon Fiber Microelectrodes. *Langmuir* **2010**, *26* (11), 9116–9122.
- (189) Haiber, S.; Ai, X.; Bubert, H.; Heintze, M.; Brüser, V.; Brandl, W.; Marginean, G. Analysis of Functional Groups on the Surface of Plasma-Treated Carbon Nanofibers. *Anal. Bioanal. Chem.* **2003**, *375* (7), 875–883.
- (190) Browne, M. P.; Redondo, E.; Pumera, M. 3D Printing for Electrochemical Energy Applications. *Chem. Rev.* **2020**, *120* (5), 2783–2810.
- (191) Wang, Z.; Wu, S.; Wang, J.; Yu, A.; Wei, G. Carbon Nanofiber-Based Functional Nanomaterials for Sensor Applications. *Nanomaterials* **2019**, *9* (7), 1045.

- (192) Chinthaginjala, J. K.; Seshan, K.; Lefferts, L. Preparation and Application of Carbon-Nanofiber Based Microstructured Materials as Catalyst Supports. *Ind. Eng. Chem. Res.* **2007**, *46* (12), 3968–3978.
- (193) Nantaphol, S.; Watanabe, T.; Nomura, N.; Siangproh, W.; Chailapakul, O.; Einaga, Y. Bimetallic Pt–Au Nanocatalysts Electrochemically Deposited on Boron-Doped Diamond Electrodes for Nonenzymatic Glucose Detection. *Biosens. Bioelectron.* **2017**, *98*, 76–82.
- (194) Wang, Y.; He, Q.; Guo, J.; Wei, H.; Ding, K.; Lin, H.; Bhana, S.; Huang, X.; Luo, Z.; Shen, T. D.; et al. Carboxyl Multiwalled Carbon-Nanotube-Stabilized Palladium Nanocatalysts toward Improved Methanol Oxidation Reaction. *ChemElectroChem* **2015**, *2*, 559–570.
- (195) Khalily, M. A.; Yurderi, M.; Haider, A.; Bulut, A.; Patil, B.; Zahmakiran, M.; Uyar, T. Atomic Layer Deposition of Ruthenium Nanoparticles on Electrospun Carbon Nanofibers: A Highly Efficient Nanocatalyst for the Hydrolytic Dehydrogenation of Methylamine Borane. *ACS Appl. Mater. Interfaces* **2018**, *10*, 26162–26169.
- (196) Sahin, O. G. Microwave-Assisted Synthesis of PtAu@C Based Bimetallic Nanocatalysts for Non-Enzymatic H<sub>2</sub>O<sub>2</sub> Sensor. *Electrochim. Acta* **2015**, *180*, 873–879.
- (197) Liu, D.; Guo, Q.; Hou, H.; Niwa, O.; You, T. Pd<sub>x</sub>Co<sub>y</sub> Nanoparticle/Carbon Nanofiber Composites with Enhanced Electrocatalytic Properties. *ACS Catal.* **2014**, *4* (6), 1825–1829.
- (198) Yang, T.; Zhu, H.; Wan, M.; Dong, L.; Zhang, M.; Du, M. Highly Efficient and Durable PtCo Alloy Nanoparticles Encapsulated in Carbon Nanofibers for Electrochemical Hydrogen Generation. *Chem. Commun.* **2016**, *52* (5), 990–993.
- (199) Lee, J. S.; Kwon, O. S.; Park, S. J.; Park, E. Y.; You, S. A.; Yoon, H.; Jang, J. Fabrication of Ultrafine Metal-Oxide-Decorated Carbon Nanofibers for DMMP Sensor Application. *ACS Nano* **2011**, *5* (10), 7992–8001.
- (200) Guo, Q.; Liu, D.; Zhang, X.; Li, L.; Hou, H.; Niwa, O.; You, T. Pd–Ni Alloy Nanoparticle/Carbon Nanofiber Composites: Preparation, Structure, and Superior Electrocatalytic Properties for Sugar Analysis. *Anal. Chem.* **2014**, *86* (12), 5898–5905.
- (201) Guan, H.; Zhao, Y.; Zhang, J.; Liu, Y.; Yuan, S.; Zhang, B. Uniformly Dispersed PtNi Alloy Nanoparticles in Porous N-Doped Carbon Nanofibers with High Selectivity and Stability for Hydrogen Peroxide Detection. *Sensors Actuators B Chem.* **2018**, *261*, 354–363.

- (202) Zhang, P.; Wang, F.; Yu, M.; Zhuang, X.; Feng, X. Two-Dimensional Materials for Miniaturized Energy Storage Devices: From Individual Devices to Smart Integrated Systems. *Chem. Soc. Rev.* **2018**, *47* (19), 7426–7451.
- (203) Lv, Z.; Li, W.; Yang, L.; Loh, X. J.; Chen, X. Custom-Made Electrochemical Energy Storage Devices. *ACS Energy Lett.* **2019**, *4* (2), 606–614.
- (204) Zarei, M. Portable Biosensing Devices for Point-of-Care Diagnostics: Recent Developments and Applications. *TrAC Trends Anal. Chem.* **2017**, *91*, 26–41.
- (205) Kim, J.; Campbell, A. S.; de Ávila, B. E.-F.; Wang, J. Wearable Biosensors for Healthcare Monitoring. *Nat. Biotechnol.* **2019**, *37* (4), 389–406.
- (206) Yalcinkaya, F.; Yalcinkaya, B.; Jirsak, O. Influence of Salts on Electrospinning of Aqueous and Nonaqueous Polymer Solutions. *J. Nanomater.* **2015**, *2015*, 134251.
- (207) Frank, J. *Electron Tomography: Methods for Three-Dimensional Visualization of Structures in the Cell*; Springer New York, 2008.
- (208) Ding, B.; Wang, M.; Wang, X.; Yu, J.; Sun, G. Electrospun Nanomaterials for Ultrasensitive Sensors. *Mater. Today* **2010**, *13* (11), 16–27.
- (209) Choi, S.-H.; Ankonina, G.; Youn, D.-Y.; Oh, S.-G.; Hong, J.-M.; Rothschild, A.; Kim, I.-D. Hollow ZnO Nanofibers Fabricated Using Electrospun Polymer Templates and Their Electronic Transport Properties. *ACS Nano* **2009**, *3* (9), 2623–2631.
- (210) Khare, P.; Ramkumar, J.; Verma, N. Carbon Nanofiber-Skinned Three Dimensional Ni/Carbon Micropillars: High Performance Electrodes of a Microbial Fuel Cell. *Electrochim. Acta* **2016**, *219*, 88–98.
- (211) Zhou, Z.; Sigdel, S.; Gong, J.; Vaagensmith, B.; Elbohy, H.; Yang, H.; Krishnan, S.; Wu, X.-F.; Qiao, Q. Graphene-Beaded Carbon Nanofibers with Incorporated Ni Nanoparticles as Efficient Counter-Electrode for Dye-Sensitized Solar Cells. *Nano Energy* **2016**, *22*, 558–563.
- (212) Zhang, C.; Chen, Q.; Zhan, H. Supercapacitors Based on Reduced Graphene Oxide Nanofibers Supported Ni(OH)<sub>2</sub> Nanoplates with Enhanced Electrochemical Performance. *ACS Appl. Mater. Interfaces* **2016**, *8* (35), 22977–22987.
- (213) van Haasterecht, T.; Ludding, C. C. I.; de Jong, K. P.; Bitter, J. H. Toward Stable Nickel Catalysts for Aqueous Phase Reforming of Biomass-Derived Feedstock under Reducing and Alkaline Conditions. *J. Catal.* **2014**, *319*, 27–35.

- (214) Wang, G.; He, X.; Wang, L.; Gu, A.; Huang, Y.; Fang, B.; Geng, B.; Zhang, X. Non-Enzymatic Electrochemical Sensing of Glucose. *Microchim. Acta* **2013**, *180* (3–4), 161–186.
- (215) Tawfic, A.; Dickson-Anderson, S.; Kim, Y.; Mekky, W.; Baraka, A.; Gobara, M. Preparation and Characterization of Nickel Hexacyanoferrate Films for the Removal of Cesium Ion by Electrically Switched Ion Exchange (ESIX). *J. Solid State Electrochem.* **2017**, *21*, 2939–2946.
- (216) Zhan, B.; Liu, C.; Chen, H.; Shi, H.; Wang, L.; Chen, P.; Huang, W.; Dong, X. Free-Standing Electrochemical Electrode Based on Ni(OH)<sub>2</sub>/3D Graphene Foam for Nonenzymatic Glucose Detection. *Nanoscale* **2014**, *6* (13), 7424–7429.
- (217) Zhang, X.; Xu, Y.; Ye, B. An Efficient Electrochemical Glucose Sensor Based on Porous Nickel-Based Metal Organic Framework/Carbon Nanotubes Composite (Ni-MOF/CNTs). *J. Alloys Compd.* **2018**, *767*, 651–656.
- (218) Rezaeinasab, M.; Benvidi, A.; Tezerjani, M. D.; Jahanbani, S.; Kianfar, A. H.; Sedighipoor, M. An Electrochemical Sensor Based on Ni(II) Complex and Multi Wall Carbon Nano Tubes Platform for Determination of Glucose in Real Samples. *Electroanalysis* **2017**, *29* (2), 423–432.
- (219) Nery, E. W.; Kundys, M.; Jeleń, P. S.; Jönsson-Niedziółka, M. Electrochemical Glucose Sensing: Is There Still Room for Improvement? *Anal. Chem.* **2016**, *88*, 11271–11282.
- (220) Argyle, M. D.; Bartholomew, C. H. Heterogeneous Catalyst Deactivation and Regeneration: A Review. *Catalysts* **2015**, *5*, 145–269.
- (221) El-Refaei, S. M.; Saleh, M. M.; Awad, M. I. Tolerance of Glucose Electrocatalytic Oxidation on NiO<sub>x</sub>/MnO<sub>x</sub>/GC Electrode to Poisoning by Halides. *J. Solid State Electrochem.* **2014**, *18* (1), 5–12.
- (222) Mu, Y.; Jia, D.; He, Y.; Miao, Y.; Wu, H. L. Nano Nickel Oxide Modified Non-Enzymatic Glucose Sensors with Enhanced Sensitivity through an Electrochemical Process Strategy at High Potential. *Biosens. Bioelectron.* **2011**, *26*, 2948–2952.
- (223) Nie, H.; Yao, Z.; Zhou, X.; Yang, Z.; Huang, S. Nonenzymatic Electrochemical Detection of Glucose Using Well-Distributed Nickel Nanoparticles on Straight Multi-Walled Carbon Nanotubes. *Biosens. Bioelectron.* **2011**, *30*, 28–34.

- (224) Qiao, N.; Zheng, J. Nonenzymatic Glucose Sensor Based on Glassy Carbon Electrode Modified with a Nanocomposite Composed of Nickel Hydroxide and Graphene. *Microchim. Acta* **2012**, *177*, 103–109.
- (225) Luo, L.; Li, F.; Zhu, L.; Ding, Y.; Zhang, Z.; Deng, D.; Lu, B. Nonenzymatic Glucose Sensor Based on Nickel(II)Oxide/Ordered Mesoporous Carbon Modified Glassy Carbon Electrode. *Colloids Surfaces B Biointerfaces* **2013**, *102*, 307–311.
- (226) Choi, T.; Kim, S. H.; Lee, C. W.; Kim, H.; Choi, S. K.; Kim, S. H.; Kim, E.; Park, J.; Kim, H. Synthesis of Carbon Nanotube-Nickel Nanocomposites Using Atomic Layer Deposition for High-Performance Non-Enzymatic Glucose Sensing. *Biosens. Bioelectron.* **2015**, *63*, 325–330.
- (227) Zhuang, X.; Tian, C.; Luan, F.; Wu, X.; Chen, L. One-Step Electrochemical Fabrication of a Nickel Oxide Nanoparticle/Polyaniline Nanowire/Graphene Oxide Hybrid on a Glassy Carbon Electrode for Use as a Non-Enzymatic Glucose Biosensor. *RSC Adv.* **2016**, *6*, 92541–92546.
- (228) Shen, Z.; Gao, W.; Li, P.; Wang, X.; Zheng, Q.; Wu, H.; Ma, Y.; Guan, W.; Wu, S.; Yu, Y.; et al. Highly Sensitive Nonenzymatic Glucose Sensor Based on Nickel Nanoparticle-Attapulgite-Reduced Graphene Oxide-Modified Glassy Carbon Electrode. *Talanta* **2016**, *159*, 194–199.
- (229) Kannan, P.; Maiyalagan, T.; Marsili, E.; Ghosh, S.; Niedziolka-Jönsson, J.; Jönsson-Niedziolka, M. Hierarchical 3-Dimensional Nickel-Iron Nanosheet Arrays on Carbon Fiber Paper as a Novel Electrode for Non-Enzymatic Glucose Sensing. *Nanoscale* **2016**, *8*, 843–855.
- (230) Ni, Y.; Xu, J.; Liang, Q.; Shao, S. Enzyme-Free Glucose Sensor Based on Heteroatom-Enriched Activated Carbon (HAC) Decorated with Hedgehog-like NiO Nanostructures. *Sensors Actuators, B Chem.* **2017**, *250*, 491–498.
- (231) Qian, Q.; Hu, Q.; Li, L.; Shi, P.; Zhou, J.; Kong, J.; Zhang, X.; Sun, G.; Huang, W. Sensitive Fiber Microelectrode Made of Nickel Hydroxide Nanosheets Embedded in Highly-Aligned Carbon Nanotube Scaffold for Nonenzymatic Glucose Determination. *Sensors Actuators, B Chem.* **2018**, *257*, 23–28.
- (232) Marini, S.; Ben Mansour, N.; Hjiri, M.; Dhahri, R.; El Mir, L.; Espro, C.; Bonavita, A.; Galvagno, S.; Neri, G.; Leonardi, S. G. Non-Enzymatic Glucose Sensor Based on Nickel/Carbon Composite. *Electroanalysis* **2018**, *30* (4), 727–733.

- (233) Koskun, Y.; Şavk, A.; Şen, B.; Şen, F. Highly Sensitive Glucose Sensor Based on Monodisperse Palladium Nickel/Activated Carbon Nanocomposites. *Anal. Chim. Acta* **2018**, *1010*, 37–43.
- (234) Gao, W.; Li, Q.; Dou, M.; Zhang, Z.; Wang, F. Self-Supported Ni Nanoparticles Embedded on Nitrogen-Doped Carbon Derived from Nickel Polyphthalocyanine for High-Performance Non-Enzymatic Glucose Detection. *J. Mater. Chem. B* **2018**, *6*, 6781–6787.
- (235) Kulkarni, T.; Slaughter, G. Application of Semipermeable Membranes in Glucose Biosensing. *Membranes (Basel)*. **2016**, *6* (4), 55.
- (236) Chen, S.-M.; Liou, C.-Y.; Thangamuthu, R. Preparation and Characterization of Mixed-Valent Nickel Oxide/Nickel Hexacyanoferrate Hybrid Films and Their Electrocatalytic Properties. *Electroanalysis* **2007**, *19* (23), 2457–2464.
- (237) Joseph, J.; Gomathi, H.; Prabhakara Rao, G. Electrochemical Characteristics of Thin Films of Nickel Hexacyanoferrate Formed on Carbon Substrates. *Electrochim. Acta* **1991**, *36* (10), 1537–1541.
- (238) Abbaspour, A.; Kamyabi, M. A. Electrochemical Formation of Prussian Blue Films with a Single Ferricyanide Solution on Gold Electrode. *J. Electroanal. Chem.* **2005**, *584* (2), 117–123.
- (239) Oliveira, P. R.; Schibelbain, A. F.; Neiva, E. G. C.; Zarbin, A. J. G.; Marcolino, L. H.; Bergamini, M. F. Nickel Hexacyanoferrate Supported at Nickel Nanoparticles for Voltammetric Determination of Rifampicin. *Sensors Actuators B Chem.* **2018**, *260*, 816–823.
- (240) Karyakin, A. A. Prussian Blue and Its Analogues: Electrochemistry and Analytical Applications. *Electroanalysis* **2001**, *13* (10), 813–819.
- (241) Stone, J. R.; Yang, S. Hydrogen Peroxide: A Signaling Messenger. *Antioxid. Redox Signal.* **2006**, *8* (3–4), 243–270.
- (242) Juven, B. J.; Pierson, M. D. Antibacterial Effects of Hydrogen Peroxide and Methods for Its Detection and Quantitation. *J. Food Prot.* **1996**, *59* (11), 1233–1241.
- (243) Loo, A. E. K.; Wong, Y. T.; Ho, R.; Wasser, M.; Du, T.; Ng, W. T.; Halliwell, B. Effects of Hydrogen Peroxide on Wound Healing in Mice in Relation to Oxidative Damage. *PLoS One* **2012**, *7* (11), e49215.



- (244) Niethammer, P.; Grabher, C.; Look, A. T.; Mitchison, T. J. A Tissue-Scale Gradient of Hydrogen Peroxide Mediates Rapid Wound Detection in Zebrafish. *Nature* **2009**, *459* (7249), 996–999.
- (245) Kanta, J. The Role of Hydrogen Peroxide and Other Reactive Oxygen Species in Wound Healing. *Acta Medica (Hradec Kralove)* **2011**, *54*, 97–101.
- (246) Wittmann, C.; Chockley, P.; Singh, S. K.; Pase, L.; Lieschke, G. J.; Grabher, C. Hydrogen Peroxide in Inflammation: Messenger, Guide, and Assassin. *Adv. Hematol.* **2012**, *2012*, 541471.
- (247) Gill, R.; Bahshi, L.; Freeman, R.; Willner, I. Optical Detection of Glucose and Acetylcholine Esterase Inhibitors by H<sub>2</sub>O<sub>2</sub>-Sensitive CdSe/ZnS Quantum Dots. *Angew. Chemie Int. Ed.* **2008**, *47* (9), 1676–1679.
- (248) Chen, S.; Hai, X.; Chen, X.-W.; Wang, J.-H. In Situ Growth of Silver Nanoparticles on Graphene Quantum Dots for Ultrasensitive Colorimetric Detection of H<sub>2</sub>O<sub>2</sub> and Glucose. *Anal. Chem.* **2014**, *86* (13), 6689–6694.
- (249) Germain, M. E.; Knapp, M. J. Turn-on Fluorescence Detection of H<sub>2</sub>O<sub>2</sub> and TATP. *Inorg. Chem.* **2008**, *47* (21), 9748–9750.
- (250) Karyakin, A. A.; Karyakina, E. E. Prussian Blue-Based ‘Artificial Peroxidase’ as a Transducer for Hydrogen Peroxide Detection. Application to Biosensors. *Sensors Actuators B Chem.* **1999**, *57* (1), 268–273.
- (251) Zhang, L.; Zhai, Y.; Gao, N.; Wen, D.; Dong, S. Sensing H<sub>2</sub>O<sub>2</sub> with Layer-by-Layer Assembled Fe<sub>3</sub>O<sub>4</sub>-PDDA Nanocomposite Film. *Electrochem. commun.* **2008**, *10* (10), 1524–1526.
- (252) Chakraborty, S.; Retna Raj, C. Pt Nanoparticle-Based Highly Sensitive Platform for the Enzyme-Free Amperometric Sensing of H<sub>2</sub>O<sub>2</sub>. *Biosens. Bioelectron.* **2009**, *24* (11), 3264–3268.
- (253) Zhang, Y.; Bai, X.; Wang, X.; Shiu, K.-K.; Zhu, Y.; Jiang, H. Highly Sensitive Graphene–Pt Nanocomposites Amperometric Biosensor and Its Application in Living Cell H<sub>2</sub>O<sub>2</sub> Detection. *Anal. Chem.* **2014**, *86* (19), 9459–9465.

- (254) Chen, D.; Zhuang, X.; Zhai, J.; Zheng, Y.; Lu, H.; Chen, L. Preparation of Highly Sensitive Pt Nanoparticles-Carbon Quantum Dots/Ionic Liquid Functionalized Graphene Oxide Nanocomposites and Application for H<sub>2</sub>O<sub>2</sub> Detection. *Sensors Actuators B Chem.* **2018**, 255, 1500–1506.
- (255) Sun, Y.; He, K.; Zhang, Z.; Zhou, A.; Duan, H. Real-Time Electrochemical Detection of Hydrogen Peroxide Secretion in Live Cells by Pt Nanoparticles Decorated Graphene-Carbon Nanotube Hybrid Paper Electrode. *Biosens. Bioelectron.* **2015**, 68, 358–364.
- (256) Liu, J.; Bo, X.; Zhao, Z.; Guo, L. Highly Exposed Pt Nanoparticles Supported on Porous Graphene for Electrochemical Detection of Hydrogen Peroxide in Living Cells. *Biosens. Bioelectron.* **2015**, 74, 71–77.
- (257) Zhang, Y.; Sun, Y.; Liu, Z.; Xu, F.; Cui, K.; Shi, Y.; Wen, Z.; Li, Z. Au Nanocages for Highly Sensitive and Selective Detection of H<sub>2</sub>O<sub>2</sub>. *J. Electroanal. Chem.* **2011**, 656 (1), 23–28.
- (258) Ning, R.; Lu, W.; Zhang, Y.; Qin, X.; Luo, Y.; Hu, J.; Asiri, A. M.; Al-Youbi, A. O.; Sun, X. A Novel Strategy to Synthesize Au Nanoplates and Their Application for Enzymeless H<sub>2</sub>O<sub>2</sub> Detection. *Electrochim. Acta* **2012**, 60, 13–16.
- (259) Ju, J.; Chen, W. In Situ Growth of Surfactant-Free Gold Nanoparticles on Nitrogen-Doped Graphene Quantum Dots for Electrochemical Detection of Hydrogen Peroxide in Biological Environments. *Anal. Chem.* **2015**, 87 (3), 1903–1910.
- (260) Ma, B.; Kong, C.; Hu, X.; Liu, K.; Huang, Q.; Lv, J.; Lu, W.; Zhang, X.; Yang, Z.; Yang, S. A Sensitive Electrochemical Nonenzymatic Biosensor for the Detection of H<sub>2</sub>O<sub>2</sub> Released from Living Cells Based on Ultrathin Concave Ag Nanosheets. *Biosens. Bioelectron.* **2018**, 106, 29–36.
- (261) Qin, X.; Luo, Y.; Lu, W.; Chang, G.; Asiri, A. M.; Al-Youbi, A. O.; Sun, X. One-Step Synthesis of Ag Nanoparticles-Decorated Reduced Graphene Oxide and Their Application for H<sub>2</sub>O<sub>2</sub> Detection. *Electrochim. Acta* **2012**, 79, 46–51.
- (262) Qin, X.; Lu, W.; Luo, Y.; Chang, G.; Sun, X. Preparation of Ag Nanoparticle-Decorated Polypyrrole Colloids and Their Application for H<sub>2</sub>O<sub>2</sub> Detection. *Electrochem. commun.* **2011**, 13 (8), 785–787.
- (263) You, J.-M.; Kim, D.; Kim, S. K.; Kim, M.-S.; Han, H. S.; Jeon, S. Novel Determination of Hydrogen Peroxide by Electrochemically Reduced Graphene Oxide Grafted with Amino thiophenol–Pd Nanoparticles. *Sensors Actuators B Chem.* **2013**, 178, 450–457.

- (264) Bozkurt, S.; Tosun, B.; Sen, B.; Akocak, S.; Savk, A.; Ebeoğlu, M. F.; Sen, F. A Hydrogen Peroxide Sensor Based on TNM Functionalized Reduced Graphene Oxide Grafted with Highly Monodisperse Pd Nanoparticles. *Anal. Chim. Acta* **2017**, 989, 88–94.
- (265) Xue, W.; Bo, X.; Zhou, M.; Guo, L. Enzymeless Electrochemical Detection of Hydrogen Peroxide at Pd Nanoparticles/Porous Graphene. *J. Electroanal. Chem.* **2016**, 781, 204–211.
- (266) Zhang, L.; Aboagye, A.; Kelkar, A.; Lai, C.; Fong, H. A Review: Carbon Nanofibers from Electrospun Polyacrylonitrile and Their Applications. *J. Mater. Sci.* **2014**, 49 (2), 463–480.
- (267) Liu, Y.; Wang, D.; Xu, L.; Hou, H.; You, T. A Novel and Simple Route to Prepare a Pt Nanoparticle-Loaded Carbon Nanofiber Electrode for Hydrogen Peroxide Sensing. *Biosens. Bioelectron.* **2011**, 26 (11), 4585–4590.
- (268) Li, Y.; Zhang, M.; Zhang, X.; Xie, G.; Su, Z.; Wei, G. Nanoporous Carbon Nanofibers Decorated with Platinum Nanoparticles for Non-Enzymatic Electrochemical Sensing of H<sub>2</sub>O<sub>2</sub>. *Nanomaterials* **2015**, 5 (4), 1891–1905.
- (269) Demir, M. M.; Gulgun, M. A.; Menciloglu, Y. Z.; Erman, B.; Abramchuk, S. S.; Makhaeva, E. E.; Khokhlov, A. R.; Matveeva, V. G.; Sulman, M. G. Palladium Nanoparticles by Electrospinning from Poly(Acrylonitrile-Co-Acrylic Acid)–PdCl<sub>2</sub> Solutions. Relations between Preparation Conditions, Particle Size, and Catalytic Activity. *Macromolecules* **2004**, 37 (5), 1787–1792.
- (270) Tsuji, J. II. Palladium Compounds and Complexes Useful in Organic Synthesis. In *Organic Synthesis with Palladium Compounds*; Tsuji, J., Ed.; Springer Berlin Heidelberg: Berlin, Heidelberg, 1980; pp 2–3.
- (271) Wen, S.; Liang, M.; Zou, R.; Wang, Z.; Yue, D.; Liu, L. Electrospinning of Palladium/Silica Nanofibers for Catalyst Applications. *RSC Adv.* **2015**, 5 (52), 41513–41519.
- (272) Cai, X.; Tanner, E. E. L.; Lin, C.; Ngamchuea, K.; Foord, J. S.; Compton, R. G. The Mechanism of Electrochemical Reduction of Hydrogen Peroxide on Silver Nanoparticles. *Phys. Chem. Chem. Phys.* **2018**, 20 (3), 1608–1614.
- (273) Prabhu, V. G.; Zarapkar, L. R.; Dhaneshwar, R. G. Electrochemical Studies of Hydrogen Peroxide at a Platinum Disc Electrode. *Electrochim. Acta* **1981**, 26 (6), 725–729.
- (274) Forman, H. J.; Bernardo, A.; Davies, K. J. A. What Is the Concentration of Hydrogen Peroxide in Blood and Plasma? *Arch. Biochem. Biophys.* **2016**, 603, 48–53.

- (275) Giorgio, M.; Trinei, M.; Migliaccio, E.; Pelicci, P. G. Hydrogen Peroxide: A Metabolic by-Product or a Common Mediator of Ageing Signals? *Nat. Rev. Mol. Cell Biol.* **2007**, *8* (9), 722–728.
- (276) Halliwell, B.; Clement, M. V.; Long, L. H. Hydrogen Peroxide in the Human Body. *FEBS Lett.* **2000**, *486* (1), 10–13.
- (277) Suzuki, N.; Mittler, R. Reactive Oxygen Species-Dependent Wound Responses in Animals and Plants. *Free Radic. Biol. Med.* **2012**, *53* 12, 2269–2276.
- (278) Wade, R. C. Catalyzed Reduction of Organofunctional Groups with Sodium Borohydride. *J. Mol. Catal.* **1983**, *18* (3), 273–297.
- (279) Chen, S.; Yuan, R.; Chai, Y.; Hu, F. Electrochemical Sensing of Hydrogen Peroxide Using Metal Nanoparticles: A Review. *Microchim. Acta* **2013**, *180* (1), 15–32.
- (280) Baghayeri, M.; Veisi, H. Fabrication of a Facile Electrochemical Biosensor for Hydrogen Peroxide Using Efficient Catalysis of Hemoglobin on the Porous Pd@Fe<sub>3</sub>O<sub>4</sub>-MWCNT Nanocomposite. *Biosens. Bioelectron.* **2015**, *74*, 190–198.
- (281) Wang, J.; Wang, Z.; Zhao, D.; Xu, C. Facile Fabrication of Nanoporous PdFe Alloy for Nonenzymatic Electrochemical Sensing of Hydrogen Peroxide and Glucose. *Anal. Chim. Acta* **2014**, *832*, 34–43.
- (282) Sitnikova, N. A.; Borisova, A. V; Komkova, M. A.; Karyakin, A. A. Superstable Advanced Hydrogen Peroxide Transducer Based on Transition Metal Hexacyanoferrates. *Anal. Chem.* **2011**, *83* (6), 2359–2363.
- (283) Fiorito, P. A.; Córdoba de Torresi, S. I. Hybrid Nickel Hexacyanoferrate/Polypyrrole Composite as Mediator for Hydrogen Peroxide Detection and Its Application in Oxidase-Based Biosensors. *J. Electroanal. Chem.* **2005**, *581* (1), 31–37.
- (284) Lin, J.; Zhou, D. M.; Hocevar, S. B.; McAdams, E. T.; Ogorevc, B.; Zhang, X. Nickel Hexacyanoferrate Modified Screen-Printed Carbon Electrode for Sensitive Detection of Ascorbic Acid and Hydrogen Peroxide. *Front. Biosci.* **2005**, *10*, 483–491.

## Curriculum Vitae

### Personal Data

---

Name	Marcel Simsek
Address	Solar B8, 91161 Hilpoltstein
Date of birth	March 8 <sup>th</sup> 1992
Place of birth	Nürnberg, Germany
Nationality	German

### Academical Education

---

10/2017 – 02/2021	<b>Ph.D. studies “Laser-Induced Functional Carbon Nanofibers for Electrochemical Sensing”</b> Analytical department, Universität Regensburg
04/2015 – 09/2017	<b>Studies of chemistry (Master of Science)</b> Universität Regensburg
10/2016 – 07/2017	<b>Master’s thesis “Electrospun Non-conductive Polyaniline and its High Efficient Post-acid Doping Processes applicable for Electrochemical Sensing”</b> Analytical department, Universität Regensburg
10/2010 – 09/2014	<b>Studies of applied chemistry (Bachelor of Science)</b> Technische Hochschule Nürnberg Georg Simon Ohm
01/2014 – 07/2014	<b>Bachelor’s thesis “Charakterisierung von pflanzlichen Tetraspaninen in <i>Arabidopsis thaliana</i>“</b> Department of cell biology Friedrich-Alexander-Universität Erlangen-Nürnberg
03/2012 – 07/2012	<b>Internship semester “Microbiology”</b> Analytik Institut Rietzler, Ansbach

---

## Education

---

- 09/2008 – 07/2010    **Advanced technical college entrance qualification  
(Fachhochschulreife)**  
Staatliche Fachoberschule Weißenburg in Bayern
- 12/2004 – 07/2008    **Intermediate school-leaving certificate (Mittlere Reife)**  
Staatliche Realschule Hilpoltstein

---

## Professional Experience

---

- 08/2017 – 09/2017    Holiday job “Assembly line”, Bolta Werke GmbH, Leinburg/Diepersdorf
- 07/2015 – 09/2015    Holiday job “Assembly line”, Robert Bosch GmbH, Nürnberg
- 09/2014 – 10/2014    Holiday job “Microbiology”, Analytik Institut Rietzler, Ansbach
- 08/2013 – 09/2013    Holiday job “Microbiology”, Analytik Institut Rietzler, Ansbach
- 07/2012 – 09/2012    Holiday job “Microbiology”, Analytik Institut Rietzler, Ansbach
- 08/2011 – 09/2011    Holiday job “Electrical trades”, Baumüller Reparaturwerk GmbH & Co.  
KG, Nürnberg
- 07/2010 – 08/2010    Holiday job “Logistics”, LEONI Kabel GmbH, Roth

## Publications

Wongkaew, N.; Simsek, M.; Griesche, C.; Baeumner, A. J. Functional Nanomaterials and Nanostructures Enhancing Electrochemical Biosensors and Lab-on-a-Chip Performances: Recent Progress, Applications, and Future Perspective. *Chem. Rev.* **2018**, 119, 120–194.

Wongkaew, N.; Simsek, M.; Arumugam, P.; Behrent, A.; Berchmans, S.; Baeumner, A. J. A Robust Strategy Enabling Addressable Porous 3D Carbon-Based Functional Nanomaterials in Miniaturized Systems. *Nanoscale* **2019**, 11, 3674–3680.

Simsek, M.; von Kruechten, L.; Buchner, M.; Duerkop, A.; Baeumner, A. J.; Wongkaew, N. An Efficient Post-Doping Strategy Creating Electrospun Conductive Nanofibers with Multi-Functionalities for Biomedical Applications. *J. Mater. Chem. C* **2019**, 7 (30), 9316–9325.

Wongkaew, N.; Simsek, M.; Heider, J.; Wegener, J.; Baeumner, A. J.; Schreml, S.; Stolwijk, J. A. Cytocompatibility of Mats Prepared from Different Electrospun Polymer Nanofibers. *ACS Appl. Bio Mater.* **2020**, 3 (8), 4912–4921.

Simsek, M.; Hoecherl, K.; Schlosser, M.; Baeumner, A. J.; Wongkaew, N. Printable 3D Carbon Nanofiber Networks with Embedded Metal Nanocatalysts. *ACS Appl. Mater. Interfaces* **2020**, 12 (35), 39533–39540.

Mobarez, S. N.; Wongkaew, N.; Simsek, M.; Baeumner, A. J.; Duerkop, A. Dipsticks with Reflectometric Readout of an NIR Dye for Determination of Biogenic Amines. *Chemosensors* **2020**, 8 (4), 99.

## **Presentations**

### **Oral Presentations**

2019 2<sup>nd</sup> European Biosensor Symposium (EBS), Florence, Italy

Poster Flash Presentation on “Carbon Nanofibers for Electrochemical Sensing Fabricated by Novel Laser-Induced Carbonization of Electrospun Polyimide”

### **Poster Presentations**

2018 European Materials Research Society (E-MRS) Spring Meeting, Strasbourg, France

“Electrospun Non-Conductive Polyaniline and its Highly Efficient Post-Acid Doping Processes Enabling Versatile Biosensing Functionalities”

2019 2<sup>nd</sup> European Biosensor Symposium (EBS), Florence, Italy

“Carbon Nanofibers for Electrochemical Sensing Fabricated by Novel Laser-Induced Carbonization of Electrospun Polyimide”





## **Eidesstattliche Erklärung**

Ich erkläre hiermit an Eides statt, dass ich die vorliegende Arbeit ohne unzulässige Hilfe Dritter und ohne Benutzung anderer als der angegebenen Hilfsmittel angefertigt habe; die aus anderen Quellen direkt oder indirekt übernommenen Daten und Konzepte sind unter Angabe des Literaturzitats gekennzeichnet.

Weitere Personen waren an der inhaltlich-materiellen Herstellung der vorliegenden Arbeit nicht beteiligt. Insbesondere habe ich hierfür nicht die entgeltliche Hilfe eines Promotionsberaters oder anderer Personen in Anspruch genommen. Niemand hat von mir weder unmittelbar noch mittelbar geldwerte Leistungen für Arbeiten erhalten, die im Zusammenhang mit dem Inhalt der vorgelegten Dissertation stehen.

Die Arbeit wurde bisher weder im In- noch im Ausland in gleicher oder ähnlicher Form einer anderen Prüfungsbehörde vorgelegt.

---

Ort, Datum

Unterschrift

